Fundamental Understandings on Electrochemical $CO_{(2)}$ Reduction on Cu and Cu-based Catalysts

Qiao, Yu

Publication date:
2023

Document Version
Publisher's PDF, also known as Version of record

DTU Physics
Department of Physics

Fundamental Understandings on Electrochemical $CO_{(2)}$ Reduction on Cu and Cu-based Catalysts

Yu Qiao

Supervisor: Professor Brian Seger

Co-Supervisor: Professor Ib Chorkendorff

Ph.D. Thesis

Section of Surface Physics & Catalysis (SurfCat)

Department of Physics

Technical University of Denmark

March 2023

Abstract

Anthropogenic activities have been strongly reliant on fossil fuels since the industrial revolution. Combustion of fossil fuels releases a great amount of greenhouse gases, particularly, carbon dioxide (CO_2), resulting in global warming and further catastrophic impacts on the earth and human beings. Inclining the primary energy source to renewable energy such as solar radiation and wind would help mitigate carbon emissions. Yet, power produced from the sun and the wind is intermittent due to its strong weather-condition dependency, and thus needs to be stored in a stable and efficient way. Electrochemical CO_2 reduction reaction (eCO2RR) is such a strategy that stores renewable energy in chemical bonds by electrochemically converting CO_2 into chemicals and fuels, and thus close the carbon cycle.

Copper (Cu) has been known as the only monometallic eCO2RR catalyst that produces a variety of fuels, such as methane, ethylene, acetaldehyde, ethanol, *etc*. However, most of the products are simultaneously produced during eCO2RR. Improving the selectivity toward specific species requires mechanistic insights into the obscure reaction mechanism and pathways of eCO2RR. To this end, Cu single crystals with well-defined surface structures are employed as a model platform for building up the structure-performance correlation. Electrochemical $CO_{(2)}$ reduction reactions are carried out on an electrochemistry-mass spectrometry (EC-MS) system which enables real-time gas and volatile liquid product detection and analyzation. Upon optimizing the mass spectrometer parameters, not only gas products (including methane, ethylene, and hydrogen from the side-reaction water splitting), but also the liquid product acetaldehyde are successfully detected and qualitatively tracked (in molar flux). The production of another volatile liquid product ethanol, on the other hand, cannot be tracked with a suitable descriptor, which may be attributed to the strong interference from hydrogen *via* the molecule-ion reaction mechanism. Considering that *CO is the most important intermediate in reducing CO_2 to multicarbon products, electrochemical CO reduction is carried out on four single crystal Cu electrodes: (100), (110), (111), and

(211). The preference of methane and ethylene production on the Cu(110) and (100) facets, respectively, as well as the shared reaction pathway between acetaldehyde and ethylene are spectrometrically testified. Acetaldehyde chemistry in alkaline is also investigated. This work provides mechanistic information on the facet-dependent eCO2RR product distribution on Cu, as well as the acetaldehyde activity under the reaction conditions, and therefore helps steer the product selectivity towards acetaldehyde and ethanol.

In addition to the surface structure of Cu catalysts, the formation of multicarbon products with high energy density requires a high coverage of *CO intermediate. Hence, combing Cu with a CO-producing co-catalyst is expected to improve the local CO concentration and thus *CO coverage, facilitating multicarbon product formation. Silver (Ag) is a promising co-catalyst in this regard. It has been found that introducing Ag atoms into the Cu lattice can modulate product preference. However, the synergistic effects between Cu and Ag, and thus the catalytic performance, are strongly influenced by catalyst morphology, electrolyzer configuration, reaction conditions, *etc. Operando* measurements can provide explicit information on the catalyst dynamic variation during the reaction, but their operation and analysis are challenging. herein, CuAg multiphase alloy catalysts are prepared by magnetron sputtering, which allowed for investigating the intrinsic interaction between Cu and Ag. Electrochemical CO_2 reduction performance exhibited an improved selectivity towards carbonyls at the expense of hydrogen and hydrocarbons. The partially alloyed Cu and Ag phases were confirmed by *operando* X-ray diffraction. By means of combining *operando* X-ray measurements and density functional theory (DFT) calculations, the preferred carbonyl production is attributed to the reduced electron density and compressive strain of Cu due to Ag incorporation, which leads to a deeper d-band center and therefore weakened intermediate adsorption and oxophilicity. This work provides evidence of the intrinsic structural and electronic interaction between Cu and Ag during eCO2RR. The obtained information will facilitate the design of new bi-/multi-phase metallic or alloy electrocatalysts.

Works presented in this thesis provide mechanistic information for a better understanding on the eCO2RR pathways, as well as for the design and fabrication of new alloy catalysts for eCO2RR.

Resumé

Anthropogene aktiviteter har været stærkt afhængige af fossile brændstoffer siden den industrielle revolution. Under forbrænding af fossile brændstoffer frigives en stor mængde drivhusgasser hvilket resulterer i global opvarmning og yderligere katastrofale indvirkninger på jorden og mennesker. Ved at udskifte den primære energikilde til vedvarende energikilder såsom sol- og vindenergi kulstofemissionerne reduceres. På grund af upålidelige vejr mønstre må strøm produceret fra sol og vinden derfor opbevares på en stabil og effektiv måde. Elektrokemisk CO_2-reduktionsreaktion (eCO2RR) er en strategi, der lagrer vedvarende energi i kemiske bindinger ved elektrokemisk at omdanne CO_2 til kemikalier og brændstoffer, og dermed lukke kulstofkredsløbet og ungå en højere CO_2 koncentration i atmosfæren.

Kobber (Cu) har været kendt som den eneste monometalliske eCO2RR-katalysator, der producerer en række forskellige brændstoffer, såsom metan, ethylen, acetaldehyd, ethanol osv. En af ulemperne ved eCO2RR er dog at de fleste af produkterne produceres samtidigt. Forbedring af selektiviteten over for specifikke kemikalier kræver mekanistisk indsigt i eCO2RR's komplexe reaktionsmekanisme og ruter. Til dette formål anvendes Cu-enkeltkrystaller med veldefinerede overfladestrukturer som en modelplatform til opbygning af korrelationen mellem krystalstruktur og ydeevne. Elektrokemiske $CO_{(2)}$-reduktionsreaktioner udføres på et elektrokemisk-massespektrometer (EC-MS) system, som muliggør realtids analyse af gas og fordampede flydende produkter. Ved optimering af massespektrometerparametrene bliver ikke kun gasprodukter (herunder methan, ethylen og brint fra sidereaktionens vandspaltning), men også det flydende produkt acetaldehyd detekteret og kvalitativt sporet (i molær flux). Produktionen af det flydende produkt, ethanol, kan derimod ikke spores med en passende deskriptor, hvilket kan tilskrives den stærke interferens fra brint via molekyle-ion-reaktionsmekanismen. I betragtning af at *CO er det vigtigste mellemprodukt til reduktion af CO_2 til multicarbonprodukter, udføres elektrokemisk CO-reduktion på fire enkeltkrystal Cu-elektroder: (100), (110), (111) og (211). Præferencen for methan- og ethylenproduktion på henholdsvis Cu(111)- og (100)-facetterne

såvel som den fælles reaktionsvej mellem acetaldehyd og ethylen er spektrometrisk bevidnet. Acetaldehyd kemi i alkalisk er også undersøgt. Dette arbejde giver mekanistisk information om den facetafhængige eCO2RR-produktfordeling på Cu, samt acetaldehydaktiviteten under reaktionsbetingelserne, og hjælper derfor med at styre produktselektiviteten mod acetaldehyd og ethanol.

Ud over overfladestrukturen af Cu-katalysatorer kræver dannelsen af multicarbon-produkter med høj energiintensitet en høj dækning af *CO-mellemprodukt. Derfor forventes kombinationen af Cu med en CO-producerende co-katalysator at forbedre den lokale CO-koncentration og dermed *CO-dækning, hvilket forbedrer dannelsen af multicarbon-produkt. Sølv (Ag) er en lovende co-katalysator i denne henseende. Det har vist sig, at indføring af Ag-atomer i Cu-gitteret kan ændre produktpræferencen. De synergistiske effekter mellem Cu og Ag, og dermed den katalytiske ydeevne, er imidlertid stærkt påvirket af katalysatormorfologi, elektrolysatorkonfiguration, reaktionsbetingelser osv. *Operando*-målinger kan give eksplicit information om katalysatorens dynamiske variation under reaktionen, men deres funktion og analyser er udfordrende. Heri fremstilles CuAg flerfasede legeringskatalysatorer ved magnetronsputtering, hvilket gjorde det muligt at undersøge interaktionen mellem Cu og Ag. Elektrokemisk CO_2-reduktion udviste en forbedret selektivitet over for carbonyler på bekostning af hydrogen og kulbrinter. De delvist legerede Cu- og Ag-faser blev bekræftet ved *operando*-røntgendiffraktion. Ved at kombinere *operando*-røntgenmålinger og density functional theory (DFT) beregninger tilskrives den foretrukne carbonylproduktion den reducerede elektrondensitet og kompressionsbelastning af Cu på grund af Ag-inkorporering, hvilket fører til et dybere d-båndscenter og derfor svækket intermediær adsorption og oxofilicitet. Dette arbejde giver bevis på den iboende strukturelle og elektroniske interaktion mellem Cu og Ag under eCO2RR. De opnåede oplysninger vil lette designet af nye bi-/flerfasede metalliske eller legerede elektrokatalysatorer.

Værker præsenteret i denne afhandling giver mekanistisk information til en bedre forståelse af eCO2RR-vejene, såvel som for design og fremstilling af nye legeringskatalysatorer til eCO2RR.

Preface

This thesis is submitted to the Technical University of Denmark (DTU) as part of the requirement for obtaining a Doctor of Philosophy (PhD) degree in Physics. The presented work was carried out at DTU, Department of Physics, the Section for Surface Physics and Catalysis (SurfCat) from February 2020 to March 2023, under the supervision of Prof. Brian Seger and Prof. Ib Chorkendorff funded by European Union's Horizon 2020 research and innovation programme under grant agreement no. 85144, (SELECT-CO2). During this time, I took an external stay at Stanford University, Department of Chemical Engineering, from January 2022 to May 2022, with Prof. Thomas F. Jaramillo as the advisor. The external stay received a travel grant from Otto Mønsted. Synchrotron measurements were conducted with the Stanford Synchrotron Radiation Lightsource, (SSRL) at the SLAC National Accelerator Laboratory.

My experiments are carried out in collaboration with other colleagues and students, and with guidance from all supervisors. Throughout this thesis, the pronoun "I" is used to highlight the works and ideas exclusively carried out by myself; while "we" is used to denote collective efforts and ideas wherever the contribution from me and the others are not differentiated. Contributors to different projects in this thesis are stated in the respective chapters.

Yu Qiao

March 2023

Acknowledgment

Doing PhD at Surfcat is such a beautiful journey in my life, not only due to the creative and stimulating research, but also because of all the fantastic colleagues and friends with whom I have worked and spent time here.

First and foremost, I would like to express my sincerest and deepest gratitude to my supervisors, Prof. Brian Seger and Prof. Ib Chorkendorff, for their patient and inspiring guidance and feedback throughout my PhD, as well as for sharing their extensive knowledge and infectious enthusiasm for science. They also trained me to think unbiasedly and critically. Brian's office is next to ours and we talked almost every day. Although having a busy schedule, he is always willing to take time to talk and share advice, as well as use his resources to help and provide support on any work-related difficulties.

Particularly, I would like to thank our entire CO_2 team. To my officemate Carlos Andres Giron Rodriguez, I am really thankful for his help and input in the synchrotron measurements. I would have no way to survive all the beamtimes without his help. Another officemate, Sahil Garg, is greatly appreciated for giving me so much valuable encouragement and suggestions in research, presentation skills, career, and all other work-related and non-work-related aspects. The small jokes, gossip, and complaints in our office are very important components of my PhD. I am also thankful to Wanyu Deng, for countless discussions and help regarding research and life. Her big smile lights up the day. My gratitude also goes to Tuğçe Yılmaz for discussions on the EC-MS measurements and her warm words when I was having a hard time. The humorous talks between us made doing experiments much more enjoyable. To Qiucheng Xu and Clara Bruun Jensen, I owe my gratitude for preparing beamtime samples and sending them to the US during my external stay there. Qiucheng has also given me helpful advice on improving my communication skills, and the snacks he shared from time to time could always energize me when I was tired. Speaking of snacks, Clara's Christmas

cookies cannot be neglected. I have learned a lot from Asger Barkholt Moss (now one of the floor managers) about the working mechanism of all kinds of setups, devices and accessories related and non-related to research. Whenever I asked a random question, he was ready to give a comprehensive introduction lecture. I would also like to thank Bjørt Óladóttir Joensen for helping with beamtime preparation, writing the Danish abstract of this thesis, and accommodating me in her place in the US for the first week of my external stay there. Unfortunately, I did not have much chance to work with Francesco Longhin, the newest team member, but I still appreciate the cookies he generously shared – his desk was like a supply station to refill my empty energy tank. Thanks are also given to Gastón O. Larrazábal and Ezra L. Clark, two former group members, who introduced me to CO_2 reduction as well as knowledge in electrochemistry and surface science. I am also grateful to Tugce, Carlos, Sahil, Asger, Qiucheng and Bjørt for proofreading this thesis.

My projects were strongly supported by computational simulations, for which I profoundly appreciate Prof. Georg Kastlunger at CatTheory for all the fruitful and constructive discussions and insights from a theoretical perspective. In addition, I owe a great debate of gratitude to Prof. Christian Danvad Damsgaard, Shaofeng Li, and Chao Wei for their insightful discussions on data processing and analysis regarding X-ray measurements. Thanks also go to Degenhart Hochfilzer for EC-MS training and all the informative discussions and inputs. I would also like to acknowledge Yarong Zheng for sharing some small yet highly useful tricks for carrying out EC-MS experiments. Ke Zhang has furnished me with knowledge in (ultra) high vacuum systems. A special thank you goes to Rasmus Nielsen, for his patience and help in solving the problems I encountered while sputtering.

I would also like to extend my heartfelt gratitude to our lab and floor managers, Jacqueline McAnulty, Brian Peter Knudsen, Jakob Ejler Sørensen, Asger Barkholt Moss, and Patrick Strøm-Hansen, for keeping everything running smoothly, and more importantly, for maintaining a safe environment for all of us to work. I am also grateful to Birgit Bohn for dealing with administrative and financial issues. I cannot remember how many times I had been frustrated with orders and payments for hours, until she came and set everything up with a couple of magic clicks. I would also like to thank Dan Shacham and Peder Heise in the workshop for making pieces that are very small in size but extremely essential in significance for my experiments. The sniffer mascot deserves a special thank you for taking care of the EC-MS setup with some “supernatural” power. None of my experiments could be running without them.

Apart from work, Katja Li and Yanxin Liu will also be missed as friends and neighbors. The delicious food they shared with me and all their generous help whenever I was in need are

truly meaningful to me. I have also gained so much help and great training from Xianbiao Fu in bike repair.

From January to May in 2023 I had the opportunity to take an external stay at Stanford University. I would like to express my sincere gratitude to Prof. Thomas F. Jaramillo for accommodating me as a visiting scholar in his research group. His optimism and enthusiasm for science and everything else have encouraged me a lot. During my external stay, I mainly worked on preparing and preliminary testing for synchrotron measurements, and I was fortunate to get help from many postdocs and PhD students there. To Peter Benedek, Junjie Chen, Johanna Schröderc, Joseph Perryman, Dong Un (Daniel) Lee, Melissa Kreider, José Zamora Zeledón, and Sihe Zhang, I owe my appreciation for their contributions to the beamtimes – preparing samples, setting up, running measurements, cleaning up, *etc.* – none of these could be done without any of them. I also had the chance to make friends and hang out with the Chinese members: Lingze (Lily) Wei, Sihe Zhang, Junjie Chen, and Yi Xu. I will always remember the delightful time in sunny California and the authentic Chinese food we had.

Synchrotron measurements would not be possible without technical support from all beamline scientists, Ryan C. Davis, Kevin Stone, Charles Troxel Jr, Matthew Latimer, and Erik Nelson and beamline engineer Sarah Gooding. I am truly thankful to them, especially Ryan, for his patient and detailed explanations of XAS mechanism understanding, measurement operation, and data processing.

Last but not least, I would like to thank my parents, for their unconditional, unwavering, and endless love and support throughout my life. I have not seen them in person for over three years due to COVID and related issues, but whenever I am stressed and feel sad, they always cheer me up. Another family member, my teddy bear Fenfen, I am grateful for his continuous accompany over the past sixteen years. All other members of the extended family and all my friends around the world have also given me significant emotional support.

Nomenclature

Abbreviation	Term
AC	Alternative current
AE	Appearance energy
AMU	Atomic mass unit
atm	Atmosphere
C_1	Electrochemical $CO_{(2)}$ reduction products with one carbon
C_2	Electrochemical $CO_{(2)}$ reduction products with two carbons
C_{2+}	Electrochemical $CO_{(2)}$ reduction products with more than 2 carbons
CA	Chronoamperometry
CE	Counter electrode
CI	Chemical ionization
CP	Chronopotentiometry
CV	Cyclic voltammetry
DAD	Diode Array Detector
DC	Direct current
DFT	Density-functional theory

EC	Electrochemical/electrochemistry
EC-MS	Electrochemistry-mass spectrometry
eCO(2)RR	Electrochemical $CO_{(2)}$ reduction reaction
ECSTM	Electrochemical scanning tunneling microscopy
EE	Electron energy
EIS	Electrochemical impedance spectroscopy
EXAFS	Extended X-ray Absorption Fine Structure
fcc	Face-centered cubic structure
FE	Faradaic efficiency
FID	Flame ionization detector
FTIR	Fourier transform infrared spectroscopy
FWHM	Full width at half maximum
GC	Gas chromatography
GHG	Greenhouse gas
GI	Grazing incident
GNI	Gross national income
HDI	Human development index
HER	Hydrogen evolution reaction
HOR	Hydrogen oxidation reaction
HPLC	High-performance liquid chromatography
HRTEM	High-resolution transmission electron microscopy
HS-GC	Headspace-gas chromatography

IPCC	Intergovernmental Panel on Climate Change
ISS	Ion scattering spectroscopy
LEIS	Low-energy ion scattering
LSV	Linear Sweep Voltammetry
MS	Mass spectrometry/mass spectrometer
MX	Fragment with the mass-to-charge ratio of X
NIST	National Institute of Standards and Technology
NMR	Nuclear magnetic resonance
OCV	Open circuit voltage
OER	Oxygen evolution reaction
OLEMS	Online electrochemical mass spectrometry
ORR	Oxygen reduction reaction
pc	Polycrystalline
PCTFE	Polychlorotrifluoroethylene
PEEK	Polyether ether ketone
PLS	Potential-limiting step
PTFE	Polytetrafluoroethylene
QCM	Quartz crystal microbalance
QMS	Quadrupole mass spectrometer
RDS	Rate-limiting step
RE	Reference electrode
RHE	Reversible hydorgen electrode

RID	Refractive Index Detector
sccm	Standard cubic centimeter per minute
SDI	Selectivity-determining intermediate
SEM	Secondary electron multiplier
SHE	Standard hydrogen electrode
TCD	Thermal conductivity detector
UHV	Ultra-high vacuum
UPD	Under-potential deposition
WE	Working electrode
WHO	World Health Organization
XANES	X-ray absorption near edge structure
XAS	X-ray absorption spectroscopy
XPS	X-ray photoelectron spectroscopy
XRD	X-ray diffraction

Symbol	Term
$*$	Adsorbed intermediate
η	Over potential
$\sim$	Approximately
r	Atomic radius
I	Current
R_{Ω}	Ohmic resistance
θ	Incident X-ray beam angle
n	Integer
λ	Wavelength
d	Lattice spacing
ω	X-ray incident angle in GIXRD
D_p	Average crystallite size
K	Scherrer constant. 0.94 is usually used for spherical crystallites with cubic symmetry.
β	FWHM of XRD peak
x	Molar fraction
a	Lattice constant
h, l, k	Miller indices
h	Planck constant. 6.626×10^{-34} J/Hz
ν	Photon frequency
φ	Work function

E_k	Kinetic energy
E_b	Binding energy
m	Atomic weight
E_0	Initial energy of the incident ion beam in ISS
E_f	Final energy of the scattered ion beam in ISS
I_0	Incident X-ray beam energy in XAS
I_t	Transmitted X-ray beam energy in XAS
$\mu(E)$	X-ray attenuation (absorption) coefficient
d_{th}	Material thickness that X-ray beam penetrates
ρ	Density
Z	Atomic number
I_f	Florescent X-ray intensity
χ	EXAFS fine-structure function
k	Wavenumber
N	Coordination number
S_0	Passive electron reduction factor
R	R space number
F_j	Scattering amplitude of back-scattered electrons
λ	Mean free path of the emitted photoelectron
σ	Debye-Waller factor
δ	Phase-shift between the outgoing and back-scattering waves
z	Number of transferred electron

F	Faraday's constant. 96485 C/mol
n_i	Amount in the number of moles of species i
t	Time
P	Pressure e
T	Temperature
v	Gas flow rate
A	Integrated peak area
f	Calibration factor
V	H-cell chamber volume
R	Ideal gas constant. 8.315 J/(mol•K)
Q	Charge
j	Current density
S	Productivity in the number of moles
m/z	Mass-to-charge ratio
U	DC voltage amplitude
V	AC voltage amplitude
ω	Angular velocity
S	MS signal intensity
$\dot{n}$	Instantaneous molar flux
$\bar{n}$	Average molar flux
l	Capillary length
η	Dynamic viscosity

a	Capillary dimension
k_B	Boltzmann constant. $1.38 \times 10^{-23}\ m^2/(kg \cdot s^2 \cdot K)$
C	Concentration
K_H	Henry's law constant
e	Electron
E	Potential
E^0	Standard equilibrium potential
ΔG	Gibbs free energy

List of Publications

Paper I – Manuscript appended

Mechanistic Insights into Aldehyde Production from Electro-chemical CO_2 Reduction on CuAg Alloy via *Operando* X-Ray Measurements

Y. Qiao, G. Kastlunger*, R. C. Davis, C. A. Giron Rodriguez, A. L. Vishart, W. Deng, S. Li, P. Benedek, J. Chen, J. Schröder, J. Perryman, D. U. Lee, T. F. Jaramillo, I. Chorkendorff, B. Seger*

Submitted

Paper II – Not appended

***Operando* Detection of Acetaldehyde Behavior in Electrochemical $CO_{(2)}$ Reduction**

Y. Qiao, D. Hochfilzer, I. Chorkendorff, B. Seger*

In preparation

Paper III – Not appended

Local reaction environment for selective electroreduction of carbon monoxide

M. Ma*, W. Deng, A. Xu, D. Hochfilzer, Y. Qiao, K. Chan, I. Chorkendorff, B. Seger

Energy Environ. Sci., 2022,15, 2470-2478

Paper IV – Not appended

Unraveling the rate-determine step of C2+ products during electrochemical CO reduction

W. Deng, Y. Qiao, G. Kastlunger, N. Govindarajan, A. Xu, P. Zhang, I. Chorkendorff, B. Seger, J. Gong*

Submitted

Content of Figures

Content of Tables

Contents

Chapter 1 Introduction

This chapter will explain the motivation of this thesis. The urgent for replacing fossil fuels with renewable energy will be stated first, followed by a brief explanation of the challenges of switching the primary energy source to renewable energy. Then I will shortly explain why CO_2 electrolysis shows promise in both aspects, namely carbon emission from fossil fuel combustion and intermittent renewable energy supply. Yet, the complicated and convoluted reaction mechanism of electrochemical CO_2 reduction reaction (eCO2RR) limits its widespread application. Therefore, the main focus of this thesis is to provide mechanistic insights into the eCO2RR pathways.

1.1 The Global Energy and Climate Crisis

The industrial revolution in the 18th century brought about significant advancements in agricultural productivity, medical care, and living standards, leading to a population explosion in the world [1]. According to statistics from the United Nations, the world's population has increased from 1 billion in 1800 to *ca.* 8 million in 2022 [2]. Accompanied by population growth is the proliferated energy consumption. Figure 1.1 shows the global energy consumption by source since 1800. Despite traditional biomass, fossil fuels (including natural gas, oil, and coal) have been serving as the main energy source for anthropogenic activities and thus the economic and social development since then, and still provides over 80% of the total energy consumption in 2021 [3]. On the other hand, as technology advances, humans aspire to achieve a higher level for living. The Human Development Index (HDI) composites three dimensions: long and healthy life, knowledge, and a decent standard of living, indicated by the life expectancy at birth, expected/mean years of schooling, and gross national income (GNI), respectively [4]. Figure 1.2 compares the HDI in 1990 (a) and 2019 (b) correlated with energy use per capita among countries with different populations (proportional to bubble size). The scattered spread reveals distinct activities among countries. For instance, the HDI of Singapore and the Netherlands are both at 0.94 in 2019, while the former consumes *ca.* 609 GJ per capita and that for the latter only 208 GJ (Figure 1.2b).

Moreover, compared to 1990, the HDI distribution is more concentrated in the top left corner, indicating a tendency of reducing energy consumption while improving human development worldwide. Taking Denmark as an example, its HDI increased from 0.81 to 0.94 whereas energy use reduced from 141 to 122 GJ per capita in the period of 1990-2019. Yet, the average energy usage per capita is reduced in general, and given the total population growth, the total energy consumption keeps rising. As can be seen from Figure 1.1, despite the traditional biomass, fossil fuels have been serving as the main energy source since 1850. Although progress has been found in renewable energies such as nuclear and hydropower, fossil fuels still account for almost 80% of the total energy supply in 2021 [3]. Additionally, the uneven distribution of these resources around the world has caused geopolitical conflicts among countries: the largest natural gas, oil and coal reserves are held by Russia, Venezuela, and the United States, respectively [5]; whereas the largest consumer of oil is the United States, and China consumes the most oil and coal [6]. Countries with limited fossil fuel storage and access have to heavily depend on imports, thus exposing themselves to supply disruptions and price fluctuation, which may further lead to significant economic, social, and political impacts [6].

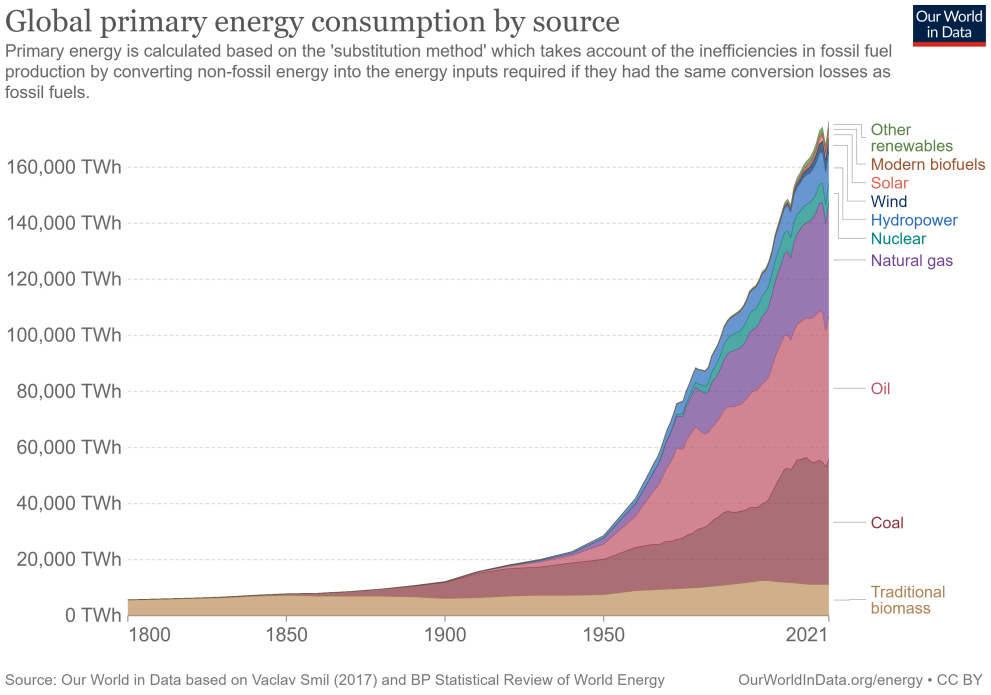

Figure 1.1 ***Global primary energy consumption by source****. Reprinted from [7] with permission. Open access.*

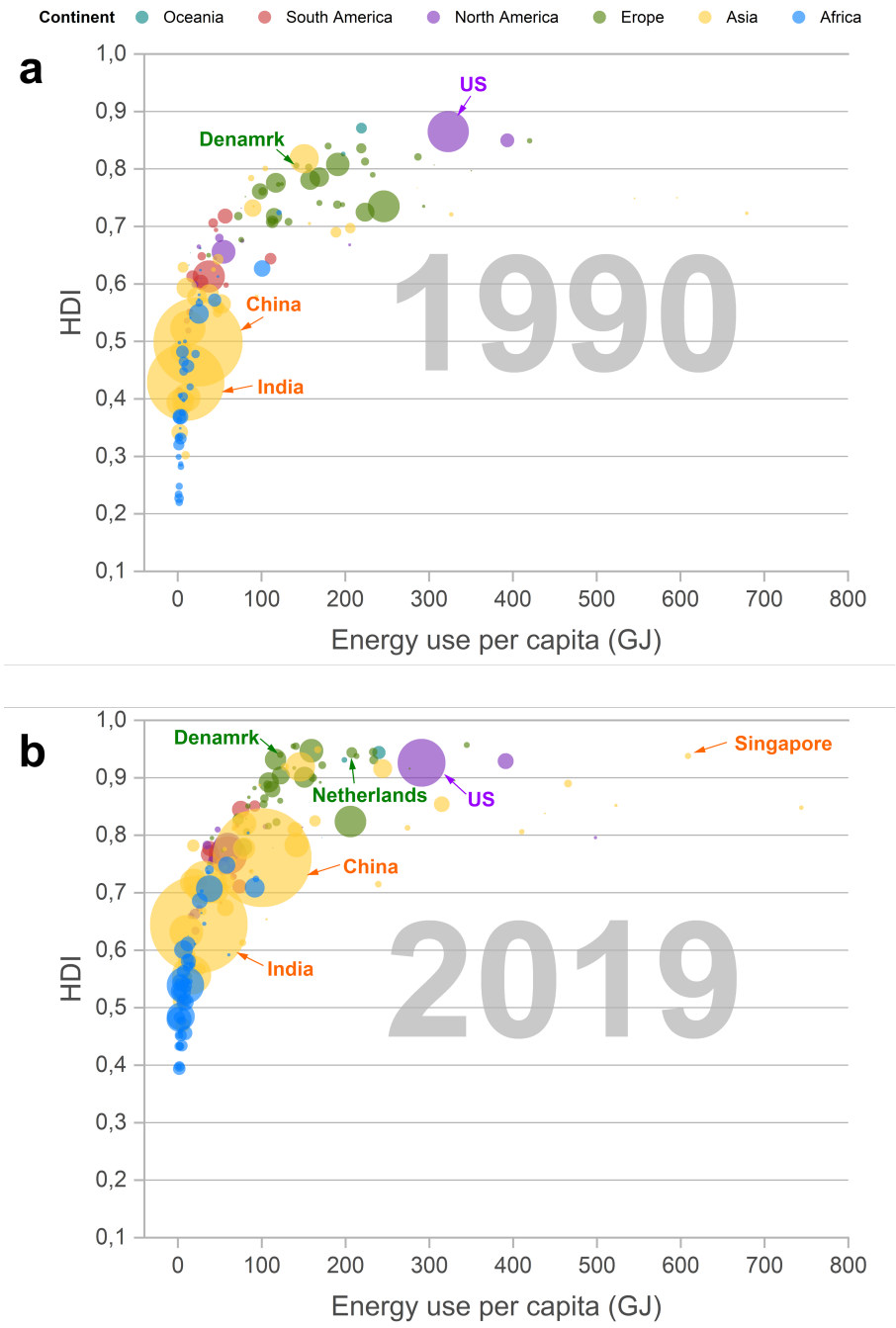

Figure 1.2 ***Human Development Index (HDI) correlated to energy use per capita*** *in (a) 1990 and (b) 2019. Continents are labeled with color. The area of bubbles is proportional to the country's population size. Reprinted from [8] with open access. Copyright 2022 VisualizingEnergy.*

On the other hand, the combustion of fossil fuels releases greenhouse gases (GHG), with carbon dioxide (CO_2) being the most important one given its largest portion of the total GHG emission and long atmospheric lifetime (for thousands of years) [9]. It leads to global warming and further detrimental environmental issues. Figure 1.3 presents a concurrent increase between the annual global CO_2 emission (left axis, blue line) and averaged annual

earth temperate (right axis, green line) since 1880, revealing the close correlation between them. Global warming results in a series of climate and environmental issues, such as increased frequency and intensity of extreme weather events, sea level rise, and changes in precipitation patterns that impact agriculture and water resources [10]. These issues further jeopardize human health. The World Health Organization (WHO) predicts a *ca.* 250000 additional deaths per year between 2030 and 2050, from malnutrition, malaria, diarrhea and heat stress, caused by climate change [11]. To avoid the catastrophic impacts of global warming, 195 nations adopted the Paris Agreement in 2015, targeting on limiting the global temperature rise to 1.5 ºC above the pre-industrial level [12]. The special report released by the Intergovernmental Panel on Climate Change (IPCC) further stressed that in order to reach this goal, a net-zero carbon emission needs to be realized by 2050 [13]. The synthesis report of the IPCC sixth assessment report (AR6) concluded that about 80% of the total carbon budgets had been released from anthropogenic activities in the period of 1850-2019, leaving *ca.* 500 Gt CO_2 of the remaining carbon budget for the 1.5 ºC goal [14]. However, energy demand is still high to meet the need for economic and human development around the world. According to the bp Statistical Review of World Energy 2022, the primary energy demand increased by 5.8% in 2021, reversing the temporary reduction in 2019 due to the COVID-19 pandemic [3]. The high energy demand and its heavy reliance on fossil fuels urge for switching to renewable energies and strategies to mitigate carbon emissions.

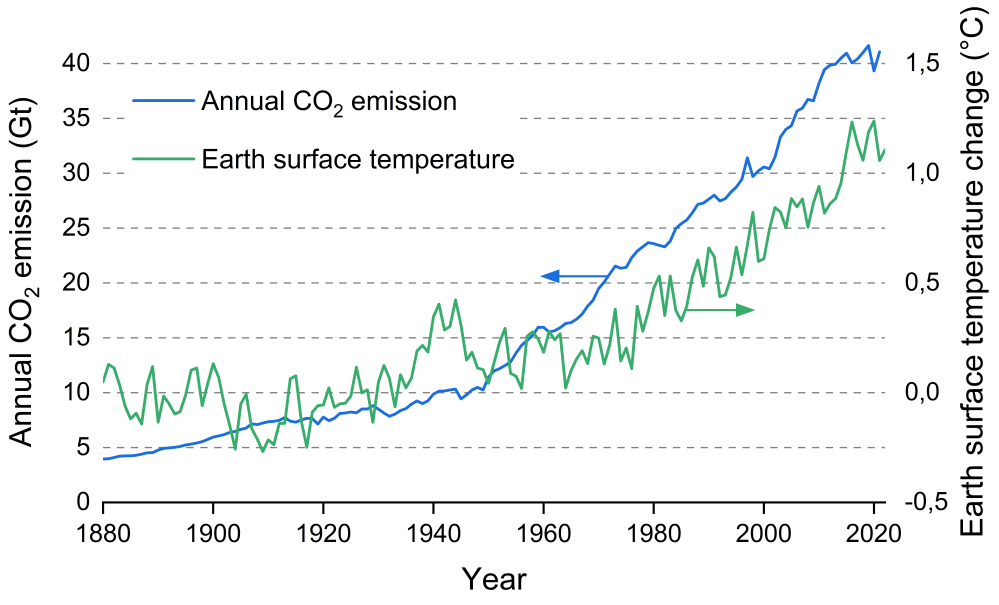

Figure 1.3 ***Correlation between the annual global CO_2 emission*** *(left axis, blue line)* ***and averaged annual earth surface temperature change*** *with respect to the average temperature between 1880 and 1900 (right axis, green line). CO_2 emission data and earth surface temperature data are from [15] and [16], respectively with permission. Open access for both.*

1.2 Renewable Energy and Challenges

Renewable energy is energy derived from natural sources that replenish faster than their consumption. As shown in Figure 1.1, hydropower and nuclear are the two main contributors out of the fossil fuel group to the total energy consumption. However, they are not suitable for widespread applications. Hydropower makes use of the kinetic energies of lowering or moving water to generate electricity. Although it is the only renewable energy that has a competitive cost compared to traditional fossil fuels (typically in the range of US2–5¢/ kWh) as well as high efficiency (typically 90% or even higher) [17], it has drawbacks that are hard to overcome, including dams damaging the pristine ecosystem, displacement of communities and limited reservoirs [18]. Nuclear energy sources generate electricity through fission, during which the nucleus of an atom splits into two or more smaller nuclei, and a considerable amount of energy is produced simultaneously. It emits zero carbon and produces minimal solid wastes, as well as a small area footprint requirement (*ca.* 1.3 mi^2/GW). Meanwhile, it is also the most controversial energy source, considering the previous nuclear abuse and accidents. Additionally, the construction of nuclear reactors and power plants is expensive and time-consuming. [19]

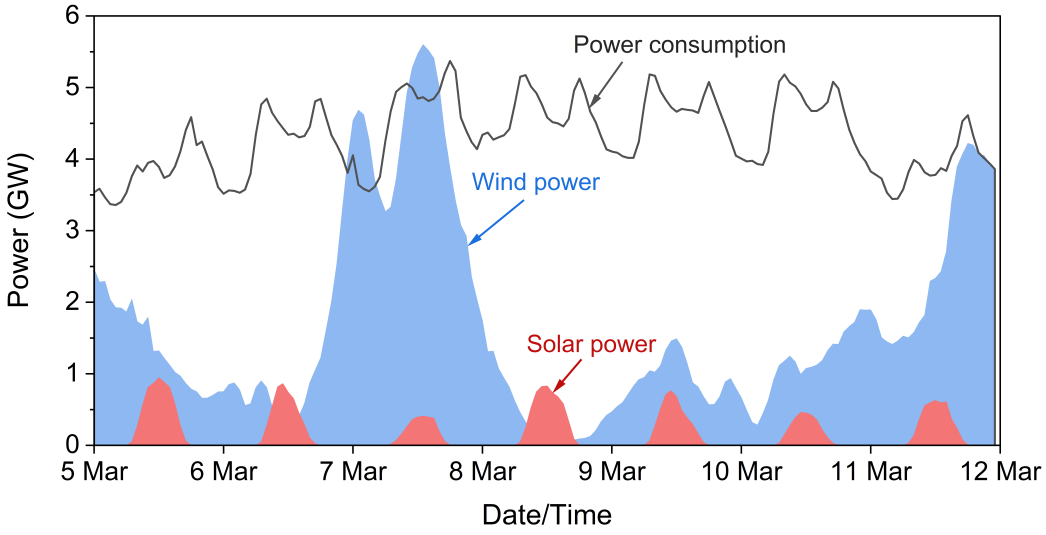

Figure 1.4 ***Total electrical power consumption*** *(black line)* ***accompanied by weather condition-dependent power production from wind*** *(blue area)* ***and solar radiation*** *(red area) during the time from 5th March 2023 to 12th March 2023. Data from[20]. Open access.*

Solar radiation and wind, on the other hand, are of the most interest, as they are abundant, carbon-free, safe, and have a very small land footprint that allows on-site use [21]. On the other hand, their generation highly depends on the weather condition and thus is intermittent. Figure 1.4 gives a good example of a periodically fluctuated power consumption (black line) together with a randomly (weather condition-dependent) varied wind- (blue area) and solar-

(red area) produced power. Furthermore, energy produced by the sun and wind has to be used immediately otherwise they will be lost. Hence, it is necessary to store energy in a stable and efficient (*i.e.*, with low or no energy lost) way for later use.

1.3 Electrochemical CO_2 Reduction

In addition to reducing CO_2 emission by inclining the primary power sources towards renewable energy, given the high energy demand from fossil fuels is still high, the emitted CO_2 also needs to be captured and stored. Converting CO_2 into fuels and chemicals with electricity produced from renewable energy provides such a strategy that integrates the benefits from multiple aspects. As illustrated in Figure 1.5, CO_2 electrolysis makes use of carbon-free renewable energy as the energy source, and converts the emitted CO_2 electrochemically into chemicals and fuels, resulting in a closed carbon cycle. During the electrochemical CO_2 reduction reaction (eCO2RR), not only fossil fuel usage is mitigated, but the intermittent power production from renewable energy is also effectively stored in the form of chemical bonds by converting the emitted CO_2, and thus helps reduce the atmospheric CO_2 concentration.

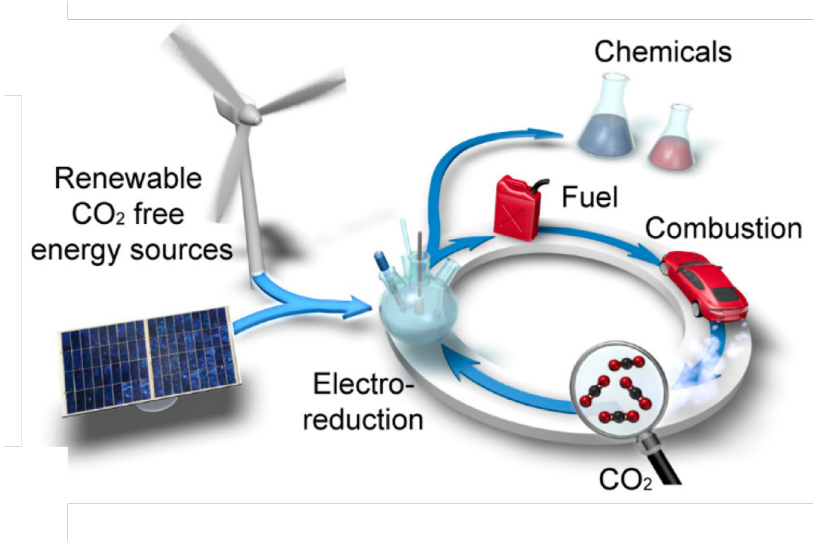

Figure 1.5 ***Schemata illustration of a closed carbon cycle realized by electrochemical CO_2 reduction.*** *Reprinted from[22] with permission. Copyright 2014 American Chemical Society.*

Copper is known to be the only monometallic catalyst that produces variable chemicals and fuels, including methane, ethylene, ethanol, acetate, *etc*. On the other hand, the products are mostly formed together, making post-separation difficult. The main reason is that the eCO2RR reaction mechanism remains obscure. Hence, mechanistic insights are needed to help steer product selectivity towards specific species.

1.4 Thesis Outline

As explained above, electrochemical CO_2 reduction is a promising strategy to close the carbon cycle with renewable energy. Copper is the most versatile catalyst in this regard, while more progress is expected to improve the product selectivity towards specific species. This requires mechanistic insights into the complicated and convoluted reaction mechanisms and pathways. My PhD project is to provide such information, namely the mechanistic insights into electrochemical CO_2 reduction on Cu and Cu-based catalysts. This thesis will present my efforts to reach this goal, structured as follows:

Chapter 1 (this chapter) explains the motivation for doing electrochemical CO_2 reduction and why the mechanistic understanding of this reaction is the main focus of this thesis.

Single crystal Cu with a well-defined surface provides a model platform for building up the structure-performance correlation. In addition to the surface structure of Cu catalysts, the formation of multicarbon products with higher energy density requires a high coverage of *CO intermediate. Hence, combing Cu with a co-catalyst (*e.g.*, Au, Ag, Zn) that produces *CO supply directly (by "spill-over" *CO to the Cu sites) or indirectly (by generating a high local CO concentration for the Cu sites to adsorb) is expected to facilitate multicarbon product formation.

Accordingly, **Chapter 2** begins with briefly introducing eCO2RR on copper (Cu). Literature reviews on single crystal Cu and CuAg bimetallic catalysts in eCO2RR will be given next, including summarization and my comments on what can be expected in the future. Then the aims of this thesis regarding the above topics will be presented.

Chapter 3 overviews experimental techniques that are used during my PhD, starting with a description of the working principle of each technique, followed by an explanation on what role it plays in my projects and what information is expected.

Chapter 4 interprets the feasibility of *operando* detection of both liquid and gaseous products in eCO2RR conducted on single crystal Cu catalysts with the electrochemistry-mass spectrometry system.

Chapter 5 presents the work on mechanistic understanding on the interaction between Cu and Ag in CuAg multiphase alloys for eCO2RR, assisted by *operando* X-ray measurements and computational simulations.

Chapter 6 summarized the main results presented in the previous chapters. A short perspective on future fundamental eCO2RR research is given at the end.

Chapter 2 Brief Overview of Electrochemical CO_2 Reduction

The first part of this chapter briefly introduces electrochemical CO_2 reduction and the uniqueness of copper in this field. It is followed by the next two subsections which are related to the two topics discussed in this thesis: Cu single crystal and CuAg bimetallic catalysts. In each subchapter, a brief literature review on state-of-the-art and development of the topic is first presented, followed by summarization and my comments on what else can be expected in the future. Then the aims of this thesis regarding each topic will be presented.

2.1 Overview of Electrochemical CO_2 Reduction

Climate change driven by the continuously increasing CO_2 concentration in the atmosphere is one of the greatest threats facing human beings. The Intergovernmental Panel on Climate Change (IPCC) released a special report (SR15) in 2018, proposing that in order to limit global warming to the safe line, which is 1.5 ºC above preindustrial levels, the global net CO_2 emission needs to reach a ”net zero” by 2050 [13]. This makes CO_2 capture and conversion pivotal.

Since CO_2 is an extremely stable molecule with a linear and centrosymmetric geometry composed of two equivalent C=O bonds (dissociation energy *ca.*750 kJ/mol), traditional industrial ways for CO_2 conversion such as methanation, methanol synthesis, and Fischer-Tropsch, operate at high temperature and pressure and therefore requires a huge amount of energy input [23]. Electrochemical CO_2 reduction reaction (eCO2RRR), on the other hand, operates under mild temperature and atmospheric pressure. It converts CO_2 into value-added fuels and feedstocks, storing the energy from electricity in the form of chemical bonds, and therefore helps with closing the anthropogenic carbon cycle, when driven by renewable energy (*e.g.*, solar and wind) [24]. In addition, eCO2RR is also appealing for its controllable

reaction rates and product selectivity through the reaction conditions (*e.g.*, applied potential, electrolyte, electrode material, mass transport, *etc.*) [25].

Among all the reported eCO2RR catalysts, Cu is the only monometallic catalyst that produces hydrocarbons and oxygenates requiring more than 2 electrons transfer (> 2 e- products) [26]. Bagger *et al.* attributed it to the negative binding energy of the *CO intermediate while positive binding towards *H, which makes further reduced products beyond *CO more facilitated than hydrogen formation from *H (Figure 2.1) [27]. Kuhl *et al.* found that the overall eCO2RR activities of seven studied metals (Au, Ag, Zn, Cu, Ni, Pt, and Fe) follow a volcano relationship with respect to their binding energies of CO, where Cu exhibited a moderate binding intensity, neither too weakly (such that adsorbed CO desorb from the electrode surface as gaseous CO before further reaction), nor too strongly (such that the electrode surface is poisoned by CO or intermediate formed during the reaction and thus H_2, evolved from the competing water reduction, is the primary product), for generating further products beyond *CO. It also enables C-C coupling to happen between two *CO or *CO-derived intermediates, which has been well-established to be the rate-limiting step (RDS) for multicarbon products (C_{2+} products) [28]–[30]. The same group then observed 16 different products from eCO2RR conducted in a three-electrode H-type electrochemical cell, and 12 of them were C_2 or C_3 species, including multiple hydrocarbons and oxygenated species (Figure 2.2) [31]. Multicarbon products (C_{2+} products, *e.g.*, C_2H_4, C_2H_6, ethanol, and propanol) generally have higher energy densities and larger economic values compared to C_1 products (CO, CH_4, and formate), and therefore provide a more attractive direction to aim for [28], [32], [33]. Products containing two or more carbons, usually have higher energy density but low productivity, and also are scarcely investigated. Therefore, in my thesis, I will focus on C_2 products, including ethylene (C_2H_4), acetaldehyde (CH_3CHO), and ethanol (C_2H_5OH).

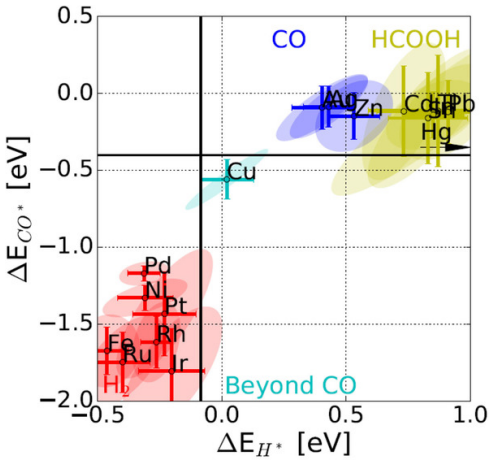

Figure 2.1 ***Classification of metals based on the main product they produce.*** *Cu stands out for its intermediate binding energies of both the *CO and *H intermediates. Reprinted from [27] with permission. Copyright 2017 Wiley-VCH Verlag GmbH & Co. KGaA, Weinheim.*

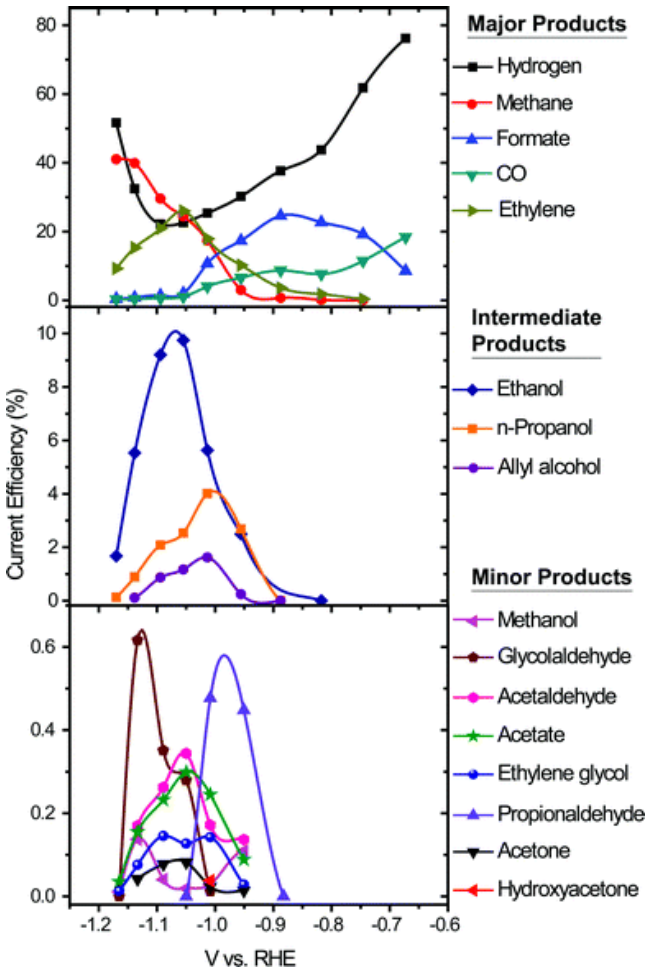

Figure 2.2 ***Current efficiency for each product as a function of potential is shown for major, intermediate range, and minor products.*** *Electrochemical CO_2 reduction was conducted in CO_2-saturated 0.1 M $KHCO_3$ aqueous solution. Each electrolysis potential was applied for 1 h. Reprinted from [31] with permission. Copyright 2012, Royal Society of Chemistry.*

Table 2.1 summarizes the standard equilibrium potentials (E^0) of possible half-reactions on the cathode in eCO2RR, where most final products have a similar E^0 at *ca.* 0 V *vs.* RHE, including the hydrogen evolution reaction (HER) from water splitting. This on the one hand, makes the simultaneous formation of various products thermodynamically feasible; while on the other hand, the thermodynamically comparable but kinetically more facile competing HER leads to an overall low eCO2RR efficiency [34], [35]. Additionally, not only are there many possible pathways from CO_2 to reach a final product, but multiple electron-transfer-coupled steps and intermediates can be involved in each pathway as well. On the other hand, an intermediate can be shared by different pathways and bifurcate at some point. [28] Furthermore, these intermediates also constrain each other, following the so-called linear scaling relationship among their adsorption energies [36]–[38]. This makes the eCO2RR mechanism an intricate network convoluted with plenty of intermediates and possible pathways.

Table 2.1 Electrochemical Reactions with Equilibrium Potentials.[*]

Reaction[†]	**E^0/ [V *vs.* RHE]**
$2H^+ + 2e^- \rightarrow H_2$	0
$CO_2 + 2H^+ + 2e^- \rightarrow HCOOH_{(aq)}$	-0.12
$CO_2 + 2H^+ + 2e^- \rightarrow CO_{(g)} + H_2O$	-0.10
$CO_2 + 6H^+ + 6e^- \rightarrow CH_3OH_{(aq)} + 2H_2O$	0.03
$CO_2 + 4H^+ + 4e^- \rightarrow C_{(s)} + 2H_2O$	0.21
$CO_2 + 8H^+ + 8e^- \rightarrow CH_{4(g)} + 2H_2O$	0.17
$2CO_2 + 2H^+ + 2e^- \rightarrow (COOH)_{2(s)}$	-0.47
$2CO_2 + 8H^+ + 8e^- \rightarrow CH_3COOH_{(aq)} + 2H_2O$	0.11
$2CO_2 + 10H^+ + 10e^- \rightarrow CH_3CHO_{(aq)} + 3H_2O$	0.06
$2CO_2 + 12H^+ + 12e^- \rightarrow C_2H_5OH_{(aq)} + 3H_2O$	0.09
$2CO_2 + 12H^+ + 12e^- \rightarrow C_2H_{4(g)} + 4H_2O$	0.08
$2CO_2 + 14H^+ + 14e^- \rightarrow C_2H_{6(g)} + 4H_2O$	0.14
$3CO_2 + 16H^+ + 16e^- \rightarrow C_2H_5CHO_{(aq)} + 5H_2O$	0.09
$2CO_2 + 18H^+ + 18e^- \rightarrow C_3H_7OH_{(aq)} + 5H_2O$	0.10

The broad product distribution, however, is accompanied by poor selectivity (described by faradaic efficiency, FE) in general, making the post-separation of desired species from the product mixture challenging, and therefore limits the further use of Cu [28], [39]. In order to tune the selectivity towards desired products, a thorough understanding on the reaction mechanism is necessary. Although numerous works have been reported regarding the eCO(2)RR mechanisms, there are still very few consensuses that have been reached.

[*] Reproduced from with permission from [28]. Coryright 2019 American Chemical Society.

[†] Subscript (aq), (g), and (s) stands for dissolved in aqueous solution, gas, and solid, respectively.

The first step in eCO2RR is thought to be the initial CO_2 activation. Although a detailed activation mechanism remains debatable, it is widely agreed that formic acid (HCOOH, or in alkaline solutions it exists in the form of formate, $HCOO^-$) is the final product desorbing from the Cu surface; and its generation pathway diverges from the CO (either desorb from the Cu surface as the final product or stay there in the form of *CO as an intermediate for generating the further > 2 e^- products) branch at the very early stage. [34], [35], [40]–[42] Additionally, previous studies have found that eCO2RR and eCORR follow the same reaction mechanisms for producing beyond *CO products, as indicated by the similar product distribution in CO and CO_2 atmosphere, both in experimental results [43]–[49] and in theoretical simulations [27], [41], [50]–[53], and further evidenced by spectroscopic observation further evidenced it [30], [54]–[56]. Therefore, when talking about the reaction mechanism (Chapter 2.2 for the single crystal Cu literature review and Chapter 4 for the single crystal Cu project), eCORR and eCO2RR are combined by using the term "eCO(2)RR".

2.2 Single Crystal Cu Electrodes on Electrochemical CO(2) Reduction

2.2.1. Literature Review

Cu has a face-centered cubic (fcc) crystal structure. According to Miller indices, it has three atomically flat low-index facets (namely (100), (110), and (111), respectively), and high-index facets which can be described as introducing periodic steps of monatomic height to a low-index facet.

Single-crystal Cu has a well-defined atomic organization, with only one type of active sites (low-index facets) or a controlled composition of different active sites (high-index facets), and can therefore be used as a model platform for understanding the structure-performance correlation of catalysts. It is also the only experimental structure that mirrors the ideal surfaces employed in computational simulations.

The first Cu single crystal work in the field of eCO2RR was conducted by Frese *et al.*, who reported that methane production rate followed the order of (111) > (110) > (100), under the same conditions (@ -1.165 V *vs.* RHE in 0.5 M $KHCO_3$ electrolyte with pH 7.5) [57]. Hori *et al.* then measured various products in eCO(2)RR with a nearly 100% total FE on the three low-index facets at 5 mA/cm^2, and found that (100) favors ethylene over methane, (111) forms methane as the main product, and (110) shows an intermediate ethylene selectivity between the other two [58]. This facet-dependent selectivity preference under eCO(2)RR

conditions has been thereafter widely confirmed by both experiments [59]–[64] and computational simulations [65]–[67].

In 2011, Koper's group proposed that eCO2RR on pc-Cu producing hydrocarbons (C_xH_y) *via* two pathways: a C_1 pathway leading to CH_4 with *CHO as the key intermediate, and a C_2 pathway leading to C_2H_4 through a CO dimer [47]. To further investigate the proposed C_2H_4 pathway with controlled surfaces, eCORR was conducted using online electrochemical mass spectrometry (OLEMS) on two basal planes, Cu (100) and Cu (111). Based on this, they suggested two pathways for C_2H_4 formation: one is pH-dependent, shares a common intermediate *CHO (from the protonation of *CO) with CH_4 and takes place preferentially at (111) facets or steps; the other occurs only at (100) terraces (whereas (100) steps are not involved in this reaction [68]) at relatively low overpotentials, proceeding *via* a CO dimer, and is pH-independent [59], [60]. The proposed pathways are further supported by DFT calculations [69], [70]. The same trend is also agreed by other groups [43], [71], [72].

In addition to the above three low-index planes, *i.e.,* (100), (110) and (111), their combination composes high-index facets containing a certain density of step sites, which enables investigating the performance of undercoordinated sites. To explore the influence of the coordination environment, Hori *et al.* examined high-index facets with various step atom densities. Results are summarized in Figure 2.3. They found that by controlling the amount of (111) or (110) step atoms, the product distribution on the (100) basal plane can be controlled [73]. Specifically, the (711)-[4(100) × (111)] facet exhibited the highest C_2H_4/CH_4 ratio in terms of current density; while introducing (110) steps to (100) facets significantly promoted the selectivity towards ethanol, with (510)-[5(100) × (110)] promoted the most [73]. This suggests that the (111) step line adjacent to the (111) terrace may be responsible for generating a common intermediate for C_2 oxygenates production. [73]–[75] This hypothesis was later rationalized by Bagger *et al.* with DFT calculations, where they identified the (110) step in the Cu(S)-[n(100) × (110)] series as a special ethanol production site, while the (100) basal plane produces C_{2+} products in general [76].

To further compare the distinctly acting (100) and (111) in CH_4 and C_2H_4 production, Schouten *et al.* compared two single crystals with the same step density, Cu (322)-[5(111) × (100)] and Cu (911)-[5(100) × (111)] [59], [68]. Results showed that (911) has a similar onset potential and cyclic voltammetric trends in terms of CH_4 and C_2H_4 production as on (100), while (322) is similar to (111). Thus, they attributed the previously noticed selective C_2H_4 formation on the (100) facet at low overpotentials [59] to the (100) terraces exclusively, while (100) steps were not involved in this reaction [68]. This could be correlated to the square orientation of atoms on the Cu (100) terrace stabilizing the *OCCO intermediate (from *CO dimerization) for C_2H_4 formation, as suggested by Gattrell *et al.* [77]. DFT simulations then revealed that the *OCCO intermediate binding on the Cu surface is both geometrically and

electronically favored at square sites [78]. Its protonated counterpart, *OCCOH was then detected on (100) using *in situ* Fourier transform infrared spectroscopy (FTIR), while it was absent on the (111) facets, which confirms that preferable *CO dimerization on square sites [79].

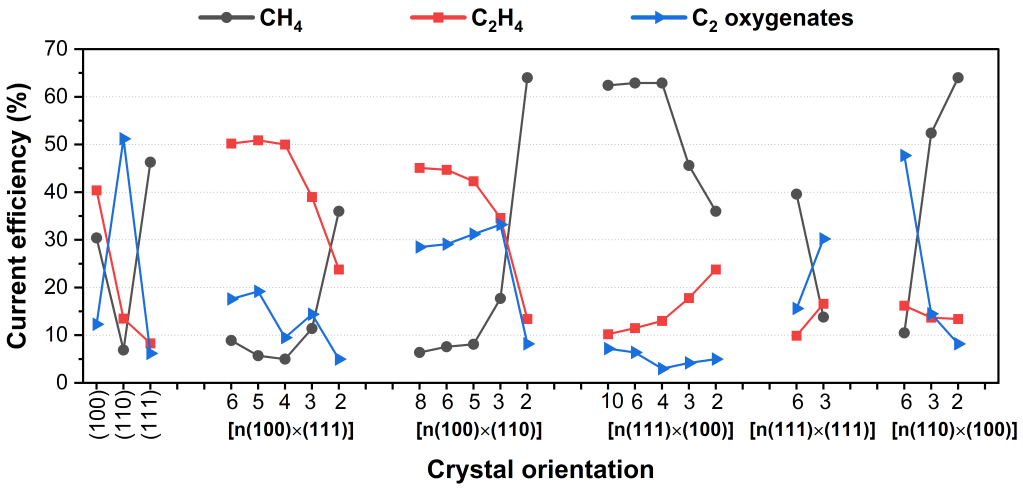

Figure 2.3 ***Electrochemical CO_2 reduction products at various copper single crystal electrodes*** *(5 mA/cm², 0.1 M $KHCO_3$). Reproduced from data from [75] with permission. Copyright Elsevier Science B.V.*

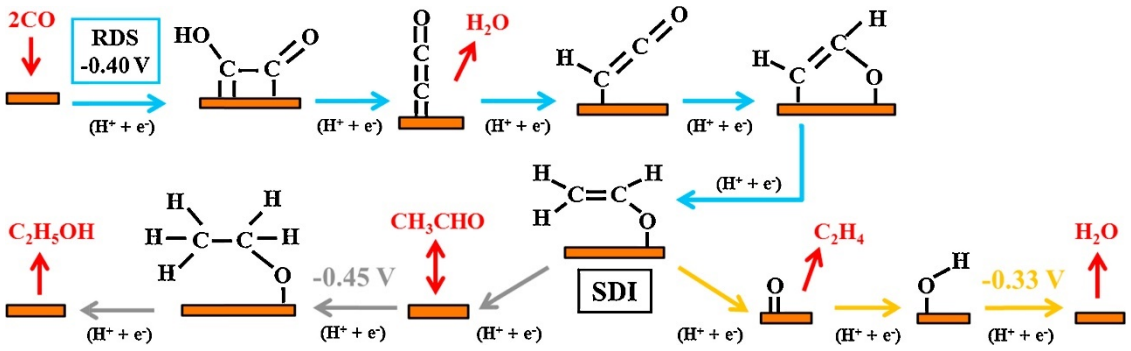

Figure 2.4 ***Mechanism of the electrochemical reduction of CO on copper to C_2 species on Cu (100).*** *The pathways for the production of acetaldehyde, ethanol and ethylene are identical up to the fifth proton–electron transfer (blue arrows). The rate-determining step (RDS at -0.40 V) is the first proton–electron transfer and *CH_2CHO is the selectivity-determining intermediate (SDI). Protonation of the SDI on the β-C requires -0.45 V and leads to acetaldehyde and ethanol (gray arrows). Protonation on the β-C requires -0.33 V and leads to ethylene and water (orange arrows). On Cu (100) the protonation of the SDI is inclined toward the ethylene pathway (orange arrows). Reprinted from [80] with permission. Copyright 2020 American Chemical Society.*

Recently, Koper *et al.* proposed that coupling undercoordinated sites with square sites can effectively improve ethanol production: square facilitates C-C coupling and thus C_{2+} products in general, and undercoordinated sites preferably generate ethanol over ethylene [80]. As schematically presented in Figure 2.4, the product preference was interpreted by their

different potential-limiting step (PLS) from the shared *CH_2=CHO intermediate: ethylene formation is desorption-limited while ethanol production is limited by the re-adoption of desorbed acetaldehyde (CH_3CHO) [80]. Considering that undercoordinated sites bind both more strongly than the terraces [47], [70], [81], selectivity was steered to facilitate ethanol. The above merits of undercoordinated square sites are comprehensively studied and vindicated by both computational simulations [81], [82] and experiments [83], as well as microscopic observations [84], [85] later.

It is worth mentioning that although the preference of C-C coupling on the Cu (100) facet has been widely observed and approved, there is no general agreement on C_{2+} formation pathway yet, and C-C coupling and the following protonation could follow different mechanisms depending on the reaction conditions, as illustrated in [28], [86]–[89]. My thesis will put some effort to help understand this unsolved mechanism.

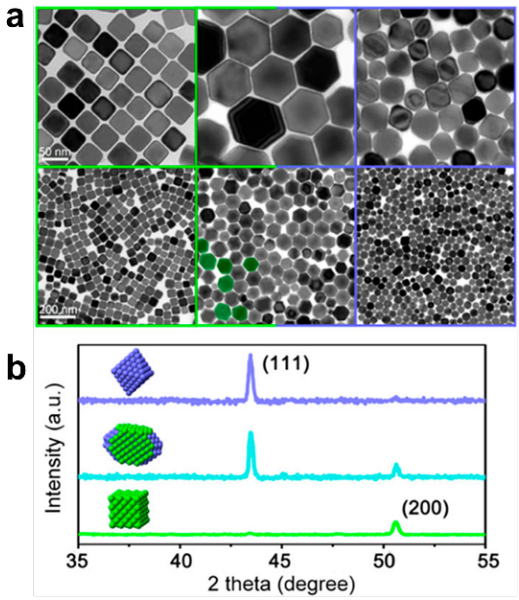

Figure 2.5 ***a. (Top) TEM images of C−Cu (left), H−Cu (middle), and O−Cu (right), and (bottom) low-magnification images*** *showing the overall condition with uniform size distribution. Some H−Cu nanoscale single crystals (bottom, middle) were colored green to emphasize the step surface features.* ***b. Powder X-ray diffraction (PXRD) pattern for C−Cu (green), H−Cu (cyan), and O−Cu (purple).*** *Reprinted from [63] with permission. Copyright 2019 American Chemical Society.*

The knowledge obtained from the mechanistic understanding of the eCO(2)RR pathways on single crystals can be applied to design Cu catalysts. By virtue of surface engineering, facet composition of the exposed catalyst surface can be controlled, and thus tune the selectivity towards target product(s) [62]–[64], [83], [90], [91]. For example, based on their DFT finding that the Cu (100) and stepped (211) facets favor C-C coupling product over (111), Jiang et al. obtained a (100)-rich surface on Cu foil through the metal ion battery cycling method and presented a sixfold improvement in C_{2+}/C_1 product selectivity ratio in eCO2RR, with a

highest C_{2+} FE of over 60% and suppressed the undesired competing HER efficiency below 20% [92]. Suen and Kong *et al.* synthesized three different Cu nanostructures with different facet compositions (morphological and crystal structures are depicted in Figure 2.5): cubelike-Cu (C-Cu), hexarhombic docadehedron-like-Cu (H-Cu), and octahedron-like Cu (O-Cu). eCO2RR exhibited that the (111)-rich O-Cu promoted CO and CH_4 production and the (100)-rich C-Cu enhanced C_2H_4 formation. H-Cu had a mixed facet structure and facilitated producing ethanol. High-resolution transmission electron microscopy (HR-TEM) revealed that H-Cu had more edge atoms in a (110) geometry. DFT calculations suggested that the Cu-O binding in the $*OCH_2CH$ intermediate (shared by ethylene and ethanol production) is destabilized on the Cu (100) surface and therefore split the reduction pathway from ethylene to ethanol. [63] Gregorio *et al.* applied a similar principle to tailor facet-controlled Cu nanocatalysts to a gas-fed flow cell and demonstrated there facet-dependent selectivity was retained under commercially relevant reaction conditions (100-300 mA/cm^2, 1 M KOH) [64].

Cu surface is known to be dynamic and undergoes restructuring under eCO(2)RR conditions [28], [30], [49], [93]–[99]. Tracking the facet composition variation over time could help maintain the catalysts' stability during long-term operation. Capitalizing on *quasi-operando* electrochemical scanning tunneling microscopy (ECSTM), Kim *et al.* observed an electropolished polycrystalline Cu (Cu (pc)) electrode underwent sequential reconstruction under -0.9 V *vs.* SHE in 0.1 M KOH, first to a Cu (111) plane and then to a Cu (100) surface; no further surface transformation occurred afterwards (Figure 2.6) [100]. Interestingly, in contrast to the transformed (111) layer atop the Cu (pc), the surface of a native Cu (111) electrode showed no such conversion. Original Cu (100) was also impervious. The topmost planes of a Cu (110) crystal, on the other hand, underwent a similar transformation procedure as on Cu (pc). [101]

In addition to microscopes, another way to inspect the surface facet of an electrochemical catalyst is *via* electrochemical methods. Cyclic voltammetry (CV) cycles in the potential range where both the *OH adsorption/desorption and Cu reduction/oxidation features occur are normally scanned in the eCO(2)RR field. Due to the different work functions (φ) of the different facets ($\varphi_{(110)} < \varphi_{(100)} < \varphi_{(111)}$) [102], they exhibit different CV features. Since the CV shape and the potential of the features are also sensitive to the experimental conditions, such as electrolyte composition and concentration, the CV geometry of a certain crystal structure scanned in the same reaction environment is characteristic and a benchmark is expected to evaluate the identity and quality of Cu single crystals. [103] In this sense, Tiwari *et al.* presented quantitatively agreed simulated and experimentally measured fingerprint CV plots of Cu (110), (100), and (111) single crystals under alkaline conditions (Figure 2.7) [104]. Moreover, Sebastián-Pascual *et al.* evaluated the lead (Pb) underpotential deposition (UPD) on Cu (100) and (111) single crystal facets, and demonstrated the possibility of using Pb-

UPD to estimate the surface atomic ordering and quantify the surface roughness factor of a Cu (pc) electrode, by comparing with those obtained on well-defined surfaces [105].

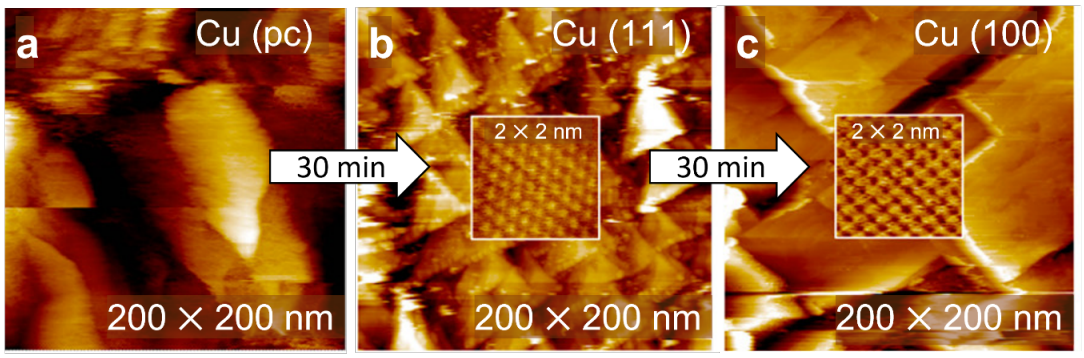

Figure 2.6 ***Low-resolution (200 nm × 200 nm) and zoomed-in (2 nm × 2 nm) operando EC-STM images at −0.9 V in 0.1 M KOH.*** *Experimental parameters: Bias voltage = −300 mV. Tunneling current for low-resolution images = 2 nA; for high-resolution images = 5 nA. Reprinted from* [100] *with permission. Copyright 2014 American Chemical Society.*

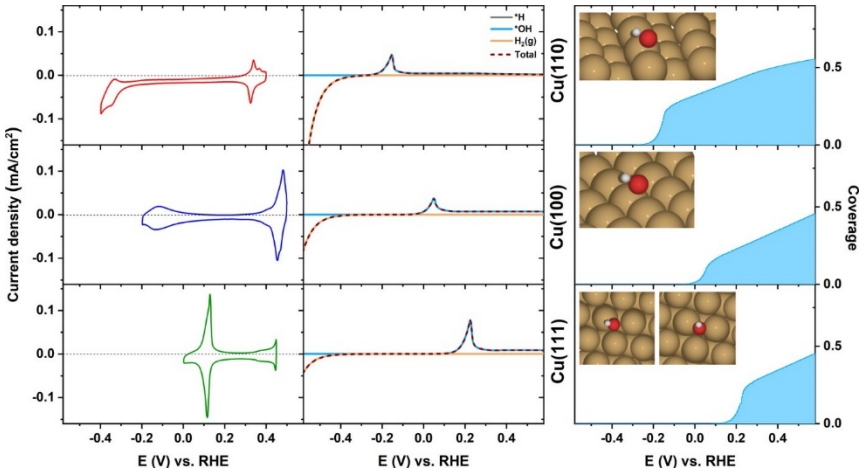

Figure 2.7 ***Experimental CVs (left) for Cu (110), Cu (100), and Cu (111)*** *depicting facet-dependent OH adsorption/desorption features in an Ar-saturated 0.1 M KOH electrolyte at a scan rate of 50 mV/s. Simulated CVs (center) for a scan rate of 50 mV/s, considering competing contributions from *H, *OH, and HER.* ***Calculated *OH coverages (right)*** *as a function of potential. Insets illustrate the optimal adsorption geometry of OH under these conditions. Reprinted from* [104] *with permission. Copyright 2021 Elsevier B.V.*

Cu single crystals also show promise as a model to investigate the effect of reaction environment and conditions on the eCO(2)RR pathways and kinetics. For instance, Pérez-Gallent *et al.* investigated the cation effect (including Li^+, Na^+, K^+, Rb^+, and Cs^+) on Cu (100), (111), and (pc) in eCORR, and found that cation effects are both potential-dependent and structure-sensitive: i) at E > -0.45 V vs RHE, selectivity towards C_2H_4 on all electrodes was promoted as cation size increases, whereas CH_4 was favored at more negative potentials; ii)

while CH_4 formation is impervious to neither the electrode structure and cation size, C_2H_4 production is dependent on both. Accordingly, a low overpotential and larger cation size are suggested for facilitating C_2H_4 generation over CH_4. [106] Comparing eCO2RR performance in 0.1 M $KClO_4$, KCl, KBr, and KI, respectively, Huang *et al.* found that the adsorbed anion could modify the electronic structure of the local Cu sites and therefore tune the coordination environment of *CO intermediate. Consequently, a remarkable total FE of 74% for C_{2+} products was obtained in KI, due to the strong binding of I- on the Cu surface. [107] Other effects such as electrolyte pH [53], [72], surface *CO coverage [61], the role of adsorbed oxygen species [108], density of surface defects[97], and the reaction temperature [109], *etc*., have also been discussed using Cu single crystals.

It is worth noting that there are a great number of studies on single crystal Cu catalysts have been done to understand eCO(2)RR, but I try not to put too many of them since my project is in experiments.

2.2.2. Summarizations and Comments

In summary, employing single crystals with a well-defined atomically flat surface as a model provides valuable information on the facet-dependent product preference on Cu catalysts, and therefore helps deconvolute the complicated eCO(2)RR mechanisms. The obtained knowledge is instructive for catalyst design to tune the selectivity towards desired products. By comparing the catalytic performance of an existing Cu catalyst with that of single crystals, one can gain insights into its facet composition, atomic structure and active sites, *etc*., and how these factors influence and can be modified to improve the catalyst's performance.

Although significant studies have been conducted to correlate the surface structure and eCO(2)RR performance of Cu catalysts, mechanistic understanding of the reaction pathways heavily relies on computational modeling (DFT calculations in most cases). In this regard, simulating the real reaction conditions with theoretical calculations remains challenging. On the one hand, simulations use perfect crystals as the model, while surface steps/defects/grain boundaries are inevitable on a real crystal, which may dominate the catalytic performance and therefore make it difficult to identify contributions from the basal plane. On the other hand, surface restructure is another factor that DFT calculations usually fail to reflect. *In situ/operando* spectroscopy is capable of providing real-time information on the structural and morphological evolution during the reaction. Surface inspection can also be done with electrochemical characterization. Therefore, applying the dynamic surface information to DFT calculations is expected to improve the precision of simulated results.

2.2.3. Aim #1 in This Thesis

Most reported Cu single crystal works only detected gas products with *in situ* or *operando* techniques, while measuring liquid products in a real-time scale remains challenging. Liquid products are usually analyzed using high-performance liquid chromatography (HPLC) [110] or nuclear magnetic resonance (NMR) [111]. For volatile liquid products, static headspace-gas chromatography (HS-GC) [46] is also used. However, some products are unstable and readily undergo a further spontaneous chemical transformation in the electrolyte if not detected on time. As a consequence, the validity of analyses based on delayed detection could be jeopardized. Aldehyde is such a chemical group that undergoes complicated organic reactions in alkaline [112], [113]. Therefore, in this thesis, I aim for validating the detection of acetaldehyde on a real-time scale and tracking its production on both polycrystalline and single crystal Cu surfaces during eCORR, such that providing insightful information on its production pathway, thus helping to improve the production selectivity towards acetaldehyde and ethanol. (Chapter 4)

2.3 State-of-the-art CuAg Bimetallic System in eCO(2)RR

2.3.1. Literature Review

As stated above, Cu is the only monometallic catalyst that produces both hydrocarbons and oxygenates, while the poor selectivity limits its further use [28], [39]. C_{2+} products (*e.g.*, C_2H_4, C_2H_6, ethanol, and propanol) generally have higher energy densities and larger economic values compared to C_1 products (CO, CH_4, and formate), and therefore provide a more attractive direction to aim for [32].

Ethylene and ethanol are of great interest because they are economically and energetically valuable and are produced in substantial quantities globally (> 30 MtC/yr) [28]. Literature has found that these two products share the same generation pathway after C-C coupling [114], [115], which is believed to be the rate-determining step (RDS) of C_{2+} product formation [116]–[118]. Considering that C-C coupling usually requires a high *CO availability, and that Cu is sluggish in converting CO_2 to *CO, tandem catalysts combining Cu and a CO-selective metal (Ag, Au, and Zn) have proven their superiority in C_{2+} product generation [114], [119]–[131].

Taking advantage of the high electrical conductivity, eCO2RR activity, and cost-effectiveness, Cu-Ag bimetallic/alloy catalysts have been widely investigated [127]–[129], [132]–[138]. The reported Cu-Ag interaction is strongly dependent on the interplay between

Ag deposition content, preparation process, and the resulting catalyst structure/morphology, as well as phase miscibility, leading to different product distributions. For example, Higgins *et al.* synthesized a nonequilibrium CuAg alloy with miscible phases by physical vapor deposition (PVD). [132] Compared to pure Cu, the CuAg selectivity of acetaldehyde increased at the expense of ethanol. This was attributed to the reduced oxophilicity when introducing Ag in the Cu lattice, which weakened the adsorption of acetaldehyde and thus its further reduction to ethanol. A similar phenomenon was also observed on CuAg bimetallic catalysts with separated Cu and Ag phases [129], [139]. Although with distinctive catalyst structures (Ag nanoparticle-decorated Cu nanocubes [129] and galvanically exchanged Cu foil with Ag [139]), Clark *et al.* [129] and Herzog *et al.* [139] both attributed the weakened carbonyl-containing intermediate adsorption to the locally compressive strain by introducing Ag in the Cu surface. In contrast, Su *et al.* suggested an improved oxygen affinity for oxygen-adsorbed intermediates instead, resulting in improved ethanol production when the Cu/Cu_2O composite was dispersed with trace amounts of Ag [140]. On the other hand, an alternative C-C coupling pathway between *CO and $*CH_x$ (x=1,2) could be activated in the presence of excessive *CO, as was proposed on both segregated [141] and alloyed [126] Cu and Ag phases. In this mechanism, the formed $*CH_xCO$ species would be eventually reduced to ethanol *via* acetaldehyde (CH_3CHO) [80], [112].

The slightly higher electronegativity of Ag (1.93 on the Pauling scale (χr)) compared to Cu (1.90 on the Pauling scale (χr)) makes electron flow from Cu to Ag at the interface thermodynamically feasible [124], regardless if the metal phases are separated [124], [142] or mixed [143]. This electronic interaction was used to explain the enhanced *CO adsorption on electron-depleted Cu and the subsequent *CO-*CO coupling into C_2H_4 observed by Huang et al [124]. On the contrary, Xu *et al.* hypothesized an electron transfer route from Ag to Cu which results in a suppressed hydrocarbon generation on Cu induced by the Ag dopant [144].

2.3.2. Summarizations and Comments

The above divergencies demonstrate a yet-to-be-fully-understood mechanism of the interaction between Cu and Ag in eCO(2)RR, which generally falls into three aspects:

i) if Cu and Ag have miscible phases;

ii) if there is electronic and/or structural interaction between Cu and Ag; and if so,

iii) how is the intermediate adsorption influenced and eventually results in a varying selectivity towards different products.

Being able to track the catalysts' variations in crystallite and coordination environment in the eCO2RR environment would provide more insightful information regarding the above points. Therefore, *operando* measurements are indispensable.

2.3.3. Aim #2 in This Thesis

Based on the above discussions, I will use flat Cu-Ag bimetallic catalysts as the model. Flat because I would like to focus on the intrinsic interaction between the two metals and try to avoid possible influence from surface engineering, such as complicated active sites on nanostructures, as much as possible. Then I expect to investigate what the (potential) Cu-Ag interactions are and how the eCO2RR performance of Cu will be tuned upon coupling with (different amount of) Ag. With these investigations, I aim for providing information that can facilitate the design of new bi-/multi-phase metallic or alloy electrocatalysts (Chapter 5).

Chapter 3 Experimental Techniques

In this chapter, I will give a brief overview of the experimental techniques that are involved in the two projects, which will be presented in Chapter 4 and Chapter 5, respectively. The techniques are used for electrode and catalyst preparation, characterization, and electrochemical performance test. For each technique, I will first introduce its working principle, followed by an explanation on what role it plays in my projects and what information is expected.

3.1 Electrochemical Setup

3.1.1. Three-electrode System

A three-electrode system consists of a working electrode (WE), a reference electrode (RE), and a counter electrode (CE), as illustrated in Figure 3.1. The potential is measured between the WE and the RE, while the current is measured between the WE and the CE. In electrochemical CO_2 reduction, WE usually works as the cathode, where CO_2 reduction reaction (Equation (3.1)) happens; whereas CE works as the anode, where oxygen evolution reaction (OER) (Equation (3.2)) occurs.

All electrochemical measurements included in this thesis were controlled using a BioLogic SP-200 potentiostat. Three configurations of three-electrode systems are involved, as will be presented subsequently.

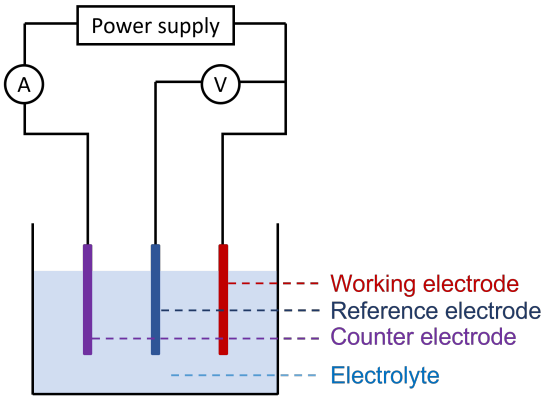

Figure 3.1 ***Schematic of three-electrode system.*** *The red, navy blue and purple bar represents working, reference, and counter electrode, respectively. The light blue area represents electrolytes. "A" stands for the current measured between the EW and the CE. "V" stands for potential measured between the WE and the RE. Power supply is provided by a potentiostat.*

$$xCO_2 + nH^+ + ne^- \rightarrow yProduct + zH_2O \quad (3.1)$$

$$2H_2O \rightarrow O_2 + 4H^+ + 4e^- \quad (3.2)$$

3.1.2. EC-MS Cell

All electrochemical CO_2 and CO reduction measurements in Chapter 4 were carried out with a commercially available microchip-based electrochemistry – mass spectrometry (EC-MS) setup (SpectroInlets ApS, Denmark) with a stagnant thin-layer cell Figure 3.2. The counter and reference electrodes were inserted in a glass tube with a ceramic frit on the tip, respectively. The working volume is defined by the distance between the working electrode and the membrane chip (100 µm). A carrier gas is normally required to equilibrate the chip pressure with the atmosphere. When the carrier gas also works as the reactant (*e.g.* CO_2 as the carrier gas for eCO2RR, and CO as the carrier gas for eCORR), it diffuses through the micro holes on the chip to the working volume, where it has the chance to reach the working electrode and participate in the electrochemical reaction. Afterwards the excessive carrier gas and produced molecules desorb from the working electrode and diffuse through the membrane chip to the quadrupole mass spectrometer (QMS). For more details regarding the design and working mechanism of the system please refer to [145], [146].

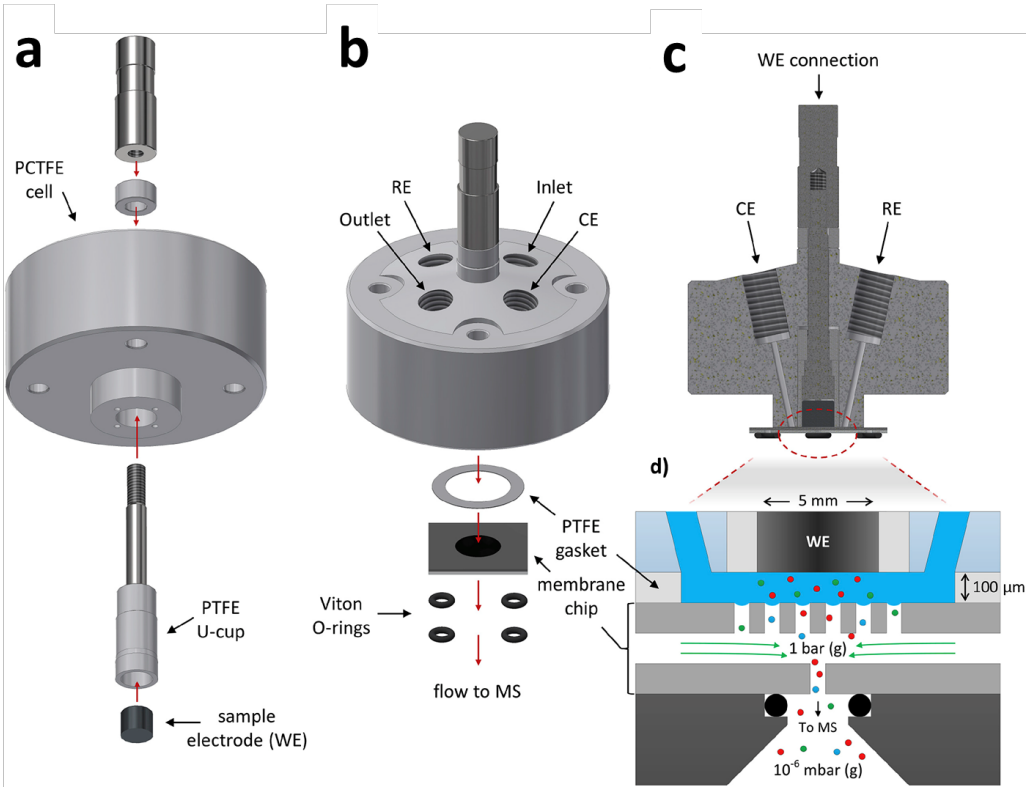

Figure 3.2 ***Schematic illustration showing the assembly of the stagnant thin-layer electrochemistry (EC) cell used in EC-MS measurements.*** *a) (bottom view) Mounting of a 5.0 mm outer diameter disk electrode in the EC cell using a rotating disk electrode (RDE) mounting system from Pine Research Instrumentation. b) (top view) Mounting of the assembled EC cell onto the membrane chip using a 100 µm thick Teflon (PTFE) spacer to define a thin-layer working volume between the electrode and the membrane. Viton O-rings are used to seal the membrane chip to the ultra-high vacuum of the mass spectrometer. Four access channels connect the working volume to an external electrolyte reservoir, a reference electrode (RE) and a counter electrode (CE) using Tefzel (ETFE) Lure adapters (not shown). c) (side cut view) Filling of the EC cell with electrolyte, creating a three-electrode configuration established with the working electrode (WE) placed in the center above the membrane. d) (Zoomed side view) Working principle showing how volatile reaction products are captured by the membrane and sent to the mass spectrometer while the carrier gas in turn equilibrates with the working volume. The assembled cell and the membrane chip interface to the mass spectrometer through an interface flange. Reprinted from* [146] *with permission. Copyright 2018 Elsevier Ltd.*

3.1.3. H-type Cell

Electrochemical CO_2 reduction in Chapter 5 (except for synchrotron measurements) was conducted in a 2-chamber H-cell in the 3-electrode configuration. Both the cathode and anode chamber bodies are made of polyetheretherketone (PEEK). The two chambers were separated by a hydrocarbon-based ion-exchange membrane (Selemion AMV, AGC Engineering CO., LTD.), activated in 0.1 M KOH (99.995% trace metals basis, Sigma-Aldrich) overnight, and stored in MilliQ water. Separated cathode and anode chambers allow for studying half-cell reactions. The liquid volume of both chambers is 6.5 mL, whereas the actual electrolyte volume was 6.0 mL in both chambers. The cathode chamber was purged with CO_2 at 10 sccm

for the duration of the experiment. An IrO_2-coated carbon paper (1.0 cm x 1.0 cm, Dioxide Materials) and a miniature leak-free Ag/AgCl electrode (Saturated KCl; Innovative Instruments Inc.) were used as the counter and reference electrode, respectively. Cell configuration and illustrations are depicted in Figure 3.3.

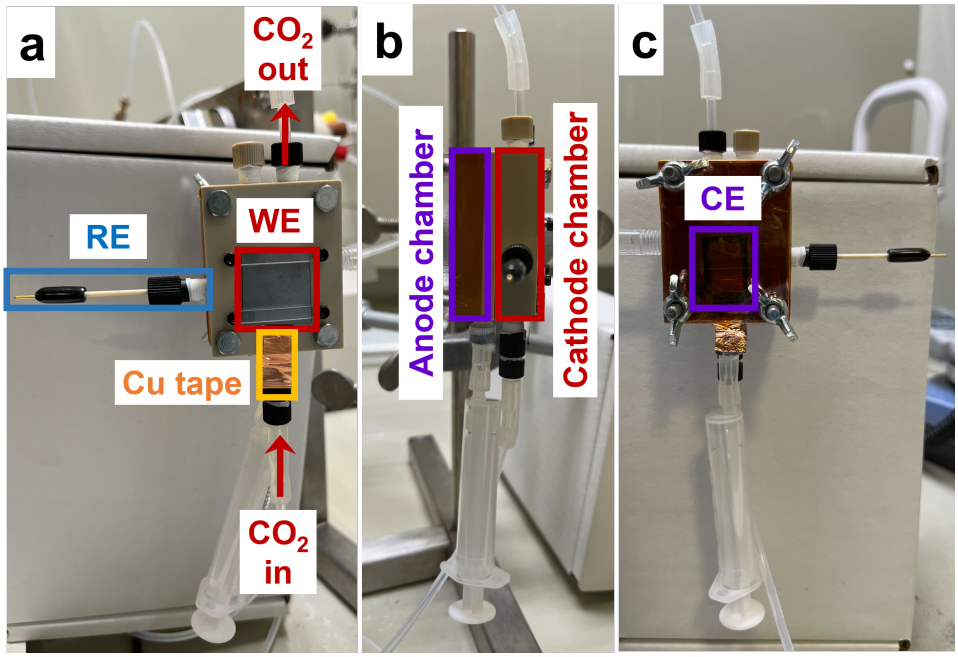

Figure 3.3 ***H-cell configuration*** *used for eCO2RR performance test on CuAg alloys. a) Cathode chamber view: WE window (red frame) with a size of 1.5 cm ✕ 1.5 cm. Catalyst was sputtered on the front side of the Si wafer. Cu tape (yellow frame) below was for electrical connection. CO_2 was bubbled through a titanium frit (installed in the connector, not shown) from the bottom to the electrolyte during the measurement. b) Side view: anode chamber (purple frame) and cathode chamber (red frame) was separated by Selemion membrane in the middle (not shown). c) Anode chamber view: CE window (purple frame) with a size of 1.0 cm ✕ 1.0 cm.*

It is worth pointing out that although ion-exchange membranes can prevent organic molecules from passing through, the produced carboxylates (*e.g.*, formate and acetate) in the cathode chamber can still pass through the membrane and reach the anode chamber, because they exist in the form of anions ($HCOO^-$ and CH_3COO^-). For this reason, post-mortem electrolytes in both chambers were collected and analyzed with high-performance liquid chromatography (HPLC).

Gas products were collected and analyzed *in situ* with gas chromatography (GC) every 10 min.

3.1.4. Operando Cell

Synchrotron *operando* grazing incident (GI) X-ray diffraction (XRD) and X-ray absorption spectroscopy (XAS) were conducted using a previously designed 3D-printed flow cell, depicted in Figure 3.4. It enables the grazing incident configuration of the sample while maintaining a higher horizontal alignment of the sample and also maintaining a high transmissivity for X-ray incidence as described in [137]. Cu_XAg_{100-X} catalyst samples were prepared on a Si (111) substrate, as will be described in Chapter 3.3.1. Two 50 µm diameter Pt wires (Alfa Aesar, 99.99%) and a miniature Ag/AgCl electrode (Innovative Instruments Inc.) served as the counter and reference electrode, respectively. During *operando* XAS, the electrolyte was purged with CO_2 gas and pumped through the cell by a 2-channel peristaltic pump (SHENCHEN LabN6) at 50 mL/min.

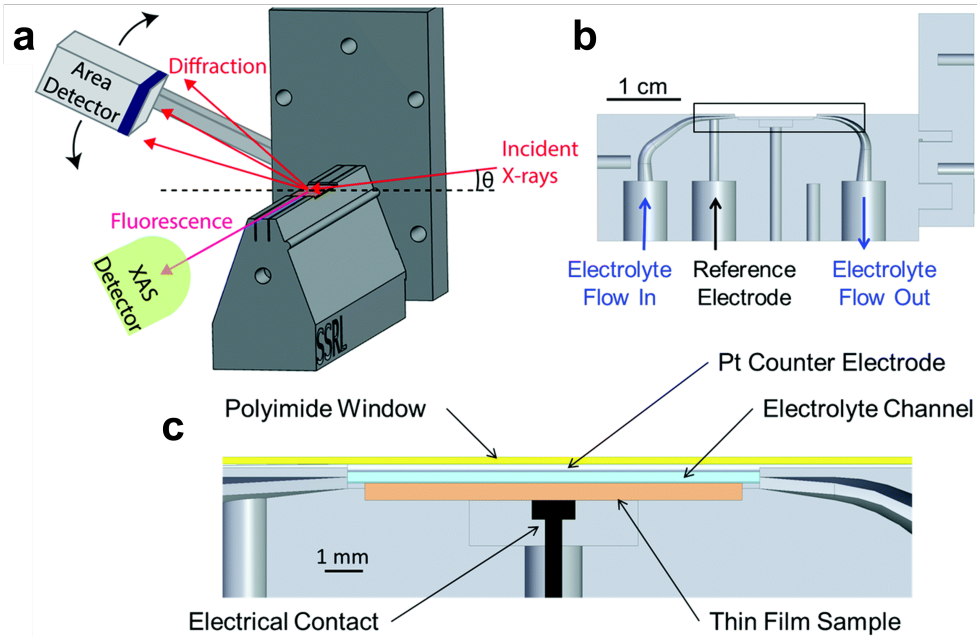

Figure 3.4 ***Electrochemical flow cell design for synchrotron operando measurements.*** *(a) Schematic illustrating the experimental geometry for grazing incident, diffracted, and fluorescent X-rays. Not to scale; the cell is enlarged and the polyimide window is excluded for clarity. (b) Side-view cross-section of the electrochemical cell, showing the electrolyte flow channels and reference electrode port. (c) Enlarged view of the indicated area in (b). X-rays enter into the page, between the thin film sample and Pt counter electrode. Note that the polyimide window also seals the sides of the electrolyte channel where the X-rays enter. Reprinted from* [137] *with permission. Copyright the Owner Societies 2019.*

3.2 Electrochemical Techniques

3.2.1. Potential Scale

As stated in Chapter 3.1.1, the half-cell potential of the cathode is recorded between the WE and the RE. However, since various REs are used in the literature, a standard potential is needed for comparison. The standard hydrogen electrode (SHE) is such a standard that has been widely used in the electrochemistry field. It is based on the half-cell reaction of a H_2/H^+ redox couple in theoretical ideal solutions on a platinum electrode (Equation (3.3)). Its potential is defined as zero volts at any temperature.[147] However, SHE does not take the electrolyte pH into account, therefore the reversible hydrogen electrode (RHE) is more often used for the comparison among different pH values. The conversion between the SHE and RHE scales follows Equation (Equation (3.4)). During eCO2RR, since the applied potential is with respect to the RE, the conversion from $E_{vs.RE}$ to $E_{vs.RHE}$ is described by Equation (3.5) and Figure 3.5. All potentials reported in this thesis are converted to be with respect to RHE unless otherwise stated.

$$H^+_{(aq)} + e^- \leftrightarrow \frac{1}{2} H_{2\,(g)} \tag{3.3}$$

$$E_{RHE} = E_{WE} - 0.059 \times pH \tag{3.4}$$

$$E_{vs.RHE} = E_{vs.WE} + E_{vs.RE} + 0.059 \times pH \tag{3.5}$$

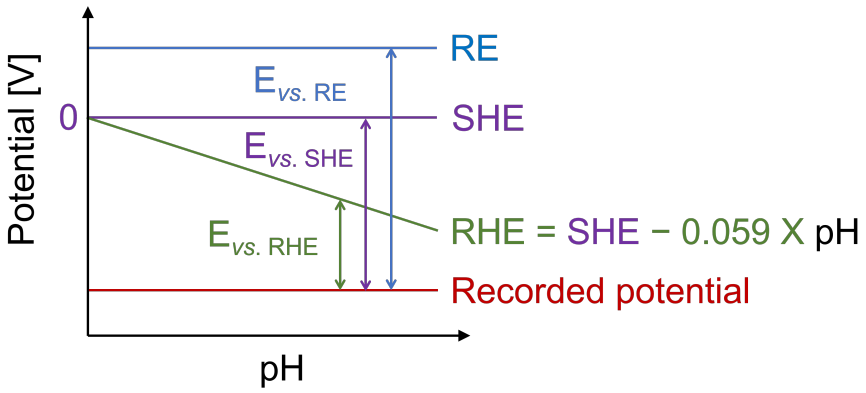

Figure 3.5 ***Conversion among different potential scales.***

3.2.2. Electrochemical Impedance Spectroscopy (EIS)

Electrochemical impedance spectroscopy (EIS) is to apply an alternating potential with a small amplitude (normally below 50 mV) in a wide range of frequencies and determine the current response at different frequencies. Similar to Ohm's law, impedance is obtained by dividing the applied potential by the current response. The obtained impedance contains information correlated with the physical properties of the testing system, including the (DC) resistance, capacitance, inductance, diffusion, and microstructure features of the electrode, *etc*. [148], [149] Processes with different time scales can be probed by varying the frequency. For example, fast processes such as ion migration respond to higher frequencies, while slower processes such as diffusion dominate in the low-frequency domain [150].

Due to the complexity of EIS, a simplified model (*i.e.,* equivalent circuit) is usually used to represent the electrochemical process. In most cases of Cu-based eCO(2)RR, Randle's circuit is widely used as the model, shown in Figure 3.6. It consists of three components: i) R_s is solution resistance mainly induced by the electrolyte between the WE and the RE; ii) C_{dl} is the double layer capacitance of the electrode/electrolyte interface; and iii) R_{ct} is the charge transfer resistance which is the general impendence of the system [151]. The combination of all three components is considered Ohmic resistance, R_Ω.

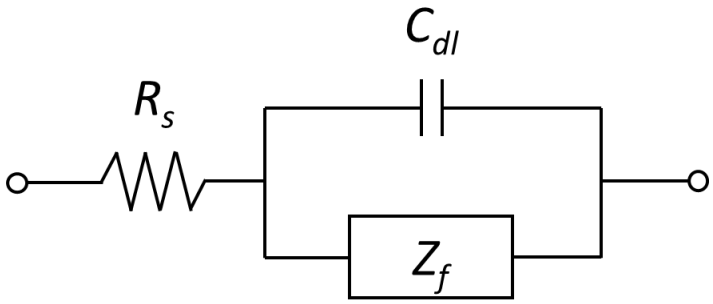

Figure 3.6 ***Equivalent circuit of a simplified Randle's cell.*** *R_Ω represents the solution resistance, C_{dl} represents the double-layer capacitance of the electrode/electrolyte interface, and Z_f represents the impedance from faradaic processes.*

3.2.3. Ohmic Drop Compensation

In a three-electrode system, although no current flows through the RE, there is current flowing between the WE and the RE. Therefore, when a potential is applied to the WE, the measured potential is lower than the actual value, and the difference is induced by the solution resistance (R_S), which is also called Ohmic drop. The relationship between the applied and actual potential is thus given by:

$$E_{Actual} = E_{Applied} - \Delta E_{Ohmic} = E_{Applied} - IR_S \quad (3.6)$$

Where, *I* is the current. In all the electrochemical measurements reported in this thesis, I used the software "EC-lab" to fit the impedance spectrum to the equivalent circuit to get the solution resistance, and then automatically compensate 85% during the measurement. The rest 15% is to avoid oscillations of the instrument.

More detailed and deeper analyses could be interesting, but it is out of the scope of this thesis.

3.2.4. Chronoamperometry (CA) *vs.* Chronopotentiometry (CP)

In a chronoamperometric (CA) process, a constant potential is applied over a period of time, and the current response is recorded. A constant potential (and thus a constant overpotential) leads to a constant thermodynamic driving force to a certain electrochemical reaction. Thus, CA is more often employed for mechanistic investigations, such as speculating reaction pathways and comparing selectivity among different catalysts.

Chronopotentiometry (CP), on the contrary, is to apply a constant current while recording the potential response. In other words, at CP, a constant charge and thus kinetic driven force is input to the reaction system. Therefore, even with the same current, the actual potential applied to different electrodes varies. On Cu electrodes, since product preference varies at different potentials, it makes investigations on the intrinsic catalytic properties difficult. For example, if one compares the eCO2RR performance on a flat Cu (denoted as Cu(f)) with that on a rough Cu (denoted as Cu(r)), Cu(r) would exhibit a higher current than Cu(f) at the same potential. Correspondingly, Cu(r) would show a lower (*i.e.,* less negative) potential than Cu(f) at the same current. As a consequence, the performance of Cu(r) in a CA measurement could be underestimated because the applied potential, and thus overpotential, is lower than expected.

Based on the above considerations, I used CA for steady-state performance tests, including mass spectrometer parameter modifications in Chapter 4 and eCO2RR performance tests on CuAg alloys in Chapter 5.

3.2.5. Linear Sweep Voltammetry (LSV)

Linear sweep voltammetry (LSV) is to linearly sweep potential in a potential range at a constant rate (scan rate = dE/dt) and record the current response over time. This technique is combined with the mass spectrometry in the EC-MS measurements in Chapter 4. By inspecting the MS signal intensity change of selected fragments during LSV scan, onset

potentials of the corresponding products can be observed, which provides mechanistic information on speculating the eCO(2)RR pathways.

3.2.6. Cyclic Voltammetry (CV)

In cyclic voltammetry (CV), the potential is cyclically linearly swept within a potential range at a constant rate (scan rate = dE/dt), and the current response is recorded, which is then plotted as a function of potential. CV is a powerful and versatile electrochemical technique that provides both qualitative and quantitative information on the studies system, such as the reaction reversibility, reduction/oxidation of the electrode, adsorption/decoration and reduction/oxidation of the reactant species, *etc*.

In this thesis, CV is used in two aspects: i) inspect the crystal structure of polycrystalline and single crystal Cu electrodes with their corresponding fingerprint CV features in Chapter 4; and ii) compare the oxophilicity of Cu and CuAg alloys in Chapter 5.

Different Cu single crystals have characteristic CV profiles in the fingerprint region, and are sensitive to the reaction conditions, including electrolyte composition and concentration, electrode surface orientation and defects, and scan rate, *etc*. Therefore, the fingerprint CV features are often used as a benchmark to inspect the crystal quality. [103], [152] Figure 3.7 depicts fingerprint CV profiles of Cu (100), (110), (111) and (211) single crystals as well as Cu (pc) as the benchmark used in Chapter 5.

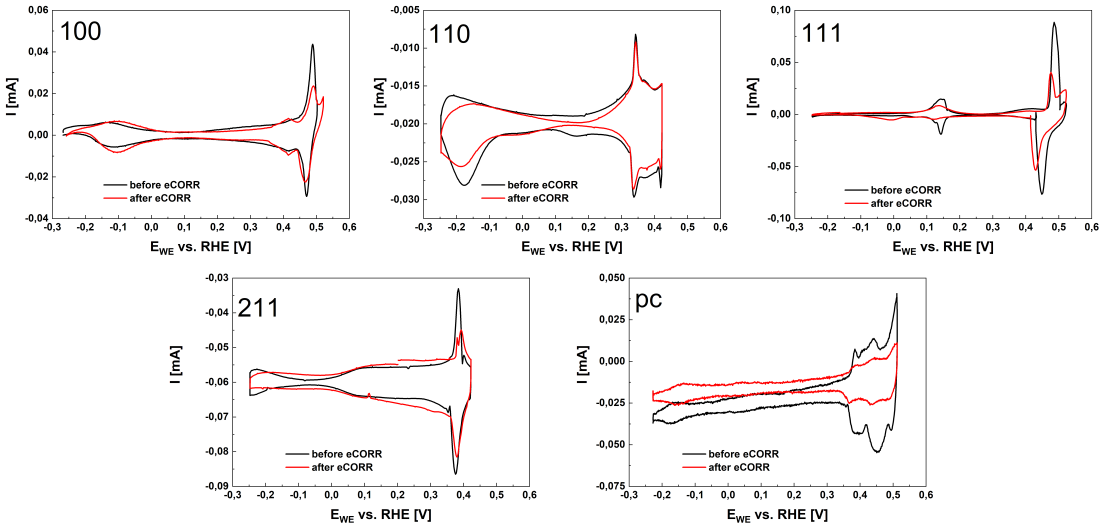

Figure 3.7 ***Fingerprint cyclic voltammograms for Cu (110), Cu (100), Cu (111), Cu (211), and Cu (pc) collected in Ar-saturated 0.1 M KOH.*** *The negatively shifted current on Cu (110) and Cu (211) is due to ORR as explained in Chapter 4. Features in the negative potential region is due to *OH adsorption/desorption, while those in the positive potential region are attributed to Cu reduction/oxidation.*

3.3 Electrode Preparation

3.3.1. Magnetron Sputtering

Magnetron sputtering has shown its superiority in thin film fabrication due to its fast deposition rate and uniform thin film growth [153]. The sputtering process is conducted in a vacuum chamber. A target material equipped with permanent magnets on the back acts as the cathode and a substrate works as the anode. When a sufficiently high voltage (hundreds to thousands of volts) is applied, a glow discharge would be ignited in the vacuum charmer and function as the ion source. Upon introducing an inert gas, which is Ar in our system, the Ar molecules are ionized to Ar^+ ions. The generated Ar^+ ions are then attracted to the negatively charged target (cathode). The bombardment ejects atoms or molecules from the target, accompanied by secondary electrons being produced. In the presence of the electromagnetic field over the target, not only the Ar^+ ions are accelerated, but the secondary electrons are also condensed there and therefore increase the flux of bombarding ions. Traveling of the ejected target atoms and molecules to the substrate, on the other hand, are impervious to the electromagnetic field since they are neutral. As a result, the deposition rate can be effectively improved. The magnetron sputtering working principle is schematically represented in Figure 3.8.

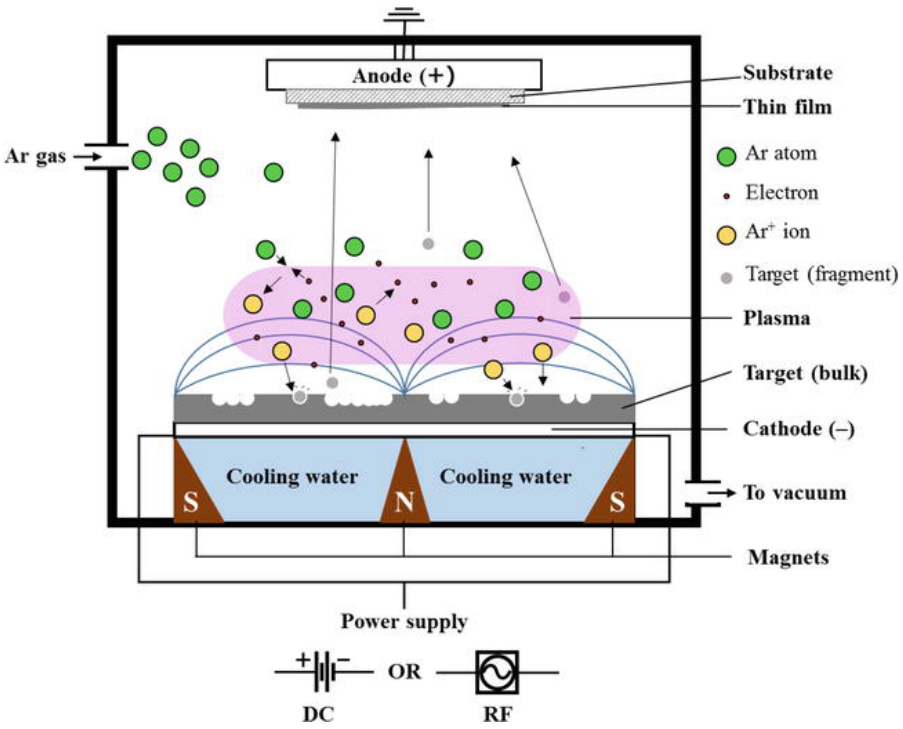

Figure 3.8 ***Schematical representation of magnetron sputtering equipment and deposition process****. The purple area above the target represents the glow discharge plasma. Reprinted from* [154] *with permission. Copyright 2020 Philipus N. Hishimone, Hiroki Nagai and Mitsunobu Sato.*

I used magnetron sputtering to prepare all samples (pure Cu, pure Ag, and CuAg alloys with various compositions) in Chapter 5. Si waters (thickness 75 nm, Wafer World Inc., boron-doped, resistivity < 0.025 Ohm-cm) were sued as the substrate. Before sputtering, both the Cu and Ag targets (Kurt–Lesker, 99.9999%) were pre-sputtered with the shutters closed for *ca.* 1 min to remove the potentially oxidized top layer. The substrate was sputter-cleaned by Ar at 40 W for *ca.* 5min to remove any surface contamination and oxide layers. A *ca.* 5 nm thick Ti adhesive layer was then sputtered at a rate of *ca.* 0.7 Å/s, followed by a *ca.* 50 nm thick Cu_XAg_{100-X} catalyst layer deposited at a rate of *ca.* 1.0 Å/s. The deposition rate and nominal composition as well as the thickness of the deposited catalyst layer were calibrated by a quartz crystal microbalance (QCM). All samples were deposited under a 5 mTorr, 10 sccm Ar (N5, Air Liquide) atmosphere at room temperature. QCM deposition rate calibration and sputter conditions are listed in Figure 3.9 and Table 3.1, respectively.

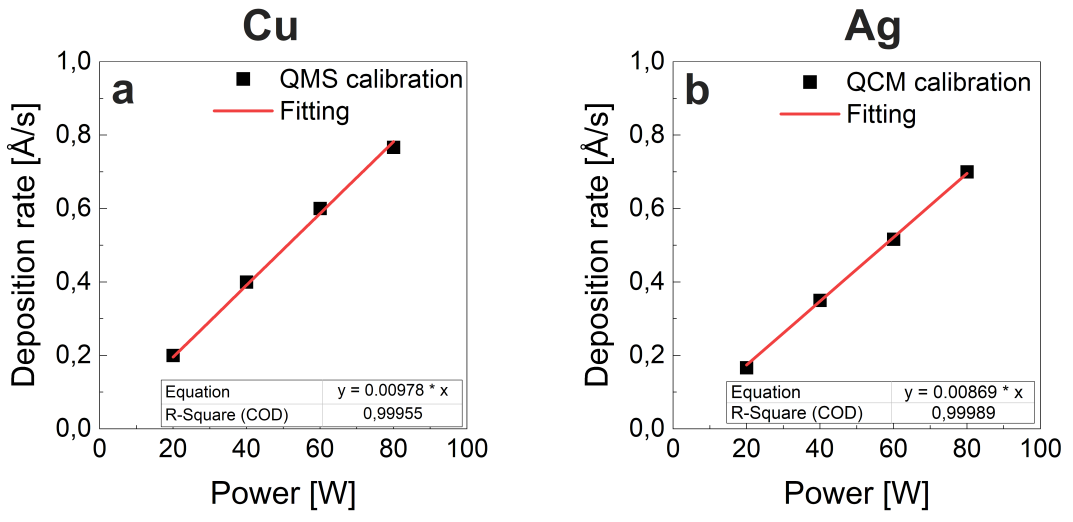

Figure 3.9 ***QCM calibration of the a) Cu and b) Ag targets.*** *Ar flow was kept at 10 sccm during sputtering. Chamber pressure was kept at 5 mTorr.*

Table 3.1 ***Magnetron sputtering parameters.***

Sample	**Power$_{Ag}$ [W]**	**Power$_{Cu}$ [W]**
Cu	-	102
$Cu_{95}Ag_5$	18	86
$Cu_{80}Ag_{20}$	98	15
$Cu_{60}Ag_{40}$	56	52
Ag	115	-

It is worth noting that QCM calibrations were conducted separately for each target. During co-sputtering, the travelling of the two ejected atom identities would inevitably influence each other which might influence the final composition. Therefore, X-ray photoelectron spectroscopy (XPS) was conducted right after sputtering to inspect the real composition, and no significant difference between the nominal and XPS-measured composition was found in all samples. More details can be found in Appendix B.1.

3.3.2. Electrode Polish – Mechanical and Electrochemical Polish

Mechanical polish is a physical process, during which an electrode is polished using mechanical abrasives. This is usually used to remove surface oxides, contaminations, or visible surface damages, such as scratches, bumps, and dents. For example, previous studies found that mechanical polishing is crucial for removing the native oxide on the Cu electrode surface, both polycrystalline and single crystals [103]. However, a mechanically polished surface still has debris and needs to be further smoothened by electropolishing.

Electropolishing is usually conducted in a two-electrode system, where the to-be-polished metal acts as the anode and a strong acid with high viscosity serves as the electrolyte. During electropolishing, a positive potential is applied to the anode, oxidizing the surface metal atoms to metal ions which then dissolve in the electrolyte. Since the current density is higher at the surface roughness peaks and edges, these features are preferably dissolved, which rounds the corners, and thereby reduces the surface roughness.

All the Cu electrodes in Chapter 4, both polycrystalline and single crystals were first mechanically polished with MicroPolish^{TM} alumina and silica slurry suspension (0.3 μm, Buehler) on a MicroCloth polishing cloth (Buehler). The mechanically polished electrodes were then thoroughly rinsed with Milli-Q water (18.2 MΩ·cm @25°C, 2ppb TOC, Q-POD®) and sonicated for 15 min. Electropolishing was subsequently conducted in 70% of phosphoric acid (ACS reagent, ≥85 wt. % in H_2O) at 2 V for 1 min with a Cu wire (> 99.95%, Goodfellow Cambridge Ltd.) counter electrode (cathode). CV features in the fingerprint region of each crystal were then recorded. The above-described mechanical-electrochemical polishing procedure was iterated until a fingerprint CV was obtained. Electrochemical $CO_{(2)}$ reduction measurements were conducted subsequently.

3.4 Catalyst Characterization

3.4.1. X-ray Diffraction (XRD)

X-ray diffraction (XRD) is an extensively used analytical technique for determining crystal structures, based on Bragg's law, as described by Figure 3.10 and (Equation (3.7)) [155]. X-ray can be considered a wave of electromagnetic radiation, and the waves can be described by sinusoidal functions. When an incident beam is reflected by an atom, the scattered waves interfere with each other. In-phase scattering leads to constructive interference, which occurs when the path difference (*i.e.,* 2dsinθ) is multiple (*i.e.,* n = 1, 2, 3, …) of the wavelength of the incident X-ray beam and amplifies the X-ray diffraction signal; whereas out-of-phase scattering causes destructive interference and therefore "cancels out" the signal.

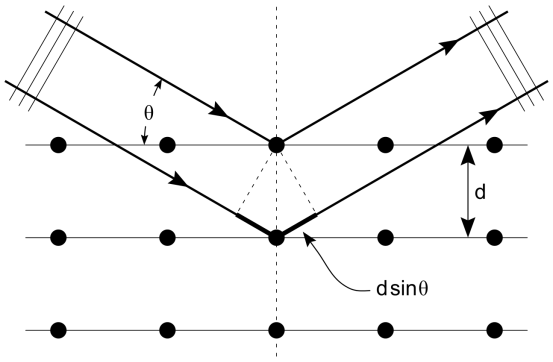

Figure 3.10 ***Schematic representation of Bragg's diffraction.*** *Reproduced from* [155] *with permission. Copyright Cambridge Philosophical Society and the Royal Institution of Great Britain (RI).*

$$n\lambda = 2dsin\theta \tag{3.7}$$

Where, n is an integer, λ is the wavelength of the X-ray, d is the lattice spacing of the crystal layers, and θ is the incident angle.

In grazing incident XRD (GIXRD), a small incident angle (ω < 5 °) is applied, such that the X-ray beam only penetrates a shallow depth and is therefore surface sensitive [156]. During the measurement, the incident angle is fixed while the detector keeps moving within a given 2θ range, as depicted in Figure 3.11.

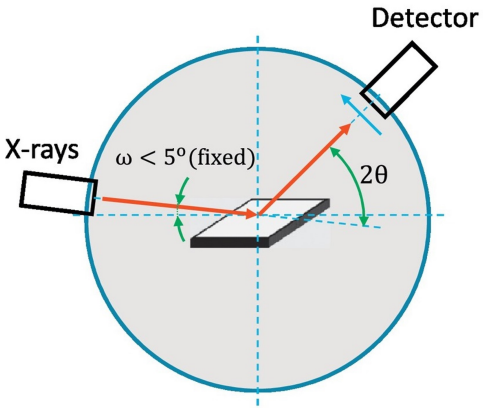

Figure 3.11 ***Grazing incident X-ray diffraction (GIXRD) geometry****. Reprinted from* [156] *with permission. Copyright 2018 Elsevier B.V.*

XRD was used in Chapter 5 for investigating the crystal structure of CuAg alloys. *Ex situ* XRD was conducted on a Malvern Panalytical Empyrean X-ray diffractometer in the grazing incident geometry with the incident beam angle at 0.7º. An Empyrean Cu LFF HR gun ($K\alpha_1$ = 1.540598 Å, 8.04 keV) was used as the X-ray source and operated at 45 kV and 40 mA. *Operando* XRD was conducted at beamline 2-1 at SSRL at SLAC, using a Si (111) monochromator and beam energy of *ca.* 17 KeV (0.729 Å).

Due to the different energy of the X-ray beam used for *operando* and *ex situ* measurements, peak positions (*i.e.,* 2θ value) are different, but can be converted according to Bragg's law (Equation (3.7)).

Crystallite size can be calculated according to Scherrer's formula:

$$D_p = \frac{K\lambda}{\beta cos\theta} \tag{3.8}$$

Where, D_p is the average crystallite size; K is the Scherrer constant, 0.94 is usually used for spherical crystallites with cubic symmetry; β is the FWHM (full width at half maximum) of XRD peak, and θ is the peak position in XRD patterns. It is worth pointing out that the peak width in an XRD pattern is not only determined by the lattice structure (*e.g.*, lattice size and strain), but is influenced by the instrumental broadening, which is mainly due to X-ray beam footprint (*i.e.*, X-ray beam spot size). During our *operando* experiments presented in Chapter 5, since there was an electrolyte layer above the sample (Figure 3.4) and the samples are not perfectly flat, X-ray refraction and scattering could also have impacts. Therefore, the calculated averaged crystal size (Appendix B.3) was a rough estimation.

In Chapter 5, since the 2θ value of the Cu-rich and Ag-rich peaks are between those of the pure Cu (111) and Ag (111) peaks, they can be assumed to be both (111) facet for estimating the elemental composition based on Vegard's law:

$$a_{Cu_xAg_{(1-x)}} = xa_{Cu} + (1-x)a_{Ag} \tag{3.9}$$

where, x is the molar fraction and a is the lattice constant calculated from Equation (3.10).

$$\frac{1}{a^2} = \frac{h^2 + k^2 + l^2}{d^2} \tag{3.10}$$

where, $h = l = k = 1$ by assuming (111) facet.

Therefore, in the case of Cu_xAg_{1-x},

$$x = \frac{a_{CuxAg(1-x)} - a_{Ag}}{a_{Cu} - a_{Ag}} \tag{3.11}$$

3.4.2. X-ray Photoelectron Spectroscopy (XPS)

X-ray photoelectron spectroscopy (XPS) is a surface-sensitive technique for determining the samples' elemental composition and oxidation state. It is based on the photoelectric effect, as schematically described in Figure 3.12. When an atom absorbs a photon with the energy hv, a core electron with a binding energy E_b would be excited and emitted to the vacuum with a kinetic energy E_k given by Equation (3.12), where φ is the work function of the analyzer. Upon emitting an electron, a hole is left at the core level and another electron from an upper level would fill this hole and emit another electron (*i.e.,* Auger electron) and its energy is given by Equation (3.13).

$$E_k = hv - E_b - \varphi \tag{3.12}$$

$$E_{k,Auger} = E_{b1} - E_{b2} - E_{b3} \tag{3.13}$$

For example, $E_{k,KLL} = E_{b,K} - E_{b,L1} - E_{b,L2,L3}$ in Figure 3.12b.

Al Kα (hv = 1486.6eV) or Mg Kα (hv = 1253.6eV) are the two most commonly used monochromatic X-ray sources in XPS. Since E_k is element- and orbital-specific, XPS can be used for elemental and oxidation state identification [157].

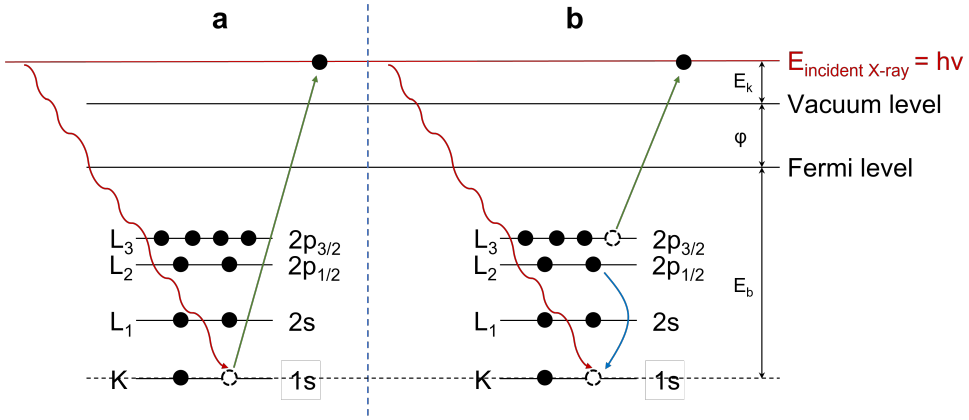

Figure 3.12 ***Schematic illustrations of: a) photoelectron emission process,*** *where a core electron is excited by the X-ray beam and emitted to the vacuum with a kinetic energy* E_k*;* ***and b) Auger electron emission process,*** *where another electron on a higher level fills up the hole left at the 1s orbital accompanied by emission of fluorescence, and a third electron is released to the vacuum.*

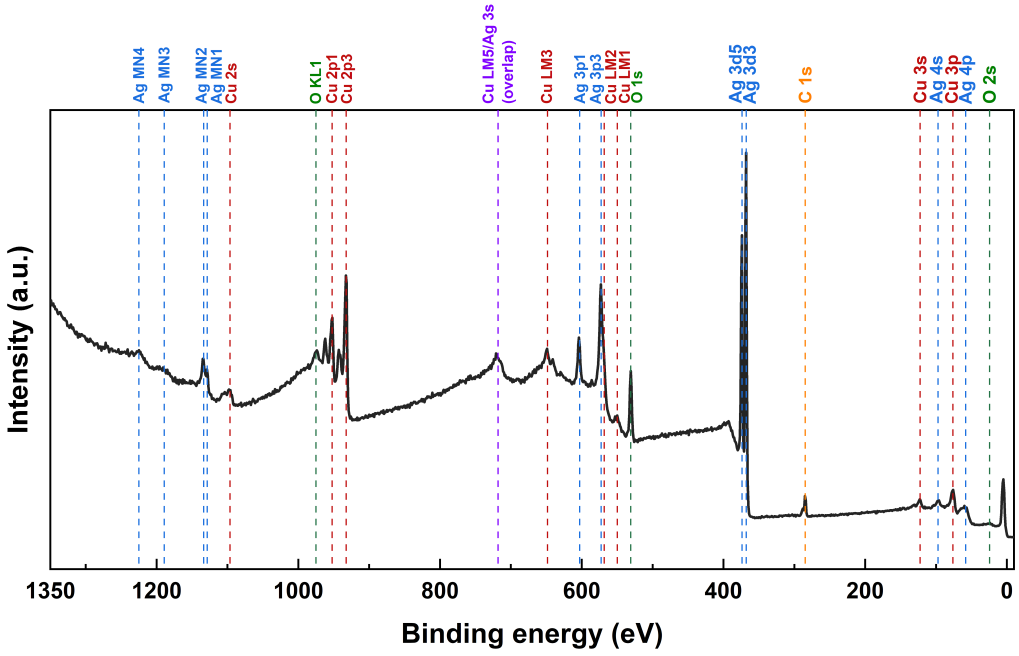

Figure 3.13 ***XPS spectrum of freshly sputtered*** $Cu_{80}Ag_{20}$ ***sample.*** *Elements are labeled with different colors.*

XPS measurements in this thesis were performed by a ThermoScientific Thetaprobe instrument equipped with an Al Kα X-ray source. The operating base pressure was kept below 1.0×10^{-10} mbar. Survey and high-resolution elemental scans were recorded with a step size of 1.0 eV and 0.1 eV, respectively; while in all cases pass energy of 200 eV and dwell time of 50 ms were used. The data were acquired and analyzed with Thermo Avantage (Thermo Fisher Scientific).

XPS was used to determine the near-surface composition of the CuAg alloys, as well as to inspect any trace of contamination. Figure 3.13 is an example of the XPS survey spectrum of a freshly prepared CuAg alloy sample, where the oxygen-related peaks are due to inevitable Cu and Ag oxidation when expose to the air; C 1s is from adventitious carbons carbon and is used for calibration. No other impurity elements are found.

3.4.3. Ion Scattering Spectroscopy (ISS)

Ion scattering spectroscopy (ISS), also known as low-energy ion scattering (LEIS), is extremely surface sensitive that only focuses on the topmost atomic layers [158]. In ISS, noble gas ions (also called projectile) with the energy (E_0) *ca.* 0.5 ~ 10 eV bombard a sample's surface, and binary elastic collision happens between an incident ion and a surface atom. The incident ion is then scattered from the sample surface at an angle θ with a kinetic energy E_f. Since binary scattering is an energy-loss and mass-selective process, elemental identification is realized by measuring the energy loss of the projectile, following the equation below:

$$\frac{E_f}{E_0} = \left(\frac{cos\theta \pm \sqrt{\left(\frac{m_2}{m_1}\right)^2 - sin^2\theta}}{1 + \frac{m_2}{m_1}} \right)^2 \tag{3.14}$$

where, E_0 and E_f is the projectile energy before and after scattering, respectively; θ is the scattering angle; m_1 and m_2 are the mass of the projectile and the surface atom, respectively. ISS typically uses a scattering angle θ at *ca.* 135°, and therefore only atoms with a mass larger than the incident ion can be detected [159]. For this reason, helium (He^+) is most often used as it provides the widest detectable region.

In this thesis, ISS is used to detect any trace amount of contaminations on the CuAg alloys in Chapter 5. It was conducted on the same instrument as XPS, utilizing a focused He ion gun (1 keV) at a base pressure of 2.0×10^{-7} mbar. The ISS spectra were acquired with a step size of 1.0 eV. Figure 3.14 is an example of ISS spectrum performed on the $Cu_{80}Ag_{20}$ sample after eCO2RR. Only elements directly from the reaction system are found: Cu, Ag, and O are from the (oxidized) sample, K was from the electrolyte $KHCO_3$ solution, and no Ir (from the counter electrode IrO_2) was detected.

Only single scattering is considered in this thesis because ISS is only used for qualitatively estimating if there were adventitious elements caused by contamination. However, for quantitative analysis, multiple scattering should be taken into account.

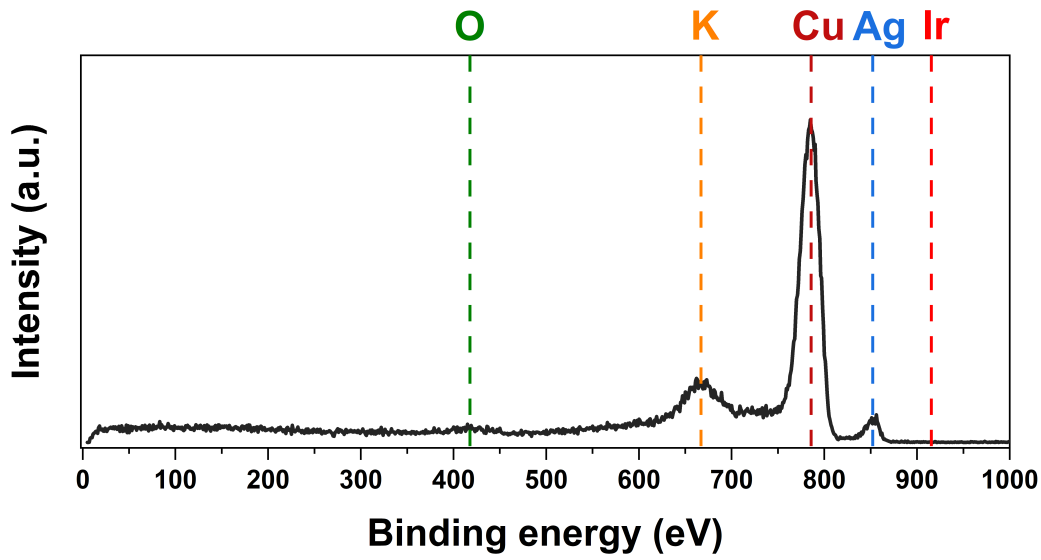

Figure 3.14 ***ISS spectrum of $Cu_{80}Ag_{20}$ sample after eCO2RR*** *in Chapter 5.*

3.4.4. X-ray Absorption Spectroscopy (XAS)

X-ray absorption spectroscopy (XAS) is a powerful X-ray technique that provides information on the oxidation state, local electronic structure, and incorporation environment of matter. It is element-specific and versatile in measuring not only crystalline solids, but amorphous structures and even solutions as well. Experiments are usually carried out at synchrotron facilities due to the required high X-ray photon energy and flux, which also favors *in situ/operando* measurements at ambient pressure because high-energy X-ray attenuate weakly in the air.

When an X-ray beam passes through a material, its intensity attenuates due to being absorbed by the material. The attenuation follows Beer-lambert law (Equation (3.15)), where I_t is the intensity transmitted through the material, I_0 is the incident energy intensity, which is proportional to the number of X-ray photons; $\mu(E)$ is the attenuation (adsorption) coefficient, which estimates the possibility of the incident X-ray to be absorbed; and d_{th} is the material thickness that X-ray beam penetrates.

$$I_t = I_0 e^{-\mu(E) d_{th}} \tag{3.15}$$

At most energies for a homogeneous monoatomic material, μ is dependent on the material's intrinsic properties and can be described with an empirical relation below:

$$\mu(E) \approx \frac{\rho Z^4}{m E_{hv}^3} \tag{3.16}$$

where E_{hv} is the X-ray energy; ρ, Z, and m are the density, atomic number and atomic mass of the material, respectively. Given the Z^4 dependence, $\mu(E)$ is element specific. It is the dependence of $\mu(E)$ on I_0 that XAS measures.

As E_{hv} increases, $\mu(E)$ reduces smoothly (unless sometimes it ejects a 1s electron to the 3d orbital and exhibits an absorption peak), until when it is sufficiently high to eject a core electron with the binding energy of the core level (E_b), the energy is strongly absorbed and therefore exhibits an intense signal increase, which is called the "white line" or absorption edge. The smoothy absorption range is called pre-edge and the absorption peak in this range is called the pre-edge peak. Since each element has well-defined core-level energies, XAS is sensitive to the electronic structure of the absorbing element.

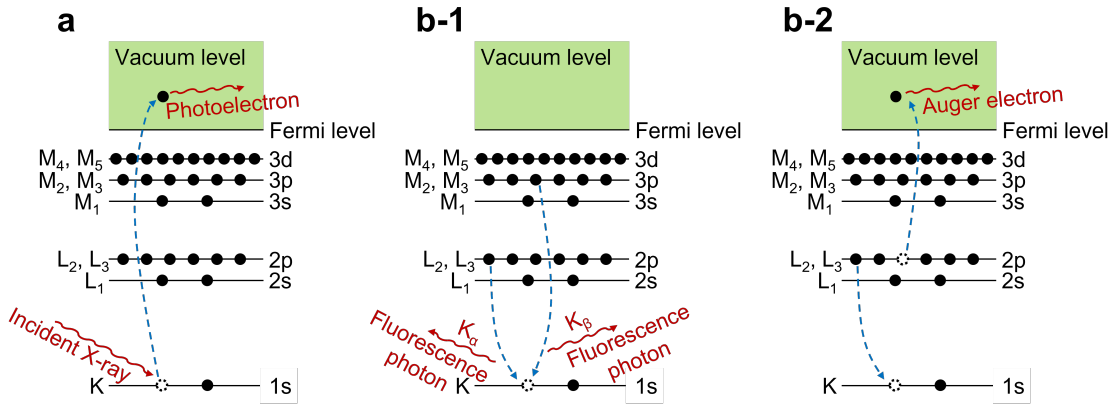

Figure 3.15 ***X-ray absorption spectroscopy mechanism.*** *a) Incident X-ray is absorbed and ejects a core electron to the vacuum as a photoelectron. b-1) Relaxation by a higher-level electron filling the core level hole, and a fluorescence photon is released. b-2) Relaxation by a higher-level electron filling the core hole, and releasing another electron at the same level, emitting an Auger electron.*

As the X-ray energy continuously increases, the ejected electron gains a kinetic energy of $E_k = E_{hv} - E_b$ and is ejected to the vacuum level (Figure 3.15a). These emitted photoelectrons can be considered as waves oscillating from the central absorbing atoms to the surrounding atoms, being scattered off (it may be scattered once, i.e., single scattering; or multiple times, i.e., multi scattering) and return, as illustrated in Figure 3.16. The constructive and destructive interference between the outgoing and back-scattered waves from the neighboring atoms provides information on the local incorporation environment of the central absorbing atom. This interference is reflected as oscillations on an XAS spectrum.

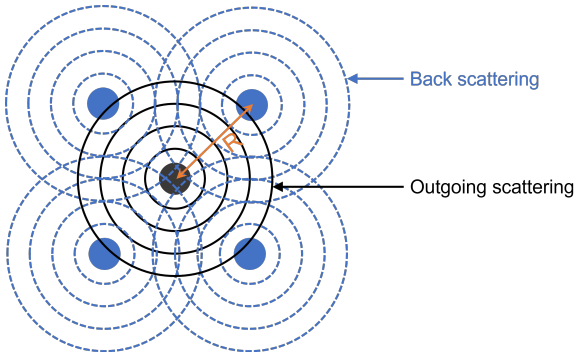

Figure 3.16 ***Photoelectron scattering schematic illustration.*** *Solid black and blue circles represent central absorbing atom and scattering atoms, respectively. Black solid lines and blue dashed lines indicate the outgoing and back-scattering waves, respectively. R stands for the distance between a central and a scattering atom.*

As a core-level electron is ejected, a hole is left behind and the material is excited (Figure 3.15a). In most cases, relaxation is realized by a higher-level electron filling the hole in two ways: either accompanied by emitting photoluminescence (Figure 3.15b), or another electron on the same higher level is ejected to the vacuum and becomes an Auger electron (Figure 3.15c). The former situation dominates in "hard" X-ray energy regions (> 2 keV) and the latter dominates in "soft" X-ray energy regions (< 2 keV).

Depending on which energy is recorded, XAS measurement has three basic modes, as schematically represented in Figure 3.17:

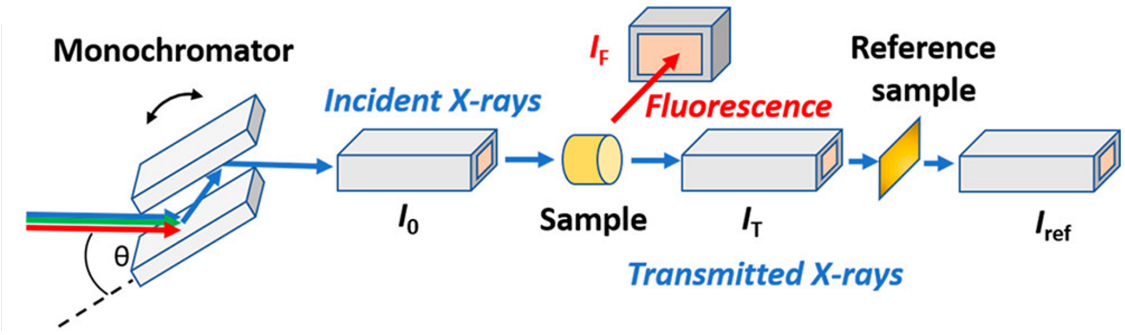

Figure 3.17 ***Schematics of a common setup for XAS measurements with double crystal monochromator.*** *The reference sample is used for X-ray beam energy calibration. Reprinted from*[160] *with permission. Copyright 2020 American Chemical Society.*

i) Transmission mode, which measures the incident (I_0) and transmitted X-ray energy (I_t). The absorption coefficient is determined by Beer-lambert law (Equation (3.15)). It is suitable for concentrated and homogenous samples.

$$\mu(E) \propto ln(\frac{I_0}{I_t}) \tag{3.17}$$

ii) Fluorescence mode, which measures the incident X-ray energy and the fluoresce intensity (I_f) emitted by the material absorbing X-ray. The absorption coefficient is given by Equation (3.18). It is suitable for dilute, thin (< 100 nm thin films), or non-homogeneous samples.

$$\mu(E) \propto \frac{I_f}{I_0} \tag{3.18}$$

iii) Total electron yield mode, which measures all electrons (mainly photoelectrons and Auger electrons) emitted from the sample. It is more surface sensitive than the other modes. However, it is normally used in soft XAS (*i.e.,* 2p → 3d transition) and needs to be carried out under high vacuum or ultra-high vacuum due to the short attenuation length of such photons in the air.

Cu K-edge XAS in Chapter 5 was conducted with a hard X-ray source (*ca.* 8 keV) in transmission mode. The theory interpretation below is based on K-edge (excitation of 1s electrons) measurements.

According to the energy range, an XAS spectrum is comprised of two regimes: the X-ray absorption near edge structure (XANES) region and the extended X-ray absorption fine structure (EXAFS) (Figure 3.18).

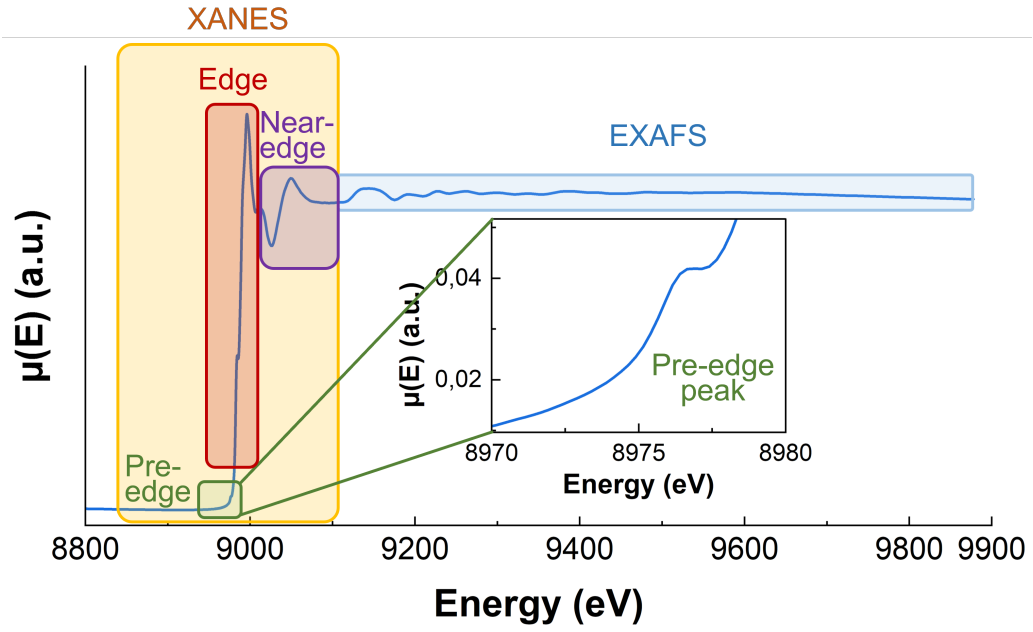

Figure 3.18 ***X-ray absorption spectroscopy spectrum of CuO.*** *Different energy regions are labeled with colors. The XANES regime includes pre-edge, edge, and near-edge. Insert is the enlarged pre-edge region, showing a pre-edge peak due to electron transmission from 1s to 3d orbital.*

3.4.4.1. X-ray Absorption Near Edge Structure (XANES)

XANES spectrum ranges from the X-ray energy *ca.* 50 eV before the absorption edge to *ca.* 1000 eV after the edge. It can provide information on the absorbing sample with respect to electronic and geometric structure, metal-ligand overlap *via* shakedown transitions, ligand arrangement, *etc*. It is based on the fact that when there are fewer electrons in the shell orbitals, the shielding effect between the nucleus and the core electrons is weaker, and thus higher binding energy. As a result, ejecting the core electron requires a higher energy, which is reflected as a higher edge energy. Therefore, the edge position can be shifted by any factor that changes the electron density of the absorbing atom, such as the oxidation state of the central atom, the electronegativity, and the number of the ligand(s) or binding atom(s), *etc*.

Moreover, XAS is an averaged signal reflecting all absorbing atoms (*e.g.*, all Cu atoms within the X-ray beam footprint for a measurement on the Cu K-edge), meaning that the final XANES signal (*i.e.*, edge shape and intensity) is a weighted average of all detected atoms with different edges.

3.4.4.2. Extended X-ray Absorption Fine Structure (EXAFS)

The EXAFS regime extends up to *ca.* 1000 keV after the absorption edge. It contains more information on the local chemical environment surrounding the central absorbing atom, such as coordination number, atomic shell distance, *etc*.

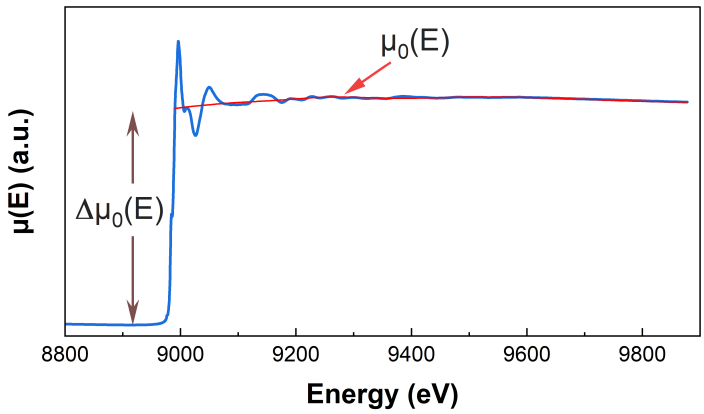

Figure 3.19 ***X-ray absorption spectroscopy spectrum of CuO*** *showing the smooth background and edge-jump.*

As mentioned earlier, the outgoing and back-scattering waves of an emitted photoelectron interfere with each other, reflected as oscillations on an XAS spectrum. EXAFS fine-structure function $\chi(E)$ is defined as:

$$\chi(E) = \frac{\mu(E) - \mu_0(E)}{\Delta\mu_0(E)} \tag{3.19}$$

where, $\mu_0(E)$ is the smooth "bare-atom" background (red line shown in Figure 3.19), and $\Delta\mu_0(E)$ is the edge-jump (indicated by the brown arrow line in Figure 3.19). As EXAFS is usually understood as a wave behavior of the emitted photoelectrons, the X-ray energy E is commonly converted to its wavenumber k, following Equation (3.20):

$$k = \sqrt{\frac{2m(E - E_0)}{h^2}} \tag{3.20}$$

where, E_0 is the absorption edge energy, m is electron mass, and h is Planck's constant. Thus, $\chi(E)$ can be converted to a function of k:

$$\chi(k) = \sum_j \left(\frac{N_j S_0^2}{kR_j^2} \times F_j(k) \times e^{\frac{-2R_j}{\lambda(k)}} \times e^{-2k^2\sigma_j^2} \times sin[2kR_j + \delta_j(k)] \right) \tag{3.21}$$

where, subscript j represents a coordination shell comprised of atoms surrounding the central absorbing atom with a similar distance R_j; N_j is the coordination number in the same shell; S_0^2 is the passive electron reduction factor, stemming from all other electrons relaxing into the core-level hole, and it is correlated with N_j; $F_j(k)$ is the scattering amplitude of back-scattered electrons; $\lambda(k)$ is the mean free path of the emitted photoelectron, therefore $e^{\frac{-2R_j}{\lambda(k)}}$ measures amplitude attenuation due to inelastic scattering; σ is the Debye-Waller factor, therefore $e^{-2k^2\sigma_j^2}$ measures the amplitude attenuation due to thermal and static disorder; $\delta_j(k)$ is the phase-shift between the outgoing and back-scattering waves; parameters following bracketed k are dependent on atom identity, while those with a subject j are dependent on the coordination structure. More details in formula derivation are out of the scope of this thesis.

The raw EXAFS $\chi(k)$ (also called the "k-space") amplitude usually decays fast as k increases, whereas high-k range usually contains useful structural information. Therefore, $\chi(k)$ is sometimes weighted by k^2 or k^3 to compensate for the decay, *i.e.,* $k^2\chi(k)$ or $k^3\chi(k)$.

From Equation (3.21), $\chi(k)$ is not only a sine function of k, but also depend on the interatomic distance (*i.e.*, chemical bond) R. Additionally, $\chi(k)$ is a summation of sine waves, where each of them is an oscillation spectrum of atoms at a distance R. Therefore, $\chi(k)$ can be further converted to $\chi(R)$ (*i.e.*, R-space) *via* Fourier transformation. By this

means, the influence of k and R on the oscillation can be isolated. Details in data processing are out of the scope of this thesis and therefore not provided.

3.5 Product Quantification

3.5.1. Gas Chromatography (GC)

Gas chromatography is a process of identifying and analyzing volatilizable chemical components in a gas mixture based on the different retention time of each component in the system. It is realized by flowing a gas (mobile phase, normally inert gas) carrying the analyte mixture through a capillary column coated with special coatings (stationary phase, which can be a porous layer of highly viscous liquid or solid particles supported in a solid layer). Components with different physical and chemical properties in the mobile phase have different extents of interaction with the stationary phase, and therefore the time being "retained" in the system varies, which enables identification.

In this thesis, GC (Thermo scientific, TRACE 1300) is used for *in situ* gas product analysis, including H_2, CO, CH_4, C_2H_4, C_2H_6, C_3H_6 and C_3H_8. The GC instrument is equipped with three columns for separating products: a packed Hayesep Q column, a packed Molsieve 5A column, and an Rt-Qbond column. Two detectors are used:

Flame ionization detector (FID) is a widely used GC detector due to its versatility in detecting most carbon-containing species (with some exceptions such as formaldehyde and formic acid). It uses a hydrogen flame to combust organic compounds in the gas and ionizes them into CH^+ ions. Component identification and quantification are realized by the mass-selective and proportional relationship between the formation of CH^+ ions and the concentration of the corresponding components in the gas phase. FID is used for detecting all gas products from eCO2RR other than H_2 in Chapter 5. A Ni catalyst is used as the mechanizer, which mechanizes CO and CO_2 to CH_4, in order to enable their detection in the FID.

Thermal conductivity detector (TCD) is a non-destructive method that measures the thermal conductivity of the mobile phase and compares it with that of a reference flow (*i.e.*, carrier gas). In this thesis, TCD is used to detect H_2, which is non-detectable by FID. Ar serves as the reference/carrier gas considering its significantly different thermal conductivity from that of H_2.

3.5.2. High-Performance Liquid Chromatography (HPLC)

HPLC is a chromatographic technique for liquid composition analysis, which has a similar working principle as GC: a mobile phase carries the analyte going through a column packed with the stationary phase (usually small porous particles), where the different extent of interaction between the analyte and the stationary phase leads to different flow rate and thus retention time, resulting in component separation and identification.

In this thesis, *ex situ* liquid product analysis was conducted with an Agilent 1260 Infinity II HPLC system, installed with an Aminex HPX-87H packed column (Bio-Rad). 5 mM H_2SO_4 solution serves as the polar mobile phase. Two detectors are equipped:

Diode Array Detector (DAD) scans each eluted component at the exit of the column across the ultraviolet and visible light range with a beam of light. Component identification is realized by comparing the light absorption at each wavelength combined with the retention time.

Refractive Index Detector (RID) measures the difference in the refractive index of the mobile phase upon introducing an analyte.

3.5.3. Faradaic Efficiency Calculation for H-cell Measurements

Faradaic efficiency is used to evaluate the selectivity toward each product, following Faraday's law:

$$FE_i = \frac{z_i \times F \times n_i}{I_T \times t} \times 100\% \qquad (3.22)$$

where, z is the number of transferred electrons for producing species i, F is Faraday's constant (96485 C/mol), n_i is the number of moles of produced species i; I_T is the total current of the reaction, and t is the reaction time.

Assuming an ideal gas mixture, gas products are calculated following the equation:

$$FE_i = \frac{z_i \times F \times P \times v_{Total}}{I_T \times R \times T} \times A_{i,GC} \times f_{i,GC} \times 100\% \qquad (3.23)$$

where, P is the atmosphere pressure (101.325 kPa), v_{Total} is the inlet CO_2 gas flow rate (10 sccm), T is room temperature (300 K), $A_{i,GC}$ is the integrated peak area of species i in GC, and $f_{i,GC}$ is the calibration factor of species i in GC. (As the total conversion is small, the inlet CO_2 gas flow rate is a reasonable approximation for the outlet flow rate in this situation.)

Liquid products are measured by the following equation:

$$FE_i = \frac{z_i \times F \times V_{Total} \times \frac{A_{i,HPLC}}{f_{i,HPLC}}}{Q} \times 100\% \tag{3.24}$$

where, V_{Total} is the total volume of the cathode chamber (6 mL), T is room temperature (300 K), $A_{i,HPLC}$ is the integrated peak area of species i in HPLC, and $f_{i,GC}$ is the calibration factor of species i in HPLC.

Current densities were based on the geometric area of the working electrode (2.25 cm^2). Partial current density of each product j_i is evaluated by the following equation:

$$j_i = j_{Total} \times FE_i \tag{3.25}$$

where, j_{Total} is the total geometric current density.

Productivity S_i of each product with respect to the produced number of moles are also calculated in Chapter 5, calculated in the following way:

$$S_i = \frac{n_i}{\sum_{i=1}^{i=n} n_i} \times 100\% \tag{3.26}$$

where, for gas products:

$$n_i = \frac{P \times v_{Total}}{R \times T} \times A_{i,GC} \times f_{i,GC} \tag{3.27}$$

For liquid products:

$$n_i = \frac{V_{Total} \times \frac{A_{i,HPLC}}{f_{i,HPLC}}}{Q} \tag{3.28}$$

3.5.4. Mass Spectrometry (MS)

3.5.4.1. General Working Principle of Mass Spectrometry

Mass spectrometry (MS) is a vacuum analytical technique that measures the mass-to-charge ratio of ionization particles (*i.e.*, ions), based on electron bombardment. It can provide information on the elemental and isotopic composition, molecular structure and weight, *etc*.

A mass spectrometer consists of at least three components:

i) Ionization source

There are several ion sources used in mass spectrometry, including electron ionization (EI), chemical ionization (CI), field ionization (FI), atmospheric pressure chemical ionization (APCI), electrospray ionization (ESI), matrix-assisted laser desorption/ionization (MALDI), *etc*. [161]

In the EC-MS system used in Chapter 4, electron ionization is used as the ion source, where a filament is heated up and produces a beam of thermionic electrons. When sample molecules are introduced into the ionization chamber, they are bombarded by electrons, which could lead to two circumstances: a) the sample molecule losses one (in most cases) or multiple electrons and form a positive ion with the same molecular weight as the pristine molecule, and b) if the electron energy is sufficiently high that cleavages the chemical bond(s) in the sample molecule, small partials with positive ions (*i.e.*, fragments) would also be formed.

ii) Mass analyzer (quadrupole in EC-MS)

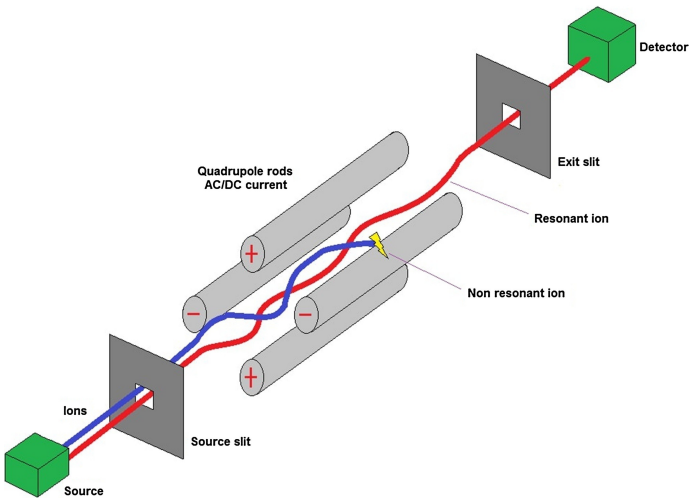

Figure 3.20 ***Schematic interpretation of the instrument operation of quadrupole mass spectrometer (QMS).*** *Reprinted from* [162] *with permission. Copyright 2023 Elsevier B.V.*

The formed ions then enter a mass analyzer to be differentiated. A traditional mass analyzer contains two fields: a negatively charged electric field to filter ions such that only positive ions can go through; and a magnetic field such that ions with different m/z are accelerated to different extents, leading to different extents of bending on their trajectories and consequently reach the detector with different time/position such that they are separated and differentiated.

In the EC-MS setup, a quadrupole mass filter (QMS) is used. It is based on two classic physical prominent: electrostatic interaction and inertia. Specifically, it consists of four parallel rods, two are positively charged and the other two are negatively charged, as depicted in Figure 3.20. The applied voltage V_{total} consists of two parts: a direct current (DC) portion with the amplitude U and an alternative current (AC) portion with an amplitude V and a frequency f (thus angular velocity ω) (Euqation (3.29)), that the positive roads keep being positively charged while the total voltage amplitude fluctuates periodically, and *vice versa* for the negative rods.

$$V_{total} = \pm(U - V cos\omega t) \tag{3.29}$$

where, t is time.

When only the two positively charged rods are working, the DC voltage directs all positive ions to go through the space in between due to electrostatic repulsion; whereas the AC voltage filtered out small ions (*i.e.*, small m/z ions). This is because compared to larger ions, small ions have smaller inertia and thus are easier to be affected by the electrical field change. Therefore, when positive rods turn to less positive, small ions are easily attracted and colloid on the rods, where they will be neutralized and cannot enter the detector. Large ions, on the other hand, are more impervious so they can still reach the detector.

Similarly, when only the two negatively charged rods are working, the DC voltage prevents all positive ions to go through due to electrostatic attraction; while the AC voltage allows small ions to go through. Since small ions have smaller inertia, as soon as the rod charge turns to less negative, they would have a chance to go through the central space without colloid on the rods and reach the detector. However, since larger ions are more impervious, they would be filtered out.

Combining the above two situations, when the four rods function together, the sample ions being too small would be filed out by the positive rods, and *vice versa* for those being too big. As a result, only m/z in a specific window can be detected, and the size of this m/z window determines the resolution of the mass spectrometer, which can be modified by modifying the applied voltage.

iii) Ion detection system

When ions strike a detector, their kinetic energy is transformed into ion current and is recorded. It is the simplest case that happens when the ion current is sufficiently high, and the detector is called a Faraday collector or Faraday cup.

However, when the ion current is so small that is below the detection limit or the signal-to-noise ratio is too low, a secondary electron multiplier (SEM) is required to amplify the signal intensity. A SEM employs the phenomenon of secondary emission. When an ion hits a dynode, more electrons will be released from the dynode surface. The released electrons then hit another dynode or the same dynode again and produce more electrons. All the released electrons from the dynode are secondary electrons and can be accelerated by applying a positive voltage to the dynode(s). Depending on the kinetic energy of the ion as well as the dynode(s)' voltage and arrangement, the resulting signal-to-noise ratio and signal intensity can be improved to several orders of magnitude higher.

In this thesis, a continuous dynode is used as the SME in order to amplify the signal intensity for a better sensitivity towards eCO(2)RR products.

Two detection modes are used in this thesis. a) Full mass scan, which is to record the signal of all m/z in a wide range (0 ~ 50). This is used to determine the characteristic m/z of each component of interest. b) Only characteristic m/z of each target component are recorded over time during eCO(2)RR.

It is also worth mentioning that only singly charged fragments/ions are considered through this thesis. This is because in the eCO(2)RR system, the largest molecular weight is from ethanol (M = 46 g/mol) with double charged m/z to be 23. All m/z considered in this thesis include M2 (H_2+ predominately contributed by hydrogen), M15 (CH_3+ mainly from methane, partially contributed by ethylene, acetaldehyde and ethanol, can be deconvoluted)), M26 (C_2H_2+ from ethylene), M31 (CH_3O+ mainly from ethanol), and M42 (CHCHO+ from acetaldehyde). Therefore, double or multiple charged m/z ions are not expected to have noticeable influence on molecule identification. Accordingly, atomic mass unit (AMU) is considered the same as m/z in this thesis, which is represented as MX (X represents the m/z value) for simplicity.

3.5.4.2.Selective Ionization

The possibility for a specific ionization process to happen is defined as ionization cross section [163]. Most organics have ionization energy (almost the same as appearance energy when mentioned in this thesis, because the former is the theoretically lowest energy required

to ionize a molecule, while the latter is the energy required to produce a detectable amount of the molecule) between 10 ~ 30 eV, and their ionization cross section usually reach the vertex between 70 and 100 eV. Therefore, the default electron energy (EE) of an EI source is set to be 70 eV.

However, since at 70 eV all interested species considered in this thesis have the maximal ionization efficiency, dissociative ionization also happens, resulting in fragmentation. Due to the similar chemical structure of the involved species (mostly hydrocarbons and oxygenates), their dissociative ionization form shared fragmentations and thus complicate component diffraction. Therefore, reducing the EE to mitigate fragmentation would promote molecular ions and help with differentiation.

Details of selective ionization in the eCO(2)RR process are interpreted in Chapter 4.1.

3.5.5. Electrochemistry – Mass Spectrometry (EC-MS)

3.5.5.1. Working Principle of the EC-MS System

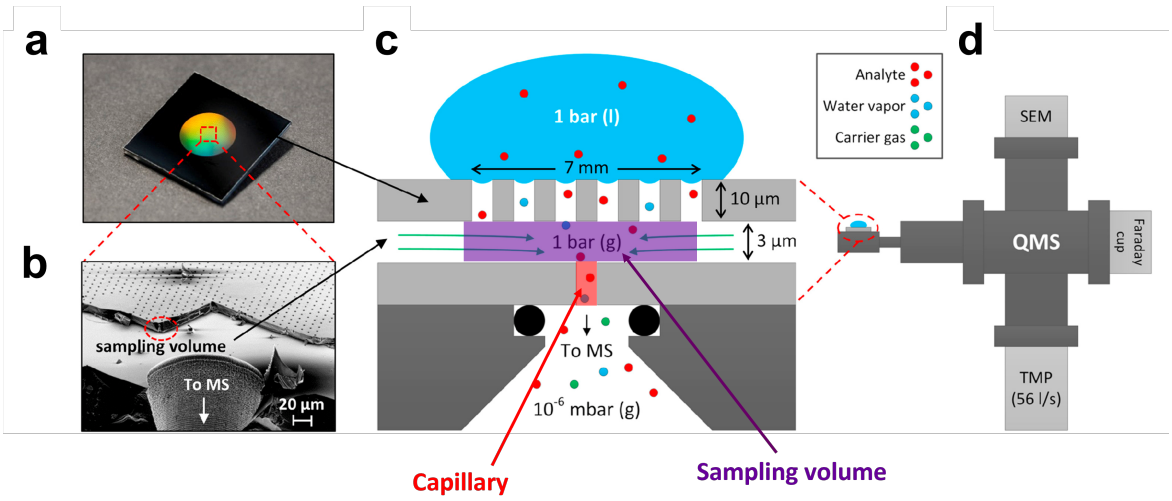

Figure 3.21 ***Membrane chip and working principle.*** *a, Photograph of the membrane chip. b, Scanning electron microscope image revealing the internal microstructure of the membrane chip, cut across the middle. The sampling volume is made apparent by the shadow below the membrane, seen clearly in the red circle.* ***c****, Schematic diagram of the membrane chip under a drop of water (blue) containing the dissolved analyte (red). Carrier gas (green) enters the sampling volume bringing the pressure up from the combined equilibrium pressure of water and analyte to atmospheric pressure. Carrier gas, water vapor, and analyte are delivered from the sampling volume through the membrane chip's capillary to the vacuum chamber.* ***d****, Schematic diagram showing the membrane chip (grey) mounted on a vacuum chamber with a quadrupole mass spectrometer (QMS). Reprinted from* [146] *with permission. Copyright 2018 Elsevier Ltd.*

Operando product detection presented in Chapter 4 is enabled on an EC-MS system purchased from SpectroInlets Aps Denmark, shown in Figure 3.21. The ambient pressure electrochemistry (EC) and the vacuum MS parts are connected with a membrane chip, where a capillary defines the molar flow rate to be on the order of nanomole/second. A series of small holes on top of the chip ensures that the solvent pressure of each analyte in the sampling volume is in its vapor pressure, and that all dissolved gases and volatile analytes are at their partial pressure according to Henry's law of volatility. The system allows real-time detection of reaction products and intermediates during electrochemical experiments *via* a QMS. Being capable of resolving and quantifying submonolayer amounts of gaseous products on a scale of seconds as sub-turnover resolution with a 100% collection efficiency [146], the EC-MS system enables us to see the early onset of the products at low overpotentials during electrochemical measurements. For more details regarding the system's working principle please refer to [146].

3.5.5.2. Quantification

Comprehensive explanations of the principles, methods and formula for quantifying QMS signal to the molar flow rate of gases have been provided in Daniel. B. Trimarco's [145] and Søren Bertelsen Scott's [164] Ph.D. theses. Therefore, gas quantification will only be briefly described in this section; whereas faradic efficiency calculation and liquid calibration will be interpreted in detail.

Quantification of the electrochemical mass spectrometry data was determined by the sensitivity factor ($S_{MX,i}$) for each analyte i at a suitable mass-to-charge ratio (m/z), at which the signal is an exclusive indicator of the desired analyte, or at least the interference of the others is negligible or easily differentiable. For example, although M28 is usually a combination of N_2 and CO signals, the contribution from N_2 is usually over three orders of magnitude lower than CO when the latter is used as the carrier gas. Alternatively, it could also be easily extracted by normalizing with the background before electrochemical measurements, which is the case for M15 (mainly contributed by methane and partially by other hydrocarbons and volatile oxygenates).

Quantification in the EC-MS uses different methods depending on the physical properties of the corresponding analyte and if it can be produced with 100% faradaic efficiency. Details are listed below. All calibrations are carried out at an electron energy of 28 eV.

Table 3.2 ***Quantified components in the EC-MS system****, including their corresponding properties and calibration method.*

Analyte	Chemical formula	Characteristic Fragment	m/z descriptor	Physical phase	Calibration method
Oxygen	O_2	O_2+	32	Gas	Internal
Hydrogen	H_2	H_2+	2	Gas	Internal
Carbon monoxide	CO	CO+	28	Gas	External – gas
Methane	CH_4	CH_3+	15	Gas	External – gas
Ethylene	C_2H_4	C_2H_2+	26	Gas	External – gas
Argon	Ar	Ar+	40	Gas	External – gas
Acetaldehyde	CH_3CHO	CHCHO+	42	Liquid	External – liquid
Ethanol	C_2H_5OH	CH_2OH+	31	Liquid	External – liquid

i) Internal calibration of hydrogen

For gases that can be produced with 100% faradaic efficiency, including hydrogen and oxygen, their calibration is conducted with chronopotentiometry. Specifically, a platinum sub served as the working electrode. HER and OER were conducted in 0.1 M $HClO_4$ kept at several constant currents (0 μA, -2.5 μA, -5μA, -10 μA, -15 μA, and -20 μA), respectively, recording the QMS signal intensity (I_{MS}). Molar flux ($\dot{n}$) is back-calculated using Faraday's law (Equation (3.22)). There is a linear relationship between the QMS signal intensity (background extracted) and the molar flux, and the slope is the calibration factor (Equation (3.30)or (3.31)). Figure 3.22 gives an example of the internal calibration of hydrogen (a) and oxygen (b).

$$F_{Cal,i} = \frac{\bar{S}_{MX,i}}{\bar{\dot{n}}_i} \tag{3.30}$$

or

$$F_{Cal,i} = \frac{\int S_{MX,i}\, dt}{\int \dot{n}_i\, dt} \tag{3.31}$$

where, the subscript i indicates the analyte to be calibrated; F_{Cal} is calibration factor; $\bar{S}_{MX}$ and S_{MX} is the averaged or instantaneous QMS signal intensity of MX, respectively; $\bar{\dot{n}}$ and $\dot{n}$ is the averaged or instantaneous molar flux, respectively; t is the time during which signals are integrated.

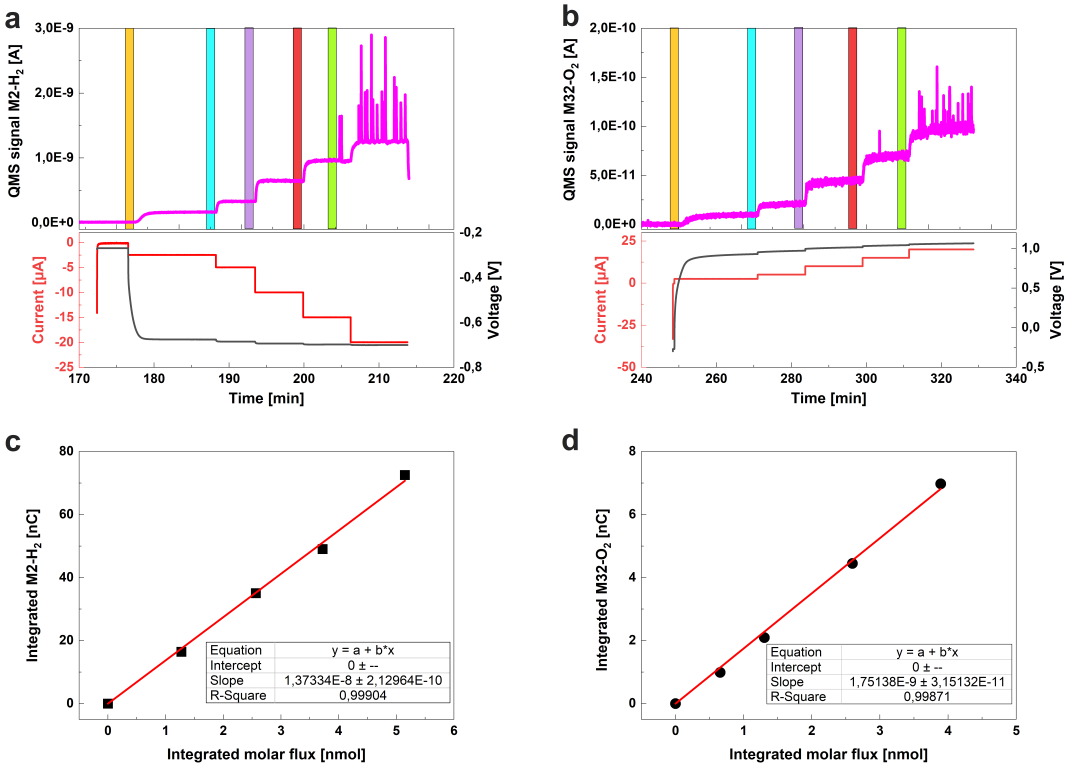

Figure 3.22 ***Internal calibration*** *of hydrogen ((a), and its linear fitting (c)) and oxygen ((b) and its linear fitting (d)). Inserts in (b) and (d) are the linear fitting parameters. Integrated EC and MS signals over the last 1 min of each constant current were used for calibration, indicated by highlighted area. Calibration data was not taken due to the noisy signal stemming from the formation of gas bubbles.*

ii) External calibration of methane and ethylene

For those gases that cannot be produced with a 100% FE, external calibration was conducted following the procedure below:

1) Calibrate the chip capillary.

The sensitivity factor towards the same analyte slightly varies from chip to chip, which is mainly attributed to the error in capillary length. Therefore, the first step is to determine the effective capillary length, l_{eff}, with respect to the standard chip, whose length l_{std} is 1 mm. This is done by comparing their air flux:

1-a) Obtain the calibration factor of oxygen from internal calibration shown in Section i).

1-b) On the same day, measure the QMS signal intensity of oxygen $\bar{S}_{M32,O_2}$ by exposing the chip to the air, then calculating the corresponding oxygen flux $\bar{\dot{n}}_{O_2}$. Given that the molar composition of oxygen in the air is *ca.* 21%, the air, air flux through the capillary $\bar{\dot{n}}_{air} = \bar{\dot{n}}_{O_2}/0.21$.

1-c) Knowing the air flux of the standard chip $\bar{\dot{n}}_{air,std}$ to be 6.86 nmol/s,

$$l_{eff} = \frac{\bar{\dot{n}}_{air,std}}{\bar{\dot{n}}_{air}} \times l_{std} \tag{3.32}$$

2) Replace the standard capillary length with the effective length in the derived analytical expression to calculate the molar flux of a certain analyte: [165]

$$\dot{n}_i = \frac{1}{RT}\frac{1}{l_{eff}}\left(\left(\frac{\pi}{8\eta}a^4\bar{p} + \frac{2\pi}{3}a^3\bar{\nu}\frac{1+2\sqrt{\frac{8}{\pi}}\frac{a}{\eta}\frac{\bar{p}}{\bar{\nu}}}{1+2{,}48\sqrt{\frac{8}{\pi}}\frac{a}{\eta}\frac{\bar{p}}{\bar{\nu}}}\right)(p_{in}-p_{tran}) + \frac{2\pi}{3}a^3\bar{\nu}p_{tran}\right) \tag{3.33}$$

where, η is the dynamic viscosity, a is the dimension of the capillary (*ca.* 3.38 µm), $\bar{p}$ is the average pressure in the viscous low regime ($\frac{p_{in}+p_{tran}}{2}$), p_{in} is the inlet pressure (1 bar), p_{tran} is the transient pressure when viscous flow to molecular flow occurs ($\frac{k_B T}{2\sqrt{2}\pi s^2 a}$), k_B is the Boltzmann constant, s is the molecular (kinetic) diameter of the analyte i, $\bar{\nu}$ is the mean thermal velocity of the gas molecules ($\sqrt{\frac{8\times k_B \times T}{\pi \times m}}$), m is the molecular mass, and p_{out} is the outlet pressure (*ca.* 0 bar).

On the same chip in the same system under room temperature and ambient pressure, the molar flux of each analyte depends on three of their physical properties: dynamic viscosity, molecular diameter, and molecular mass. The molar flux of calibrated gases and their properties are listed in the table below:

Table 3.3 ***Molar flux of calibrated gases and their physical properties.*** *Physical property data are from NIST* [166].

Analyte	Physical properties			Molar flux (nmol/s)
	Dynamic viscosity (Pa•s)	Molecular diameter (Å)	Molecular weight (Da)	
CO	1.78×10^{-5}	3.76	28.00	6.59
CH_4	1.11×10^{-5}	3.80	16.04	10.27
C_2H_4	1.03×10^{-5}	4.16	28.02	10.53
Ar	2.23×10^{-5}	3.63	39.94	5.30

3) Flow the to-be-calibrated gas through the chip (with cell installed and electrolyte filed up the cell), and record the QMS signal intensity. The calibration factor is then calculated:

$$F_{Cal,i} = \frac{\bar{S}_{MX,i}}{\dot{n}_i} \tag{3.34}$$

It is worth noting that ideally, the to-be-calibrated gas should be diluted to a similar concentration in the carrier gas as it is produced during the electrochemical reactions.

iii) External calibration of acetaldehyde and ethanol

External calibration of volatile liquids follows a similar principle as gases. The only difference is that, since liquids are soluble in water and aqueous solutions, concentration is used in calibration:

$$F_{Cal,i} = \frac{\bar{S}_{MX,i}}{C_i} \tag{3.35}$$

which is then converted to molar flow rate, following Henry's law:

$$C_i = K_H^i \times P_i \tag{3.36}$$

where, C_i, K_H^i, and P_i are the concentration, Henry's law constant and partial pressure of analyte i, respectively. Calibration of acetaldehyde concentration is shown in Figure 3.23.

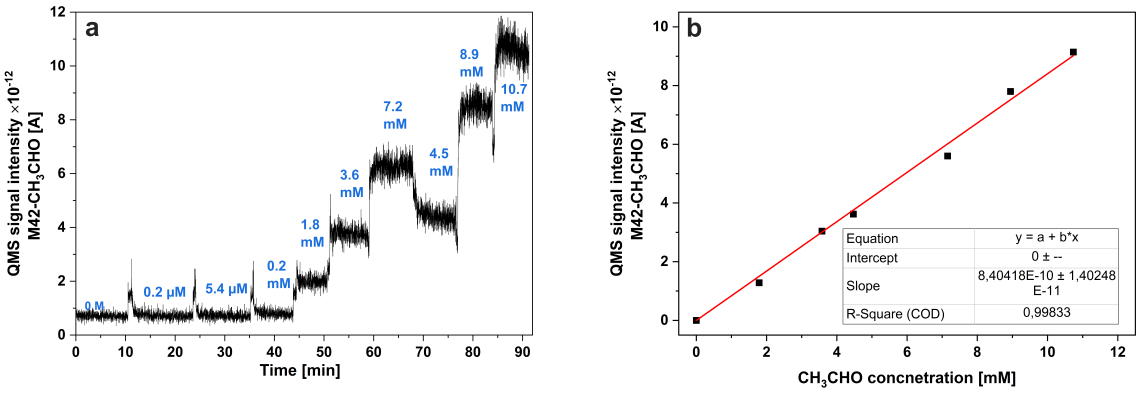

Figure 3.23 ***Acetaldehyde concentration calibration:*** *a) M42 signal intensity tracked over time, and b) linear fitting. Acetaldehyde solution with each concentration was freshly prepared by adding acetaldehyde in 0.1 M KOH. Then waited for ca. 5min before taking the data.*

Assuming an ideal gas mixture, when the evaporated analyte i enters a gas mixture, its molar flow rate is proportional to the ratio of its partial pressure over the total pressure:

$$\dot{n}_i \approx \frac{P_i}{P_{tot}} \times \dot{n}_{tot} \tag{3.37}$$

where, P_i and P_{tot} is the partial pressure of analyte i and total pressure, respectively; $\dot{n}_{tot}$ is the total molar flux of the gas mixture, which is approximately equal to that of the carrier gas $\dot{n}_{carrier}$ in this system. During eCORR, since CO is used as the carrier gas, $\dot{n}_{carrier} = \dot{n}_{CO} \approx 6.59\ nmol/s$. Therefore,

$$\dot{n}_i = P_i \times \frac{\dot{n}_{CO}}{P_{tot}} = \frac{C_i}{K_H^i} \times \frac{\dot{n}_{CO}}{P_{tot}} = \frac{S_{MX,i}/F_{cal}^i}{K_H^p} \times \frac{\dot{n}_{CO}}{P_{tot}} \tag{3.38}$$

Since liquid products, not like gases that diffuse out of the electrolyte and enter the MS immediately after being produced, dissolve in the electrolyte and therefore their concentration is accumulated over time. The molar flow rate of a liquid going from the electrolyte to the MS can be evaluated. Taking acetaldehyde as an example, its Henry's law constant is *ca.* 12 mol/(L•bar), then:

$$\dot{n}_i = \frac{C_i}{K_H^i} \times \frac{\dot{n}_{CO}}{P_{tot}} = \frac{C_i \left[\frac{mol}{L}\right]}{11{,}81 \left[\frac{mol}{L \times bar}\right]} \times \frac{6{,}59 \times 10^{-9} \left[\frac{mol}{s}\right]}{1{,}015\ [bar]} = C_i \times 5.5 \times 10^{-10} \left[\frac{mol}{s}\right] \tag{3.39}$$

In the case of ethanol, since its Henry's law constant is even larger is *ca.* 158 mol/(L•bar), its evaporation is even slower. This indicates that the loss of molecules of a volatile liquid analyte due to evaporation is negligible.

3.5.5.3. Faradaic Efficiency Calculation

For gases, since they are collected with a nearly 100% collection efficiency right after being produced, their faradic efficiency can be directly calculated from Faraday's law (Equation (3.22)). Unfortunately, it is not as simple as expected in eCORR due to the complexity of the reaction itself as well as the system configuration. Detailed discussion will be provided in Chapter 4.2.5.

As mentioned above, liquid products are dissolved in the electrolyte and kept accumulated over time during the reaction. Therefore, their faradaic efficiency needs to use the integrated concentration and current, as the following:

$$FE_i = \frac{(\int_{t1}^{t2} S_{MX,i}\, dt / F_{cal}) \times V \times F \times z}{\int_{t1}^{t2} I_{EC}\, dt} \times 100\% \tag{3.40}$$

where, V is the reaction volume (2μL); from t_1 to t_2 is the time during which the QMS signal and EC signal (*i.e.*, total current I_{EC}) are integrated.

The above calculation is valid for steady-state reaction conditions, such as CA or CP. However, it cannot be used for a sweeping potential as in LSV measurements conducted in Chapter 4. This is because electrochemical $CO_{(2)}$ reduction is such a complicated process that its reaction mechanism, pathway, as well as product distribution vary as potential changes. Especially for acetaldehyde, as it is a precursor of ethanol, its production and consumption (due to chemical reactions in alkaline as well as a further reduction to ethanol) take place simultaneously. Therefore, for an accurate FE calculation, both the production and consumption rates need to be known.

3.5.5.4. Selectivity Comparison

For some measurements where the trend of product distribution under different reaction conditions is compared, quantification is not necessary, while qualitative comparison gives a more straightforward evaluation. It is carried out in the following way:

As mentioned before, the molar flow rate of an analyte i going from the electrochemical cell to the QMS ($\dot{n}_i$) is in a linear relationship with the QMS signal ($S_{MX,i}$) by the factor of ($F_{Cal,i}$) (Equation (3.34)). For a certain reaction (*e.g.*, eCORR) conducted on the same membrane chip, the calibration factor of an analyte keeps the same. Therefore, the comparison between two analytes, i and j, either can be gas and/or liquid, can be expressed as below:

Productivity (rate of production) ratio:

$$\frac{P_i}{P_j} = \frac{\dot{n}_i}{\dot{n}_j} = \frac{S_{MX,i}/F_{Cal,i}}{S_{MX,j}/F_{Cal,j}} = \frac{S_{MX,i}}{S_{MX,j}} \times \boxed{\frac{F_{Cal,j}}{F_{Cal,i}}} \tag{3.41}$$

Combined with faraday's law (Equation (3.22)), selectivity (*i.e.*, faradaic efficiency) ratio:

$$\frac{FE_i}{FE_j} = \frac{z_i \times F \times \dot{n}_i/I_{EC,i}}{z_j \times F \times \dot{n}_j/I_{EC,j}} = \frac{\dot{n}_i}{\dot{n}_j} \times \frac{z_i}{z_j} \times \frac{I_{EC,j}}{I_{EC,i}} = \frac{S_{MX,i}}{S_{MX,j}} \times \boxed{\frac{z_i}{z_j} \times \frac{F_{Cal,j}}{F_{Cal,i}}} \times \left(\frac{I_{EC,j}}{I_{EC,i}}\right) \tag{3.42}$$

Fractions in boxes are constants only dependent on the analyte; the fraction in brackets is a constant in the same measurement.

Therefore, productivity comparison can be carried out among analytes produced from the same or different reaction(s) by directly comparing their QMS signals; while FE comparison among various products is directly comparable in the same measurement.

Chapter 4 Electrochemical $CO_{(2)}$ Reduction on Cu – *Operando* Acetaldehyde Detection

As the most both economically and energetically valuable products with a reasonable productivity (> 30 MtC/yr) from CO_2 recycling [28], ethylene and ethanol have been two of the main focuses of the above field. Literature have agreed that the two products share the same generation pathways after C-C coupling [74], [114], [115], which is believed to be the rate-determining step (RDS) of C_{2+} product formation [116]–[118]. Therefore, figuring out the bifurcation point and mechanism of ethylene and ethanol will help increase the selectivity towards either of them. Additionally, previous studies have found that acetaldehyde is the precursor of ethanol [31], [47], [141], [167], meaning that the earliest branching happens between ethylene and acetaldehyde, which will be further reduced to ethanol. However, since ethylene is a gaseous product while acetaldehyde is a liquid, they are usually analyzed *via* different techniques with separate equipment, making their simultaneous detection challenging. Moreover, acetaldehyde undergoes complicated chemical reactions in alkaline [112], [113], [167], [168]. As a consequence, the precision of analyses based on delayed acetaldehyde detection would be jeopardized. To this end, realizing its real-time detection would provide valuable information on the eCO(2)RR mechanism.

On the other hand, although the selectivity of both ethylene and ethanol was suggested to be surface structure-dependent, with the (100) orientation favoring ethylene while undercoordinated sites facilitate ethanol [46], [49], [52], [81], [169], no such information has been found on acetaldehyde yet.

To contribute to the above two aspects, in this chapter, I will first explain the possibility of *operando* acetaldehyde and ethanol reduction during eCO(2)RR on our EC-MS system with deliberately modified mass spectrometer (MS) parameters. Then, the scientific and technical feasibility of the selected mass/charge ratio (m/z) being the descriptor of the corresponding liquid product will be interpreted in detail. It is followed by a detailed investigation of acetaldehyde chemistry in alkaline. Subsequently, with the validated MS descriptors, I will

present *operando* acetaldehyde production on polycrystalline and various single crystal Cu electrodes during eCORR. Conclusions will be given in the last subsection.

All experiments were conducted by myself. Degenhart Hochfilzer (PhD student at SurfCat) suggested modifying the electron energy of the MS ion source.

All electrochemical reductions in this chapter were conducted with the EC-MS system, and all reported current densities are normalized to the electrode's geometric surface area, which is 0.196 cm^2 in all cases. Also note that only singly charged ions are considered in this thesis, and thus m/z is regarded the same as an atomic mass unit (AMU). In this thesis, I will use the term "MX" to represent the fragment with m/z or AMU of "X". For instance, M2 stands for the mass spectrometer signal intensity at m/z or AMU of 2.

In this chapter, the word "direct" MS signal refers to MS data directly acquired without further processing; whereas "deconvoluted" MS signal means the contribution of different analytes to the same m/z fragment have been deconvoluted.

Moreover, as interpreted in Chapter 3.5.5.4., the MS signal intensity is proportional to the absolute amount of an analyte in the system. Accordingly, when a MS signal is described as increasing/decreasing, it refers to the productivity or selectivity variation of the corresponding analyte.

4.1 Electrochemical $CO_{(2)}$ Reduction on Polycrystalline Cu with Electron Energy at 70 eV

The initial attempt was on eCO2RR on a polycrystalline Cu electrode with the default cathode potential of the ion source (*i.e.*, electron energy, EE) at 70 eV, as shown in Figure 4.1a. M2 was used as the descriptor for hydrogen. Hydrogen evolution reaction (HER) onset at -0.15V *vs.* RHE illustrates the high sensitivity of EC-MS. From the plot, it is obvious that HER predominated during the entire experiment course. Ethylene (C_2H_4 at M26 (C_2H_2+)) production onset at -0.50V *vs*. RHE, but only had a faint increment and did not increase further. It was because when the E_{WE} exceeded -0.55 V *vs*. RHE, not only did eCO2RR become mass transfer limited, but as H_2 was continuously produced, gas bubbles were formed over time and accumulated at the tips of the reference electrode (RE) and counter electrode (CE) chambers, leading to an open circuit and thereby obstructed potential and current flow. As a result, the potentiostat was overloaded. The bubble-induced overload problem is inevitable when a large number of bubbles are produced, which is a technical limitation of stagnant thin-layer EC cell of EC-MS setup.

One way to avert this issue is to do eCORR instead. Literature have found that compared to eCO2RR conducted in neutral electrolytes, eCORR under alkaline conditions provides a higher *CO local concentration, which facilitates C-C coupling and thus C_{2+} product generation as well as hindering HER [46], [170], [171]. Upon switching from CO_2 to CO reduction (Figure 4.1), more products in addition to H_2 were formed as expected. H_2 and C_2H_4 onset at -0.15 V and -0.4 V vs. RHE, respectively. Methane (CH_4 at M15 (CH_3+) onset at -0.52V *vs*. RHE was also noticeable. The potentiostat was overloaded again when E_{WE} exceeded -0.60V *vs*. RHE due to the accumulated gas bubbles, which further manifests the high sensitivity yet low bubble resistance of the EC-MS setup.

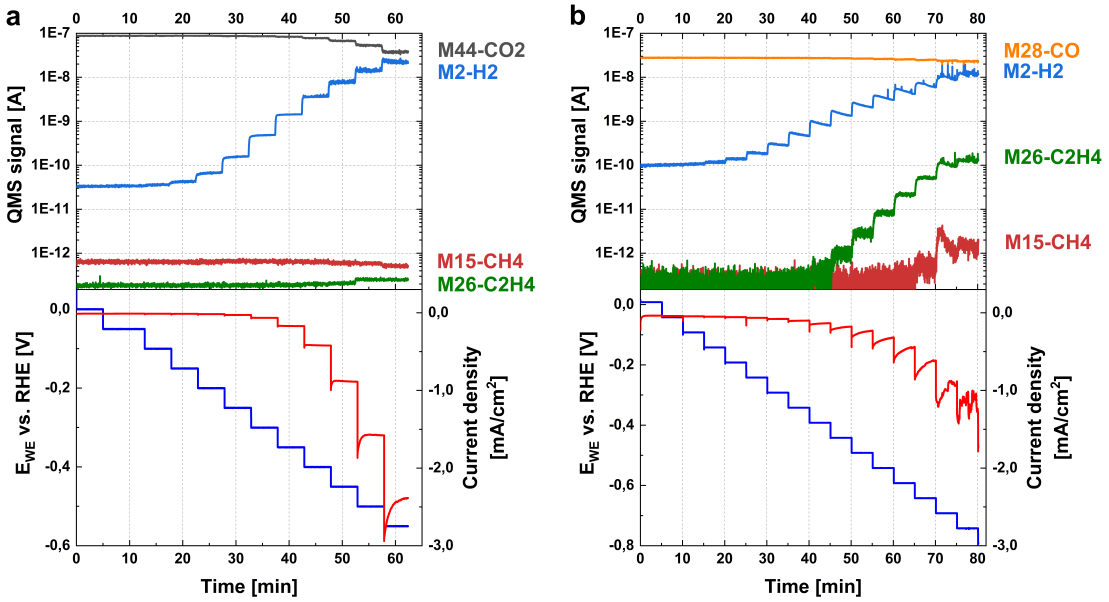

Figure 4.1 ***a) Electrochemical CO_2 reduction*** *in 0.1 M $KHCO_3$ electrolyte purged with CO_2 at 8 sccm.* ***b) Electrochemical CO reduction*** *in 0.1 M KOH electrolyte purged with CO at 10 sccm. The same polycrystalline Cu electrode was used in both measurements. Upper panels: direct mass spectrometer (MS) signal intensity of H_2, CH_4, C_2H_4, CO_2, and CO at M2, M15, M26, M44, and M28, respectively, with the MS electron energy (EE) at 70 eV; lower panels: electrochemistry data of the working electrode potential (blue) and total geometric current density (red). The applied potential stepped down 50 mV every 5 min.*

Given the small reaction volume (2 µL) as well as the low applied potential and thus current density, the amount of generated liquid products (*i.e.*, acetaldehyde and ethanol within the reachable potential window) are expected to be extremely small. Thus, finding out their detection limit is necessary. It is done by assuming a series of productivity of the species of interest and adding the corresponding amount to the electrolyte. The only few references that reported acetaldehyde faradaic efficiency (FE) at -0,4 ~ -0,6 V *vs*. RHE on monometallic Cu electrodes under similar conditions was below 5% on OD-Cu [46], [49], [112], and for ethanol, the FE maximizes at ca.10%. Furthermore, it was also reported that grain

boundaries/surface defective sites are more selective towards C_{2+} oxygenates than flat surfaces [49], [52], [172]. Considering my Cu electrode is electrochemically polished, its acetaldehyde and ethanol FE would be even smaller. Therefore, 1 ~ 5% FE for acetaldehyde and 1 ~ 10% FE for ethanol would be a reasonable assumption (Table 4.1). Since Henry's law constant of ethanol (*ca.* 200 mol/(L•atm) at 25ºC) is one order of magnitude high than that of acetaldehyde (*ca.* 15 mol/(L•atm) at 25ºC) [166], 1 mM and 10 mM was used for acetaldehyde and ethanol, respectively. The detection limit of acetaldehyde and ethanol was found to be ca. 0.2 μm and 2.0μm, respectively (Figure A.1). Therefore, the selected concentrations were suitable.

With respect to the characteristic m/z, the standard MS spectrum with IE of 70 eV of acetaldehyde and ethanol has characteristic m/z at M29 (CHO^+) and M31 (CH_3O^+), respectively [166]. However, the standards are collected with pure chemicals and do not represent the cases of dilute solutions, because the background would be significantly influenced in the latter case. Therefore, to determine reliable descriptors for the liquids, Figure 4.2 compares the magnified full mass spectra of 0.1 M KOH and with acetaldehyde or ethanol added separately. For all scans, the EC-MS cell and all electrodes, as well as purged CO gas were kept identical as in a regular eCORR measurement.

Table 4.1 ***Expected acetaldehyde and ethanol concentration*** *in the reaction volume.*

	Assumed faradaic efficiency (%)	**Expected concentration in the reaction volume (mM)**
Acetaldehyde	1	0.21
	2	0.42
	5	1.04
Ethanol	1	0.26
	2	0.32
	5	0.78
	10	1.56

M28 had the predominant signal intensity because CO was purged as the carrier gas. The intensity of M15 (CH_3^+) and M26 ($C_2H_2^+$) fragments, which are shared by methane and ethylene, respectively, increased in both cases, but are easily deconvoluted. Ethanol had a unique increment at M31 as expected. M29 did not show a visible change upon adding

acetaldehyde, due to the overwhelming background caused by isotopic CO (*i.e.*, $^{13}C^{16}O$ and $^{12}C^{17}O$). Interestingly, acetaldehyde and ethanol share a wide peak centered at M42 (highlighted in purple), while more prominent on acetaldehyde, even with a 10 times lower concentration. Hence, although not ideal, M42 and M31 were used as the descriptor for acetaldehyde and ethanol, respectively, in the subsequent preliminary test.

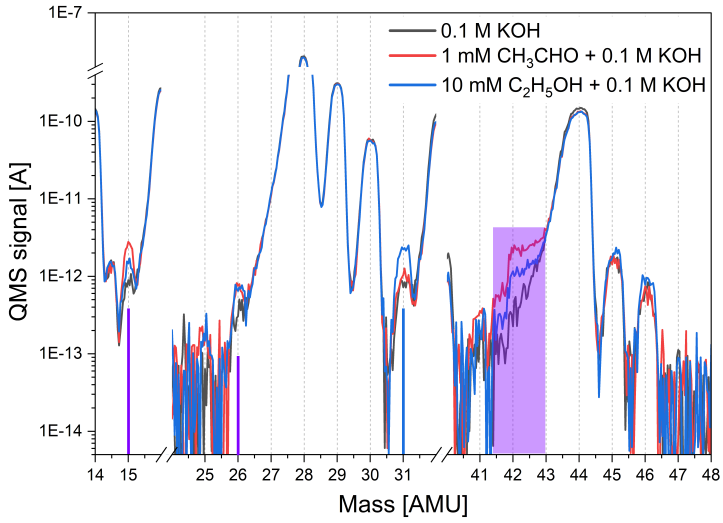

Figure 4.2 ***Enlarged region of full mass spectra*** *of 0.1 M KOH electrolyte (black) and it added with 1 mM acetaldehyde (red) and 10 mM ethanol (blue), respectively (EE = 70 eV). Purple bar and area indicate the mass where both acetaldehyde and ethanol show a difference; blue bar indicates the mass where only ethanol shows a difference. Spectra in the full mass region (0-50 m/z) are shown in Figure A.2.*

Figure 4.3 depicts eCORR with M31 and M42 tracked (same data set as Figure 4.1b). Unexpectedly, neither of them exhibited a noticeable change. Given that EC-MS is capable of detecting volatile products as proved above, and that the applied potential already exceeds their onset potentials under eCORR conditions [46], [49], [112], [173], there should be acetaldehyde and ethanol produced. Hence, the reason for not observing the MS signal increase is that the produced amount could not be reflected by the MS signals. It might have two causes: i) the produced amount is so few that is below the MS detection limit – it is indeed possible considering the low current density; and ii) the corresponding m/z is overlapped and dominated by other fragments. Accordingly, to enable acetaldehyde and ethanol detection, there are two options: a) increasing the productivity of the species and/or b) improving the system's sensitivity to the analytes.

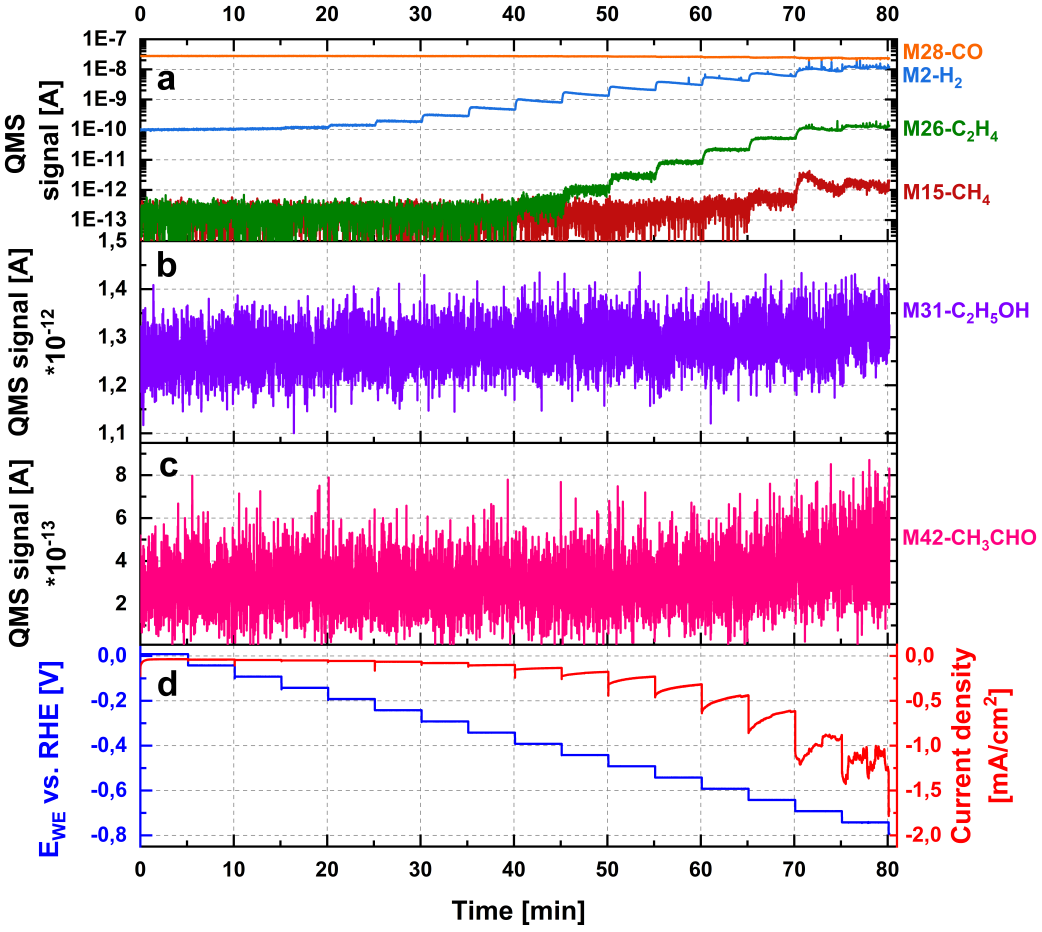

Figure 4.3 ***Electrochemical CO reduction*** *in 0.1 M KOH electrolyte purged with CO at 10 sccm. Note it is the same data set as Figure 4.1b (EE = 70 eV), where M31 and M42 were hidden. a) Direct MS signal plotted on a logarithmic scale. b-c) Direct MS signal plotted in an absolute scale to emphasize the variation. d) Electrochemical data.*

Increasing productivity could be realized by enlarging the reaction volume (in the case of mass-transfer limited), enhancing the electrolyte alkalinity, and increasing the electrode's geometric or active surface area. However, each way has unsurmountable drawbacks: a larger reaction volume would compromise the product collection efficiency, the membrane chip cannot resist pH above 13, and a larger electrode surface would deteriorate the aforementioned bubble issue. Moreover, eCORR will be conducted on Cu single crystals in the future such that the catalyst surface needs to be intact.

Improving the system sensitivity, on the other hand, is a feasible way without affecting eCORR itself. Ideally, by using a sufficiently low EE that is right above the appearance energy (AE) of the molecular ion (almost the same as ionization energy in EC-MS). However, since the AE of acetaldehyde and ethanol are both ca. 10 eV [166], which is below the minimal EE energy of the EC-MS (*i.e.*, 19eV), molecular ions could not be obtained before being further ionized to smaller fragments. Additionally, the applied EE should be low

enough in case the target analyte molecules are severely ionized such that too many small fragments (*e.g.*, CH_2+, CH+, CO+, *etc.*) that are shared by most hydrocarbons and hydroxides are produced on the one hand; while on the other hand, an excessively low EE might produce so few fragments that below the system's detection limit. Furthermore, since acetaldehyde and ethanol have similar molecular structures and thus ionized fragments, their differentiation requires dedicated determined EE.

4.2 Enable Volatile Liquid Product Detection by Adjusting Electron Energy and Validation

4.2.1. Selective Ionization

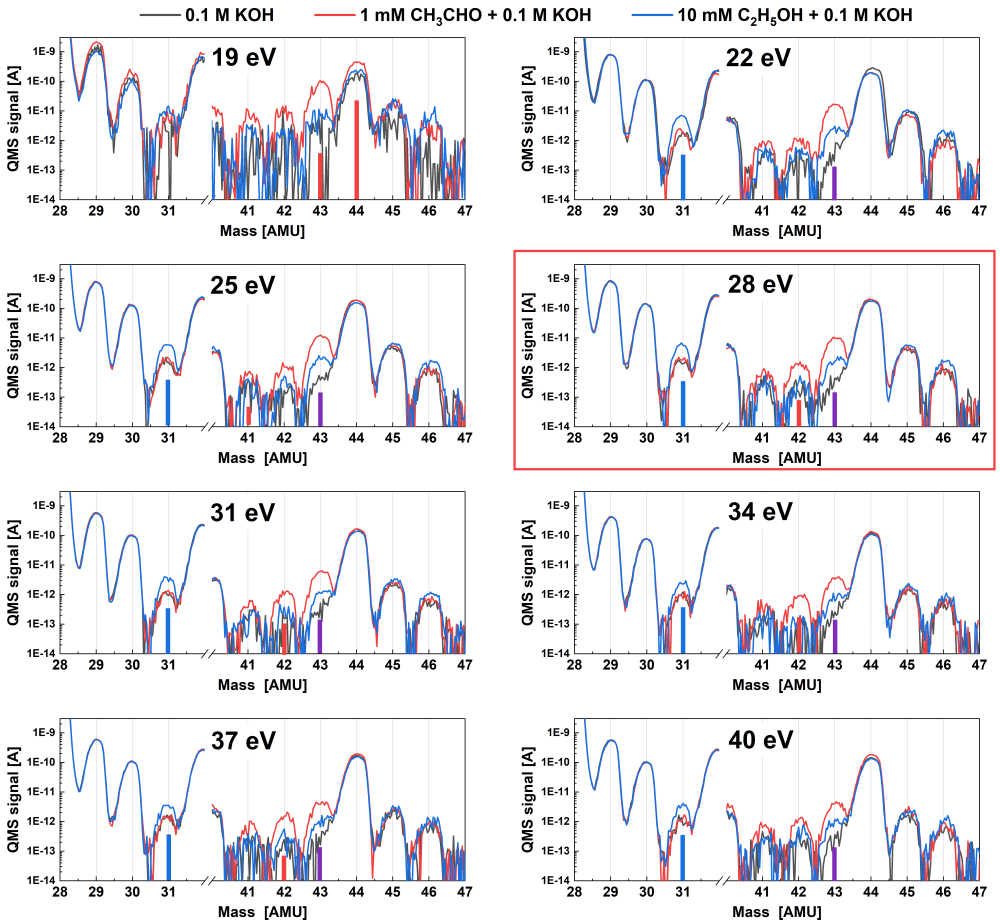

Figure 4.4 ***Magnified full mass scans at various electron energies.*** *All cell and system settings were kept as identical as in regular eCORR measurements at 70 eV. Blue and red bars indicate the m/z where only ethanol and acetaldehyde show an increased intensity, respectively. Purple bars indicate the m/z where an increased intensity is found with both species. Only regions with observable peak intensity change are shown here. Spectra with the full m/z range (0-50) are in Figure A.3.*

To find the optimal EE, full mass scans at various EEs are compared in Figure 4.4. Considering the AE of acetaldehyde and ethanol are both relatively small, as explained above, EEs were tested between 19 and 40 eV. Blue and red bars indicate the m/z where only ethanol and acetaldehyde show an increased intensity, respectively. Purple bars indicate the m/z where an increased intensity is found with both species. Only enlarged regions with observable peak intensity change are shown here. Spectra with full m/z range (0 ~ 50) are in Figure A.3. It can be seen that the wide peak spreading between 41.5 ~ 43 eV appeared at EE 70 eV is split into two peaks upon reducing EE below 40 eV. More importantly, acetaldehyde and ethanol exhibit a unique increment at M42 (C_2H_2O+) and M31 (CH_3O+), respectively; and at 28 eV, the increment in both species was the most prominent. The electron energy of 28 eV has been thereafter used for all eCORR measurements in this chapter.

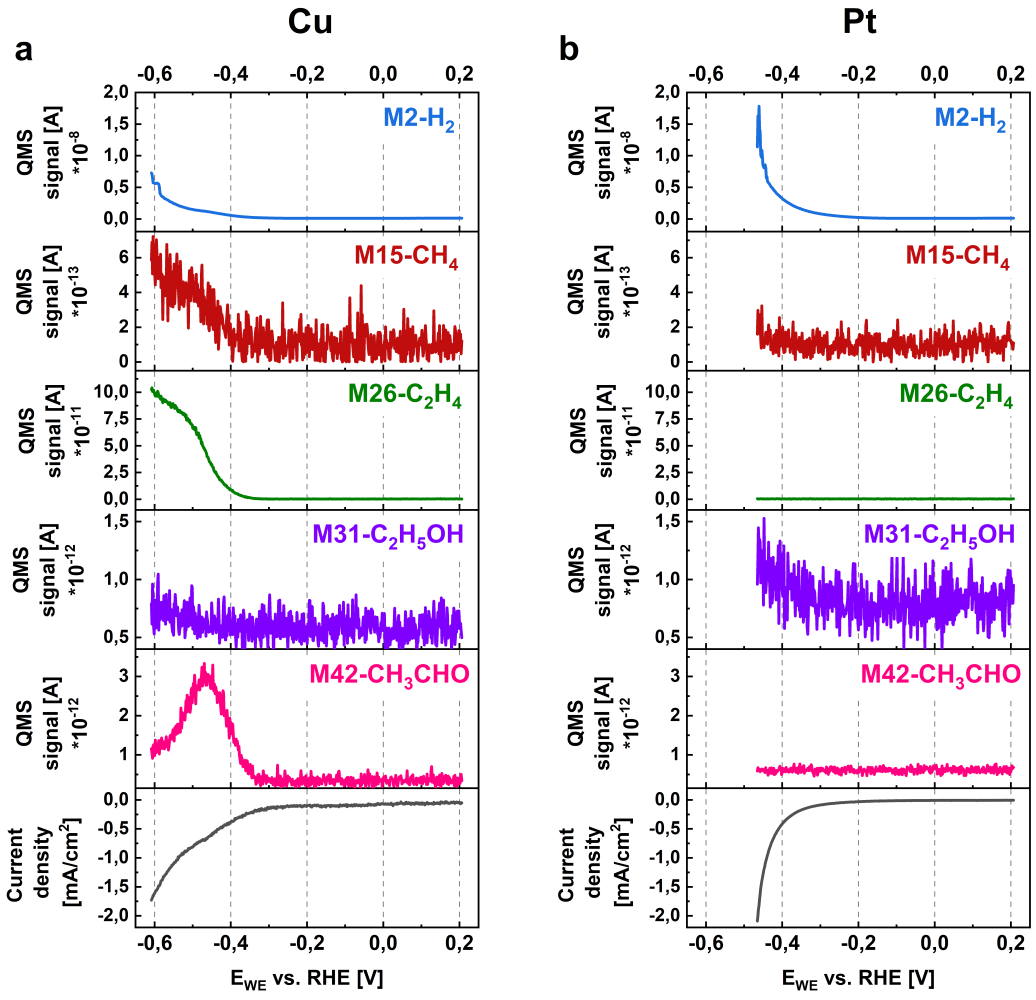

Figure 4.5 ***Linear sweep voltammetry scans and deconvoluted MS signals of electrochemical CO reduction*** *on a) Cu and b) Pt. Scan rate was 2 mV/s to keep the system at a pseudo-steady state. The Cu electrode was kept at 0 V vs. RHE for 5min to reduce oxidized Cu on the surface to its metallic state, then started LSV scan without going back to OCV. The same scales are used for the same m/z and electrochemistry data on the two metals.*

Figure 4.5a shows the linear sweep voltammetry (LSV) scans and tracked m/z fragments of corresponding species as a function of E_{WE} during eCORR. It looks promising at the first glance: M42 started increasing at *ca.*-0.35 V and dropped at *ca.* -0.48V. M31 began increasing, although with a faint increment, at the same point where M42 went down. It seems to support previous finds that ethanol is produced by the further reduction of acetaldehyde [112] and it becomes prominent at a relatively low overpotential (-0.35 ~ -0.59 V) [49], [173]. However, in my previous tests I noticed that when H_2 is introduced in the system, either externally (*e.g.*, mixed with the carrier gas) or internally (*i.e.*, being produced during the reaction), the background signal of some MX shifted while others did not. Interestingly, some of the shifted MX could not be assigned to any component existing in the system (including those from air dissolved in the electrolyte). Therefore, it is necessary to ensure that the faint increment in M31 is indeed due to ethanol production from eCORR instead of a background shift affected by the accompanying HER. To this end, Pt was chosen as the benchmark for its nearly 100% FE under the same reaction conditions [27]. Figure 4.5b compares each MX on Pt and on Cu in the same coordinate scale. Unexpectedly, M31 increased even more on Pt, as a consequence of HER.

4.2.2. Why Does Hydrogen Elevate M31?

The reason could be that when the produced H_2 enters carrier gas, the physical properties (*e.g.*, dynamic viscosity, mean molecular dynamic mass and diameter) of the latter would change, leading to a varied total molar flow rate, and hence change MX background intensities. However, it fails to explain why only M31 was evidently affected while the others were not.

Given the background shift occurred uniquely on M31 (among all tracked MXs), which has a close AMU to that of the carrier gas CO (M28), it could be related to isotopes. In CO atmosphere, MXs that are dominated by CO-related fragments include: M28 ($^{12}C^{16}O+$), MS12 (^{12}C), MS13 ($^{13}C+$), MS16 ($^{16}O+$), MS18 ($^{18}O+$), M29 ($^{13}C^{16}O+$) and MS30 ($^{12}C^{18}O+$). M31 happens to be one AMU more than M30. Keeping this in mind, chemical ionization (CI) could be a cause.

In chemical ionization, reagent gas molecules MH_n ($n\geq1$) are ionized and form reagent ions MH_n+ (Equation (4.1)). When an analyte molecule (A) is introduced into the ionization chamber, MH_n+ donates a proton to A, forming a protonated ion [A-H]+ through an ion-molecule reaction mechanism (Equation (4.2)). [174] In the current circumstance, H_2 acts as the reagent gas, and the isotopic M30 fragment was protonated and exhibited a “fake” increment as HER proceeded. The same phenomenon was also observed on M41 when Ar (M40) was mixed with 5% H_2 (Figure A.4).

$$MH_n \xrightarrow{\text{Electron ionization}} MH_n{}^+ + e^- \tag{4.1}$$

$$MH_n{}^+ + A \xrightarrow{\text{Ion-molecule reaction}} [A-H]^+ + MH_{n-1} \tag{4.2}$$

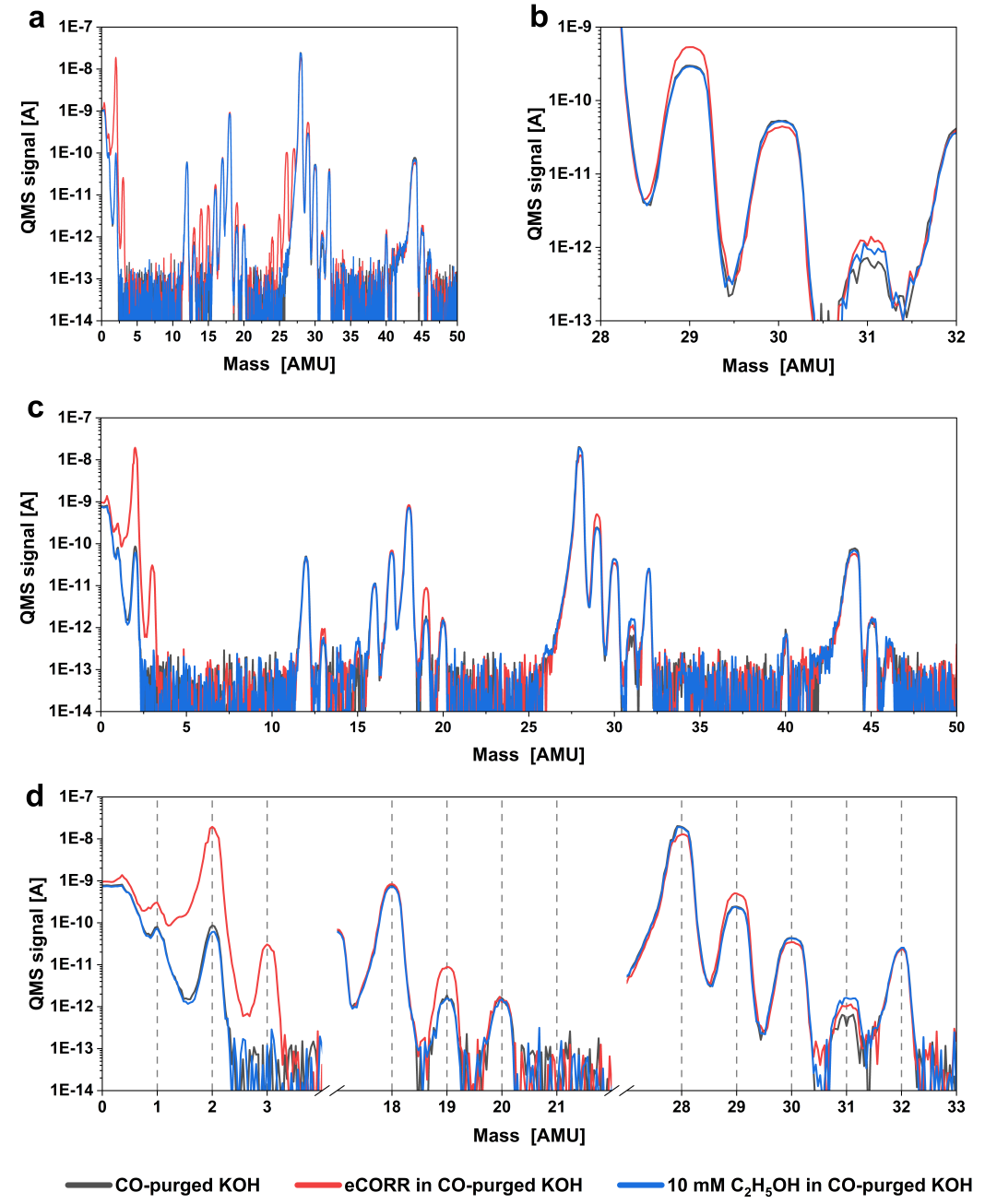

Figure 4.6 ***Full mass scans for comparing influence of different ethanol sources on the MS31 background signal:*** *no ethanol (black), ethanol produced in situ during eCORR (blue), and externally added ethanol (red) on Cu (a, b) and Pt (c, d).*

To justify the influence from CI as well as to differentiate protonated $^{12}C^{18}O+$ from CH_3O^+ at M31, Figure 4.6 compares full mass scans of CO-saturated KOH electrolyte (black) with externally introduced ethanol (blue) and during eCORR at *ca.* -0.7 V *vs.* RHE (red). Figure 4.6a and b show the full and enlarged mass range on Cu, respectively. An increased M29 is only exhibited in the eCORR scan and M31 increased both ethanol sources. The scan accompanied by HER exhibits an increase at both M29 and M31, while externally added ethanol only elevates M31. This supports the hypothesis of the CI-induced M31 background elevation. To further confirm the influence from CI, the same scans were taken and compared on Pt. Figure 4.6d shows the enlarged AMU range where QMS signal intensity change are found. In addition to M31, the increased signal at M3, M19, and M29 are due to the ion-molecule reaction between the H_2+ ion with H_2 (MS2), H_2O (M18), and CO (M28) molecules, respectively, considering that these are the three most abundant molecules in the reaction volume. Thus, the hypothesis of CI-induced background shift on M31 is confirmed, and M31 can not serve as a reliable descriptor for detecting ethanol.

It is worth noting that this CI-scrambled M31 issue may not be significant when ethanol productivity reaches a certain level, as was shown in some DEMS research [113], [173], [175], [176]. However, due to the low productivity in EC-MS, it is inevitably dominating.

4.2.3. Validation and Calibration on Detected Acetaldehyde

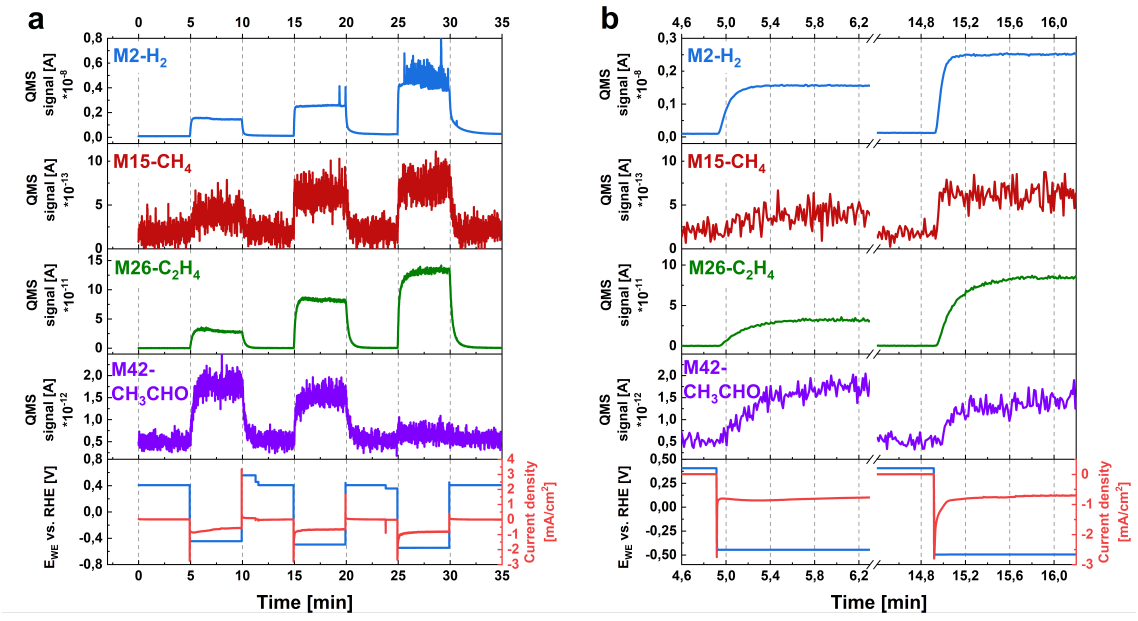

Figure 4.7 ***Chronoamperometric eCORR on a polycrystalline Cu electrode at three different potentials.*** *Each potential was held for 5 min and stepped back to open circuit voltage for 5 min before stepping to another. The three CA potentials (vs. RHE) were chosen from Figure 4.5a: -0.45 V at the MS42 vertex, -0.50 V after the MS42, and -0.55 V when M26 reached a high level before the aforementioned HER-induced bubble issue occurred. QMS signals of M15 and M26 are deconvoluted.*

Albeit ethanol does not have a reliable descriptor, tracking M42 could still give some insights into the acetaldehyde activity during eCORR. Figure 4.5a shows an interesting trend of M42 growing as a function of E_{WE}. Combined with full mass scan tests, M42 can be used as a suitable descriptor for acetaldehyde.

LSV has been combined with mass spectrometry studies to help understand the convoluted eCO(2)RR pathways. By comparing the onset potential of different products, it can be speculated if they share the same intermediate(s) and accordingly formation pathway(s). [47], [59], [177] For example, ethylene and acetaldehyde onsetting together seen in Figure 4.5a seem to support the previous finding that the two products share the same pathway [74], [114], [115]. Yet, care should be taken in this manner because different sensitivity and detection limits of mass spectrometers on different analytes might present misleading information and consequently lead to imprecise conclusions.

To evaluate the sensitivity of EC-MS to ethylene and acetaldehyde, chronoamperometry (CA) was held at three potentials (*vs.* RHE) chosen from Figure 4.5a: a) at -0.45 V, MS42 reached vertex; ii) at -0.50 V, M42 started to decrease; iii) at -0.55 V, MS42 has reduced to a low level while M26 dominated (Figure 4.7a). Before going to each CA, the potential was held at open circuit voltage (OCV) for 5min to "recover" to the initial reaction state. The magnified potential-switch region (Figure 4.7b) shows an immediate signal rising of all tracked MXs upon potential stepping down, indicating the high detection sensitivity. All MXs exhibit a gradual growth before reaching a steady state within 0.4 min, which can be owing to: i) non-faraday current due to electrical double layer charge as indicated by the transient current drop; and ii) time for eCORR itself and related reversible reactions (*e.g.*, HER/HOR [178]) as well as the post-reaction gas stream to reach equilibrium. This is true for gas products, as their collection efficiency is nearly 100% [146]. For acetaldehyde, however, given the negligible evaporated amount compared to its concentration (Chapter 3.5.5.2), the plateaued MS42 suggests acetaldehyde production and consumption by further reduction to ethanol reached an equilibrium [112].

4.2.4. More Investigations on Acetaldehyde Chemistry

Acetaldehyde is known to undergo complicated chemical reactions in alkaline, such as "Cannizzaro-type" disproportionation [65], [129] and aldol condensation [113], [167]. To get a better idea of acetaldehyde chemistry, I first calibrated acetaldehyde concentration (Chapter 3.5.5.2). Results show a well-fitted linear relationship with the M42 signal intensity. Concentration (*ca.* 4.5 mM) corresponding to the highest M42 signal in the eCORR LSV scan was then chosen for the subsequent measurements.

Figure 4.8a tracks the M42 signal after freshly introducing acetaldehyde in 0.1 M KOH. A *ca.*37% drop was observed after 45 min. Considering the negligible consumption from evaporation compared to its total concentration, and there was no electrical supply, chemical reactions must be playing a significant role. To prove this hypothesis, 0.1 M KOH solution with the same acetaldehyde concentration was analyzed with HPLC every hour for 10 h. A similar decrement as in EC-MS was found in the first hour. The presence of other components in addition to acetaldehyde at 0 h is owing to time delay during the HPLC test. Instead of being analyzed immediately after mixing acetaldehyde with KOH as in EC-MS, the HPLC sample solution was prepared *ca.*10 min before injecting to the analyzing column, and analysis took another 30 min. Nevertheless, this inevitable time delay does not influence the trend of concentration variation on each analyte.

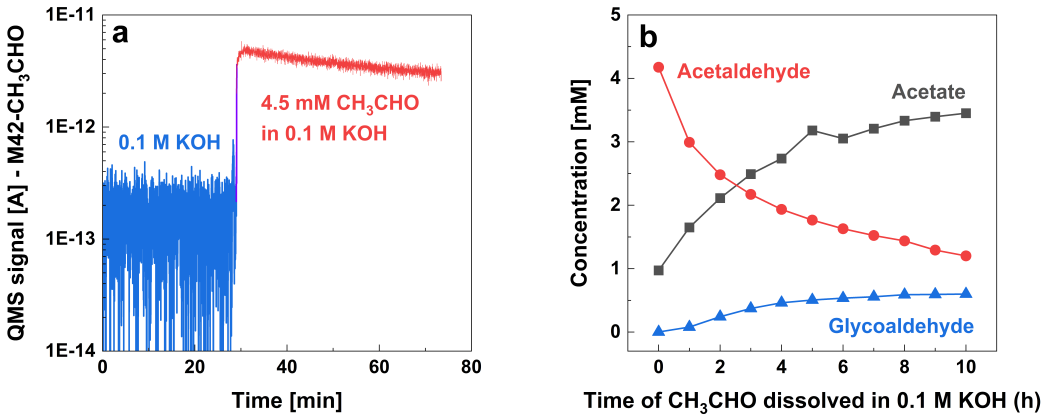

Figure 4.8 ***a) Direct QMS signal of M42 background*** *in 0.1 M KOH (blue) and shifting (red) in 45 min after acetaldehyde was introduced.* ***b) Change in composition of 0.1 M KOH solution*** *after introducing 4.5 mM acetaldehyde measured with HPLC. Only composites with over 0.1 mM of composition are shown. Other detected composites with < 1 mM concentration as well as un-assigned HPLC spectra peaks are plotted in Figure A.5.*

From Figure 4.8, it can be seen that acetate is the main product of acetaldehyde conversion in alkaline. Literature usually assigned it to "Cannizzaro-type" disproportionation, through which two acetaldehyde molecules form one ethanol and one acetate molecule [65], [129]. However, HPLC did not detect ethanol in my case. Given the similar detection limit of ethanol and acetate in our HPLC equipment, it is reasonable to infer that (almost) no ethanol was formed in the solution. Additionally, Birdja and Koper pointed out that the Cannizzaro reaction requires a devoid of α-H atoms, whereas the α-C of acetaldehyde is fully protonated. As a result, Aldol condensation is much faster. [113] Therefore, Cannizzaro reaction is not very like to be the cause of the current test. Yet, considering that the local pH is usually higher at the electrode surface than in the bulk in eCO(2)RR [35], [55], [113], [179]–[181], especially in stagnant electrolyzers, the possibility of Cannizzaro reaction cannot be fully ruled out.

Acetaldehyde self-polymerization is another possibility. Unfortunately, I could not detect condensate or polymerized products with HPLC. Nonetheless, Figure 4.9 shows the change in color of 10 mM acetaldehyde mixed in 0.1 M KOH solution for 24 hours. The yellowish color suggests the formation of larger molecules.

In contrast, the same chemical reaction was not found when the same concentration of acetaldehyde was dissolved in 0.1 M $KHCO_3$ (pH 6.8, the most commonly used electrolyte for eCO2RR) in the course of 10 hours, which confirms the impact is owing to the alkalinity of electrolyte. Therefore, if acetaldehyde-containing post-mortem alkaline electrolyte cannot be analyzed on time, neutralizing it to a neutral pH before storing could help maintain its stability.

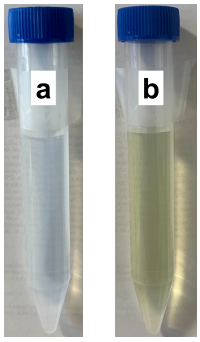

Figure 4.9 ***Acetaldehyde (10 mM) mixed in 0.1 M KOH solution****; a) freshly mixed, and b) after 24 hours.*

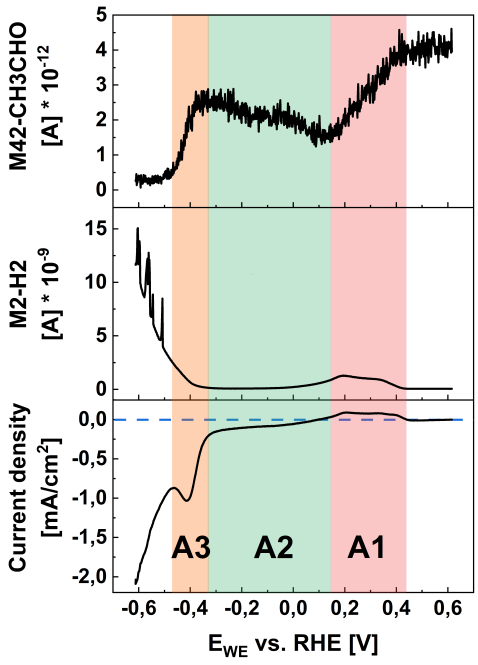

Figure 4.10 ***Acetaldehyde reduction with 4.5 mM concentration mixed in 0.1 M KOH.*** *LSV scan started from open circuit voltage. The acetaldehyde-added electrolyte was injected into the EC-MS cell 5 min before initiating electrochemistry. 5 min because on the one hand, it is long enough to stabilize all MX signals; while*

on the other hand, it is not so long that M42 background shifting started to take a significant role, as shown in Figure 4.8a. It is also worth noting that the acetaldehyde reduction reaction was completed within 15 min after it was introduced, and therefore M42 background shifting would not affect its signal intensity change during the reaction.

To investigate more on the activity of acetaldehyde under eCO(2)RR conditions, I did direct reduction of acetaldehyde (same concentration as in the above background investigation) in Ar-saturated 0.1 M KOH *via* LSV scan starting at open circuit voltage (OCV) (Figure 4.10). The LSV potential window can be divided into three regions, based on the M42 signal variation trend:

i) A1: +0.44 V ~ +0.14 V *vs*. RHE

M42 dropped nearly 65% with a slightly increased M2, accompanied by a subtly positive current. Since the standard reduction potential for acetaldehyde reduction to ethanol (Equation (4.3)) is at +0.02 V *vs*. RHE (Equation (4.4)), it is unlikely to be the reason.

On the other hand, acetaldehyde can be thermodynamically oxidized to acetate (CH_3COO^-) and oxalate ($(COO)_2^{2-}$) in alkaline without electrical supply [182]–[184], following Equation (4.5) and (4.6), respectively. A positive potential might accelerate this reaction, leading to a decreasing M42 signal as well as a slightly positive current.

The M2 increment cannot come from H_2 evolution at the applied potential. Although the cause remains unknown, it is certainly related to acetaldehyde oxidation, as this feature was missing when an identical measurement was conducted in the absence of acetaldehyde (Figure A.6a-c).

$$CH_3CHO + H_2 + 2e^- \rightarrow C_2H_5OH \tag{4.3}$$

$$E^0 = \frac{\Delta G}{nF} = \frac{\Delta G_{C_2H_5OH} - \Delta G_{CH_3CHO} - \Delta G_{H2}}{nF}$$

$$= \frac{[-277.6 - (-133.4) - 0][\text{kJ/mol}]}{2 \times 96485\ [\text{C/mol}]} \tag{4.4}$$

$$= -0.75\ \text{V}\ vs.\ \text{SHE} = +0.02\ \text{V}\ vs.\ \text{RHE (pH 13)}$$

$$CH_3CHO + \frac{1}{2}O_2 + OH^- \rightarrow CH_3COO^- + H_2O \quad (4.5)$$

$$CH_3CHO + 4O_2 + 2OH^- \rightarrow (COO)_2{}^{2-} + 3H_2O \quad (4.6)$$

ii) A2: +0.14 ~ -0.22 V *vs*. RHE

M42 elevated again in this potential window, which can be attributed to the electrochemically assisted reduction of the previously produced nonvolatile acetate and oxalate.

iii) A3: -0.22 V ~ -0.47 V *vs*. RHE

M42 decrease in this potential window is believed to be its actual electrochemical reduction. HER onset at -0.41 V *vs*. RHE and competed with acetaldehyde reduction, as indicated by the current wave. As overpotential continuously increased, acetaldehyde was consumed and HER took over after -0.47 V *vs*. RHE.

Integrating all the above discussions, acetaldehyde undergoes complex and fast (in the order of hours) chemical reactions in alkaline, and the major product under eCO(2)RR conditions (without applying a potential) is acetate. Therefore, *ex situ* and/or postmortem liquid product analyses are very likely to overestimate acetate production if not conducted on time, for instance, the collected post-reaction electrolyte has been stored for over 30 min before being analyzed.

Acetaldehyde reduction was also conducted on Cu single crystals: (100), (111), (110), and (211) (Figure A.6d-f). Although not much certain information can be extracted from the results yet, acetaldehyde oxidation and the following re-production (from the reduction of produced acetate and oxalate) is highly facet-dependent. More investigations in this regard will be done in the future.

4.2.5. Discussions on Faradaic Efficiency Calculation for eCORR on EC-MS

Figure 4.11f-i show the faradaic efficiency of each detected product. Details of the calculation and formula are in Chapter 3.5.5.3. Interestingly, on all facets, FE(H_2) was 0 before HER onset, and gradually rose as the overpotential increased subsequently (Figure 4.11f). This is unanticipated because HER would be predominating at a very low overpotential and therefore its FE is expected to be almost 100% when it onsets and reduces afterwards [61].

It might be related to the non-zero current at 0 V *vs*. RHE such that the non-faradaic current and/or ORR (Chapter 4.3) lead to an overestimated total current and therefore an underestimated FE. If it was the case, then if the onset current at 0 V *vs*. RHE was intentionally "zeroed", the rest of the current would be purely eCORR-related (*i.e.*, HER and COR). However, the trend remained the same (Figure A.9).

It may also be related to the time delay between EC and MS. Although EC-MS has a sub-second time scale with 100% collection efficiency towards gas molecules [146], it still takes a few seconds for the produced species to reach the MS, as can be seen in Figure 4.7b. Although LSV scan rate was slow (2 mV/s), it was still not a strictly steady state and therefore cause a slight delay between potential (and therefore current) change and MS intensity change. Especially close to the onset potential, where the current increases exponentially, and therefore the value of current between two data points could be big, the same also occurs on the MS signal as the corresponding product formation onsets. Therefore, at the moment of an electrochemical current I_{EC}, the corresponding MS signal intensity S_M^i (where the subscript M stands for a m/z and superscript i for the corresponding species) would be underestimated and consequently I_{EC}/S_M^i and FE_i would be underetsimated as well.

Owing to the above reasons, faradaic efficiency calculation on gas products at very low overpotentials (*ca.* < 0.4 V) may not give very precise estimations. Conducting eCORR at steady-state such as chronoamperometry and chronopotentiometry might give a more precise FE distribution, but it is not the main focus here.

Faradaic efficiency calculation on the liquid product (*i.e.* acetaldehyde) is even more complicated. On the one hand, it also suffers more from mismatched EC and MS time than gases do, owing to their slower evaporation and diffusion rate. On the other hand, since acetaldehyde, although volatile, only partially evaporates and most of the produced molecules accumulated in the electrolyte over time, and therefore accumulated QMS signal instead of the instantaneous value should be used. As overpotential goes up during LSV scan, acetaldehyde is being produced and consumed (due to further reduction to ethanol as well as chemical reactions in alkaline) simultaneously, whereas the absolute or relative productivity and consumption cannot be known. More details regarding FE calculation are presented in Chapter 3.5.5.3.

4.3 Electrochemical CO Reduction on Single Crystal Cu

Before each measurement, all single crystal Cu electrodes were mechanically polished first, followed by electrochemical polishing multiple times, until fingerprint CV features were obtained. Fingerprint CVs were also checked after each measurement and compared with

their before-reaction counterparts. More details are described in Chapter 2.2.1 and Chapter 3.2.6.

Figure 4.11 compares the eCORR performance on polycrystalline (pc) Cu and four single crystals: (100), (110), (111), and (211).

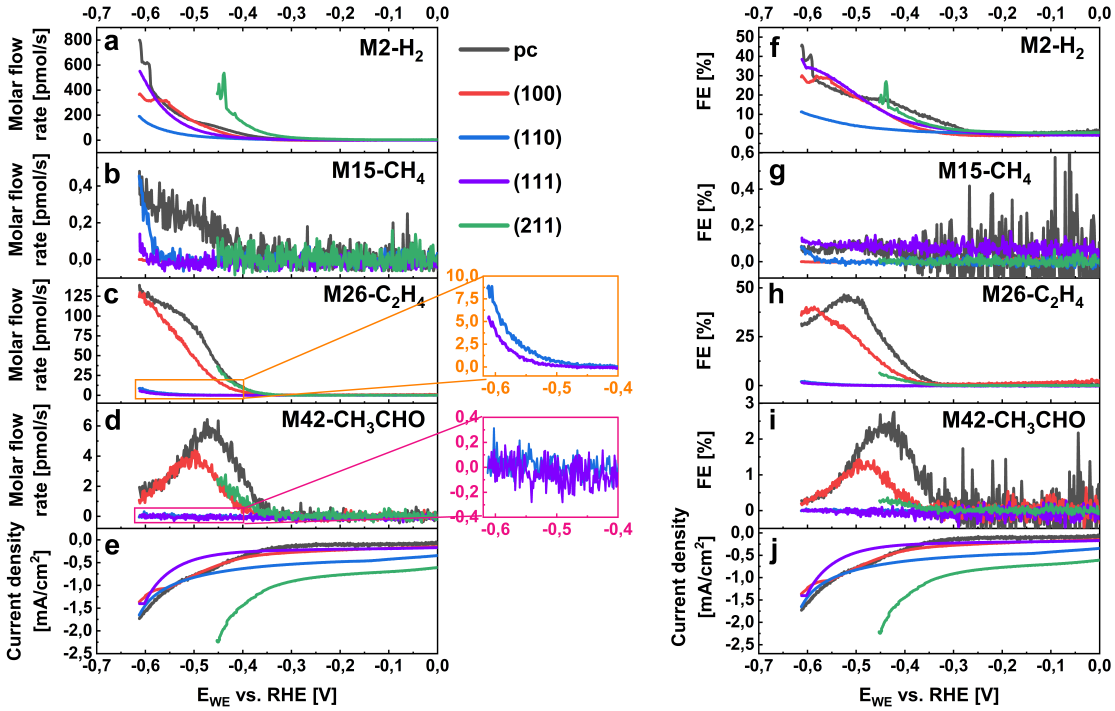

Figure 4.11 ***Electrochemical CO reduction performance comparison among polycrystalline Cu and single crystals.*** *LSV scans start from -0.1 V vs. RHE until the potentiostat is overloaded, at the scan rate of 2 mV/s. The WE was kept at 0 V vs. RHE for 5 min to reduce oxidized Cu to its metallic state, then continued with LSV without going back to OCV. All MS signals are converted to the molar flow rate (a-d) and faradaic efficiency (f-i) of the corresponding species. Details are presented in Chapter 3.5.5.2 and 3.5.5.3. Beside is the magnified region in the boxes. In panel c (M26-C_2H_4), (211) (green) and pc (black) were overlapped.*

4.3.1. Unexpected High Current Density at 0 V *vs.* RHE

Noticeably, the total current density at 0 V *vs*. RHE on Cu (110) and Cu (211) was relatively high (Figure 4.11e). It may be attributed to non-faradic current due to double layer charge, since overpotential keeps increasing during LSV. Therefore, I scanned CV starting from OCV to the LSV ending potential. Only *ca.*0.12 mA/cm2 and *ca.*0.04 mA/cm2 difference in the total current density between the cathodic (forward) and anodic (backward) scans were found on (110) and (211), respectively, (Figure A.7) meaning that double-layer capacitance charge is only partially responsible for the unexpected current the reason for the unexpected current and there must be other reasons.

Reduction of oxidized Cu surface is another possibility. Yet, before each measurement, the Cu electrode was reduced *in situ* at 0 V *vs*. RHE for 5 min, during which oxidized Cu is expected to be fully reduced to its metallic state [100], as can be seen from the transient current at the moment when potential changed from OCV to 0 V. However, instead of gradually decreasing afterwards until reaching nearly zero, as on the other three electrodes (Figure A.8), the total current density slightly increased, as depicted in Figure 4.12. Oxygen reduction reaction (ORR) is a possible explanation [185]. Considering the very small amount of air dissolved in the electrolyte (Chapter 3.1.2 for cell geometry), and that ORR was operating with a 0.77 V overpotential at 0 V *vs*. RHE (Equation (4.7)), it was very likely to be mas-transfer limited. It means the consumption of O_2 is at the same rate all the time, and since the assumed amount was so small that was below the MS detection limit, change in M32 (descriptor for O_2) signal intensity was not observed. If it was the case, ORR on Cu might be facet-dependent and is the most favored on the (211) facet. Moreover, as OH^- being produced, the (local) pH would increase which might be reflected in the observed current increment over time. Unfortunately, I could not find literature explaining the facet or pH dependence of ORR on pure Cu in alkaline, thus I do not have a good explanation for the slightly increasing current yet. Nevertheless, ORR is very likely to be another contribution to the unexpected current at 0 V *vs*. RHE.

$$O_2 + 2H_2O + 4e^- \rightarrow 4OH^- \qquad E^0 = +0.40\ \text{V}\ vs.\ \text{SHE} \tag{4.7}$$

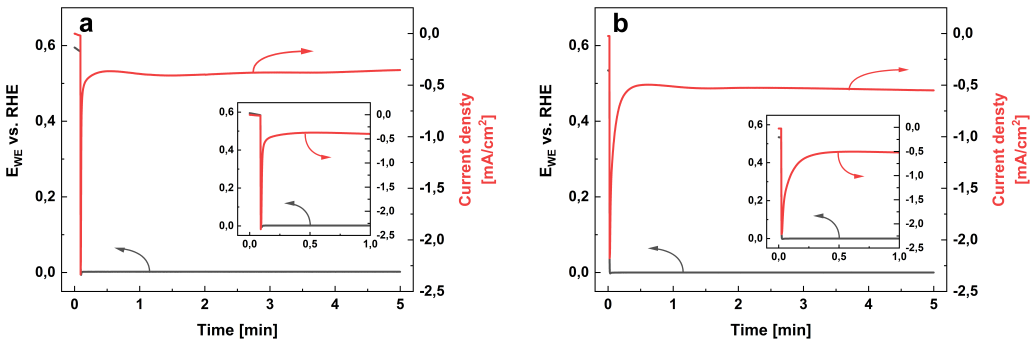

Figure 4.12 ***Cu reducing chronoamperometry at 0 V vs. RHE*** *on a) Cu (110) and b) Cu (211). Spikes at the beginning are because of the sharp potential change from OCV, as magnified in the inserts.*

4.3.2. Facet-dependent eCORR Performance

Ignoring the unexpected current for now and going back to eCORR (Figure 4.11). Methane formation onset at the same potential on (111) and (110) facets (Figure 4.11b). Given that (110) can be described as [2(111x(111)], composed of (111) terraces and (111) steps, it acts similarly to (111) [68]. Moreover, DFT studies have found that (110) binds *CO the strongest among the three low-index facets [186], [187], and since its (111) geometry does not favor

*CO dimerization [81], [188], it would be protonated to CH_4. It explains the higher CH_4 productivity on (110) than on (111). These two facets have a similar onset potential of ethylene production (Figure 4.11c) which was *ca.* 100 mV more negative than on (100). Acetaldehyde, as another C_2 product, was not found on (111) or (110) facets (Figure 4.11d). It is most likely to be because acetaldehyde was not produced or the produced amount was below the detection limit, considering that C-C coupling is not preferred on the (111) geometry as has been widely proved [58], [59], [65], [188]. It may also be that not only the produced amount was very few, but its further reduction to ethanol was so fast that acetaldehyde has been consumed already before being detected. It is possible because Hori *et al.* have observed high selectivity towards C_2 oxygenates (acetaldehyde, ethanol and acetate) on (110) at 5 mA/cm^2 (*ca.* -1.12 V *vs*. RHE for both CO and CO_2 reduction) [58], [73]–[75]. They attributed it to the (111) step sites with a certain length adjacent to the (111) terrace. [75] Koper's group also observed alcohol production from eCORR occurred only on (110) but not on other tested facets ((100), (111), (322) and (911)) below -0.6 V *vs*. RHE [68]. Moreover, Figure 4.10 and Figure A.9 show acetaldehyde further reduction to ethanol onset at -0.3 ~ -0.4 V *vs*. RHE. Therefore, there is reason to believe that the produced small amount of acetaldehyde converted to ethanol so fast that was not detected.

Comparing product preference on the three low-index Cu (hlk), ethylene is most favored on (100), which is in line with most previous Cu (hlk) studies both experimentally [58], [62], [106] and theoretically [43], [65], [76]. The same onset potential of acetaldehyde (Figure 4.11d) and ethylene (Figure 4.11c) is found on both (100) and (211) and was earlier than methane (Figure 4.11b), which acted similarly as Cu (pc), suggesting that they share the same intermediate on all the three electrodes after C-C coupling [43], [181]. (211) facet could not reach potential over ca. -0.46 V *vs*. RHE due to the aforementioned unexpected current issue (Figure 4.11e). Yet, within the scanned potential window, its ethylene (Figure 4.11c) and acetaldehyde (Figure 4.11d) formation acts similarly to (100). Considering the fact at (211) can be described as [3(111)x(100)] composing (111) terraces and (100) steps, it proves that surface activity is dominated by its step sites [50], [62], [97].

4.4 Conclusions

- In the potential window 0 ~ -0.75 V *vs*. RHE, polycrystalline Cu produces hydrogen, as the major gas products from eCO2RR conducted 0.1 M $KHCO_3$; whereas in eCORR, ethylene and methane are also produced.

- By means of reducing the electron energy of the mass spectrometer to 28eV, acetaldehyde and ethanol were successfully differentiated and have a unique m/z at

M42 and M31, respectively, which are used as their descriptors in the subsequent measurements.

- M31 background shifts as a consequence of chemical ionization happened between isotopic CO ($^{12}C^{18}O+$) and H_2, and therefore is not a suitable descriptor for ethanol production in eCORR in my case.

- Acetaldehyde production and consumption by further reducing to ethanol (not detected) would reach an equilibrium at a constant potential.

- Acetaldehyde would be oxidized to acetate thermodynamically in alkaline. Therefore, *ex situ* and/or postmortem liquid product analyses are very likely to overestimate acetate production if not conducted on time.

- Acetaldehyde oxidation is advantaged when a mildly positive potential (*ca.* +0.15 ~ +0.45 V *vs*. RHE) is applied, and its oxidation is highly facet-dependent, while the reason remains unknown.

- (110) and (211) facets both exhibited an unexpected onset current at 0 V *vs*. RHE, which is most likely related to double-layer capacitance charge as well as mass-transfer-limited ORR.

- Electrochemical CO reduction reaction was conducted on four single crystal Cu electrodes, (100), (110), (111), and (211), and compared to that of Cu (pc). The (100) step sites on Cu (211) and Cu (pc) surfaces dominate their product preference. Among the three low-index facets, ethylene production was most favored on (100) and methane was most preferred on (110).

- It is testified spectrometrically that ethylene and acetaldehyde share the same intermediate and formation pathways in eCO(2)RR.

- Sweeping voltage makes the faradaic calculation of eCORR on the EC-MS system imprecise due to double-layer capacitance charge, mass transfer delay, as well as the oxygen reduction reaction.

The presented results and discussions in this chapter emphasize the necessity of considering possible background shift in MS signals when it is employed to investigate reaction mechanisms, induced by system configurations, such as chemical ionization, convoluted fragments, and ion gauge pressure. In addition, it is suggested to be careful and on time when quantifying products that are unstable in the reaction environment, and make sure the precision of analysis is not jeopardized by any potential transformation of the unstable components.

Chapter 5 *Operando* X-Ray Measurements on CuAg Alloy in Electrochemical CO_2 Reduction

Although monometallic Cu is versatile in producing C_{2+} fuels, the production efficiency is limited by CO availability, mainly due to its low solubility in aqueous electrolytes (~1 mM at 1 atm and 25°C) [189]. Earlier studies have found that a high *CO at the Cu surface not only enhances C-C coupling and thus C_{2+} production formation, but also weakens *H binding, suppressing the competing HER [47], [190]. Therefore, combining Cu with Ag, a CO-producing metal, has shown promise in improving the C-C coupling efficiency [127]–[129], [132]–[138]. However, the synergistic effect between Cu and Ag on promoting C-C coupling is not limited to increasing CO availability, but is also highly dependent on the Cu-Ag hybrid composition and structure. The resulting discrepancies regarding the Cu-Ag interplay thus fall into three aspects: phase miscibility, electronic/structural interaction, and product preference. Although several previous studies on similar systems have proposed a variety of possible Cu-Ag interaction mechanisms, this work evidenced these hypotheses by *operando* X-ray measurements combined with computational simulations to make the argument more solid.

To get more insights into the Cu/Ag interaction, in this chapter, we prepared CuAg bimetallic catalysts with various compositions *via* magnetron sputtering. Their eCO2RR performance exhibited improved selectivity towards carbonyls (including aldehydes and carboxylates), especially acetaldehyde, upon introducing Ag into Cu. To better understand how the Cu/Ag interface tuned the selectivity under the actual reaction conditions, we did *operando* X-ray measurements at beamlines 2-1, 11-2, and 4-3 at the Stanford Synchrotron Radiation Lightsource (SSRL) at the SLAC National Accelerator Laboratory.

The main results are included in the submitted manuscript Paper I in the main text and the supporting information. I led the project with my supervisors (Prof. Brian Seger and Prof. Ib Chorkendorff), including writing the beamtime proposal, making plans for the whole project, designing and conducting electrochemical measurements and beamtime experiments, data processing and interpretation, as well as writing the first draft of the manuscript. Georg

Kastlunger (Asst. Prof. at CatTheory) carried out all DFT calculations with Andreas Lynge Vishart (PhD student at CatTheory). Ryan C. Davis (beamline scientist at BL 11-2) helped with XAS data processing. Carlos Andres Giron Rodriguez (PhD student at SurfCat) helped with benchmarking the *operando* EC cell and helped with most of the beamtimes with me. Wanyu Deng (visiting PhD student from Tianjin University) helped modify the H-type cell. Shaofeng Li (postdoc at SurfCat) helped with XAS data processing. Peter Benedek, Junjie Chen, Johanna Schröder, Joseph Perryman and Dong Un Lee (postdocs from the Jaramillo group at Stanford University) helped with setting up and carrying out beamtime experiments. All the above collaborators are listed as co-authors in the manuscript and contributed to revising the manuscript.

5.1 Catalyst Preparation and *Ex Situ* Characterizations

All catalysts were co-deposited on a silicon wafer by magnetron sputtering. More deposition details are described in Chapter 3.3.1. In such a way, not only a controllable composition is enabled, but these two thermodynamically immiscible metals can yield metastable miscibility, as has been proved by [133]. Meanwhile, it also ensures the presence of Cu/Ag interfaces, with a minimized influence of geometric and structural engineering and therefore enables focusing on the intrinsic performance of the CuAg system.

The near-surface Cu/Ag composition of each sputtered sample was examined by X-ray photoelectron spectroscopy (XPS). Figure 5.1 shows the *ex situ* high-resolution XPS spectra on the Cu 2p (Figure 5.1a) and Ag 3d (Figure 5.1b) orbitals of all as-prepared catalysts with various Ag concentrations. Two satellite peaks in Cu 2p orbital (Figure 5.1a) indicate the existence of Cu^{2+}, which is inevitable for *ex situ* XPS measurements considering that Cu is easily oxidized once exposed to air. The weaker peak intensity of Ag 3d scans (Figure 5.1b) after eCO2RR compared to their as-prepared counterparts appeared in all compositions suggests a less concentrated Ag surface composition after eCO2RR. Near-surface composition (5-10 nm) of all samples before and after eCO2RR are listed in Table A.1. It is worth pointing out that since Cu and Ag are both susceptible to oxygen in the air, information on the oxidation state and near-surface element composition obtained from *ex situ* XPS can only provide a preliminary evaluation, while *operando* X-ray measurements (*vide infra*) will be able to give better insight into the catalyst in its active state. Note that although the real Cu-Ag composition is slightly different than expected, the nominal composition was used in this paper for convenience and simplification.

Moreover, full-range XPS survey scans give an overview of the element distribution of the as-prepared and post-mortem catalysts, where no impurity elements are found in all cases

(Figure A.11). Ion scattering spectroscopy (ISS), with a higher surface sensitivity, further verifies the sample purity (Figure A.12).

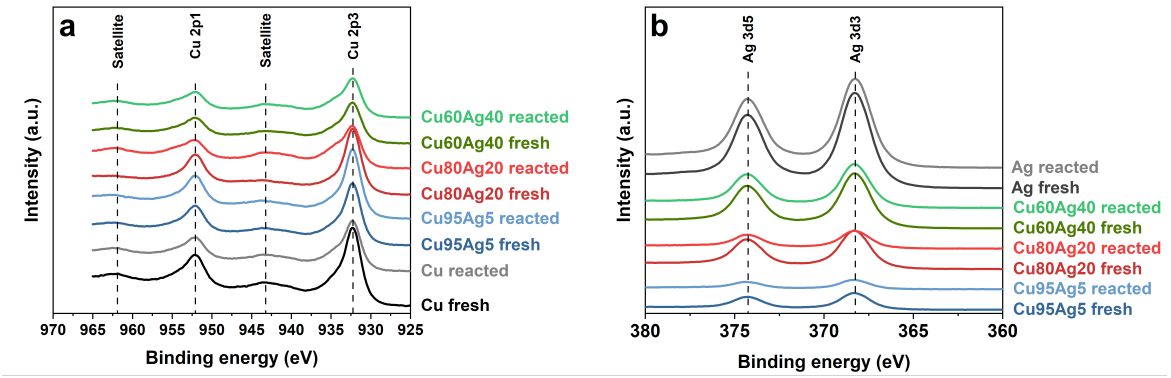

Figure 5.1 ***Ex situ high-resolution XPS element scan spectra*** *of samples with various Ag compositions: a) Cu 2p orbital and b) Ag 3d orbital.*

To inspect if Ag is incorporated into the Cu lattice and if so, what is the structural influence of Ag incorporation, we then collected *ex situ* grazing incident (GI)XRD patterns of the as-prepared samples (Figure 5.2). Both pure Cu and Ag samples agree well with the characteristic Cu and Ag peaks without noticeable position shifting. After Ag was introduced into the Cu, two broad peaks appeared at a 2θ of 35-45º, where peak A (blue area) and peak B (green area) most likely stem from the shifted and broadened Ag (111) and Cu (111) peaks, respectively. Peak shifting indicates lattice strain of the Cu and Ag phases induced by each other [191], [192]. Additionally, the reduced signal-to-charge ratio and broadened peaks may be attributed to the worse atomic arrangement and smaller crystallite size, respectively, as a result of inter-diffused Cu and Ag domains. Thus, the XRD results suggest the formation of multiphase alloys in the CuAg samples, where one is Cu-rich (with Ag being the minority), and the other is Ag-rich (with Cu being the minority). This conclusion is supported by the DFT-based convex hull, as shown in Figure A.22. No uniform phases of CuAg with fixed composition could be identified by theoretically sampling varying CuAg compositions and arrangements, suggesting a phase separation proficiency of the two elements. Nevertheless, since it is the Cu sites that produce multicarbon products, the Cu-rich phase is expected to be dominating. Therefore, our following analyses will mainly focus on the Cu-rich phase (however both phases will still be considered for H_2 and CO production as explained below).

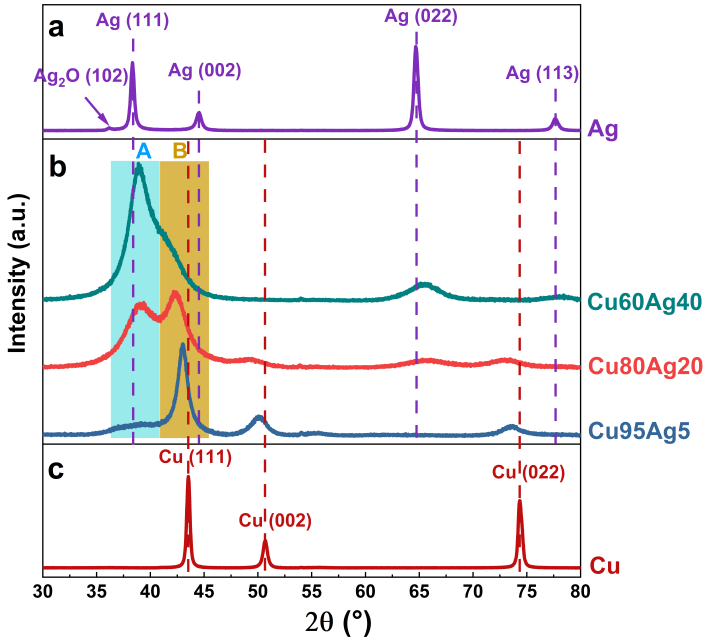

Figure 5.2 ***Ex situ XRD pattern*** *of a) Ag, b) Cu_xAg_{100-x}, and c) Cu. Dash lines indicate the peak position of each facet in the pure metal samples. Highlighted A and B areas indicate the Ag- and Cu-rich phase, respectively*

Furthermore, the absence of peaks related to oxidized Cu in the pure Cu sample indicates that the incident beam penetrated much deeper than the topmost sample layers. Although *ex situ* XRD measurements were conducted in a grazing incident geometry, the incident angle could only be as shallow as 0.7° beyond which the signal-to-noise ratio was insufficiently high for an accurate analysis.

5.2 Electrochemical CO_2 Reduction Performance

Figure 5.3a gives an overview of the distribution of all detected products for Cu, Ag and various Cu-Ag alloys as reflected by their faradaic efficiency (FE). (Selectivity regarding the produced number of moles of each detected product is plotted in Figure A.13). In contrast to Cu being able to produce a variety of products, Ag mainly produces CO, as well as a small amount of H_2 and formate under eCO2RR conditions. The slightly above 100% total FE may be due either to an experimental error in measuring or not using outlet flow rates from the reactor due to experimental difficulties. Either way, this slight offset is not expected to affect the trends and conclusions of this work.

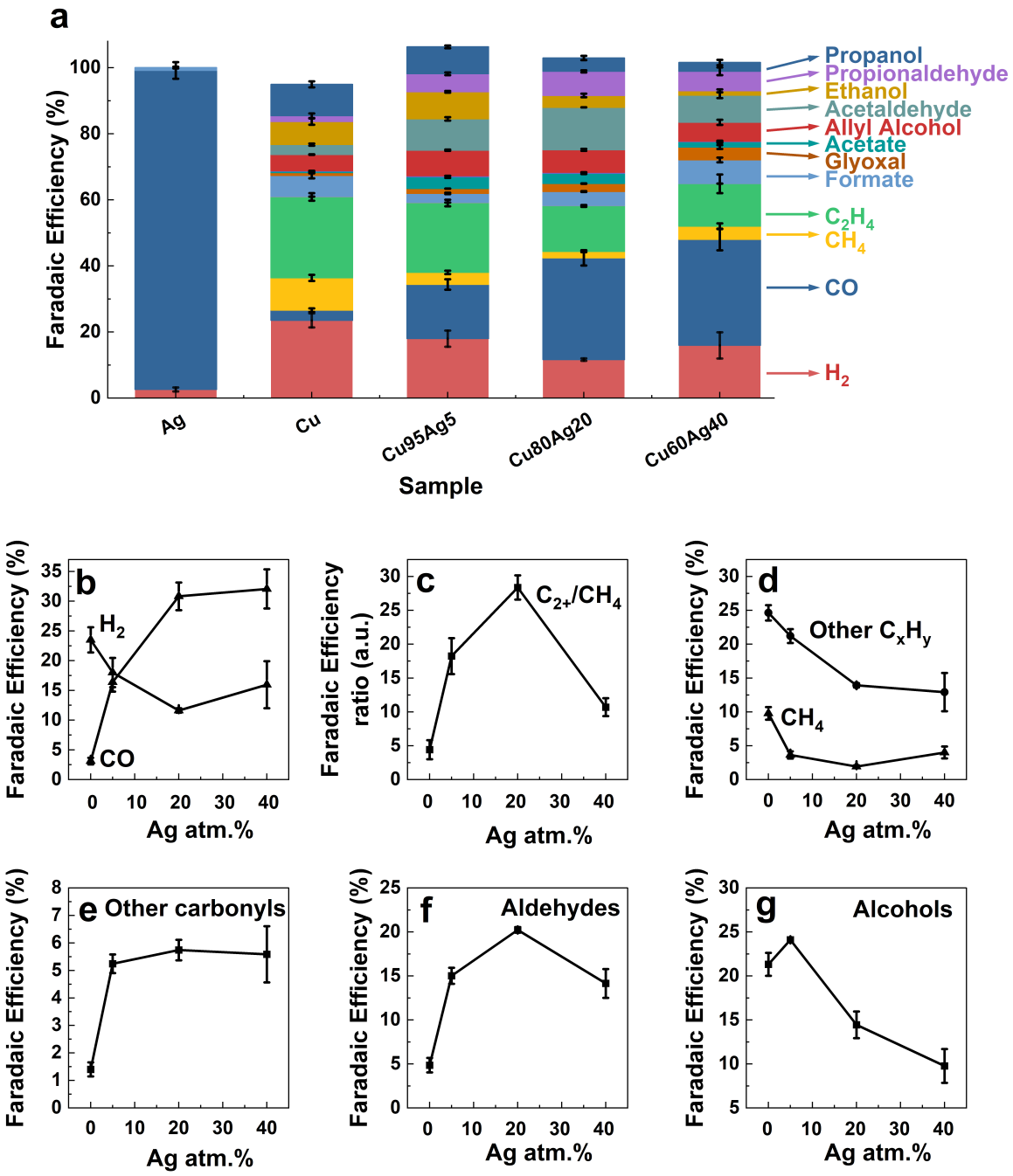

*Figure 5.3 Electroc**hemical CO_2 reduction performance test** conducted in an H-cell with CO_2-saturated 0.1 M $KHCO_3$ aqueous solution at -1 V vs. RHE for 2 hours. The electrolyte was continuously purged with CO_2 at 10 sccm during eCO2RR. a) Faradaic efficiency of all detected products. b) Faradaic efficiency of H_2 and CO as a function of Ag content, and c) Faradaic efficiency ratio between C_{2+} products and CH_4 (all are *CO-originated) as a function of Ag content. d) Faradaic efficiency of CH_4 and other hydrocarbons (CH_4, C_2H_4, C_2H_6, C_3H_6, and C_3H_8) as a function of Ag content. e)-g) Faradaic efficiencies of *CO-originated products containing C-O bond as a function of Ag content: e) other carbonyls (glyoxal, acetate, and hydroxy acetone; formate is not included), f) aldehydes (glycolaldehyde, acetaldehyde, and propionaldehyde), g) alcohols (ally alcohol, ethanol, and propanol).*

Figure 5.3a gives an overview of the distribution of all detected products for Cu, Ag and various Cu-Ag alloys as reflected by their Faradaic Efficiency (FE). (Selectivity regarding the produced number of moles of each detected product is plotted in Figure A.13) In contrast to Cu being able to produce a variety of products, Ag mainly produces CO, as well as a small amount of H_2 and formate under eCO2RR conditions. The slightly above 100% total FE may be due either to an experimental error in measuring or not using outlet flow rates from the reactor due to experimental difficulties. Either way, this slight offset is not expected to affect the trends and conclusions of this work.

Figure 5.3b shows a promoted CO while suppressed H_2 production, as the Ag concentration increased. This is as expected given that Cu is known to have a higher H_2 selectivity, whereas Ag has a strong selectivity towards CO. In CuAg alloys, CO produced on Ag can also create a high local CO partial pressure at the adjacent Cu sites [123], [127], [129], leading to a CO-enriched local environment, which facilitates the following C-C coupling and thus suppresses direct *CO hydrogenation to produce CH_4, as shown in Figure 5.4b and c. Previous DFT calculations also revealed weakened *H binding on the Cu surface as *CO coverage increases [190] with experimental results validating this [193]. Considering that Cu is located at the weak binding side of the volcano plot of H_2 evolution, a weaker *H binding energy will further suppress H_2 production [194]. This may be one reason for the hampered production of H_2 (Figure 5.3b) [83], [129].

Aldehydes and other carbonyls (excluding formate since it branches from CO and other *CO-originated products in an early stage [28]) both exhibit a selectivity peak with $Cu_{80}Ag_{20}$ (Figure 5.3e and f), accompanied by restrained alcohol (Figure 5.3g) and hydrocarbon (Figure 5.3d) production.

Introducing Ag would be expected to induce a local compressive strain of the Cu lattice, due to the larger atomic size of Ag (r ~ 172 pm) compared to Cu (r ~ 128 pm). This strain effect should shift the Cu valence band structure to deeper levels, which reduces the binding energy of intermediates [195], [196] as well as the oxophilicity (the tendency to form a chemical bond with oxygen atoms of intermediate molecules) of Cu, leading to weakened adsorption of carbonyl intermediates on the Cu surface [129], [197], [198]. Another theory that has been proposed to explain the reduced oxophilicity of Cu is that electron density shifts from Cu to Ag at the interface, driven by the difference in their electron chemical potential [124], [143]. The above electronic interaction would decrease the electron density of Cu [124], [144], [191], [198] at a negative potential [95], [139], [199]. As a result, aldehyde would desorb from the catalyst surface before being further reduced to alcohols [95], [129], [139].

To gain more insights into the effects of Ag on C-C coupling, Figure 5.3c looks at the branching point between C-C coupling to C_{2+} products versus protonation to the C_1 product CH_4. The promoted C_{2+}/CH_4 ratio primarily occurs by the suppressed CH_4 formation upon

alloying with Ag, as shown in Figure 5.4b. This can be a convolution of multiple reasons: i) modified adsorption strength of *CO versus *H as mentioned above (previous studies have found that the rate-limiting step for methane production is involved with *H [53]), ii) preferential Ag deposition on undercoordinated sites versus terraces, and iii) Ag tends to agglomerate into small islands due to its lower surface energy [200]. A prominent decline of the C_{2+}/CH_4 ratio occurs with alloys with Ag content greater than 20 atm.%. This could be attributed to that as Ag composition continuously increases, the excessive Ag atoms will cover too many Cu sites, leaving fewer Cu-Cu neighbors where *CO adsorption and C-C coupling happen. Considering that C-C coupling requires two adsorbed *CO in adjacent while CH_4 formation only requires one, a lower C_{2+}/CH_4 ratio is expected. This phenomenon has been observed by scanning electron microscope (SEM) on CuAg thin films under eCO2RR conditions, where the importance of an optimal *CO availability was emphasized for an efficient C-C coupling [143].

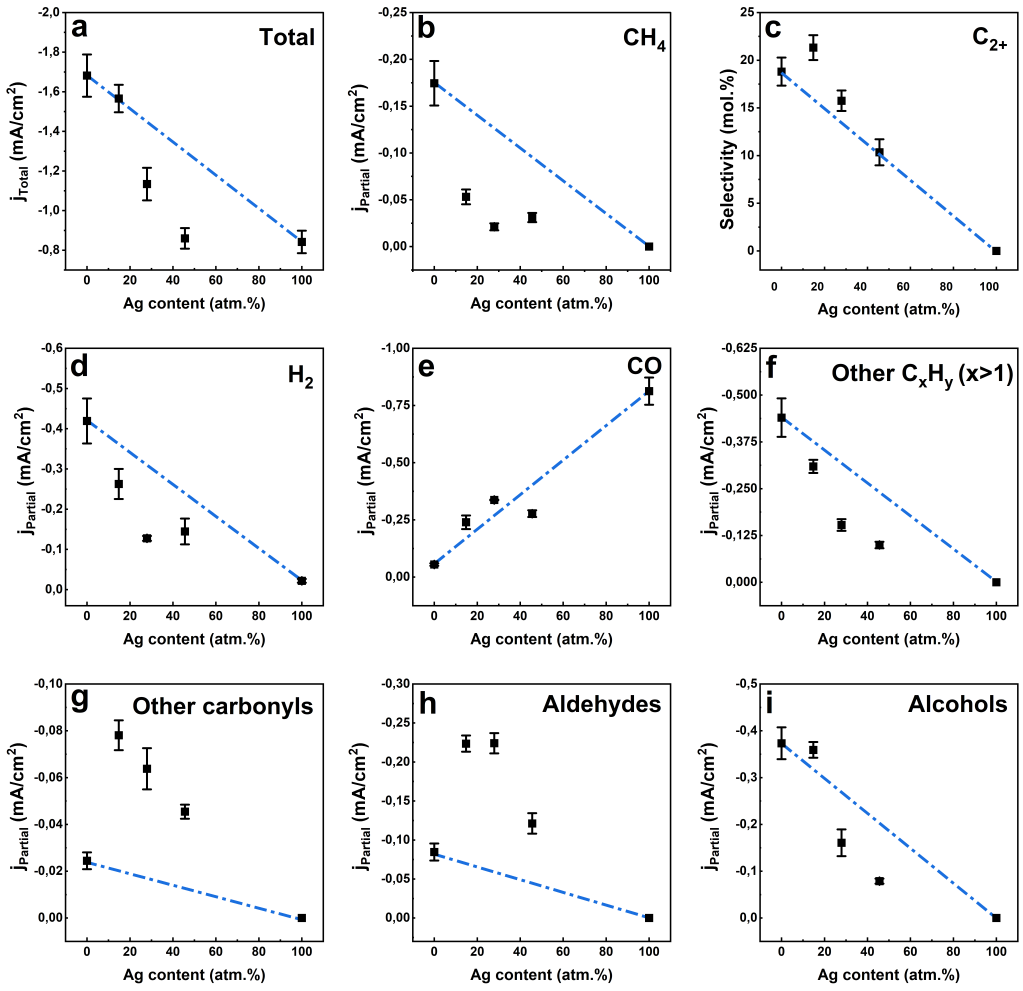

Figure 5.4 ***Current density as a function of Ag content.*** *a) Total current density. Partial current density of b) CH_4, c) C_{2+} products, d) H_2, e) CO, f) other C_xH_y excluding CH_4, g) other carbonyls excluding aldehydes, h) aldehydes, and i) alcohols.*

Current density (at a constant potential) as a function of the near-surface Ag composition (as measured *via* XPS) enables investigating the reaction kinetics influenced by Ag incorporation. This is plotted in Figure 5.4. The dashed lines are linear predictions by assuming that the Cu and Ag sites function separately without interaction between them. The lower total current density relative to the linear expectation shown in Figure 4a indicates a reduced overall activity upon Ag introduction. DFT calculations on the segregation energy of Ag on various Cu facets indicate the propensity of introduced Ag to distribute on the Cu under-coordinated sites compared to terraces (Figure A.21). Considering that literature has widely shown that under-coordinated sites are generally more active than terraces in polycrystalline Cu [28], [201]–[203], the overall activity is expected to be reduced. Moreover, previous studies have found that by occupying Cu undercoordinated sites with Ag, not only was *H binding energy weakened and thus suppressed HER (as explained in Figure 5.3b) [132], but the further reduction of acetaldehyde to ethanol would also be mitigated [135]. With Ag preferentially depositing on the undercoordinated sites, this effect can also influence the C_{2+} versus methane product ratio.

The good agreement of Figure 5.4 (partial current density) and Figure 5.3 (faradaic efficiency) of each product classification reveals a synergistic effect between Cu and the incorporated Ag on the facilitated aldehydes/other carbonyls production at an expense of H_2/C_xH_y formation.

From the above discussion with the assistance of *ex situ* X-ray measurements, the altered product preference could be a convolution of several effects created by introducing Ag in Cu, including spatial effects, compressive strain, oxophilicity variations, electronic interaction between Cu and Ag, *CO and *H adsorption, Ag incorporation site, *etc*. To deconvolute these possibilities, we then employed *operando* X-ray measurements to provide structural and electronic information on the Cu-Ag interaction in the course of eCO2RR. Considering that the most promising performance (*i.e.* the most promoted aldehydes/other carbonyls generation and facilitated C-C coupling) occurs on sample $Cu_{80}Ag_{20}$, this alloy was used in the following synchrotron measurements.

5.3 *Operando* Grazing Incident X-Ray Diffraction (GIXRD)

To monitor the crystal structure of the catalyst during eCO2RR, we conducted *operando* GIXRD with synchrotron facility at SSRL (beamline 2-1). Given that catalysis occurs at the surface, the surface sensitivity of the measurement geometry was analyzed with pure Cu initially. Since Cu is known to be easily oxidized when exposed to air, the top surface is expected to resemble an oxidized Cu (CuO_x). Figure 5.5a exhibits a prominent peak related to CuO at open circuit voltage (OCV), which is in stark contrast to its absence at -1 V *vs*.

RHE. Oxidized Cu being reduced to metallic Cu under eCO2RR conditions has been widely observed by SERS. [204], [204], [205] The poor signal-to-charge ratio is a consequence of the fast scan rate due to limited beamtime. Nevertheless, the disappearance of the prominent CuO (211) peak at negative potential further validated the surface sensitivity of the incident angle of 0.15º (this is much shallower than what was used in *ex situ* XRD since the *operando* X-ray beam source energy is higher), corresponding to *ca.* 2.8 nm of penetration depth (*ca.* 13.3 monolayers). The corresponding X-ray attenuation depth and penetrated monolayer numbers of each sample are listed in Table A.2.

The different peak position from that in *ex situ* XRD is induced by the applied X-ray source energy.

Table A.3. demonstrates peak matching between *ex situ* (8.04 keV) and *operando* (17 keV) GIXRD measurements.

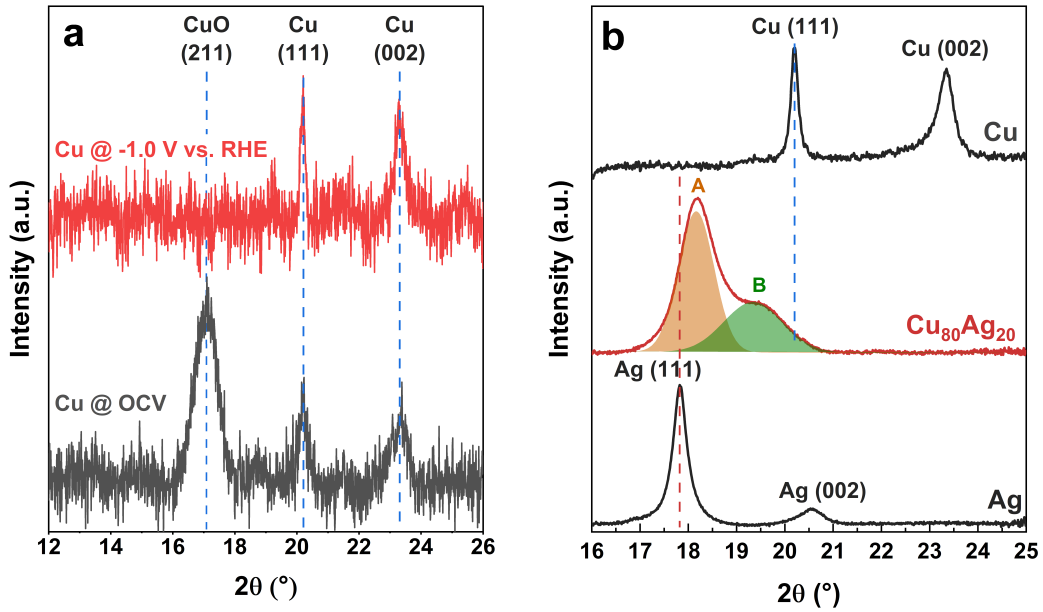

Figure 5.5 ***a) Operando GIXRD surface sensitivity verification on Cu at the incident angle of 0.15º.*** *The broad peak between 2θ 16-18º in the OCV scan (black) is assigned to the phase resulting from the mixture of CuO (0 0 2) and (1 1 -1), and its disappearance at -1.0 V vs. RHE (red) indicates the absence of oxidized Cu, which validates the surface sensitivity.* ***b) Operando GIXRD spectra of Ag (top), $Cu_{80}Ag_{20}$ (middle), and Cu (bottom), respectively.*** *Dashed lines indicate the peak position of corresponding facets in pure metal samples. Dashed lines indicate the corresponding peak position in the pure Cu and Ag samples. Highlighted areas A and B indicate the deconvoluted Ag- and Cu-rich phases in the $Cu_{80}Ag_{20}$ sample, respectively. The background of each spectrum was removed. Raw data before background removal are in Figure A.14.*

During *operando* measurements, a working electrode potential of -1 V *vs*. RHE was applied to the catalyst and kept for 1 hour, during which 6 consecutive scans (*ca.* 10 min for each scan) were collected and averaged to reduce the signal/noise ratio. Figure 5.5b shows the

same phenomenon regarding peak shift as seen *via ex situ* measurements (Figure 5.2). More details regarding *operando* GIXRD-related calculations on the samples can be found in Appendix 7.2.3.2.

5.4 *Operando* Grazing Incident X-Ray Absorption Spectroscopy (GIXAS)

An XAS spectrum is comprised of two regimes: the X-ray absorption near edge structure (XANES) region, which is located within *ca.* 100 eV around the absorption edge; and the extended X-ray absorption fine structure (EXAFS) region, which extends up to *ca.* 1000 eV after the absorption edge. The XANES spectra identify the oxidation state and local geometric structure of the absorber atom; while the EXAFS region contains information on the local chemical environment surrounding the central absorber atom, such as coordination number, atomic shell distance, *etc*. [206]

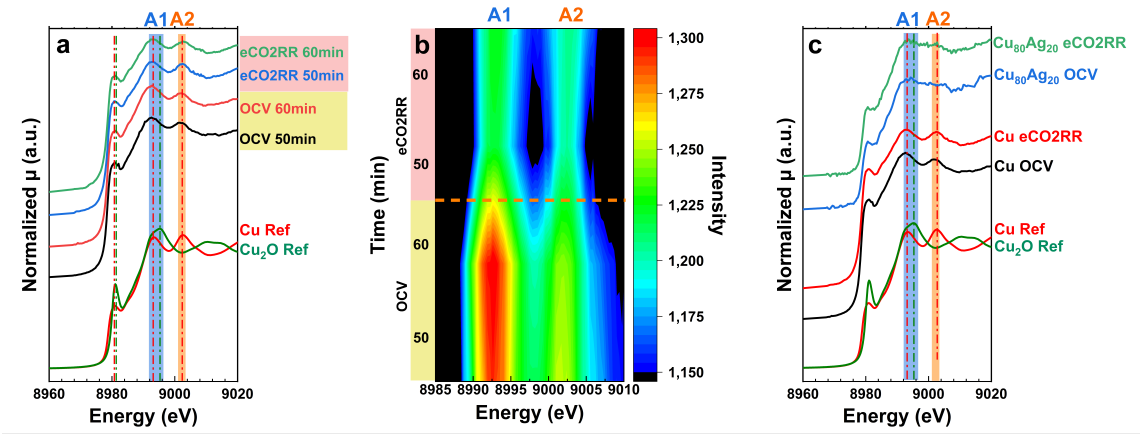

Figure 5.6 ***Operando XAS scans at the Cu K-edge.*** *a) XANES region of Cu and Cu_2O references (bottom), and the pure Cu sample at open circuit voltage (OCV) and -1 V vs. RHE (eCO2RR), respectively. The labels 50 min and 60 min mean the amount of time the samples had been exposed to the corresponding conditions. b) Heat map of the highlighted energy ranges A1 and A2 in a) within 8985-9010 eV. c) Comparison of Cu and $Cu_{80}Ag_{20}$ samples at OCV and COR conditions, respectively. Each spectrum was the average of two scans at 50 and 60 min exposure to the corresponding condition, respectively. Spectra of the Cu and Cu_2O references are plotted at the bottom. Each spectrum was subtracted by its pre-edge and post-edge background and normalized by peak intensity.*

Surface sensitivity of GIXAS was verified by comparing XANES spectra taken at different incident angles. To produce a reasonable signal-to-charge ratio, an incident angle of 0.25° corresponding to a penetration depth of *ca.* 2.9 nm (13.9 monolayers) was used for the following GIXAS measurements. Further details can be found in Table A.5 and Figure A.15. At the bottom of Figure 5.6a, both pure Cu and Cu_2O reference XANES spectra are shown. While the absorption edge (8980-8982 eV) has a subtle difference, there is a notable

difference in the energy range of 8990-9020 eV under open circuit voltage (OCV) and eCO2RR (-1 V *vs*. RHE) conditions: metallic Cu has one peak in the energy range of 8991-8997 eV (noted as A1) and one peak at *ca.* 9002 eV (noted as A2), with the same intensity; while Cu_2O only exhibits one peak in A1. Since XANES gives integral information of all detected Cu atoms regardless of oxidation state, a combination of metallic and oxidized Cu would have a higher intensity of A1 relative to A2, since both oxidation states contribute to the former while only metallic Cu contributes to the latter. Therefore, the more distorted intensity of A1 to A2 is, the more Cu_2O there is. This enables a qualitative indication of the transformation from Cu_2O to Cu at the surface.

The top four scans in Figure 5.6a show the pure Cu sample at OCV and subsequently exposed to eCO2RR conditions (@ -1.0 V *vs*. RHE). The spectra at OCV appear to be primarily metallic Cu, which is expected given that the penetration depth of 2.9 nm is a bit thicker than the native oxide layer, entailing a strong background Cu signal. However, a detailed look at the data showed there is a noticeable difference. To make the spectra difference more explicit, Figure 5.6b enlarges the energy range of 8985-9010 eV and transforms it into a heat map plot. It can be clearly seen that A1 has a higher intensity than A2 at OCV while both areas reached the same intensity under eCO2RR conditions.

Figure 5.6c compares pure Cu to the $Cu_{80}Ag_{20}$ sample, where an evident difference can be seen. The worse signal-to-noise ratio of the $Cu_{80}Ag_{20}$ spectra can be attributed to the lower Cu composition as well as smaller crystallite sizes and/or worse crystallinity, as also indicated by the XRD results (Figure 5.5). In contrast to pure Cu, where two separated peaks in A1 and A2 are present, only one wide wave in the energy range of 8985-9010 eV exists in the $Cu_{80}Ag_{20}$ spectra. Thus, these spectra appear to be more similar to the Cu_2O reference. This suggests a reduced electron density in the Cu phase upon introducing Ag, compared to the case of pure Cu. Furthermore, this reduced electron density would also suggest that less electron density variation would be seen when switching from open circuit voltage to eCO2RR conditions. As expected, a zoom-in of the $Cu_{80}Ag_{20}$ during the transition from OCV to eCO2RR similar to Figure 5.6b shows a much less noticeable variation in A1 relative to A2 in the corresponding energy range (Figure A.16). XANES spectra at the Ag L3-edge were also analyzed but did not show significant changes as Ag composition varies (Figure A.20). In order to build a concrete conclusion from these trends, DFT calculations were also employed later in this work.

To investigate how the electronic interaction contributes to the facilitated acetaldehyde and other carbonyl production, EXAFS measurements on the Cu-edge were Fourier-transformed to radial distance R (*i.e.*, R space) to inspect its local chemical environment. Figure A.17 gives a primary assignment of peak positions in the pure Cu sample compared with the metallic and Cu_2O references, where the interatomic distance information surrounding the

central atom (*i.e.*, Cu) is given as the R-value. Since atoms in the first shell predominantly contribute to the coordination environment of the central atom [128], [139], only R values below 3 Å are considered in this work. This is because 3 Å is normally the maximal bond length of the first shell and greater R numbers usually suggest atoms beyond the first shell or multiple scattering [207]. The peak at R ~2.25 Å is assigned to the first Cu-Cu shell (all R values in this work are phase uncorrected without further notice), while the peak located at *ca.* 1.6 Å is attributed to the first Cu-O shell, which agrees with the previous studies [95], [144].

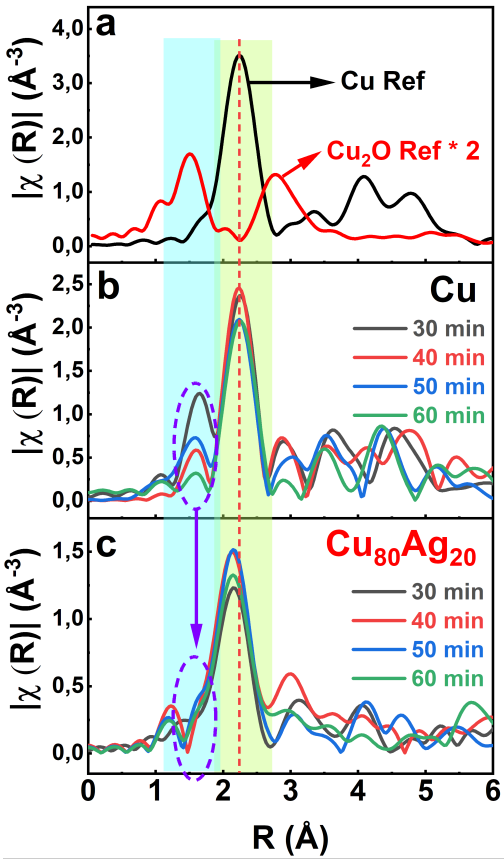

Figure 5.7 ***Fourier-transformed EXAFS R space spectra (k-2 weight) on the Cu K-edge*** *on a) Cu and Cu_2O references, b) pure Cu sample, and c) $Cu_{80}Ag_{20}$ sample as a function of time during eCO2RR. The dashed line indicated the Cu-Cu shell position in the Cu reference and pure Cu sample.*

Figure 5.7b and c depict R space starting after 30 minutes of testing (Cu-30 min) on Cu and $Cu_{80}Ag_{20}$, respectively. The observed peaks can be attributed to two main areas contributed by different atomic shells, as compared to Cu and Cu_2O references (Figure 5.7a). The peak centered at R ~ 1.5 Å is usually assigned to the Cu-O or Cu-C shell, which is normally attributed as the indication of CuO_x [139], [143]. However, our GIXRD (Figure 5.5) and XANES (Figure 5.6) results have pointed out that Cu was in its metallic state after the first 20 min. Additionally, considering that all intermediates produced during eCO2RR bind on

the Cu surface with either C or O atom(s), and that EXAFS only indicates the existence of an atom at a given distance while fails in atom identification, one potential explanation for peak B is the adsorption of intermediate species. Therefore, the greatly attenuated peak B upon Ag adsorption might suggest a suppressed intermediate adsorption upon Ag incorporation.

The peak centered at R ~ 2.25 Å is normally attributed to the first Cu-Cu (in pure Cu) or Cu-Ag shell (in Cu-Ag hybrids) [95], [143], [208]. Again, since EXFAS does not identify the neighboring atoms, both shells can contribute to this wide peak in the $Cu_{80}Ag_{20}$ sample. Specifically, the prominent peak at R ~ 2.10 Å in $Cu_{80}Ag_{20}$ gives the averaged information of the first shell coordinate information of all detected Cu atoms. It means that the peak reflects all possibilities in the closest neighbors of Cu atoms with a similar bond distance, including both Cu and Ag atoms. I initially assigned the peak only to the Cu-Cu distance without taking the Cu-Ag distance into account. The reason was that from the literature, the Cu-Ag distance is slightly larger than the Cu-Cu distance [95], [128], [139], since our peak shifted to a smaller number compared to the pure Cu sample, it cannot be induced by the longer Cu-Ag bond but because of the decreased Cu-Cu bond. Therefore, I speculated a compressively strained Cu-Cu upon Ag introduction from the spectra.

However, the above "Cu-Ag bond length is longer than that of the Cu-Cu bond" argument is from the literature, which is made based on well-defined structures (*e.g.*, very small clusters containing only a couple of atoms). This argument may not remain valid in our illy defined structure, as indicated by the broad *ex situ* (Figure 5.2) and *operando* GIXRD (Figure 5.5) spectra. In other words, in our CuAg multi-phase alloys, the peak centered at *ca.* 2.25 Å contains all possibilities surrounding Cu atoms, including compressive strained Cu-Cu and short Cu-Ag bond (due to the disordered structure) upon Ag introduction. Again, since EXAFS gives an averaged information of Cu atoms in the detection area, and considering the surface sensitivity (*ca.* 13 atomic monolayers, which is kind of the sensitivity limitation for our measurements as explained in Figure S4), the EXAFS results convolute the information from all the possibilities below: i) Cu-Cu right next to Ag in the Cu-rich phase, ii) Cu-Cu outreached the close neighbor of Ag in the Cu-rich phase, iii) Cu-Ag in the Cu-rich phase, iv) Cu-Cu right next to Ag in the Ag-rich phase, v) Cu-Cu outreach the closest neighbor of Ag in the Ag-rich phase, and vi) Cu-Ag in the Ag-rich phase. With such complicated and convoluted information, it is unfortunately difficult to draw any concrete conclusion on the strain effect of Ag introduction on the Cu-Cu bond solely from EXAFS. Although EXAFS does provide valuable information on small and/or well-defined structures such as single atoms [209]–[211] and nano-structures [143], [212], [213], based on the above analysis it does not seem to convey very explicit information on illy defined multiphase alloy structures.

EXAFS data fitting might help, but fitting itself involves too many modifiable (manipulatable) parameters, and with the data quality we have (due to very limited beamline) as well as the illy defined crystal structures, no reasonable fitting results could be obtained.

5.5 Computational Simulations

All DFT calculations are conducted by Georg Kastlunger and Andreas Lynge Vishart. Since I did not do it myself, I will only briefly summarize how simulations support our experimental observations. More details can be found in Appendix 7.2 and Paper I manuscript.

In order to verify the strength of the found charge transfer and strain effects and their influence on the binding of eCO2RR reaction intermediates, we performed DFT calculations on the CuAg system. Although our XRD results indicate the existence of two phases, one Cu-rich and the other Ag-rich (Figure 5.2 and Figure 5.5), considering that both the nominal and near-surface composition (

Table A.1 and Figure A.11) indicate the dominating composition of Cu in general, and that it is the Cu sites that are active for C_{2+} product formation, our simulation focused on the Cu-rich phase. Both the bulk and surface structures of Cu with varying Ag content (x_{Ag}) were screened, where for each x_{Ag} all symmetrically unique atomic arrangements were sampled and the most stable motifs were identified (see Methods section for further details). Note that only metallic Cu was considered in the simulations based on the experimentally observed disappearance of CuO_x under eCO2RR conditions.

The performed DFT calculations support the spectroscopic suggestions of an electron density shifting in the Cu phase upon Ag introduction compared to pure Cu. An increased electron density in Ag was found upon its introduction into both bulk (Figure A.24) three Cu facet models, including Cu (100), (111), and (211) (Figure 5.8). After Ag coverage was above 30%, the electron density increment in Ag reduced, as Ag atoms star to adjoin each other.

Our calculations indicate that introducing Ag into a Cu bulk crystal leads to an overall increase in the Cu-Cu distances (Figure A.25) as a consequence of the crystal lattice expanding linearly with the Ag content (Figure A.23), reflecting the GIXRD measurements (Figure 5.5b). In contrast, introducing Ag atoms on the Cu surface leads to a net compressive strain among surface Cu atoms, as shown in Figure 5.8d-f.

Simulations on the effect of Ag on eCO2RR adsorbate binding on the Cu-rich phase confirm that the binding of *CO on surface-Ag is strongly disfavored compared to Cu-sites.

Independent of the adsorbate and surface facet, adsorption strength is reduced upon introducing Ag, a consequence of a downshift in the d-band center (Figure A.26). Furthermore, the effect of introducing Ag is strongly enhanced on the (100) terrace (Figure A.28 a-b) compared to the (211) step sites (Figure A.28 c-d). Results reveal a weakened *CO binding upon increasing the number of in-plane neighboring Ag atoms. Additionally, introducing Ag atoms into Cu leads to a distancing of the Cu-atoms from Ag, while at the same time reducing the distance to the neighboring Cu-atoms. This compressive strain of the Cu lattice further reduces *CO binding strength.

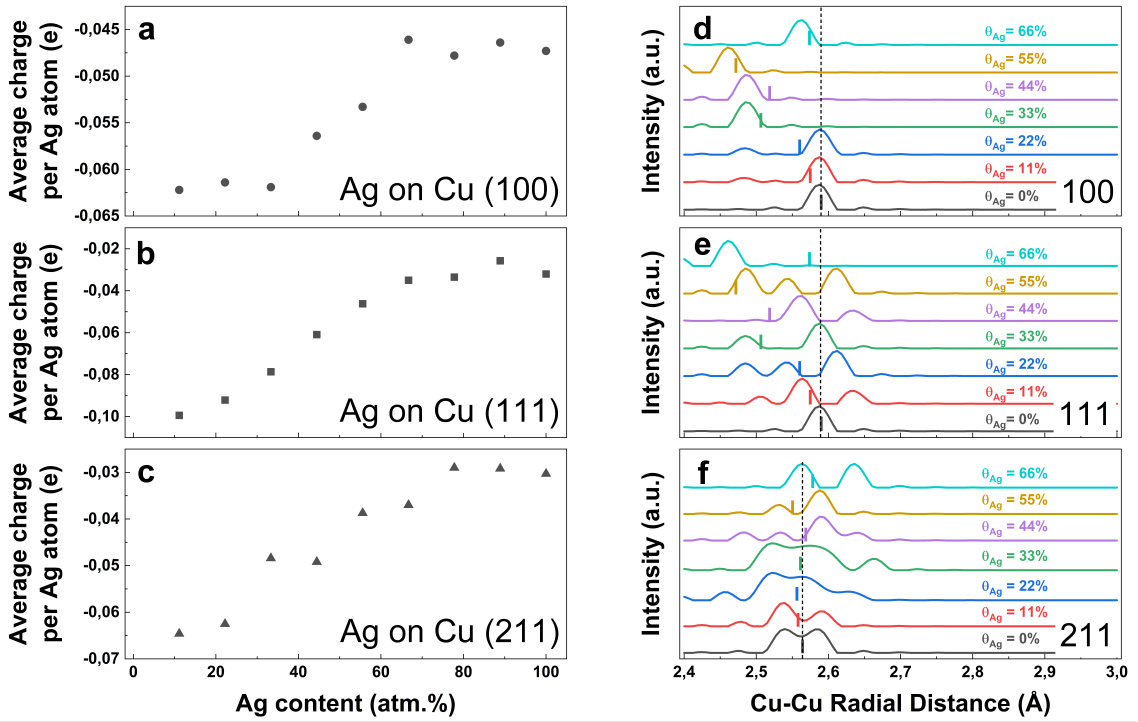

Figure 5.8 ***DFT calculated charge transfer and Cu-Cu distances on Cu_xAg_{100-x} surfaces****. a-c) Average partial charges per Ag atom in Cu_xAg_{100-x} when Ag atoms are introduced on Cu (100) (a), (111) (b), and (211) (c) facets, respectively. d-f) Cu-Cu radial distance distribution in Cu_xAg_{100-x} when Ag atoms are introduced to Cu (100) (d), Cu (111) (e), and Cu (211) (f), respectively. Averaged Cu-Cu bond length of each Ag content on each facet is indicated by a bar with the same color. Dashed lines represent the Cu-Cu bond length without Ag introduction.*

It is worth noting that we used *OH as a descriptor for the binning of the $*OCH_2CH_3$ intermediate because their binding energies scale linearly (Figure A.27). While *CO tends to adsorb in a top site, we identified the binding site of *OH as the fourfold-hollow site on the (100) facet (Figure A.28b) and in a bridge site on the (211) step (Figure A.28b). These binding motifs make *OH much more sensitive to strain effects compared to *CO. Considering that carbonyl products, especially aldehydes, bind on Cu with *O before desorbing or being further reduced, the large reduction in binding strength due to strain explains their promoted production.

5.6 Oxophilicity

It has been found that both a compressive strain and the slightly reduced electron density in the Cu sites, as demonstrated by XANES results, could shift the pristine Cu d-band center to a deeper level and hence weaken the intermediate adsorption [195]–[198], which coincides with the attenuated Cu-*C/*O shell (peak B) in EXAFS spectra on the Cu K-edge shown in Figure 5.7.

The compressive strain was also found to reduce the oxophilicity of transient metals [140], [214], [215] and thus weaken the adsorption of species binding on the metal surface with *O (*e.g.*, aldehydes and other carbonyls). It has been found that the oxophilicity of transition metal surfaces is highly correlated with their standard reduction/oxidation potential [129]. Therefore, cyclic voltammetry scans in the potential window between -0.2 to 0.7 V *vs*. RHE were performed to investigate the redox properties (Figure 5.9). As expected, an anodic shift of the Cu^{2+}/ Cu^{+} reduction wave is observed, confirming a reduced oxophilicity upon the introduction of Ag in Cu [129]. This is further evidence to help explain the promoted production of aldehydes and other carbonyls observed in Figure 5.3.

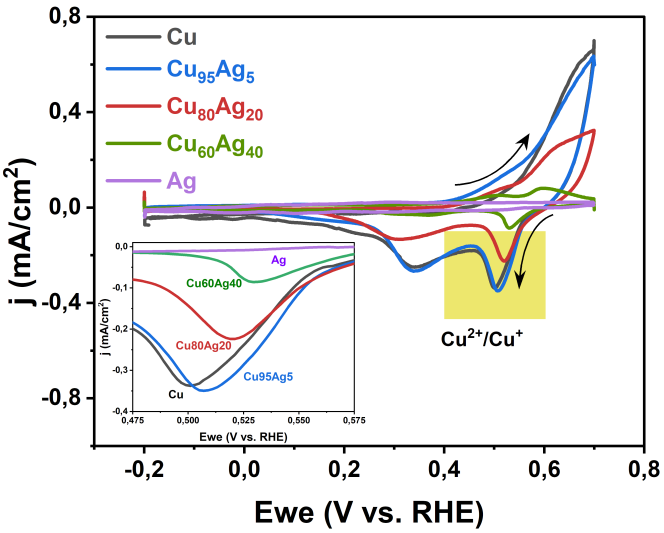

Figure 5.9 ***Cyclic voltammetry scans for determining oxophilicity of Cu from Ag incorporation*** *in CO_2-saturated 0.1 M $KHCO_3$ at the scan rate of 50 mV/s. Inset is the enlarged highlighted area of the Cu^{2+}/Cu^{+} wave.*

It is worth pointing out that for Cu catalysts, it is often the Cu^{2+}/Cu^{+} onset potential that is compared to evaluate the catalysts' oxophilicity. However, onset potential is convoluted with kinetic information and is thus not suitable for bimetallic catalysts. Specifically, onset potential is when sufficient faradaic current has been accumulated and detected. Thus, an earlier onset potential occurs not only due to a lower oxophilicity, but also with a higher surface Cu composition. In this regard, CV feature position is more straightforward.

5.7 Conclusions

- In this work, we prepared a series of CuAg multiphase alloys with varying Ag content for a better understanding of product selectivity resulting from electrochemical CO_2 reduction. *Ex situ* XRD confirmed the partially mixed phases composed of both Cu and Ag atoms. This confirms that magnetron sputtering enables a partially mixed phase composed of the thermodynamically immersible Cu and Ag.

- Among the alloys, $Cu_{80}Ag_{20}$ (nominal composition) exhibited the highest selectivity towards C-C coupling and carbonyl production, especially aldehydes.

- *Operando* GIXRD confirmed the spatial strain effect between Cu and Ag phases under eCO2RR conditions.

- The Cu K-edge XANES suggests a slight electron density decrease in the Cu phase upon Ag introduction, compared to pure Cu.

- EXAFS analysis is not suitable for analyzing non-well-defined atomic structures of alloys, mainly due to the uncertainties in atom identities contributing to ab atomic shell.

- DFT calculations demonstrated both the electronic interaction and strain effect of Cu upon Ag incorporation, which shifted the Cu d-band center to a deeper level and thus weakened intermediate adsorption.

- The oxophilicity of Cu was also reduced as a consequence of compressive strain.

Taking together, the facilitated generation of multicarbon aldehydes and carbonyls at the expense of hydrogen and hydrocarbon production can be attributed to a combined effect of a deeper d-band center and reduced oxophilicity as Ag is introduced. This work provides insights into the interaction between alloyed metals during electrochemical CO_2 reduction on an atomic scale, which can be used to direct new bi-/multi- metallic/alloy designs in this field.

Chapter 6 Conclusions and Perspectives

This thesis provides mechanistic information to facilitate the fundamental understanding of electrochemical CO_2 reduction reaction pathways on Cu and Cu-based catalysts. Since the conclusions of each chapter have been given earlier, this chapter will give a summarization of the key findings. Perspectives on future research of the fundamental understanding of eCO2RR will be given at the end.

6.1 Conclusions

The EC-MS setup enables real-time detection of both gaseous products during electrochemical $CO_{(2)}$ reduction on Cu. By employing selective ionization on the mass spectrometer, volatile liquid products ethanol and acetaldehyde are both successfully detected and can be differentiated with a characteristic m/z at M31 and M42, respectively. However, ionized H_2 molecules produced from the side reaction HER shift the M31 background via an ion-molecule reaction and therefore make it an unreliable descriptor for ethanol. The validation of M42 being the descriptor for acetaldehyde is confirmed. Electrochemical CO reduction on three low-index single crystal Cu facets, (100), (110), and (111), verified the facts-depending product preference spectrometrically, with methane and ethylene being most favored on (110) and (100), repetitively. Faradaic efficiency calculation on the EC-MS is challenging as a result of a combined impact from double-layer capacitance charge, mass transfer delay, and the side reaction ORR. Moreover, acetaldehyde chemistry under eCORR conditions is dominated by its oxidation to acetate, which is also a facet-sensitive process.

In addition to surface structure, the production of multicarbon products with high energy intensity requires sufficient CO availability. Given the low solubility of CO in aqueous solutions, a CO-favored co-catalyst Ag is alloyed with CO to promote the local CO concentration. Electrochemical CO2 reduction on the CuAg alloys exhibited an improved selectivity towards aldehydes, at the expense of hydrogen and hydrocarbons. With the

assistance of operando X-ray measurements and computational simulations, the improvement is attributed to a reduced electron density and compressive strain on Cu upon alloying with Ag.

Results presented in this thesis provide insightful information for a better understanding of eCO2RR mechanisms, and for the guidance of new catalyst design with a desired facet or surface/alloy structure to regulate the product proficiency towards target products.

6.2 Perspectives

Despite significant progress and development that have been made in the mechanistic understanding of electrochemical CO_2 reduction pathways in recent years, further improvements are still required for understanding the reaction mechanism and thus regulating the selectivity towards specific species.

Single crystal Cu catalysts provide a model platform for correlating the experimental structure and ideal surfaces employed in computational simulation. Based on the knowledge on the facet-dependent product distribution/preference, nanostructures rich in desired facets can be designed and fabricated accordingly to tune the selectivity towards the target product(s). Additionally, studies investigating Cu single crystals should inspect the crystal structure quality frequently. It can be carried out by checking cyclic voltametric features in the fingerprint region, or more straightforwardly by microscopies, such as atomic force microscopy (AFM), scanning tunneling microscopy (STM), scanning transmission electron microscopy (STEM), *etc.*

Not limited to single crystals, Cu and Cu-based catalyst structures are known to be dynamic and their alternation during the reaction can be reversible and therefore hard to be captured once it is removed from the reaction environment, hence *in situ/operando* characterizations are preferred. However, operating *in situ/operando* measurements and data collection can be challenging due to the small footprint of the detection area, and thus hard to represent the entire catalyst surface. Time resolution is also important in capturing transient changes, alternations, transformations, *etc.* Challenges also exist in improving the measurement resolution/signal-to-noise ratio since the signal can be interfered by operational conditions, such as electrolyte flow, bubble formation, catalyst structure (*e.g.*, grazing incident X-ray measurements require flat catalyst surface), low active site concentration, *etc.* X-ray beams, in particular, often possess high energy and therefore might possibly change or even damage the radiated surface. Moreover, each technique has limitations and therefore combining multiple techniques is expected to provide more comprehensive information. A good example is coupling XRD and XAS in scrutinizing nanostructures, where XRD provides

information on the crystallinity on a long-range scale while XAS focuses on the local coordination environment as well as the oxidation state. In addition to catalyst structure, the detection of reaction intermediate adsorption/desorption and identification of active sites also conveys valuable knowledge on the reaction pathways and therefore help direct the modification and design of catalyst and reaction conditions. Computational simulations also offer valuable insights in this regard, while it is often difficult for them to take the actual reaction conditions as well as catalysts' dynamic structural alternation into account. Thus, multiple iterations between *in situ/operando* measurements and simulations may be expected in order for a more precise and comprehensive understanding of the catalyst structure-performance correlation.

Aside from monitoring intermediates, real-time product detection combined with isotope labeling in the EC-MS system would greatly benefit investigating eCO2RR product formation pathways. Yet, using MS should pay attention to possible background shift due to system configuration, such as the chemical ionization impact discussed in Chapter 5.

Fundamental understanding on the eCO2RR mechanism is complicated and challenging, but assisted the advanced experimental techniques and couple with computational simulations, deconvolution of the intricate mechanism networks can be expected. The obtained knowledge will facilitate catalyst and setup design for promoting the selectivity and productivity of product(s) of interest.

Bibliography

[1] G. Brooks, *Healthy Development*. The World Bank, 2007.

[2] UN, "Population Division World Population Prospects 2022," *Population Division World Population Prospects 2022*, 2022. www.un.org/development/ desa/pd/.

[3] BP, "Statistical Review of World Energy 2022,(71st edition)," 2022. [Online]. Available: https://www.bp.com/content/dam/bp/business-sites/en/global/corporate/pdfs/energy-economics/statistical-review/bp-stats-review-2022-full-report.pdf.

[4] United Nations Development Programme, "Human Development Index (HDI)," *Human Development Reports*, 2023. https://hdr.undp.org/data-center/human-development-index#/indicies/HDI (accessed Mar. 20, 2023).

[5] I. A. WGI, *Climate Change 2021 The Physical Science Basis WGI*, vol. 34, no. 2. 2021.

[6] V. P. Wright, "World Energy Outlook 2022," 2022.

[7] H. Ritchie, M. Roser, and P. Rosado, "Energy," *Our World Data*, 2022, [Online]. Available: https://ourworldindata.org/energy.

[8] visualizingEnergy, "The Human Development Index (HDI) and energy use per capita, 1990-2019," 2022. https://visualizingenergy.org/does-more-energy-use-increase-the-level-of-human-development/.

[9] D. A. Vallero, *Air Pollution Calculations*. Elsevier, 2019.

[10] IEA, "Net Zero by 2050: A Roadmap for the Global Energy Sector," *Int. Energy Agency*, p. 224, 2021, [Online]. Available: https://www.iea.org/reports/net-zero-by-2050.

[11] World Health Organization, "Climate change and health," 2021. https://www.who.int/news-room/fact-sheets/detail/climate-change-and-health.

[12] U. N. T. Collection, *Paris Agreement (adopted 12 Dec. 2015, entered into force 4 Nov. 2016)*, no. 54113. 2015.

[13] J. S. Masson-Delmotte, V., P. Zhai, H.-O. Pörtner, D. Roberts, E. L. P.R. Shukla, A. Pirani, W. Moufouma-Okia, C. Péan, R. Pidcock, S. Connors, J.B.R. Matthews, Y. Chen, X. Zhou, M.I. Gomis, and and T. W. (eds. . T. Maycock, M. Tignor, "Summary for Policymakers," in *Global Warming of 1.5°C*, Cambridge University Press, 2022, pp. 1–24.

[14] IPCC, *Climate Change 2022, Mitigation of Climate Change Summary for Policymakers (SPM)*, no. 1. 2022.

[15] H. Ritchie, M. Roser, and P. Rosado, "CO_2 and Greenhouse Gas Emissions," *Our World Data*, 2020, [Online]. Available: https://ourworldindata.org/co2-and-greenhouse-gas-emissions.

[16] GISTEMP Team, "Surface temperature_NASA," *NASA Goddard Institute for Space Studies*, 2023. https://data.giss.nasa.gov/gistemp/ (accessed Mar. 20, 2023).

[17] Å. Killingtveit, *Hydropower*. 2018.

[18] C. S. Kaunda, C. Z. Kimambo, and T. K. Nielsen, "Hydropower in the Context of Sustainable Energy Supply: A Review of Technologies and Challenges," *ISRN Renew. Energy*, vol. 2012, pp. 1–15, 2012, doi: 10.5402/2012/730631.

[19] S. Suman, "Hybrid nuclear-renewable energy systems: A review," *J. Clean. Prod.*, vol. 181, pp. 166–177, 2018, doi: 10.1016/j.jclepro.2018.01.262.

[20] Energi Data Service, "Electricity Balance Non-Validated," 2023. https://demanda.ree.es/visionaBal/VisionaIbiFor.html%7B#%7D (accessed Mar. 20, 2023).

[21] S. Ruangpattana, D. Klabjan, J. Arinez, and S. Biller, "Optimization of on-site renewable energy generation for industrial sites," *2011 IEEE/PES Power Syst. Conf. Expo. PSCE 2011*, pp. 1–8, 2011, doi: 10.1109/PSCE.2011.5772448.

[22] K. P. Kuhl, T. Hatsukade, E. R. Cave, D. N. Abram, J. Kibsgaard, and T. F. Jaramillo, "Electrocatalytic conversion of carbon dioxide to methane and methanol on transition metal surfaces," *J. Am. Chem. Soc.*, vol. 136, no. 40, pp. 14107–14113, 2014, doi: 10.1021/ja505791r.

[23] V. Dieterich, A. Buttler, A. Hanel, H. Spliethoff, and S. Fendt, "Power-to-liquid via synthesis of methanol, DME or Fischer–Tropsch-fuels: a review," *Energy Environ. Sci.*, vol. 13, no. 10, pp. 3207–3252, 2020, doi: 10.1039/d0ee01187h.

[24] O. S. Bushuyev *et al.*, "What Should We Make with CO2 and How Can We Make It?," *Joule*, vol. 2, no. 5. Elsevier Inc., pp. 825–832, 2018, doi: 10.1016/j.joule.2017.09.003.

[25] J. H. Montoya, A. A. Peterson, and J. K. Nørskov, "Insights into C-C Coupling in CO2 Electroreduction on Copper Electrodes," *ChemCatChem*, vol. 5, no. 3, pp. 737–742, 2013, doi: 10.1002/cctc.201200564.

[26] Y. Hori, H. Wakebe, T. Tsukamoto, and O. Koga, "Electrocatalytic process of CO selectivity in electrochemical reduction of CO2 at metal electrodes in aqueous media," *Electrochim. Acta*, vol. 39, no. 11–12, pp. 1833–1839, 1994, doi: 10.1016/0013-4686(94)85172-7.

[27] A. Bagger, W. Ju, A. S. Varela, P. Strasser, and J. Rossmeisl, "Electrochemical CO2 Reduction: A Classification Problem," *ChemPhysChem*, vol. 18, no. 22, pp. 3266–3273, 2017, doi: 10.1002/cphc.201700736.

[28] S. Nitopi *et al.*, "Progress and Perspectives of Electrochemical CO2 Reduction on Copper in Aqueous Electrolyte," *Chem. Rev.*, vol. 119, no. 12, pp. 7610–7672, Jun. 2019, doi: 10.1021/acs.chemrev.8b00705.

[29] F. Chang *et al.*, *Copper-Based Catalysts for Electrochemical Carbon Dioxide Reduction to Multicarbon Products*, vol. 5, no. 3. Springer Nature Singapore, 2022.

[30] D. Karapinar, C. E. Creissen, J. G. Rivera De La Cruz, M. W. Schreiber, and M. Fontecave, "Electrochemical CO2 Reduction to Ethanol with Copper-Based Catalysts," *ACS Energy Lett.*, vol. 6, no. 2, pp. 694–706, 2021, doi: 10.1021/acsenergylett.0c02610.

[31] K. P. Kuhl, E. R. Cave, D. N. Abram, and T. F. Jaramillo, "New insights into the electrochemical reduction of carbon dioxide on metallic copper surfaces," *Energy Environ. Sci.*, vol. 5, no. 5, pp. 7050–7059, 2012, doi: 10.1039/c2ee21234j.

[32] H. Jia *et al.*, "Symmetry-Broken Au–Cu Heterostructures and their Tandem Catalysis Process in Electrochemical CO2 Reduction," *Adv. Funct. Mater.*, vol. 2101255, pp. 1–11, 2021, doi: 10.1002/adfm.202101255.

[33] H. Du *et al.*, "Recent progress in electrochemical reduction of carbon monoxide toward multi-carbon products," *Mater. Today*, vol. 59, no. October, pp. 182–199, 2022, doi: 10.1016/j.mattod.2022.08.012.

[34] Y. Zhang, S. X. Guo, X. Zhang, A. M. Bond, and J. Zhang, "Mechanistic understanding of the electrocatalytic CO2 reduction reaction – New developments based on advanced instrumental techniques," *Nano Today*, vol. 31, p. 100835, 2020, doi: 10.1016/j.nantod.2019.100835.

[35] T. K. Todorova, M. W. Schreiber, and M. Fontecave, "Mechanistic Understanding of CO2 Reduction Reaction (CO2RR) Toward Multicarbon Products by Heterogeneous Copper-Based Catalysts," *ACS Catal.*, vol. 10, no. 3, pp. 1754–1768, 2020, doi: 10.1021/acscatal.9b04746.

[36] A. O. Elnabawy, J. Schumann, P. Bothra, A. Cao, and J. K. Nørskov, "The Challenge of CO Hydrogenation to Methanol: Fundamental Limitations Imposed by Linear Scaling Relations," *Top. Catal.*, vol. 63, no. 7–8, pp. 635–648, 2020, doi: 10.1007/s11244-020-01283-2.

[37] Y. Li and Q. Sun, "Recent Advances in Breaking Scaling Relations for Effective Electrochemical Conversion of CO2," *Adv. Energy Mater.*, vol. 6, no. 17, pp. 1–19, 2016, doi: 10.1002/aenm.201600463.

[38] R. P. Jansonius, L. M. Reid, C. N. Virca, and C. P. Berlinguette, "Strain engineering electrocatalysts for selective CO2 reduction," *ACS Energy Lett.*, vol. 4, no. 4, pp. 980–986, 2019, doi: 10.1021/acsenergylett.9b00191.

[39] E. L. Clark *et al.*, "Standards and Protocols for Data Acquisition and Reporting for Studies of the Electrochemical Reduction of Carbon Dioxide," *ACS Catal.*, vol. 8, no. 7, pp. 6560–6570, 2018, doi: 10.1021/acscatal.8b01340.

[40] Y. Y. Birdja, E. Pérez-Gallent, M. C. Figueiredo, A. J. Göttle, F. Calle-Vallejo, and M. T. M. Koper, "Advances and challenges in understanding the electrocatalytic conversion of carbon dioxide to fuels," *Nat. Energy*, vol. 4, no. 9, pp. 732–745, Sep. 2019, doi: 10.1038/s41560-019-0450-y.

[41] X. Liu, J. Xiao, H. Peng, X. Hong, K. Chan, and J. K. Nørskov, "Understanding trends in electrochemical carbon dioxide reduction rates," *Nat. Commun.*, vol. 8, no. May, pp. 1–7, 2017, doi: 10.1038/ncomms15438.

[42] T. Zhao *et al.*, "Substrate engineering for wafer-scale two-dimensional material growth: strategies, mechanisms, and perspectives," *Chem. Soc. Rev.*, vol. 46, no. 15, pp. 1–20, 2023, doi: 10.1039/D2CS00657J.

[43] G. Kastlunger *et al.*, "Using pH Dependence to Understand Mechanisms in Electrochemical CO Reduction," *ACS Catal.*, vol. 12, no. 8, pp. 4344–4357, Apr. 2022, doi: 10.1021/acscatal.1c05520.

[44] Y. Hori, R. Takahashi, Y. Yoshinami, and A. Murata, "Electrochemical reduction of CO at a copper electrode," *J. Phys. Chem. B*, vol. 101, no. 36, pp. 7075–7081, 1997, doi: 10.1021/jp970284i.

[45] Y. Hori, A. Murata, and R. Takahashi, "Formation of hydrocarbons in the electrochemical reduction of carbon dioxide at a copper electrode in aqueous solution," *J. Chem. Soc. Faraday Trans. 1 Phys. Chem. Condens. Phases*, vol. 85, no. 8, pp. 2309–2326, 1989, doi: 10.1039/F19898502309.

[46] L. Wang *et al.*, "Electrochemical Carbon Monoxide Reduction on Polycrystalline Copper: Effects of Potential, Pressure, and pH on Selectivity toward Multicarbon and Oxygenated Products," *ACS Catal.*, vol. 8, no. 8, pp. 7445–7454, 2018, doi: 10.1021/acscatal.8b01200.

[47] K. J. P. Schouten, Y. Kwon, C. J. M. Van Der Ham, Z. Qin, and M. T. M. Koper, "A new mechanism for the selectivity to C1 and C2 species in the electrochemical reduction of carbon dioxide on copper electrodes," *Chem. Sci.*, vol. 2, no. 10, pp. 1902–1909, 2011, doi: 10.1039/c1sc00277e.

[48] D. W. DeWulf, T. Jin, and A. J. Bard, "Electrochemical and Surface Studies of Carbon Dioxide Reduction to Methane and Ethylene at Copper Electrodes in Aqueous Solutions," *J. Electrochem. Soc.*, vol. 136, no. 6, pp. 1686–1691, 1989, doi: 10.1149/1.2096993.

[49] E. Bertheussen, T. V. Hogg, Y. Abghoui, A. K. Engstfeld, I. Chorkendorff, and I. E. L. Stephens, "Electroreduction of CO on Polycrystalline Copper at Low Overpotentials," *ACS Energy Lett.*, vol. 3, no. 3, pp. 634–640, 2018, doi: 10.1021/acsenergylett.8b00092.

[50] X. Liu *et al.*, "pH effects on the electrochemical reduction of CO(2) towards C2 products on stepped copper," *Nat. Commun.*, vol. 10, no. 1, pp. 1–10, Dec. 2019, doi: 10.1038/s41467-018-07970-9.

[51] J. T. Feaster *et al.*, "Understanding Selectivity for the Electrochemical Reduction of Carbon Dioxide to Formic Acid and Carbon Monoxide on Metal Electrodes," *ACS Catal.*, vol. 7, no. 7, pp. 4822–4827, 2017, doi: 10.1021/acscatal.7b00687.

[52] D. Cheng *et al.*, "The nature of active sites for carbon dioxide electroreduction over oxide-derived copper catalysts," *Nat. Commun.*, vol. 12, no. 1, pp. 1–8, 2021, doi: 10.1038/s41467-020-20615-0.

[53] H. J. Peng, M. T. Tang, J. Halldin Stenlid, X. Liu, and F. Abild-Pedersen, "Trends in oxygenate/hydrocarbon selectivity for electrochemical CO(2) reduction to C2 products," *Nat. Commun.*, vol. 13, no. 1, pp. 1–11, 2022, doi: 10.1038/s41467-022-29140-8.

[54] M. B. Ross *et al.*, "Tunable Cu Enrichment Enables Designer Syngas Electrosynthesis from CO2," *J. Am. Chem. Soc.*, vol. 139, no. 27, pp. 9359–9363, 2017, doi: 10.1021/jacs.7b04892.

[55] C. M. Gunathunge, V. J. Ovalle, Y. Li, M. J. Janik, and M. M. Waegele, "Existence of an Electrochemically Inert CO Population on Cu Electrodes in Alkaline pH," *ACS*

Catal., vol. 8, no. 8, pp. 7507–7516, 2018, doi: 10.1021/acscatal.8b01552.

[56] S. Wang, T. Kou, S. E. Baker, E. B. Duoss, and Y. Li, "Electrochemical Reduction of CO2 to Alcohols: Current Understanding, Progress, and Challenges," *Adv. Energy Sustain. Res.*, vol. 3, no. 1, p. 2100131, 2022, doi: 10.1002/aesr.202100131.

[57] K. W. Frese, *Electrochemical and Electrocatalytic Reactions of Carbon Dioxide*. Elsevier, 2012, 1993.

[58] Y. Hori, H. Wakebe, T. Tsukamoto, and O. Koga, "Adsorption of CO accompanied with simultaneous charge transfer on copper single crystal electrodes related with electrochemical reduction of CO2 to hydrocarbons," *Surf. Sci.*, vol. 335, no. C, pp. 258–263, 1995, doi: 10.1016/0039-6028(95)00441-6.

[59] K. J. P. Schouten, Z. Qin, E. P. Gallent, and M. T. M. Koper, "Two pathways for the formation of ethylene in CO reduction on single-crystal copper electrodes," *J. Am. Chem. Soc.*, vol. 134, no. 24, pp. 9864–9867, 2012, doi: 10.1021/ja302668n.

[60] K. J. P. Schouten, E. Pérez Gallent, and M. T. M. Koper, "The influence of pH on the reduction of CO and CO2 to hydrocarbons on copper electrodes," *J. Electroanal. Chem.*, vol. 716, pp. 53–57, Mar. 2014, doi: 10.1016/j.jelechem.2013.08.033.

[61] Y. Huang, A. D. Handoko, P. Hirunsit, and B. S. Yeo, "Electrochemical Reduction of CO2 Using Copper Single-Crystal Surfaces: Effects of CO∗ Coverage on the Selective Formation of Ethylene," *ACS Catal.*, vol. 7, no. 3, pp. 1749–1756, 2017, doi: 10.1021/acscatal.6b03147.

[62] F. S. Roberts, K. P. Kuhl, and A. Nilsson, "High selectivity for ethylene from carbon dioxide reduction over copper nanocube electrocatalysts," *Angew. Chemie - Int. Ed.*, vol. 54, no. 17, pp. 5179–5182, 2015, doi: 10.1002/anie.201412214.

[63] N. T. Suen *et al.*, "Morphology Manipulation of Copper Nanocrystals and Product Selectivity in the Electrocatalytic Reduction of Carbon Dioxide," *ACS Catal.*, vol. 9, no. 6, pp. 5217–5222, 2019, doi: 10.1021/acscatal.9b00790.

[64] G. L. De Gregorio, T. Burdyny, A. Loiudice, P. Iyengar, W. A. Smith, and R. Buonsanti, "Facet-Dependent Selectivity of Cu Catalysts in Electrochemical CO2 Reduction at Commercially Viable Current Densities," *ACS Catal.*, vol. 10, no. 9, pp. 4854–4862, 2020, doi: 10.1021/acscatal.0c00297.

[65] A. J. Garza, A. T. Bell, and M. Head-Gordon, "Mechanism of CO2 Reduction at Copper Surfaces: Pathways to C2 Products," *ACS Catal.*, vol. 8, no. 2, pp. 1490–1499, 2018, doi: 10.1021/acscatal.7b03477.

[66] W. J. Durand, A. A. Peterson, F. Studt, F. Abild-Pedersen, and J. K. Nørskov, "Structure effects on the energetics of the electrochemical reduction of CO2 by copper surfaces," *Surf. Sci.*, vol. 605, no. 15–16, pp. 1354–1359, 2011, doi: 10.1016/j.susc.2011.04.028.

[67] A. Bagger, L. Arnarson, M. H. Hansen, E. Spohr, and J. Rossmeisl, "Electrochemical CO Reduction: A Property of the Electrochemical Interface," *J. Am. Chem. Soc.*, vol. 141, no. 4, pp. 1506–1514, 2019, doi: 10.1021/jacs.8b08839.

[68] K. J. P. Schouten, E. Pérez Gallent, and M. T. M. Koper, "Structure sensitivity of the electrochemical reduction of carbon monoxide on copper single crystals," *ACS Catal.*, vol. 3, no. 6, pp. 1292–1295, 2013, doi: 10.1021/cs4002404.

[69] X. Nie, W. Luo, M. J. Janik, and A. Asthagiri, "Reaction mechanisms of CO2 electrochemical reduction on Cu(1 1 1) determined with density functional theory," *J. Catal.*, vol. 312, pp. 108–122, 2014, doi: 10.1016/j.jcat.2014.01.013.

[70] F. Calle-Vallejo and M. T. M. Koper, "Theoretical considerations on the electroreduction of CO to C2 Species on Cu(100) electrodes," *Angew. Chemie - Int. Ed.*, vol. 52, no. 28, pp. 7282–7285, 2013, doi: 10.1002/anie.201301470.

[71] T. Cheng, H. Xiao, and W. A. Goddard, "Full atomistic reaction mechanism with kinetics for CO reduction on Cu(100) from ab initio molecular dynamics free-energy calculations at 298 K," *Proc. Natl. Acad. Sci. U. S. A.*, vol. 114, no. 8, pp. 1795–1800, 2017, doi: 10.1073/pnas.1612106114.

[72] H. Xiao, T. Cheng, W. A. Goddard, and R. Sundararaman, "Mechanistic Explanation of the pH Dependence and Onset Potentials for Hydrocarbon Products from Electrochemical Reduction of CO on Cu (111)," *J. Am. Chem. Soc.*, vol. 138, no. 2, pp. 483–486, 2016, doi: 10.1021/jacs.5b11390.

[73] Y. Hori, I. Takahashi, O. Koga, and N. Hoshi, "Selective formation of C2 compounds from electrochemical reduction of CO2 at a series of copper single crystal electrodes," *J. Phys. Chem. B*, vol. 106, no. 1, pp. 15–17, 2002, doi: 10.1021/jp013478d.

[74] I. Takahashi, O. Koga, N. Hoshi, and Y. Hori, "Electrochemical reduction of CO2 at copper single crystal Cu(S)-[n(111) × (111)] and Cu(S)-[n(110) × (100)] electrodes," *J. Electroanal. Chem.*, vol. 533, no. 1–2, pp. 135–143, 2002, doi: 10.1016/S0022-0728(02)01081-1.

[75] Y. Hori, I. Takahashi, O. Koga, and N. Hoshi, "Electrochemical reduction of carbon dioxide at various series of copper single crystal electrodes," *J. Mol. Catal. A Chem.*, vol. 199, no. 1–2, pp. 39–47, 2003, doi: 10.1016/S1381-1169(03)00016-5.

[76] A. Bagger, W. Ju, A. S. Varela, P. Strasser, and J. Rossmeisl, "Electrochemical CO2 Reduction: Classifying Cu Facets," *ACS Catal.*, vol. 9, no. 9, pp. 7894–7899, 2019, doi: 10.1021/acscatal.9b01899.

[77] M. Gattrell, N. Gupta, and A. Co, "A review of the aqueous electrochemical reduction of CO2 to hydrocarbons at copper," *J. Electroanal. Chem.*, vol. 594, no. 1, pp. 1–19, 2006, doi: 10.1016/j.jelechem.2006.05.013.

[78] H. Li, Y. Li, M. T. M. Koper, and F. Calle-Vallejo, "Bond-making and breaking between carbon, nitrogen, and oxygen in electrocatalysis," *J. Am. Chem. Soc.*, vol. 136, no. 44, pp. 15694–15701, 2014, doi: 10.1021/ja508649p.

[79] E. Pérez-Gallent, M. C. Figueiredo, F. Calle-Vallejo, and M. T. M. Koper, "Spectroscopic Observation of a Hydrogenated CO Dimer Intermediate During CO Reduction on Cu(100) Electrodes," *Angew. Chemie - Int. Ed.*, vol. 56, no. 13, pp. 3621–3624, 2017, doi: 10.1002/anie.201700580.

[80] I. Ledezma-Yanez, E. P. Gallent, M. T. M. Koper, and F. Calle-Vallejo, "Structure-sensitive electroreduction of acetaldehyde to ethanol on copper and its mechanistic implications for CO and CO2 reduction," *Catal. Today*, vol. 262, no. 111, pp. 90–94, Mar. 2016, doi: 10.1016/j.cattod.2015.09.029.

[81] O. Pique, F. Vines, F. Illas, and F. Calle-Vallejo, "Elucidating the Structure of Ethanol-Producing Active Sites at Oxide-Derived Cu Electrocatalysts," *ACS Catal.*, vol. 10, no. 18, pp. 10488–10494, 2020, doi: 10.1021/acscatal.0c01880.

[82] D. Zhong *et al.*, "Coupling of Cu(100) and (110) Facets Promotes Carbon Dioxide Conversion to Hydrocarbons and Alcohols," *Angew. Chemie - Int. Ed.*, vol. 60, no. 9, pp. 4879–4885, 2021, doi: 10.1002/anie.202015159.

[83] C. Hahn *et al.*, "Engineering Cu surfaces for the electrocatalytic conversion of CO2: Controlling selectivity toward oxygenates and hydrocarbons," *Proc. Natl. Acad. Sci. U. S. A.*, vol. 114, no. 23, pp. 5918–5923, 2017, doi: 10.1073/pnas.1618935114.

[84] Y. G. Kim, A. Javier, J. H. Baricuatro, and M. P. Soriaga, "Regulating the Product Distribution of CO Reduction by the Atomic-Level Structural Modification of the Cu Electrode Surface," *Electrocatalysis*, vol. 7, no. 5, pp. 391–399, 2016, doi: 10.1007/s12678-016-0314-1.

[85] J. H. Baricuatro, Y. G. Kim, C. F. Tsang, A. C. Javier, K. D. Cummins, and J. C. Hemminger, "Selective conversion of CO into ethanol on Cu(511) surface reconstructed from Cu(pc): Operando studies by electrochemical scanning tunneling microscopy, mass spectrometry, quartz crystal nanobalance, and infrared spectroscopy," *J. Electroanal. Chem.*, vol. 857, p. 113704, 2020, doi: 10.1016/j.jelechem.2019.113704.

[86] Y. Lum, T. Cheng, W. A. Goddard, and J. W. Ager, "Electrochemical CO Reduction Builds Solvent Water into Oxygenate Products," *J. Am. Chem. Soc.*, vol. 140, no. 30, pp. 9337–9340, 2018, doi: 10.1021/jacs.8b03986.

[87] J. Li *et al.*, "Intercepting Elusive Intermediates in Cu-Mediated CO Electrochemical Reduction with Alkyl Species," *J. Am. Chem. Soc.*, vol. 144, no. 44, pp. 20495–20506, 2022, doi: 10.1021/jacs.2c09378.

[88] D. Ren, J. Fong, and B. S. Yeo, "The effects of currents and potentials on the selectivities of copper toward carbon dioxide electroreduction," *Nat. Commun.*, vol. 9, no. 1, 2018, doi: 10.1038/s41467-018-03286-w.

[89] M. Ma *et al.*, "Local reaction environment for selective electroreduction of carbon monoxide," *Energy Environ. Sci.*, vol. 15, no. 6, pp. 2470–2478, 2022, doi: 10.1039/d1ee03838a.

[90] Y. Wang *et al.*, "Copper Nanocubes for CO2 Reduction in Gas Diffusion Electrodes," *Nano Lett.*, pp. 8461–8468, 2019, doi: 10.1021/acs.nanolett.9b02748.

[91] C. Choi *et al.*, "Highly active and stable stepped Cu surface for enhanced electrochemical CO2 reduction to C2H4," *Nat. Catal.*, vol. 3, no. 10, pp. 804–812, 2020, doi: 10.1038/s41929-020-00504-x.

[92] K. Jiang *et al.*, "Metal ion cycling of Cu foil for selective C–C coupling in electrochemical CO2 reduction," *Nat. Catal.*, vol. 1, no. 2, pp. 111–119, Jan. 2018, doi: 10.1038/s41929-017-0009-x.

[93] A. K. Engstfeld, S. Brimaud, and R. J. Behm, "Potential-induced surface restructuring - The need for structural characterization in electrocatalysis research," *Angew. Chemie - Int. Ed.*, vol. 53, no. 47, pp. 12936–12940, 2014, doi: 10.1002/anie.201404479.

[94] C. Zhu, S. Zhao, G. Shi, and L. Zhang, "Structure-Function Correlation and Dynamic Restructuring of Cu for Highly Efficient Electrochemical CO2 Conversion," *ChemSusChem*, vol. 15, no. 7, 2022, doi: 10.1002/cssc.202200068.

[95] C. J. Chang *et al.*, "Dynamic Reoxidation/Reduction-Driven Atomic Interdiffusion for

Highly Selective CO2Reduction toward Methane," *J. Am. Chem. Soc.*, vol. 142, no. 28, pp. 12119–12132, 2020, doi: 10.1021/jacs.0c01859.

[96] S. J. Raaijman, N. Arulmozhi, and M. T. M. Koper, "Morphological Stability of Copper Surfaces under Reducing Conditions," *ACS Appl. Mater. Interfaces*, vol. 13, no. 41, pp. 48730–48744, 2021, doi: 10.1021/acsami.1c13989.

[97] R. M. Arán-Ais, F. Scholten, S. Kunze, R. Rizo, and B. Roldan Cuenya, "The role of in situ generated morphological motifs and Cu(i) species in C2+ product selectivity during CO2 pulsed electroreduction," *Nat. Energy*, vol. 5, no. 4, pp. 317–325, Apr. 2020, doi: 10.1038/s41560-020-0594-9.

[98] D. Gao, R. M. Arán-Ais, H. S. Jeon, and B. Roldan Cuenya, "Rational catalyst and electrolyte design for CO2 electroreduction towards multicarbon products," *Nat. Catal.*, vol. 2, no. 3, pp. 198–210, 2019, doi: 10.1038/s41929-019-0235-5.

[99] J. Timoshenko and B. Roldan Cuenya, " In Situ / Operando Electrocatalyst Characterization by X-ray Absorption Spectroscopy ," *Chem. Rev.*, 2020, doi: 10.1021/acs.chemrev.0c00396.

[100] Y. G. Kim, J. H. Baricuatro, A. Javier, J. M. Gregoire, and M. P. Soriaga, "The evolution of the polycrystalline copper surface, first to Cu(111) and then to Cu(100), at a fixed CO2RR potential: A study by operando EC-STM," *Langmuir*, vol. 30, no. 50, pp. 15053–15056, 2014, doi: 10.1021/la504445g.

[101] Y. G. Kim *et al.*, "Surface reconstruction of pure-Cu single-crystal electrodes under CO-reduction potentials in alkaline solutions: A study by seriatim ECSTM-DEMS," *J. Electroanal. Chem.*, vol. 780, pp. 290–295, 2016, doi: 10.1016/j.jelechem.2016.09.029.

[102] H. Kawano, "Effective work functions for ionic and electronic emissions from mono- and polycrystalline surfaces," *Prog. Surf. Sci.*, vol. 83, no. 1–2, pp. 1–165, 2008, doi: 10.1016/j.progsurf.2007.11.001.

[103] A. K. Engstfeld, T. Maagaard, S. Horch, I. Chorkendorff, and I. E. L. Stephens, "Polycrystalline and Single-Crystal Cu Electrodes: Influence of Experimental Conditions on the Electrochemical Properties in Alkaline Media," *Chem. - A Eur. J.*, vol. 24, no. 67, pp. 17743–17755, Dec. 2018, doi: 10.1002/chem.201803418.

[104] A. Tiwari *et al.*, "Fingerprint Voltammograms of Copper Single Crystals under Alkaline Conditions: A Fundamental Mechanistic Analysis," *J. Phys. Chem. Lett.*, vol. 11, no. 4, pp. 1450–1455, 2020, doi: 10.1021/acs.jpclett.9b03728.

[105] P. Sebastián-Pascual and M. Escudero-Escribano, "Surface characterization of copper electrocatalysts by lead underpotential deposition," *J. Electroanal. Chem.*, vol. 896, no. February, 2021, doi: 10.1016/j.jelechem.2021.115446.

[106] E. Pérez-Gallent, G. Marcandalli, M. C. Figueiredo, F. Calle-Vallejo, and M. T. M. Koper, "Structure- and Potential-Dependent Cation Effects on CO Reduction at Copper Single-Crystal Electrodes," *J. Am. Chem. Soc.*, vol. 139, no. 45, pp. 16412–16419, 2017, doi: 10.1021/jacs.7b10142.

[107] Y. Huang, C. W. Ong, and B. S. Yeo, "Effects of Electrolyte Anions on the Reduction of Carbon Dioxide to Ethylene and Ethanol on Copper (100) and (111) Surfaces," *ChemSusChem*, vol. 11, no. 18, pp. 3299–3306, 2018, doi: 10.1002/cssc.201801078.

[108] C. S. Le Duff, M. J. Lawrence, and P. Rodriguez, "Role of the Adsorbed Oxygen Species in the Selective Electrochemical Reduction of CO2 to Alcohols and Carbonyls on Copper Electrodes," *Angew. Chemie - Int. Ed.*, vol. 56, no. 42, pp. 12919–12924, 2017, doi: 10.1002/anie.201706463.

[109] Z. Tang, E. Nishiwaki, K. E. Fritz, T. Hanrath, and J. Suntivich, "Cu(I) Reducibility Controls Ethylene vs Ethanol Selectivity on (100)-Textured Copper during Pulsed CO2Reduction," *ACS Appl. Mater. Interfaces*, vol. 13, no. 12, pp. 14050–14055, 2021, doi: 10.1021/acsami.0c17668.

[110] Y. Kwon, Y. Lum, E. L. Clark, J. W. Ager, and A. T. Bell, "CO2 Electroreduction with Enhanced Ethylene and Ethanol Selectivity by Nanostructuring Polycrystalline Copper," *ChemElectroChem*, vol. 3, no. 6, pp. 1012–1019, 2016, doi: 10.1002/celc.201600068.

[111] X. Wang *et al.*, "Efficient electrically powered CO2-to-ethanol via suppression of deoxygenation," *Nat. Energy*, vol. 5, no. 6, pp. 478–486, 2020, doi: 10.1038/s41560-020-0607-8.

[112] E. Bertheussen *et al.*, "Acetaldehyde as an Intermediate in the Electroreduction of Carbon Monoxide to Ethanol on Oxide-Derived Copper," *Angew. Chemie - Int. Ed.*, vol. 55, no. 4, pp. 1450–1454, 2016, doi: 10.1002/anie.201508851.

[113] Y. Y. Birdja and M. T. M. Koper, "The importance of cannizzaro-type reactions during electrocatalytic reduction of carbon dioxide," *J. Am. Chem. Soc.*, vol. 139, no. 5, pp. 2030–2034, 2017, doi: 10.1021/jacs.6b12008.

[114] S. Shen *et al.*, "AuCu Alloy Nanoparticle Embedded Cu Submicrocone Arrays for Selective Conversion of CO2 to Ethanol," *Small*, vol. 15, no. 37, pp. 1–7, 2019, doi: 10.1002/smll.201902229.

[115] Y. C. Li *et al.*, "Binding Site Diversity Promotes CO2 Electroreduction to Ethanol," *J. Am. Chem. Soc.*, vol. 141, no. 21, pp. 8584–8591, 2019, doi: 10.1021/jacs.9b02945.

[116] R. Kortlever, J. Shen, K. J. P. Schouten, F. Calle-Vallejo, and M. T. M. Koper, "Catalysts and Reaction Pathways for the Electrochemical Reduction of Carbon Dioxide," *J. Phys. Chem. Lett.*, vol. 6, no. 20, pp. 4073–4082, 2015, doi: 10.1021/acs.jpclett.5b01559.

[117] H. Song, J. T. Song, B. Kim, Y. C. Tan, and J. Oh, "Activation of C2H4 reaction pathways in electrochemical CO2 reduction under low CO2 partial pressure," *Appl. Catal. B Environ.*, vol. 272, no. November 2019, p. 119049, 2020, doi: 10.1016/j.apcatb.2020.119049.

[118] Y. Kim *et al.*, "Time-resolved observation of C-C coupling intermediates on Cu electrodes for selective electrochemical CO2reduction," *Energy Environ. Sci.*, vol. 13, no. 11, pp. 4301–4311, 2020, doi: 10.1039/d0ee01690j.

[119] Z. Zhang *et al.*, "Tailoring the Surface and Interface Structures of Copper-Based Catalysts for Electrochemical Reduction of CO2 to Ethylene and Ethanol," *Small*, vol. 18, no. 18, pp. 1–24, 2022, doi: 10.1002/smll.202107450.

[120] X. Su *et al.*, "Hierarchically porous Cu/Zn bimetallic catalysts for highly selective CO2 electroreduction to liquid C2 products," *Appl. Catal. B Environ.*, vol. 269, no. February, p. 118800, 2020, doi: 10.1016/j.apcatb.2020.118800.

[121] F. Jia, X. Yu, and L. Zhang, “Enhanced selectivity for the electrochemical reduction of CO2 to alcohols in aqueous solution with nanostructured Cu-Au alloy as catalyst,” *J. Power Sources*, vol. 252, pp. 85–89, 2014, doi: 10.1016/j.jpowsour.2013.12.002.

[122] J. Gao, D. Ren, X. Guo, S. M. Zakeeruddin, and M. Grätzel, “Sequential catalysis enables enhanced C-C coupling towards multi-carbon alkenes and alcohols in carbon dioxide reduction: A study on bifunctional Cu/Au electrocatalysts,” *Faraday Discuss.*, vol. 215, pp. 282–296, 2019, doi: 10.1039/c8fd00219c.

[123] Y. Lum and J. W. Ager, “Sequential catalysis controls selectivity in electrochemical CO2 reduction on Cu,” *Energy Environ. Sci.*, vol. 11, no. 10, pp. 2935–2944, 2018, doi: 10.1039/c8ee01501e.

[124] J. Huang, M. Mensi, E. Oveisi, V. Mantella, and R. Buonsanti, “Structural Sensitivities in Bimetallic Catalysts for Electrochemical CO2 Reduction Revealed by Ag-Cu Nanodimers,” *J. Am. Chem. Soc.*, vol. 141, no. 6, pp. 2490–2499, 2019, doi: 10.1021/jacs.8b12381.

[125] Y. Zhong *et al.*, “Adjusting Local CO Confinement in Porous-Shell Ag@Cu Catalysts for Enhancing C-C Coupling toward CO2 Eletroreduction,” *Nano Lett.*, vol. 22, no. 6, pp. 2554–2560, 2022, doi: 10.1021/acs.nanolett.1c04815.

[126] S. Lee, G. Park, and J. Lee, “Importance of Ag-Cu Biphasic Boundaries for Selective Electrochemical Reduction of CO2 to Ethanol,” *ACS Catal.*, vol. 7, no. 12, pp. 8594–8604, 2017, doi: 10.1021/acscatal.7b02822.

[127] C. Chen *et al.*, “Cu-Ag Tandem Catalysts for High-Rate CO2 Electrolysis toward Multicarbons,” *Joule*, vol. 4, no. 8, pp. 1688–1699, 2020, doi: 10.1016/j.joule.2020.07.009.

[128] X. Wang *et al.*, “Efficient upgrading of CO to C3 fuel using asymmetric C-C coupling active sites,” *Nat. Commun.*, vol. 10, no. 1, p. 5186, Dec. 2019, doi: 10.1038/s41467-019-13190-6.

[129] E. L. Clark, C. Hahn, T. F. Jaramillo, and A. T. Bell, “Electrochemical CO2 Reduction over Compressively Strained CuAg Surface Alloys with Enhanced Multi-Carbon Oxygenate Selectivity,” *J. Am. Chem. Soc.*, vol. 139, no. 44, pp. 15848–15857, Nov. 2017, doi: 10.1021/jacs.7b08607.

[130] Y. Feng *et al.*, “Laser-Prepared CuZn Alloy Catalyst for Selective Electrochemical Reduction of CO2 to Ethylene,” *Langmuir*, vol. 34, no. 45, pp. 13544–13549, 2018, doi: 10.1021/acs.langmuir.8b02837.

[131] S. Dongare, N. Singh, and H. Bhunia, “Oxide-derived Cu-Zn nanoparticles supported on N-doped graphene for electrochemical reduction of CO2 to ethanol,” *Appl. Surf. Sci.*, vol. 556, no. April, p. 149790, 2021, doi: 10.1016/j.apsusc.2021.149790.

[132] D. Higgins *et al.*, “Guiding Electrochemical Carbon Dioxide Reduction toward Carbonyls Using Copper Silver Thin Films with Interphase Miscibility,” *ACS Energy Lett.*, vol. 3, no. 12, pp. 2947–2955, 2018, doi: 10.1021/acsenergylett.8b01736.

[133] D. Higgins *et al.*, “Copper Silver Thin Films with Metastable Miscibility for Oxygen Reduction Electrocatalysis in Alkaline Electrolytes,” *ACS Appl. Energy Mater.*, vol. 1, no. 5, pp. 1990–1999, 2018, doi: 10.1021/acsaem.8b00090.

[134] B. M. Gibbons *et al.*, “In Situ X-Ray Absorption Spectroscopy Disentangles the Roles

of Copper and Silver in a Bimetallic Catalyst for the Oxygen Reduction Reaction," *Chem. Mater.*, vol. 32, no. 5, pp. 1819–1827, 2020, doi: 10.1021/acs.chemmater.9b03963.

[135] L. Wang *et al.*, "Selective reduction of CO to acetaldehyde with CuAg electrocatalysts," *Proc. Natl. Acad. Sci. U. S. A.*, vol. 117, no. 23, pp. 12572–12575, 2020, doi: 10.1073/pnas.1821683117.

[136] Y. F. Nishimura *et al.*, "Guiding the Catalytic Properties of Copper for Electrochemical CO2 Reduction by Metal Atom Decoration," *ACS Appl. Mater. Interfaces*, vol. 13, no. 44, pp. 52044–52054, Nov. 2021, doi: 10.1021/acsami.1c09128.

[137] M. Farmand *et al.*, "Electrochemical flow cell enabling: Operando probing of electrocatalyst surfaces by X-ray spectroscopy and diffraction," *Phys. Chem. Chem. Phys.*, vol. 21, no. 10, pp. 5402–5408, 2019, doi: 10.1039/c8cp07423b.

[138] H. Zhang *et al.*, "Computational and experimental demonstrations of one-pot tandem catalysis for electrochemical carbon dioxide reduction to methane," *Nat. Commun.*, vol. 10, no. 1, pp. 1–9, 2019, doi: 10.1038/s41467-019-11292-9.

[139] A. Herzog *et al.*, "Operando Investigation of Ag-Decorated Cu2O Nanocube Catalysts with Enhanced CO2 Electroreduction toward Liquid Products," *Angew. Chemie - Int. Ed.*, vol. 60, no. 13, pp. 7426–7435, 2021, doi: 10.1002/anie.202017070.

[140] W. Su *et al.*, "Highly dispersive trace silver decorated Cu/Cu2O composites boosting electrochemical CO2 reduction to ethanol," *J. CO2 Util.*, vol. 52, no. August, p. 101698, 2021, doi: 10.1016/j.jcou.2021.101698.

[141] L. R. L. Ting, O. Piqué, S. Y. Lim, M. Tanhaei, F. Calle-Vallejo, and B. S. Yeo, "Enhancing CO2 Electroreduction to Ethanol on Copper-Silver Composites by Opening an Alternative Catalytic Pathway," *ACS Catal.*, vol. 10, no. 7, pp. 4059–4069, 2020, doi: 10.1021/acscatal.9b05319.

[142] L. Hou *et al.*, "Ag nanoparticle embedded Cu nanoporous hybrid arrays for the selective electrocatalytic reduction of CO2 towards ethylene," *Inorg. Chem. Front.*, vol. 7, no. 10, pp. 2097–2106, 2020, doi: 10.1039/d0qi00025f.

[143] T. T. H. Hoang *et al.*, "Nanoporous Copper-Silver Alloys by Additive-Controlled Electrodeposition for the Selective Electroreduction of CO2 to Ethylene and Ethanol," *J. Am. Chem. Soc.*, vol. 140, no. 17, pp. 5791–5797, 2018, doi: 10.1021/jacs.8b01868.

[144] Y. Xu *et al.*, "Tuning the Selectivity of Liquid Products of CO2RR by Cu-Ag Alloying," *ACS Applied Materials and Interfaces*, vol. 14, no. 9. pp. 11567–11574, 2022, doi: 10.1021/acsami.2c00593.

[145] D. B. Trimarco, "Real-time detection of sub-monolayer desorption phenomena during electrochemical reactions: Instrument development and applications," Technical University of Denmark, 2017.

[146] D. B. Trimarco *et al.*, "Enabling real-time detection of electrochemical desorption phenomena with sub-monolayer sensitivity," *Electrochim. Acta*, vol. 268, pp. 520–530, 2018, doi: 10.1016/j.electacta.2018.02.060.

[147] M. Lok, *The IUPAC Compendium of Chemical Terminology*. Research Triangle Park, NC: International Union of Pure and Applied Chemistry (IUPAC), 2019.

[148] F. Ciucci, "Modeling electrochemical impedance spectroscopy," *Curr. Opin.*

Electrochem., vol. 13, pp. 132–139, 2019, doi: 10.1016/j.coelec.2018.12.003.

[149] S. Wang, J. Zhang, O. Gharbi, V. Vivier, M. Gao, and M. E. Orazem, "Electrochemical impedance spectroscopy," *Nat. Rev. Methods Prim.*, vol. 1, no. 1, 2021, doi: 10.1038/s43586-021-00039-w.

[150] P. Vadhva *et al.*, "Electrochemical Impedance Spectroscopy for All-Solid-State Batteries: Theory, Methods and Future Outlook," *ChemElectroChem*, vol. 8, no. 11, pp. 1930–1947, 2021, doi: 10.1002/celc.202100108.

[151] H. L. Lord, W. Zhan, and J. Pawliszyn, *Fundamentals and applications of needle trap devices*. 2012.

[152] P. Strasser, M. Gliech, S. Kuehl, and T. Moeller, "Electrochemical processes on solid shaped nanoparticles with defined facets," *Chem. Soc. Rev.*, vol. 47, no. 3, pp. 715–735, 2018, doi: 10.1039/c7cs00759k.

[153] M. Bellardita, A. Di Paola, S. Yurdakal, and L. Palmisano, *Preparation of catalysts and photocatalysts used for similar processes*. Elsevier B.V., 2019.

[154] P. N. Hishimone, H. Nagai, and M. Sato, "Methods of Fabricating Thin Films for Energy Materials and Devices," in *Lithium-ion Batteries - Thin Film for Energy Materials and Devices*, vol. 11, no. tourism, IntechOpen, 2020, p. 13.

[155] W. L. Bragg, "The Diffraction of Short Electromagnetic Waves by a Crystal," *Proc. Camb. Philol. Soc.*, no. 17, pp. 43–57, 1913.

[156] I. Stabrawa *et al.*, "Characterization of the morphology of titanium and titanium (IV) oxide nanolayers deposited on different substrates by application of grazing incidence X-ray diffraction and X-ray reflectometry techniques," *Thin Solid Films*, vol. 671, no. December 2018, pp. 103–110, 2019, doi: 10.1016/j.tsf.2018.12.034.

[157] M. Sardela, *Practical materials characterization*. 2014.

[158] H. H. Brongersma, M. Draxler, M. de Ridder, and P. Bauer, "Surface composition analysis by low-energy ion scattering," *Surf. Sci. Rep.*, vol. 62, no. 3, pp. 63–109, 2007, doi: 10.1016/j.surfrep.2006.12.002.

[159] G. G. Andersson, *Ion Scattering Spectroscopy*. Elsevier Inc., 2013.

[160] J. Timoshenko and B. Roldan Cuenya, "In Situ/ Operando Electrocatalyst Characterization by X-ray Absorption Spectroscopy," *Chem. Rev.*, vol. 121, no. 2, pp. 882–961, 2021, doi: 10.1021/acs.chemrev.0c00396.

[161] J. H. Gross, *Mass Spectrometry, A Textbook*, 3rd ed. Springer Cham, 2017.

[162] G. Santoiemma, "Recent methodologies for studying the soil organic matter," *Appl. Soil Ecol.*, vol. 123, no. September 2017, pp. 546–550, 2018, doi: 10.1016/j.apsoil.2017.09.011.

[163] S. Pal, M. Kumar, R. Singh, and N. Kumar, "Evaluation of Electron-Impact Ionization Cross Sections for Molecules," *J. Phys. Chem. A*, vol. 123, no. 19, pp. 4314–4321, 2019, doi: 10.1021/acs.jpca.9b02021.

[164] S. B. Scott, "Isotope-Labeling Studies in Electrocatalysis for Renewable Energy Conversion, and the Net Carbon Impact of this PhD Project," Technical University of Denmark, 2019.

[165] U. J. Quaade, S. Jensen, and O. Hansen, "Fabrication and modeling of narrow

capillaries for vacuum system gas inlets," *J. Appl. Phys.*, vol. 97, no. 4, pp. 1–5, 2005, doi: 10.1063/1.1829377.

[166] P. J. Linstrom and W. G. Mallard, "The NIST Chemistry WebBook: A Chemical Data Resource on the Internet," *J. Chem. Eng. Data*, vol. 46, no. 5, pp. 1059–1063, Sep. 2001, doi: 10.1021/je000236i.

[167] X. Chang, A. Malkani, X. Yang, and B. Xu, "Mechanistic Insights into Electroreductive C-C Coupling between CO and Acetaldehyde into Multicarbon Products," *J. Am. Chem. Soc.*, vol. 142, no. 6, pp. 2975–2983, Feb. 2020, doi: 10.1021/jacs.9b11817.

[168] L. R. L. Ting *et al.*, "Electrochemical Reduction of Carbon Dioxide to 1-Butanol on Oxide-Derived Copper," *Angew. Chemie Int. Ed.*, vol. 59, no. 47, pp. 21072–21079, Nov. 2020, doi: 10.1002/anie.202008289.

[169] B. P. Charnay, Z. Cui, M. A. Marx, J. Palazzo, and A. C. Co, "Insights into the CO2Reduction Pathway through the Electrolysis of Aldehydes on Copper," *ACS Catal.*, vol. 11, no. 7, pp. 3867–3876, 2021, doi: 10.1021/acscatal.0c05615.

[170] A. A. Peterson, F. Abild-Pedersen, F. Studt, J. Rossmeisl, and J. K. Nørskov, "How copper catalyzes the electroreduction of carbon dioxide into hydrocarbon fuels," *Energy Environ. Sci.*, vol. 3, no. 9, pp. 1311–1315, 2010, doi: 10.1039/c0ee00071j.

[171] J. Heyes, M. Dunwell, and B. Xu, "CO2 Reduction on Cu at Low Overpotentials with Surface-Enhanced in Situ Spectroscopy," *J. Phys. Chem. C*, vol. 120, no. 31, pp. 17334–17341, Aug. 2016, doi: 10.1021/acs.jpcc.6b03065.

[172] C. W. Li, J. Ciston, and M. W. Kanan, "Electroreduction of carbon monoxide to liquid fuel on oxide-derived nanocrystalline copper," *Nature*, vol. 508, no. 7497, pp. 504–507, 2014, doi: 10.1038/nature13249.

[173] M. Löffler, P. Khanipour, N. Kulyk, K. J. J. Mayrhofer, and I. Katsounaros, "Insights into Liquid Product Formation during Carbon Dioxide Reduction on Copper and Oxide-Derived Copper from Quantitative Real-Time Measurements," *ACS Catal.*, vol. 10, no. 12, pp. 6735–6740, 2020, doi: 10.1021/acscatal.0c01388.

[174] F. H. Munson, M.S.B.; Field, "Physical chemistry," *J. Am. Chem. Soc.*, vol. 88, pp. 2621–2630, 1966, doi: 10.1038/156283a0.

[175] C. Kim, L. C. Weng, and A. T. Bell, "Impact of Pulsed Electrochemical Reduction of CO2on the Formation of C2+Products over Cu," *ACS Catal.*, vol. 10, no. 21, pp. 12403–12413, 2020, doi: 10.1021/acscatal.0c02915.

[176] B. Hasa, M. Jouny, B. H. Ko, B. Xu, and F. Jiao, "Flow Electrolyzer Mass Spectrometry with a Gas-Diffusion Electrode Design," *Angew. Chemie - Int. Ed.*, vol. 60, no. 6, pp. 3277–3282, 2021, doi: 10.1002/anie.202013713.

[177] H. Ren *et al.*, "Operando proton-transfer-reaction time-of-flight mass spectrometry of carbon dioxide reduction electrocatalysis," *Nat. Catal.*, 2022, doi: 10.1038/s41929-022-00891-3.

[178] K. Krempl *et al.*, "Dynamic Interfacial Reaction Rates from Electrochemistry-Mass Spectrometry," *Anal. Chem.*, vol. 93, no. 18, pp. 7022–7028, 2021, doi: 10.1021/acs.analchem.1c00110.

[179] H. Ooka, M. C. Figueiredo, and M. T. M. Koper, "Competition between Hydrogen

Evolution and Carbon Dioxide Reduction on Copper Electrodes in Mildly Acidic Media," *Langmuir*, vol. 33, no. 37, pp. 9307–9313, 2017, doi: 10.1021/acs.langmuir.7b00696.

[180] M. Jouny, W. Luc, and F. Jiao, "High-rate electroreduction of carbon monoxide to multi-carbon products," *Nat. Catal.*, vol. 1, no. 10, pp. 748–755, 2018, doi: 10.1038/s41929-018-0133-2.

[181] J. Li *et al.*, "Constraining CO coverage on copper promotes high-efficiency ethylene electroproduction," *Nat. Catal.*, vol. 2, no. 12, pp. 1124–1131, 2019, doi: 10.1038/s41929-019-0380-x.

[182] W. L. Evans and H. Adkins, "THE OXIDATION OF ORGANIC COMPOUNDS WITH ALKALINE POTASSIUM PERMANGANATE. Part I.—The Oxidation of Acetaldehyde. Part II.—The Oxidation of Glycol, Glycollic Aldehyde, Glyoxal, Glycollic Acid and Glyoxalic Acid.," *J. Am. Chem. Soc.*, vol. 41, no. 9, pp. 1385–1414, Sep. 1919, doi: 10.1021/ja02230a010.

[183] S. Yamada, D. Morizono, and K. Yamamoto, "Mild oxidation of aldehydes to the corresponding carboxylic acids and esters: alkaline iodine oxidation revisited," *Tetrahedron Lett.*, vol. 33, no. 30, pp. 4329–4332, Jul. 1992, doi: 10.1016/S0040-4039(00)74252-3.

[184] J. B. Conant and M. F. Pratt, "The Irreversible Oxidation of Organic Compounds II. The Apparent Oxidation Potential of Certain Phenols and Enols," *J. Am. Chem. Soc.*, vol. 48, no. 12, pp. 3220–3232, Dec. 1926, doi: 10.1021/ja01691a032.

[185] P. A. Kempler and A. C. Nielander, "Reliable reporting of Faradaic ef fi ciencies for electrocatalysis research," doi: 10.1038/s41467-023-36880-8.

[186] J. Christophe, T. Doneux, and C. Buess-Herman, "Electroreduction of Carbon Dioxide on Copper-Based Electrodes: Activity of Copper Single Crystals and Copper-Gold Alloys," *Electrocatalysis*, vol. 3, no. 2, pp. 139–146, 2012, doi: 10.1007/s12678-012-0095-0.

[187] S. T. Gao, S. Q. Xiang, J. L. Shi, W. Zhang, and L. Bin Zhao, "Theoretical understanding of the electrochemical reaction barrier: A kinetic study of CO2 reduction reaction on copper electrodes," *Phys. Chem. Chem. Phys.*, vol. 22, no. 17, pp. 9607–9615, 2020, doi: 10.1039/c9cp06824d.

[188] J. H. Montoya, C. Shi, K. Chan, and J. K. Nørskov, "Theoretical insights into a CO dimerization mechanism in CO2 electroreduction," *J. Phys. Chem. Lett.*, vol. 6, no. 11, pp. 2032–2037, 2015, doi: 10.1021/acs.jpclett.5b00722.

[189] T. J. Haynes, W. M., Lide, D. R., & Bruno, *CRC handbook of chemistry and physics: a ready-reference book of chemical and physical data*, 97th ed. Florida: CRC Press, 2016.

[190] Y.-J. Zhang, V. Sethuraman, R. Michalsky, and A. Peterson, "Supporting information for Competition between CO2 reduction and H 2 evolution on transition-metal electrocatalysts," *ACS Catal.*, vol. 4, pp. 3742–3748, 2014.

[191] X. Lv *et al.*, "Electron-Deficient Cu Sites on Cu3Ag1 Catalyst Promoting CO2 Electroreduction to Alcohols," *Adv. Energy Mater.*, vol. 10, no. 37, pp. 1–8, 2020, doi: 10.1002/aenm.202001987.

[192] A. N. Kuhn *et al.*, "Engineering Silver-Enriched Copper Core-Shell Electrocatalysts to Enhance the Production of Ethylene and C2+ Chemicals from Carbon Dioxide at Low Cell Potentials," *Adv. Funct. Mater.*, vol. 31, no. 26, pp. 2–11, 2021, doi: 10.1002/adfm.202101668.

[193] E. R. Cave *et al.*, "Trends in the Catalytic Activity of Hydrogen Evolution during CO2 Electroreduction on Transition Metals," *ACS Catal.*, vol. 8, no. 4, pp. 3035–3040, 2018, doi: 10.1021/acscatal.7b03807.

[194] J. K. Nørskov *et al.*, "Trends in the Exchange Current for Hydrogen Evolution," *J. Electrochem. Soc.*, vol. 152, no. 3, p. J23, 2005, doi: 10.1149/1.1856988.

[195] B. Hammer and J. K. Nørskov, "Electronic factors determining the reactivity of metal surfaces," *Surf. Sci.*, vol. 343, no. 3, pp. 211–220, Dec. 1995, doi: 10.1016/0039-6028(96)80007-0.

[196] A. Ruban, B. Hammer, P. Stoltze, H. . Skriver, and J. . Nørskov, "Surface electronic structure and reactivity of transition and noble metals1Communication presented at the First Francqui Colloquium, Brussels, 19–20 February 1996.1," *J. Mol. Catal. A Chem.*, vol. 115, no. 3, pp. 421–429, Feb. 1997, doi: 10.1016/S1381-1169(96)00348-2.

[197] Z. Chang, S. Huo, W. Zhang, J. Fang, and H. Wang, "The Tunable and Highly Selective Reduction Products on Ag@Cu Bimetallic Catalysts Toward CO2 Electrochemical Reduction Reaction," *J. Phys. Chem. C*, vol. 121, no. 21, pp. 11368–11379, 2017, doi: 10.1021/acs.jpcc.7b01586.

[198] N. Martić *et al.*, "Ag2Cu2O3-a catalyst template material for selective electroreduction of CO to C2+products," *Energy Environ. Sci.*, vol. 13, no. 9, pp. 2993–3006, 2020, doi: 10.1039/d0ee01100b.

[199] X. Chen *et al.*, "Controlling Speciation during CO2 Reduction on Cu-Alloy Electrodes," *ACS Catal.*, vol. 10, no. 1, pp. 672–682, 2020, doi: 10.1021/acscatal.9b04368.

[200] L. Vitos, A. V. Ruban, H. L. Skriver, and J. Kollár, "The surface energy of metals," *Surf. Sci.*, vol. 411, no. 1–2, pp. 186–202, Aug. 1998, doi: 10.1016/S0039-6028(98)00363-X.

[201] W. Tang *et al.*, "The importance of surface morphology in controlling the selectivity of polycrystalline copper for CO2 electroreduction," *Phys. Chem. Chem. Phys.*, vol. 14, no. 1, pp. 76–81, 2012, doi: 10.1039/c1cp22700a.

[202] T. Möller *et al.*, "Electrocatalytic CO2 Reduction on CuOx Nanocubes: Tracking the Evolution of Chemical State, Geometric Structure, and Catalytic Selectivity using Operando Spectroscopy," *Angew. Chemie - Int. Ed.*, vol. 59, no. 41, pp. 17974–17983, 2020, doi: 10.1002/anie.202007136.

[203] D. Karapinar, C. E. Creissen, J. G. Rivera De La Cruz, M. W. Schreiber, and M. Fontecave, "Electrochemical CO2Reduction to Ethanol with Copper-Based Catalysts," *ACS Energy Lett.*, vol. 6, no. 2, pp. 694–706, 2021, doi: 10.1021/acsenergylett.0c02610.

[204] X. Chang, S. Vijay, Y. Zhao, N. J. Oliveira, K. Chan, and B. Xu, "Understanding the complementarities of surface-enhanced infrared and Raman spectroscopies in CO adsorption and electrochemical reduction," *Nat. Commun.*, vol. 13, no. 1, pp. 1–12,

2022, doi: 10.1038/s41467-022-30262-2.

[205] H. An *et al.*, “Sub-Second Time-Resolved Surface-Enhanced Raman Spectroscopy Reveals Dynamic CO Intermediates during Electrochemical CO2 Reduction on Copper,” *Angew. Chemie - Int. Ed.*, vol. 60, no. 30, pp. 16576–16584, 2021, doi: 10.1002/anie.202104114.

[206] M. L. Baker, M. W. Mara, J. J. Yan, K. O. Hodgson, B. Hedman, and E. I. Solomon, “K- and L-edge X-ray absorption spectroscopy (XAS) and resonant inelastic X-ray scattering (RIXS) determination of differential orbital covalency (DOC) of transition metal sites,” *Coord. Chem. Rev.*, vol. 345, pp. 182–208, 2017, doi: 10.1016/j.ccr.2017.02.004.

[207] M. Newville, “Fundamentals of XAFS,” *Rev. Mineral. Geochemistry*, vol. 78, no. 1, pp. 33–74, Jan. 2014, doi: 10.2138/rmg.2014.78.2.

[208] T. Kottakkat *et al.*, “Electrodeposited AgCu Foam Catalysts for Enhanced Reduction of CO2 to CO,” *ACS Appl. Mater. Interfaces*, vol. 11, no. 16, pp. 14734–14744, 2019, doi: 10.1021/acsami.8b22071.

[209] L. Fang, S. Seifert, R. E. Winans, and T. Li, “Operando XAS/SAXS: Guiding Design of Single-Atom and Subnanocluster Catalysts,” *Small Methods*, vol. 5, no. 5, pp. 1–13, 2021, doi: 10.1002/smtd.202001194.

[210] X. Li, X. Yang, J. Zhang, Y. Huang, and B. Liu, “In Situ/Operando Techniques for Characterization of Single-Atom Catalysts,” *ACS Catal.*, vol. 9, no. 3, pp. 2521–2531, 2019, doi: 10.1021/acscatal.8b04937.

[211] X. Liu *et al.*, “Dynamic Surface Reconstruction of Single-Atom Bimetallic Alloy under Operando Electrochemical Conditions,” *Nano Lett.*, vol. 20, no. 11, pp. 8319–8325, 2020, doi: 10.1021/acs.nanolett.0c03475.

[212] E. V. Golubina *et al.*, “The role of metal–support interaction in catalytic activity of nanodiamond-supported nickel in selective phenylacetylene hydrogenation,” *J. Catal.*, vol. 344, pp. 90–99, 2016, doi: 10.1016/j.jcat.2016.08.017.

[213] J. Timoshenko, H. S. Jeon, I. Sinev, F. T. Haase, A. Herzog, and B. Roldan Cuenya, “Linking the evolution of catalytic properties and structural changes in copper-zinc nanocatalysts using: Operando EXAFS and neural-networks,” *Chem. Sci.*, vol. 11, no. 14, pp. 3727–3736, 2020, doi: 10.1039/d0sc00382d.

[214] J. Lim *et al.*, “Ga-Doped Pt-Ni Octahedral Nanoparticles as a Highly Active and Durable Electrocatalyst for Oxygen Reduction Reaction,” *Nano Lett.*, vol. 18, no. 4, pp. 2450–2458, 2018, doi: 10.1021/acs.nanolett.8b00028.

[215] Z. Xia and S. Guo, “Strain engineering of metal-based nanomaterials for energy electrocatalysis,” *Chem. Soc. Rev.*, vol. 48, no. 12, pp. 3265–3278, 2019, doi: 10.1039/c8cs00846a.

[216] J. A. Zamora Zeledón, A. Jackson, M. B. Stevens, G. A. Kamat, and T. F. Jaramillo, “Methods—A Practical Approach to the Reversible Hydrogen Electrode Scale,” *J. Electrochem. Soc.*, vol. 169, no. 6, p. 066505, 2022, doi: 10.1149/1945-7111/ac71d1.

[217] S. M. Webb, “SIXpack: A graphical user interface for XAS analysis using IFEFFIT,” *Phys. Scr. T*, vol. T115, pp. 1011–1014, 2005, doi: 10.1238/Physica.Topical.115a01011.

[218] B. Ravel and M. Newville, “ATHENA, ARTEMIS, HEPHAESTUS: Data analysis for X-ray absorption spectroscopy using IFEFFIT,” *J. Synchrotron Radiat.*, vol. 12, no. 4, pp. 537–541, 2005, doi: 10.1107/S0909049505012719.

[219] B. L. Henke, E. M. Gullikson, and J. C. Davis, “X-ray interactions: Photoabsorption, scattering, transmission, and reflection at E = 50-30, 000 eV, Z = 1-92,” *Atomic Data and Nuclear Data Tables*, vol. 54, no. 2. pp. 181–342, 1993, doi: 10.1006/adnd.1993.1013.

[220] G. Kresse and J. Furthmüller, “Efficiency of ab-initio total energy calculations for metals and semiconductors using a plane-wave basis set,” *Comput. Mater. Sci.*, vol. 6, no. 1, pp. 15–50, 1996, doi: 10.1016/0927-0256(96)00008-0.

[221] J. Wellendorff *et al.*, “Density functionals for surface science: Exchange-correlation model development with Bayesian error estimation,” *Phys. Rev. B*, vol. 85, no. 23, p. 235149, Jun. 2012, doi: 10.1103/PhysRevB.85.235149.

Appendices

A. More Information for Chapter 4

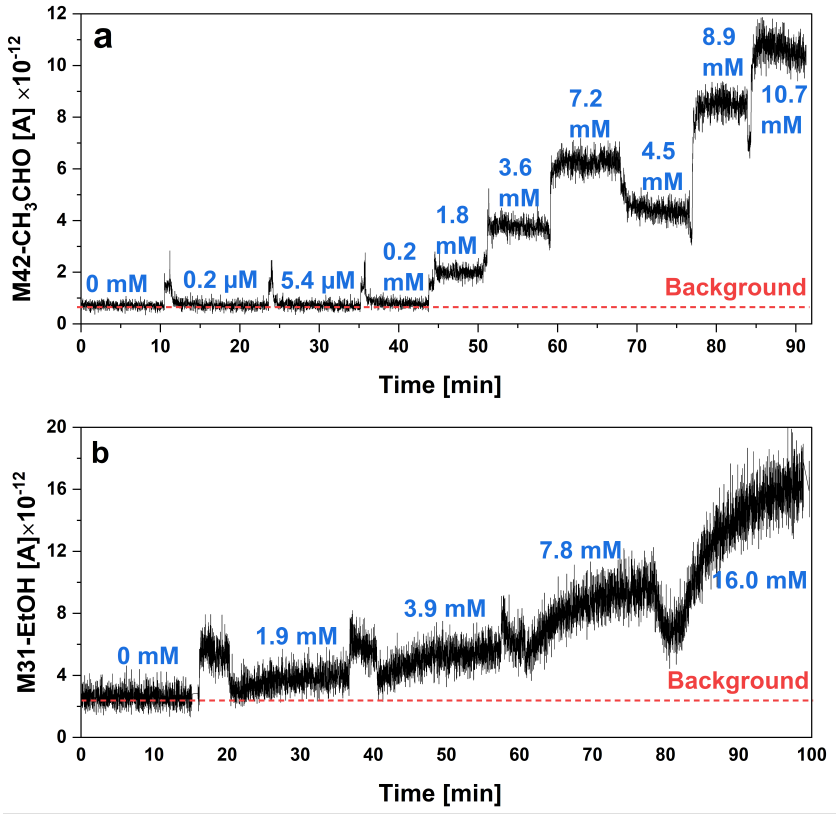

Figure A.1 ***Mass spectrometer detection limit test*** *on a) acetaldehyde and b) ethanol. Spikes in each spectrum were due to ion gauge background pressure change caused by liquid injection.*

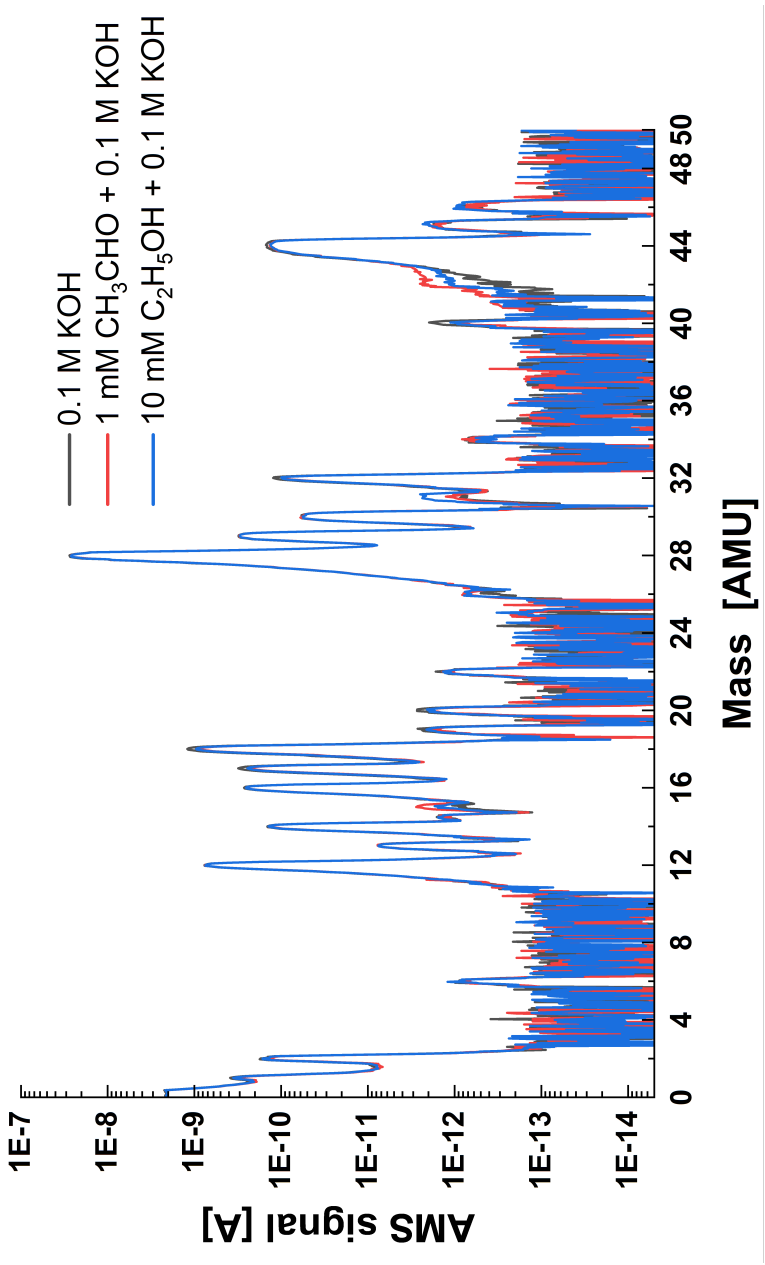

Figure A.2 ***Full mass spectra*** *of 0.1 M KOH electrolyte (black) and it added with 1 mM acetaldehyde (red) and 10 mM ethanol (blue), respectively (EE = 70 eV).*

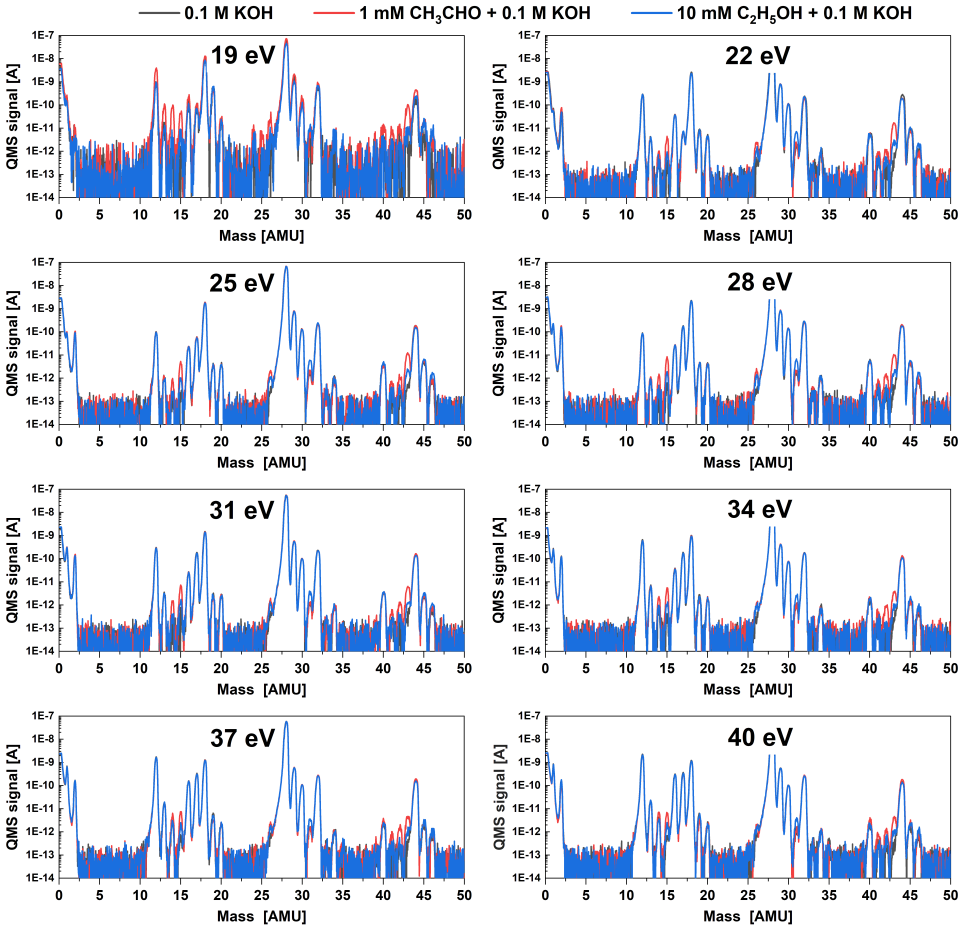

Figure A.3 ***Full mass spectra*** *of 0.1 M KOH electrolyte (black) and it added with 1 mM acetaldehyde (red) and 10 mM ethanol (blue), respectively (EE = 19 ~ 40 eV).*

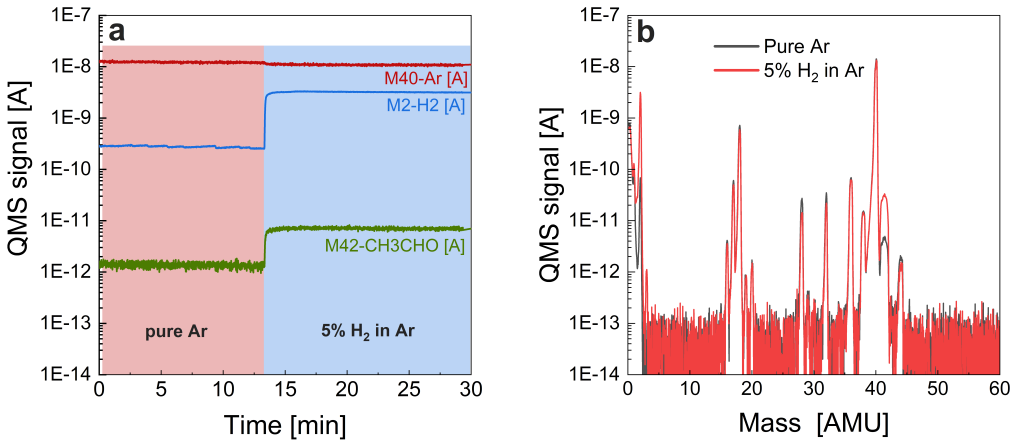

Figure A.4 ***M42 background check*** *in pure Ar and 5% H_2 in Ar: a) M2 (H_2), M40 (Ar) and M42 (acetaldehyde) background track and b) full mass scans.*

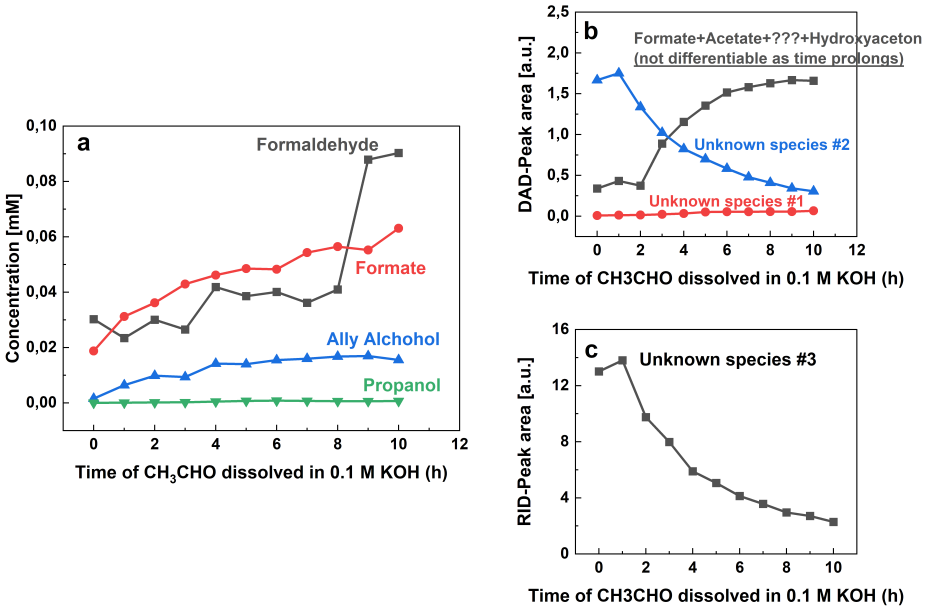

Figure A.5 ***Change in composition of 0.1 M KOH solution*** *after introducing 4.5 mM acetaldehyde measured with HPLC: a) composites with concentration below 0.1 mM, b) un-assigned peak area from the DAD spectra, and c) un-assigned peak area from the RID spectra. Un-assigned HPLC peak area is because either multiple peaks are overlapped, or no calibration has been done on the corresponding species.*

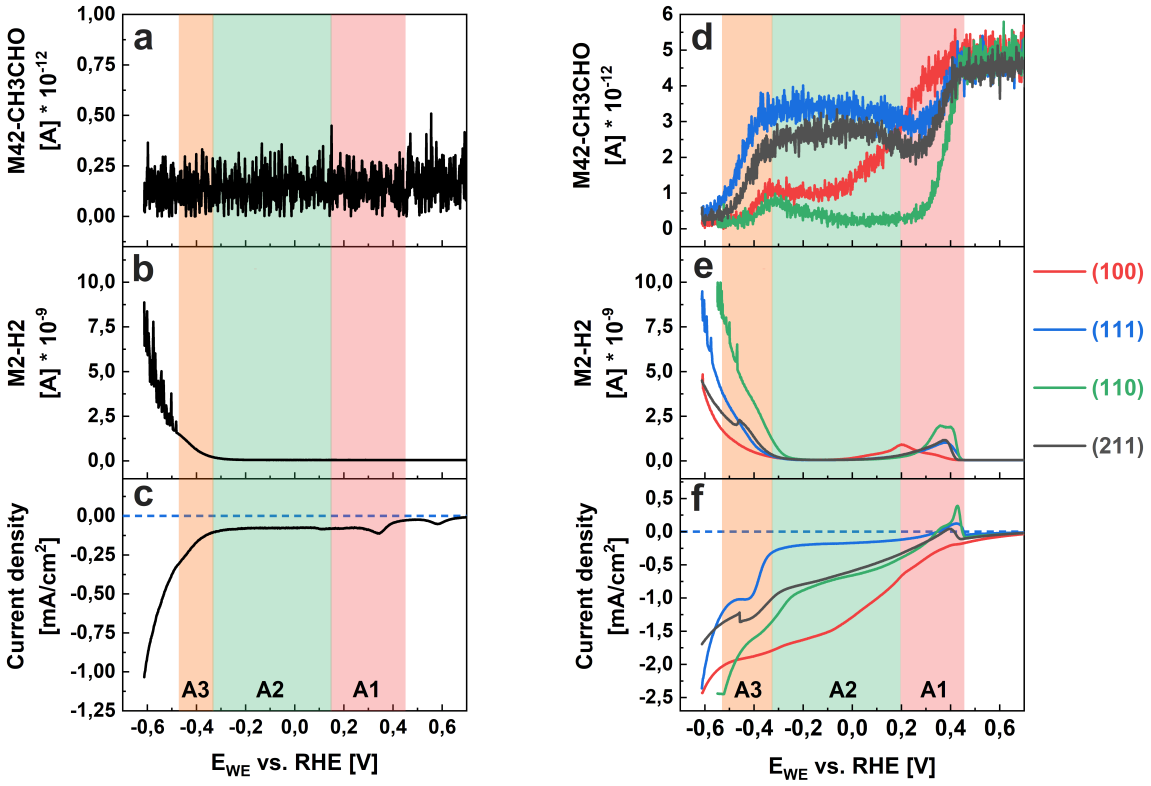

Figure A.6 ***Acetaldehyde reduction with 4.5 mM concentration mixed in 0.1 M KOH*** *on a-c) polycrystalline Cu without adding acetaldehyde for benchmark; d-f) Cu single crystals.*

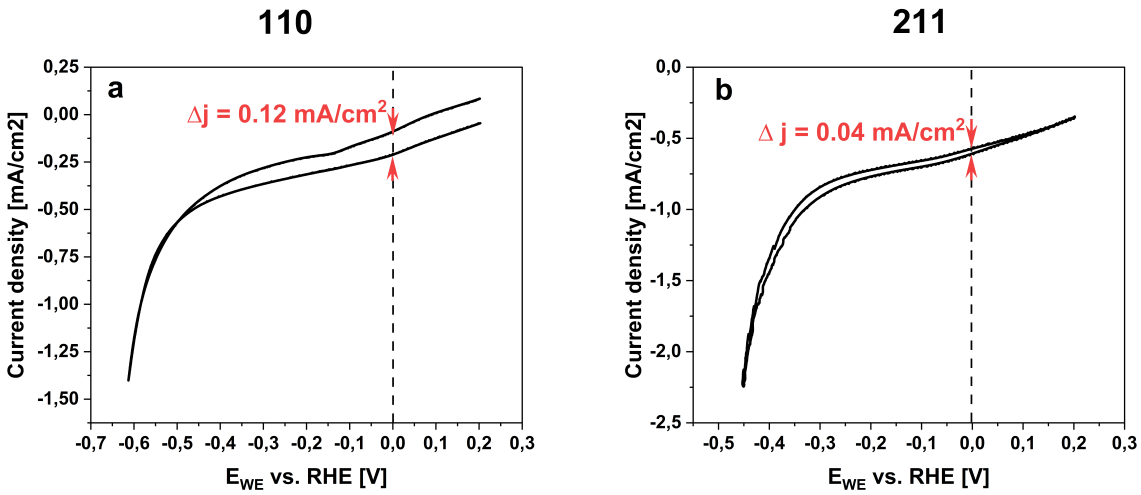

Figure A.7 ***Double layer capacitance check*** *on a) Cu (100) and b) Cu (211). Cyclic voltammograms scanned from OCV to the most negative potential limited by the setup geometry. Scan rate was at 2mV/s.*

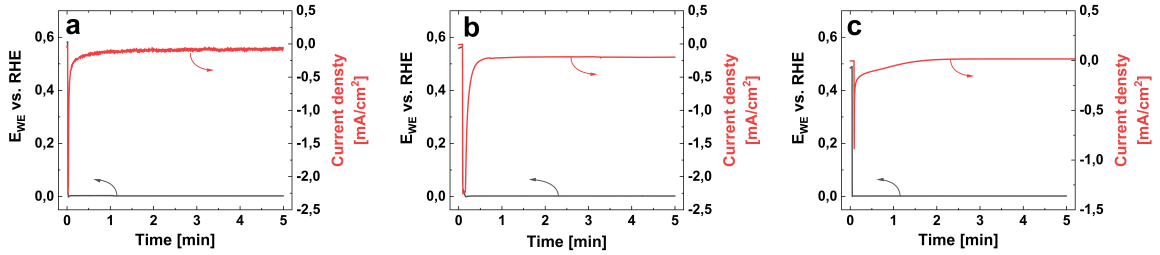

Figure A.8 ***Cu reducing chronoamperometry at 0 V vs. RHE*** *on a) Cu (pc), b) Cu (100) and c) Cu (111). Spikes at the beginning are because of the sharp potential change from OCV, as magnified in the inserts.*

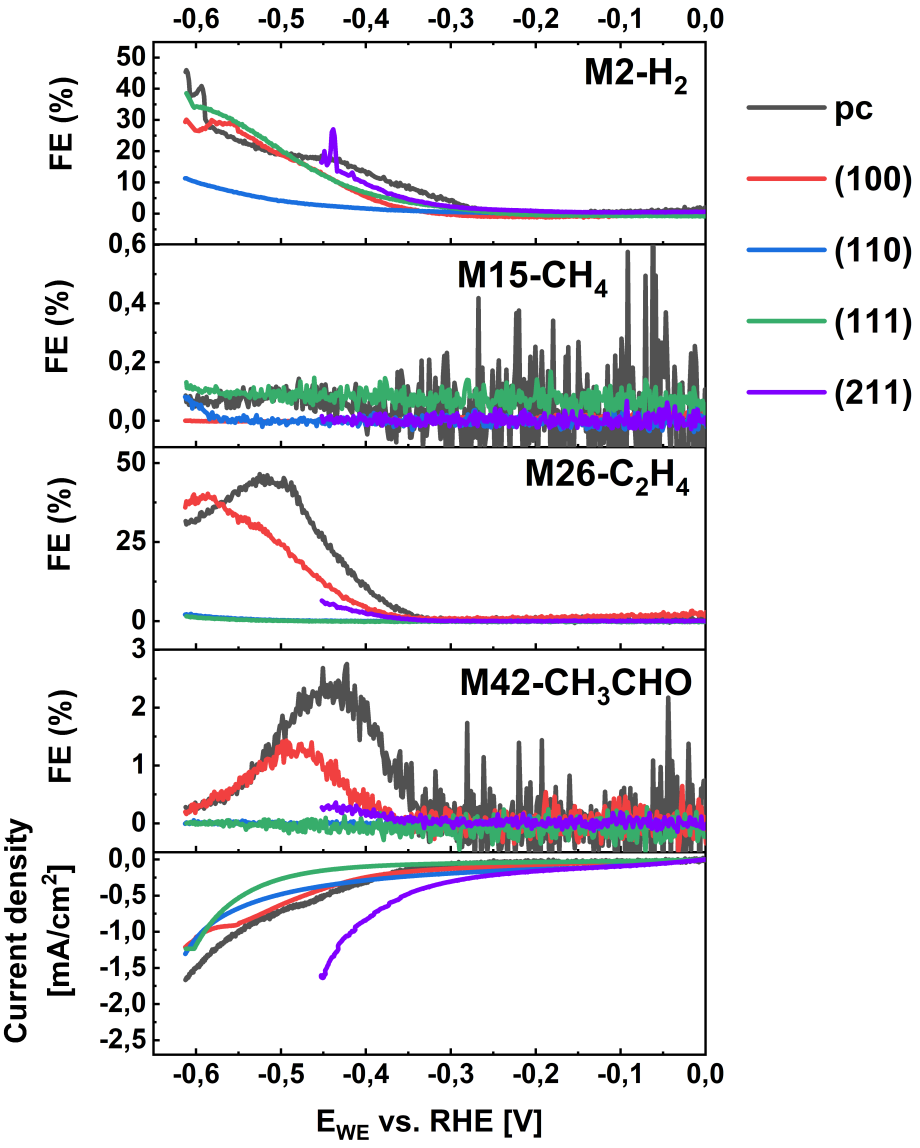

Figure A.9 ***Faradaic efficiency comparison among polycrystalline Cu and single crystals in electrochemical CO reduction.*** *The onset total current (at 0 V vs. RHE) was intentionally shifted to 0 mA in order to investigate the hypothesized ORR argument.*

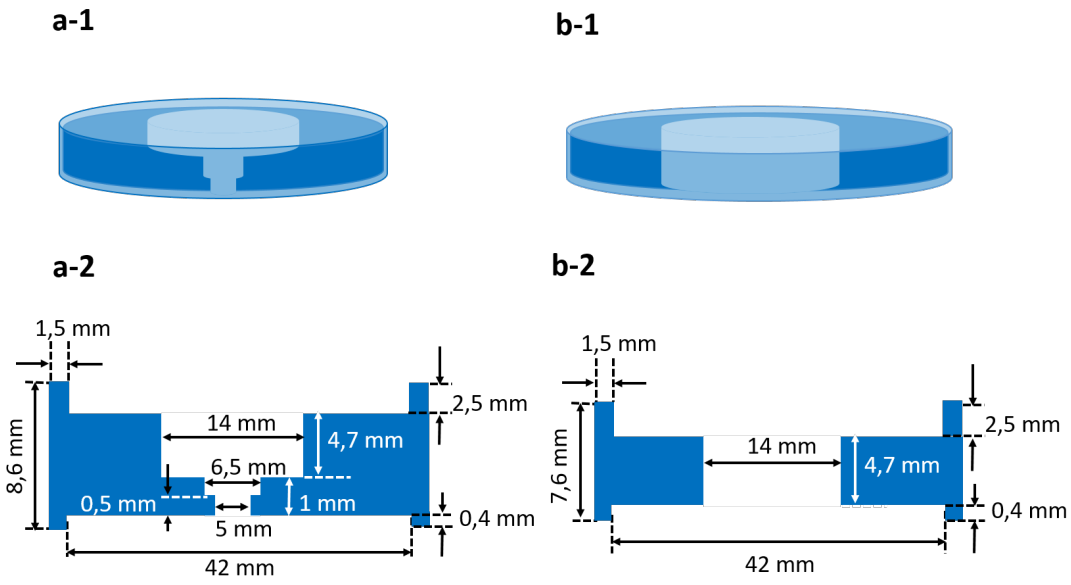

Figure A.10 ***Single crystal mounting holder design for the EC-MS cell.*** *a-1) Three-dimensional diagram of holder #1, a-2) cross-section of holder #1, b-1) three- dimensional diagram of holder #2, d) cross-section of holder #2. This is a two-step process. Step1. A piece of single crystal silicon wafer (111) will be placed below holder #1, with a piece of lens paper in between, then the Cu single crystal electrode will be placed upside-down (i.e., the surface to be exposed to electrochemistry faces down). The electrode will then be placed into the cell following the general procedure with care.Step2. When the electrode is loosely grabbed by the cell, the second holder will be used. The cell holding the holder will be placed on top of holder #2, then slightly push from the top until the electrode is completely pushed into the cell. By this means, the single crystal configuration of the electrode will be protected to the greatest extent.*

B. More Information for Chapter 5

B.1 Thin Film Catalyst Fabrication and Characterization

Cu_XAg_{100-X} (X = 100, 95, 80 and 60, nominal content) were fabricated with a high vacuum (base pressure < 1 x 10-7 mbar) magnetron sputtering chamber (AJA International, Inc.) using direct current (DC) mode. The Cu and Ag targets (Kurt–Lesker, 99.9999%) were (co)-deposited on 75 nm thick Si wafers (Wafer World Inc., boron-doped, resistivity < 0.025 Ohm-cm) or Kapton foil (DuPont, only for XAS at Ag L3-edge) as the substrate. In both cases, the substrate was sputter-cleaned by Ar at 40 W for *ca.* 5min to remove any surface contaminations and oxide layers. A *ca.* 5 nm thick Ti adhesive layer was then sputtered at a rate of *ca.* 0.7 Å/s, followed by a *ca.* 50 nm thick Cu_XAg_{100-X} catalyst layer deposited at a rate of *ca.* 1.0 Å/s. The deposition rate and nominal composition as well as the thickness of the deposited catalyst layer were calibrated by a quartz crystal microbalance (QCM). All samples were deposited under a 5 mTorr, 10 sccm Ar (N5, Air Liquide) atmosphere at room temperature.

X-ray photoelectron spectroscopy (XPS) was performed by a ThermoScientific Thetaprobe instrument equipped with an Al Kα X-ray source. The operating base pressure was kept below 1.0×10^{-10} mbar. Survey and high-resolution elemental scans were recorded with a step size of 1.0 eV and 0.1 eV, respectively; while in all cases pass energy of 200 eV and dwell time of 50 ms were used. The data were acquired and analyzed with Thermo Avantage (Thermo Fisher Scientific). Ion scattering spectroscopy (ISS) was processed on the same instrument, utilizing a focused He ion gun (1 keV) at a base pressure of 2.0×10^{-7} mbar. The ISS spectra were acquired with a step size of 1.0 eV.

X-ray diffraction (XRD) was conducted on a Malvern Panalytical Empyrean X-ray diffractometer in the grazing incident geometry with the incident beam angle at 0.7º. An Empyrean Cu LFF HR gun ($K\alpha_1$ = 1.540598 Å, 8.04 keV) was used as the X-ray source and operated at 45 kV and 40 mA.

Table A.1 ***Element composition acquired from ex situ XPS.*** *Three spots were taken on each sample and the average is listed in the table.*

Sample (nominal composition)	Element Distribution										
	As-prepared					After eCO2RR					
	Cu	Ag	Cu in CuAg	O	C	Cu	Ag	Cu in CuAg	O	C	K
Cu	37.0	0	100.0	42.2	20.8	26.1	0	100.0	42.8	31.1	0
$Cu_{95}Ag_5$	33.4	5.8	85.2	38.1	22.7	36.5	2.9	92.6	42.29	17.4	1.5
$Cu_{80}Ag_{20}$	36.4	14.1	72.1	28.7	20.8	28.4	7.4	79.4	41	23.17	0
$Cu_{60}Ag_{40}$	24.9	20.8	54.4	28.3	26.0	25.2	14.9	62.8	34.6	25.0	0
Ag	0	49.2	0.0	13.5	37.3	0.0	44.8	0.00	13.6	41.6	0

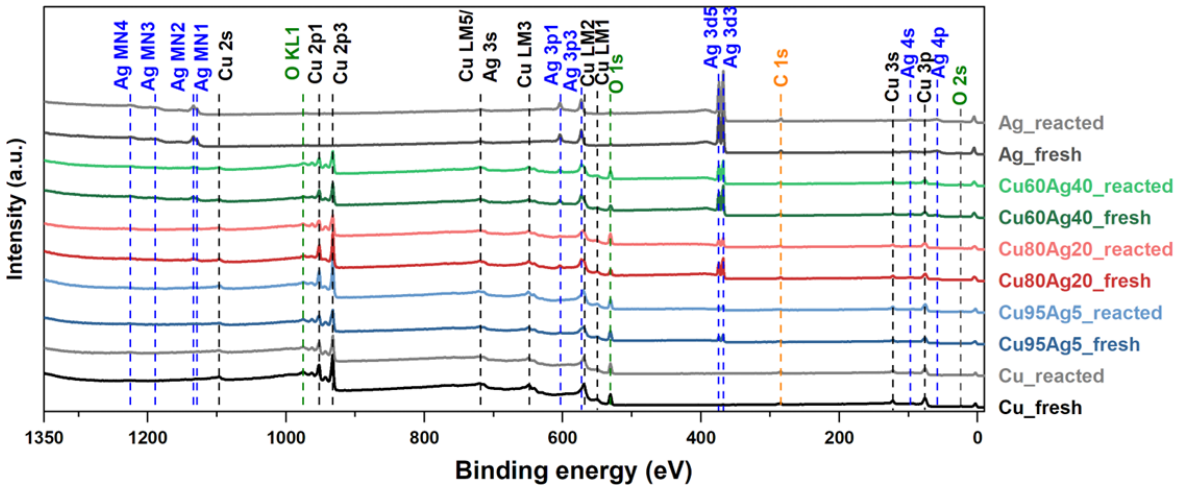

Figure A.11 ***XPS survey*** *of samples with varying Ag contents.*

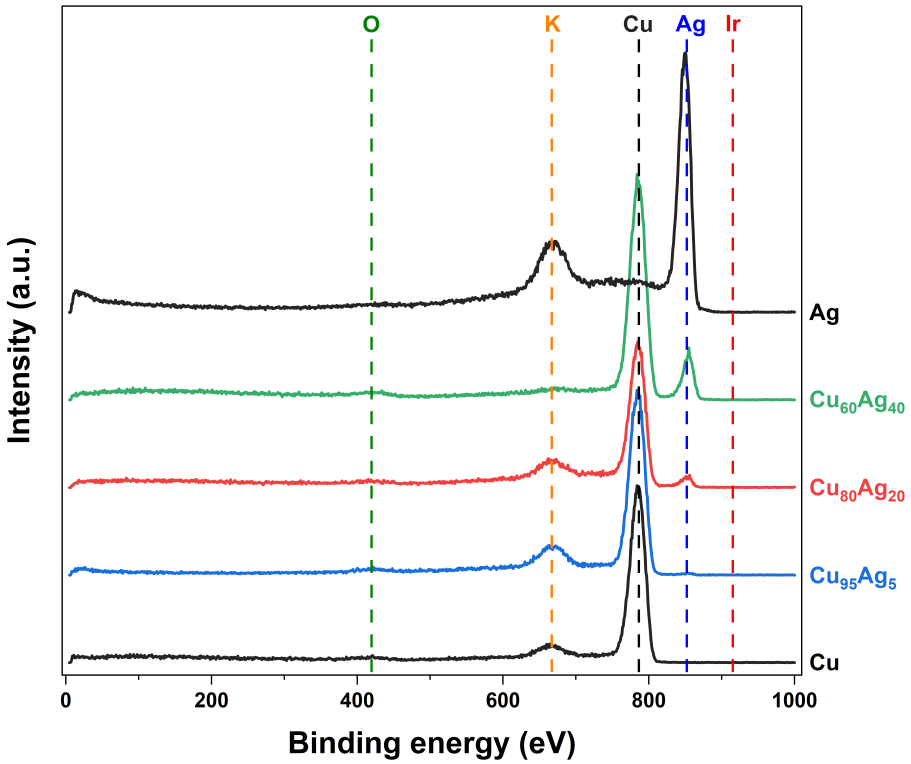

Figure A.12 ***ISS survey of postmortem samples with various Ag concentrations after eCO2RR for 2 hours.*** *The sample surface was carefully rinsed with MilliQ water and dried with pressed air before the test. Dash lines indicate the peak position of the corresponding element. K was from the not fully removed electrolyte after eCO2RR. No signal related to Ir was found in any sample.*

B.2 Electrochemical CO2 Reduction Measurements

K_2CO_3 solutions were prepared by dissolving K_2CO_3 (99.995% trace metals basis, Aldrich) into MilliQ water (18.2 MΩ.cm @25°C, 2ppb TOC, Q-POD®). 0.1M $KHCO_3$ solution was prepared by purging CO_2 (N45, Air Liquide) into 0.05 M K_2CO_3 solution for at least 30min, until pH ~ 6.8.

Electrochemical CO_2 reduction was carried out in a 2-chamber H-cell in the 3-electrode configuration. The two chambers were separated by a hydrocarbon-based ion-exchange membrane (Selemion AMV, AGC Engineering CO., LTD.), activated in 0.1 M KOH (99.995% trace metals basis, Sigma-Aldrich) overnight, and stored in MilliQ water. The liquid volume of both chambers is 6.5 mL, whereas the actual electrolyte volume was 6.0 mL in both chambers. The cathode chamber was purged with CO_2 at 10 sccm for the duration of the experiment. An IrO_2-coated carbon paper (1.0 cm x 1.0 cm, Dioxide Materials) and a miniature leak-free Ag/AgCl/Saturated KCl electrode (Innovative Instruments Inc.) were used as the counter and reference electrode, respectively.

A stagnant H-cell was chosen because the current is more stable without electrolyte flow. Moreover, it allows for concentrating on the intrinsic performance of the catalysts by minimizing potential influence from unstable liquid flow and/or dead volumes, as well as varied mass transfer conditions in different runs.

Electrochemical experiments were controlled using a BioLogic SP-200 potentiostat. Unless otherwise stated, the working electrode potential (E_{WE}) was recorded and referenced against the Ag/AgCl reference electrode (RE), which was then converted and reported in terms of the reversible hydrogen electrode (RHE) scale following the equation below. The RE was calibrated following the procedure described in [216] before use.

$$E_{RHE} = E_{WE} + E_{RE} + 0.059 \times pH \quad (1)$$

Prior to each measurement, a 10 min chronoamperometry (CA) at -0.2 V *vs.* RHE was applied to reduce the CuO_x layer, which was naturally formed when metallic Cu (or the Cu phase in CuAg bimetallic catalysts) was exposed to air. This potential was chosen because it is more negative than the CuO_x reduction potential (0.35 V *vs*. RHE) while not sufficiently reductive to produce detectable products. Cyclic voltammetry (CV) was then scanned in the potential window of -0.2 to +0.7 V three times. The redox features were used to primarily check the consistency of the same sample in different runs. A constant potential of -1.0 V *vs*. RHE was then applied and kept for 2 hours. Gas products were analyzed *in situ* with gas chromatography (GC, Thermo-Scientific, TRACE 1300), while liquid products were collected at the end of the experiment and analyzed with high-performance liquid chromatography (HPLC, Agilent 1200 series). Electrochemical CO_2 measurements were conducted three times for each sample.

The selectivity of each product was determined by its Faradaic efficiency, following calculations interpreted in Chapter 3.5.3:

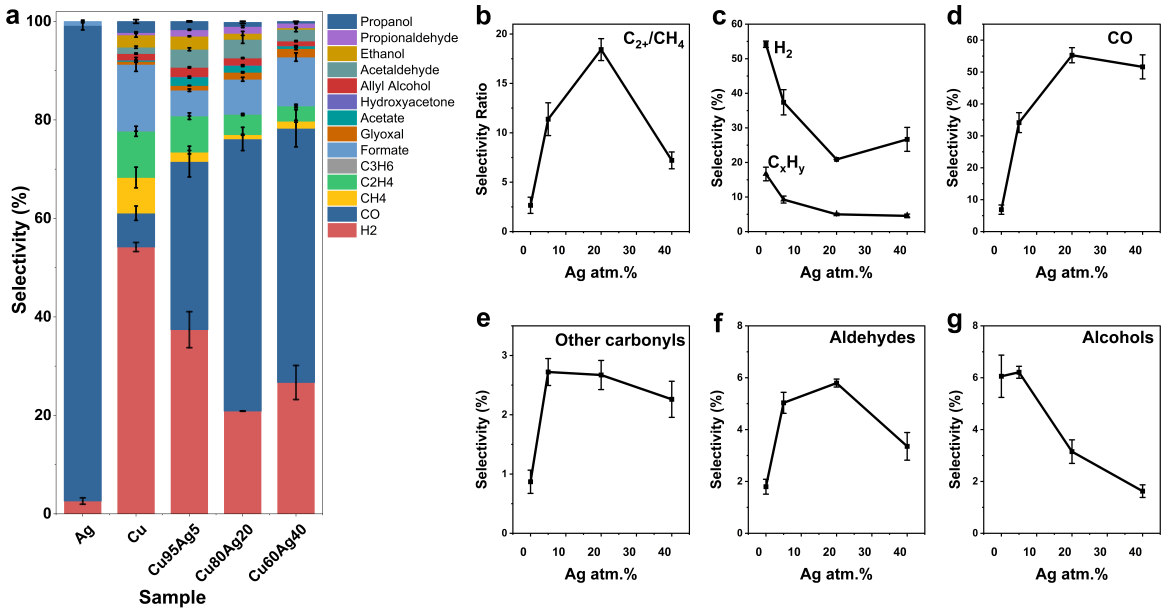

Figure A.13 ***Electrochemical CO_2 reduction performance*** *test conducted in an H-cell in CO_2-saturated 0.1 M $KHCO_3$ aqueous solution at -1 V vs. RHE for 2 hours, plotted in selectivity regarding the produced number of moles. CO_2 was continuously purged to the solution at 10 sccm during eCO2RR. a) Faradaic efficiency of all detected products. b) Faradaic efficiency ratio between *CO-originated products depending on the involvement of C-C coupling during the formation process as a function of Ag contents. c) Faradaic efficiency of H_2 and C_xH_y (CH_4, C_2H_4, C_2H_6, C_3H_6, and C_3H_8) as a function of Ag content. d) Faradaic efficiencies of CO_2 as a function of Ag content. e)-g) Faradaic efficiencies of *CO-originated products classified on C-O bond as a function of Ag content: e) other carbonyls (glyoxal, acetate, and hydroxy acetone; formate is not included), f) aldehydes (glycolaldehyde, acetaldehyde, and propionaldehyde), g) alcohols (ally alcohol, ethanol, and propanol).*

B.3 Operando X-ray Measurements

B.3-1 Experimental Details

All *operando* X-ray measurements were conducted at the Stanford Synchrotron Radiation Lightsource (SSRL) at ambient pressure and room temperature. Electrochemistry was controlled using a BioLogic SP-200 potentiostat.

Operando GIXRD was conducted at beamline 2-1, using a Si (111) monochromator and beam energy of *ca.* 17 KeV (0.729 Å). *Operando* GIXAS on the Cu K-edge in both X-ray absorption near edge structure (XANES) and the extended X-ray absorption fine structure (EXAFS) regions were collected at beamline 11-2, using a Si (220) LN2-cooled monochromator and a 100-pixel monolithic solid-state Ge detector array, in the fluorescence mode.

A previously designed 3D-printed flow cell was employed in XRD and XAS at the Cu K-edge (*ca.* 9 keV) to enable the grazing incident configuration of the sample while maintaining a higher horizontal alignment of the sample and also maintaining a high transmissivity for X-ray incidence as described in [137]. During *operando* XAS, the electrolyte being purged with CO_2 gas was pumped through the cell by a 2-channel peristaltic pump (SHENCHEN LabN6) at 50 mL/min. Cu_XAg_{100-X} catalyst samples were prepared on a Si (111) substrate, as described in Session 2.1. Two 50 μm diameter Pt wires (Alfa Aesar, 99.99%) and a miniature Ag/AgCl electrode (Innovative Instruments Inc.) served as the counter and reference electrode, respectively.

XAS data analysis was processed using SixPack156 [217], Athena and Artemis software [218].

B.3-2 X-ray Diffraction (XRD)

Table A.2 ***Operando XRD surface sensitivity verification****: attenuation and penetration depth calculation at α = 0.15º, E = 17 keV.*

Sample	Density (g/cm3)*	Penetration depth (nm)†	Lattice spacing (Å) ‡	Penetrated monolayer numbers
Cu	8.96	2.76	2.08	13.89
Ag	10.49	2.42	2.35	10.77
Ag-rich phase in $Cu_{80}Ag_{20}$	N/A	N/A	2.31	N/A
Cu-rich phase in $Cu_{80}Ag_{20}$	N/A	N/A	2.17	N/A

Peak identification converting from normal Cu kα to synchrotron setting at 17 keV is calculated according to Bragg's law:

* The density of each phase in $Cu_{80}Ag_{20}$ cannot be estimated by assuming a linear combination of the density of Cu and Ag., because we do not know how much of Cu is in the Ag-rich phase and *vice versa*.

† Penetration depth was calculated based on Beer-Lambert law.

‡ Lattice spacing was calculated from XRD, based on (111) facet for both Cu and Ag, as it is the most prominent phase shown in XRD.

$$n\lambda = 2dsin\theta$$

Where, λ is the wavelength of the x-ray, d is the spacing of the crystal layers (path difference), θ is the incident angle (the angle between incident ray and the scatter plane), and n is an integer.

$$\frac{n_1\lambda_1}{2d_1sin\theta_1} = \frac{n_2\lambda_2}{2d_2sin\theta_2}$$

For the same crystal lattice (*i.e.*, $d_1 = d_2$) and at the same n,

$$\frac{\lambda_1}{sin\theta_1} = \frac{\lambda_2}{sin\theta_2} \rightarrow \frac{sin\theta_1}{sin\theta_2} = \frac{\lambda_1}{\lambda_2} \rightarrow \frac{sin\theta_1}{sin\theta_2} = \frac{0{,}729\ \text{Å}\ (from\ synchrotron)}{1{,}5406\ \text{Å}\ (from\ ex\ situ\ XRD)}$$

$$\rightarrow \theta_1 = \sin^{-1}\left(\frac{0{,}729\ \text{Å}\ (from\ synchrotron)}{1{,}5406\ \text{Å}\ (from\ ex\ situ\ XRD)} sin\theta_2\right)$$

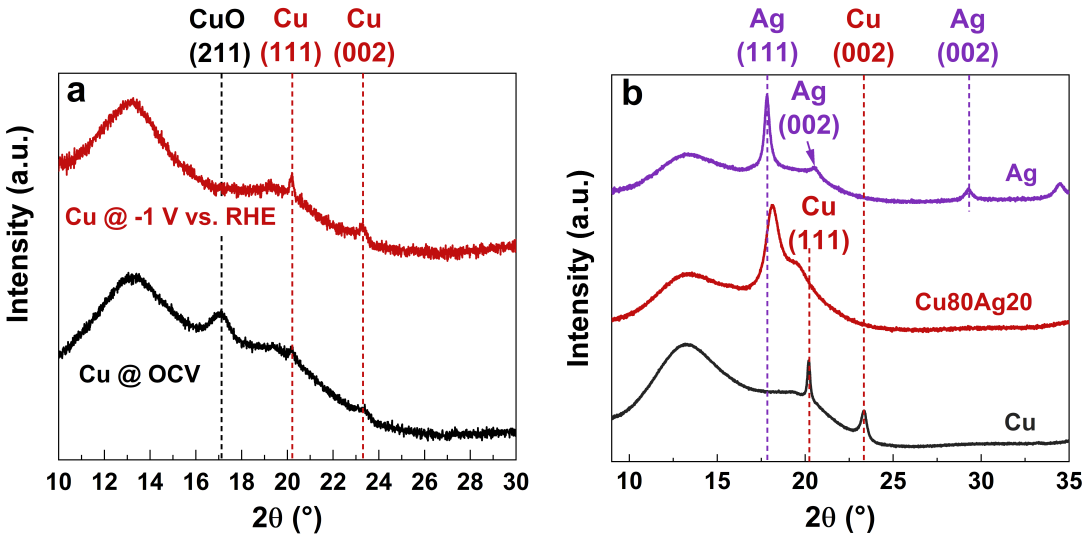

Figure A.14 ***a) Operando GIXRD surface sensitivity verification on Cu at the incident angle of 0.15°.*** *The broad peak between 2θ 16-18° in the OCV scan (black) is assigned to the phase resulting from the mixture of CuO (0 0 2) and (1 1 -1), and its disappearance at -1.0 V vs. RHE (red) indicates the absence of oxidized Cu, which validates the surface sensitivity.* ***b) Operando GIXRD spectra of Ag (top), $Cu_{80}Ag_{20}$ (middle), and Cu (bottom), respectively.*** *Dashed lines indicate the peak position of corresponding facets in pure metal samples. Dashed lines indicate the corresponding peak position in the pure Cu and Ag samples. Highlighted area A and B indicate the deconvoluted Ag- and Cu-rich phase in the $Cu_{80}Ag_{20}$ sample, respectively. The data are directly collected at the beamline without background removal. The broad peak centered at 2θ ca. 13.3° is due to the Kapton foil on the top.*

Table A.3 ***XRD peak match*** *between operando and ex situ measurements*

Facet	2θ (º)	
	Operando **(17keV)**	***Ex situ*** **(8.04 keV)**
Ag (1 1 1)	17.88	38.33
Ag (0 0 2)	20.67	44.54
Ag (0 0 2)	29.29	64.56
Cu (1 1 1)	20.23	43.54
Cu (0 0 2)	23.36	50.63
Cu (0 2 2)	33.24	74.34
CuO (2 1 1)	17.01	36.43
CuO (1 1 1)	18.07	38.75
CuO (2 0 0)	18.15	38.93
CuO (1 1 -3)	28.04	61.55

More calculations on GIXRD:

If regard each phase as a grain or a cluster composed of different concentration of Cu and Ag atoms, more information can be extracted from the GIXRD spectra pseudo-quantitatively, as listed in Table A.4.

Table A.4 ***Crystal structure parameters*** *of the pure Cu and Ag samples, as well as the two phases in the $Cu_{80}Ag_{20}$ sample.*

Sample*	Phase	Averaged crystal size¤ D_P (nm)†	Lattice spacing d (nm)‡
Cu	-	12.22	0.19
$Cu_{80}Ag_{20}$	Cu-rich	2.77	0.22
	Ag-rich	4.56	0.23
Ag	-	7.44	0.22

Number of atoms per cluster (assuming clusters are square):

Ag-rich phase: $\#_{Ag} = \frac{\left(D_{Ag}/2\right)^3}{\mathrm{d}_{Ag}^3} = \frac{(4{,}56/2)^3}{0{,}231^3} \approx 959$

Cu-rich phase: $\#_{Cu} = \frac{(D_{Cu}/2)^3}{\mathrm{d}_{Cu}^3} = \frac{(2{,}77/2)^3}{0{,}217^3} \approx 259$

Nominal (≈ obtained from XPS) molar composition:

$$\frac{n_{Cu}}{n_{Ag}} = \frac{4}{1}$$

$$\frac{\#_{Cu} * N_{Cu}}{\#_{Ag} * N_{Ag}} = \frac{4}{1}$$

Where, N_{Cu} and N_{Ag} are the number of Cu-rich and Ag-rich clusters within the detection area, respectively.

$$\frac{N_{Cu}}{N_{Ag}} \approx 14.8$$

* Calculations are based on data collected with all samples were exposed to eCO2RR conditions at -1 V *vs.* RHE for 1 h.

† Averaged crystal size was calculated based on Scherrer's Formula.

‡ Lattice spacing was calculated based on Bragg's law.

Summaries:

1. The $Cu_{80}Ag_{20}$ sample is composed of two phases: one Cu-rich and the other Ag-rich phase.

2. According to Scherrer's Formula, the average grain size of the Cu-rich phase is *ca.* 2.77mn, and that of the Ag-rich phase is *ca.* 4.56nm. Note the grain size here is an averaged value of all grains with the same phase.

3. Based on Bragg's law, we can know the averaged lattice spacing of each phase, and therefore the number of atoms in each phase: *ca.* 259 atoms in the Cu-rich phase and *ca.* 959 atoms in the Ag-rich phase. Note that each phase contains both Cu and Ag atoms, and the number of atoms here includes both atoms in each phase.

4. According to Vegard's law. In the Cu-rich phase, there is 67% of Cu and 33% of Ag; while in the Ag-rich phase, there is 84% of Ag and 16% of Cu. However, whether the minor atoms exist in the major atoms in the form of separated single atoms or agglomerated small clusters cannot be determined by the current experimental data. But I would think both circumstances exist, and based on your DFT-calculated segregation energy, the latter should be dominating (*i.e.*, most of the minor atoms are in their small clusters while the rest distributes in the major atoms "sea" as doped single atoms).

B.3-3 X-ray Absorption Spectroscopy (XAS) on the Cu K-edge

Table A.5 ***Operando GIXAS surface sensitivity verification:*** *attenuation and penetration depth calculation at $\alpha = 0.25^{o}$, E = 9 keV*

Sample	Density (g/cm3)	Penetration depth (nm)*	Lattice spacing (Å)†	Penetrated monolayer numbers
Cu	8.96	2.89	2.08	13.89
Ag	10.49	2.53	2.35	10.77

* Penetration depth was calculated based on Beer-Lambert law.

† Lattice spacing was calculated from XRD, based on (111) facet for both Cu and Ag, as it is the most prominent phase shown in XRD.

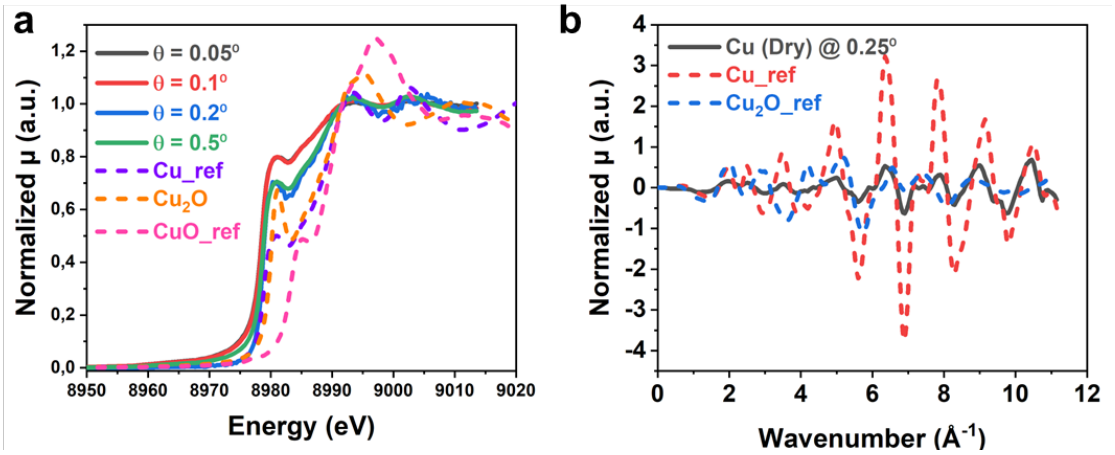

Figure A.15 ***Operando GIXAS surface sensitivity verification on Cu****: a) XANES region at different grazing incident angles. Solid lines: XANES scans at various incident angle θ; dash lines: reference scans of different Cu oxidation state that were previously taken at the same beamline with the identical setup* [137]*. The stronger absorption intensity at θ < 0.2° at the edge energy (ca. 9 keV) compared to θ ≥ 0.2° indicates a more oxidative Cu state. However, a slightly large incident angle is necessary to compensate the weak absorption intensity. Therefore, 0.25° was chosen as the incident angle for the following GIXAS measurements. B) EXAFS plotted in the k space at θ 0.25°. Solid line: scan plotted in the k space at the incident angle θ 0.25°. Dashed lines: reference scans of Cu and Cu_2O. The incident angle of 0.25° was chosen for the following GIXAS measurements. It is because the surface sensitivity check was on dry samples, as can be seen from the much better signal-to-noise ratio compared to wet (OCV, no EC connection) scans. Although when the sample was dry, even at theta 0.1 the signal quality is quite good, when the electrolyte is flowing through the reaction volume above the sample, the signal-to-noise ratio was significantly worse. This can be attributed to two reasons: i) the samples are not perfectly flat, and ii) X-ray beam refraction. When the electrolyte is flowing (driven by a parataxic pump), the liquid layer height above the sample fluctuated, plus the not perfectly flat sample surface, the signal-to-noise ratio was severely harmed as a consequence.*

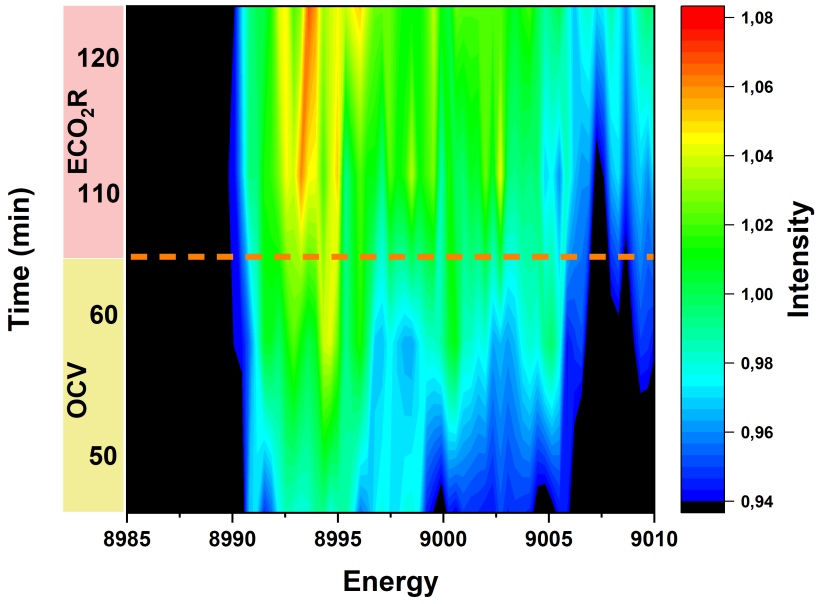

Figure A.16 ***Heat map of operando XAS scans ay the Cu K-edge in the zoomed in XANES region*** *of 8985-9010 eV of the $Cu_{80}Ag_{20}$ sample.*

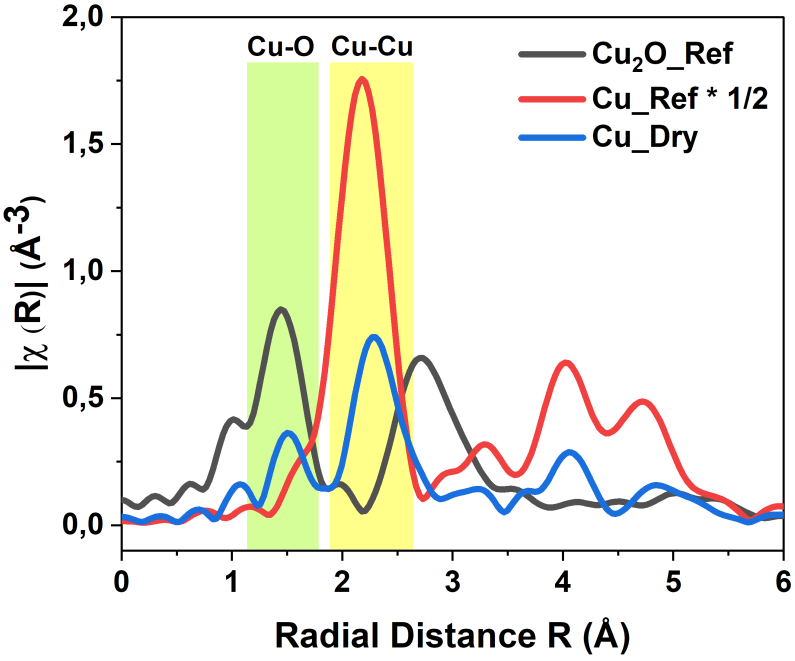

Figure A.17 ***XAS R space (k-2 weight) peak identification on the Cu K-edge.***

B.3-4 X-ray Absorption Spectroscopy (XAS) on the Ag L-edge

Ag L_3-edge (*ca.* 3.4 keV) tender XANES was performed at beamline 4-3 using a LN2 cooled Si (111) monochromator at ϕ =0°, in the fluorescence mode with a Lytle detector. A custom-designed back illumination bottle cell allowed the X-ray incident to transmit [134]. Owing to the soft excitation energy required for Ag L_3-edge, the catalysts were deposited on an ultra-thin 7.5 µm thick Kapton foil to mitigate X-ray attenuation. The layer configuration from the bottom (right next to the substrate) to the top is as the following (Figure S1): i) Ti interlayer (*ca.* 10 nm) providing a better adhesion); ii) Cu sublayer (*ca.* 100 nm) to help maintain the mechanical stability without introducing foreign elements in addition to Cu and Ag during deposition; and iii) the catalyst layer CuAg (*ca.* 5 nm), which is so thin that the incident X-ray beam can easily reach the catalyst/electrolyte interface. The total transmission at the Ag L-edge energy (*ca.* 3.35 keV) was calculated to be above 85% [219]. During the *operando* XANES scans, CO_2 was continuously purged in the electrolyte at 10 sccm. A graphite rod (Ted Pella) and the same miniature Ag/AgCl electrode as the abovementioned functioned as the counter and reference electrode, respectively. While XANES experiments were also employed to record the Ag L_3-edge, these variations were quite small and were relatively inconclusive.

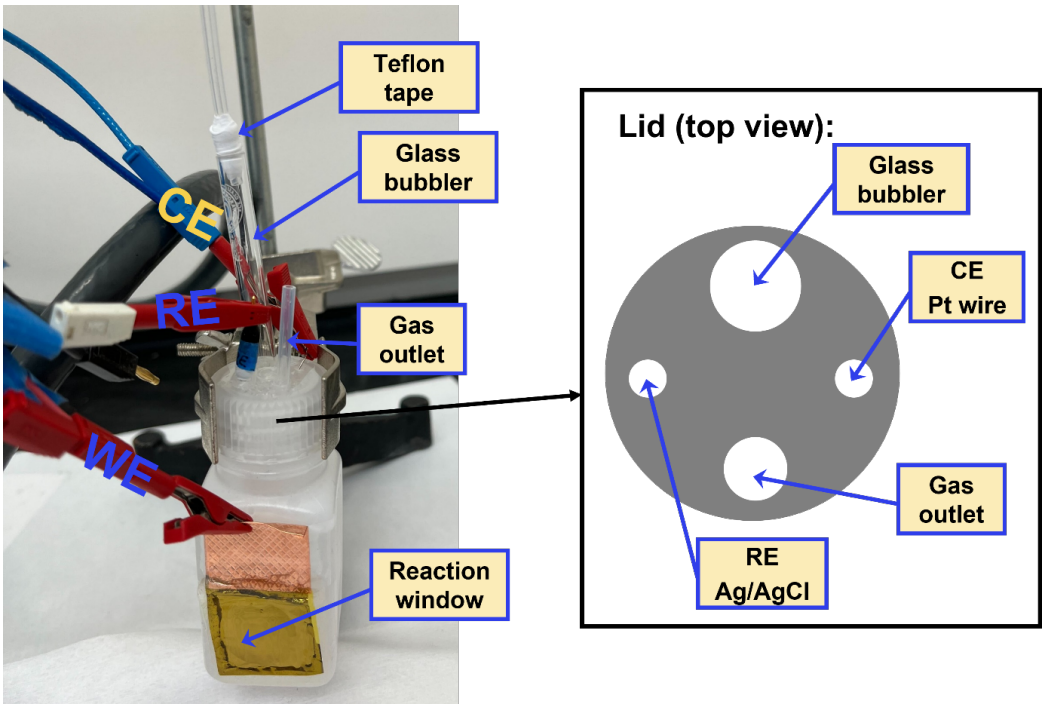

Figure A.18 ***Experiment set up for XAS measurement on the Ag L-edge.***

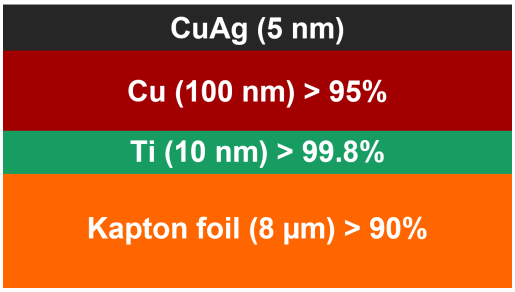

Figure A.19 ***Sample configuration and X-ray transmission of each layer*** *of back-scattered bottle cell used for XAS measurements on the Ag L_3-edge at beamline 4-3.*

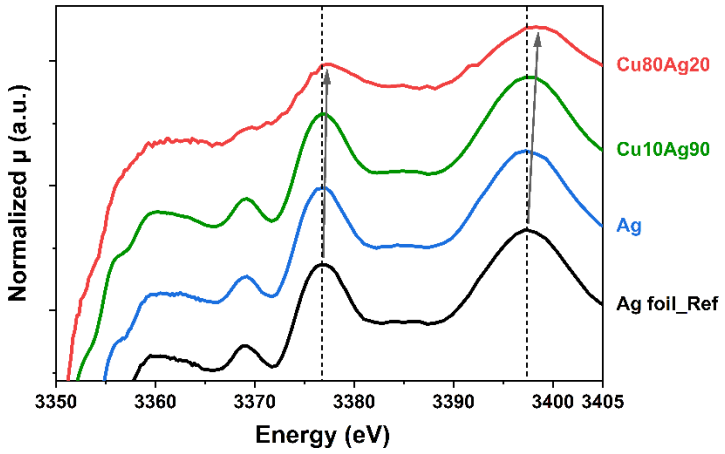

Figure A.20 ***Operando XAS scans at Ag L3-edge in the near-edge region (XANES)*** *during eCO2RR of samples with different Ag content, compared with the Ag foil reference, indicated by dashed lines. Arrows emphasize peak position shifts.*

B.4 Computational Methods

All computational simulations were conducted by Georg Kastlunger and Andreas Lynge Vishart.

The first principles analyses have been performed by density functional theory (DFT) calculations applying the Vienna ab initio package (VASP) [220]. A plane wave cut-off energy of 500 eV was used throughout, combined with the BEEF-vdW exchange correlation functional [221]. Periodic boundary conditions were applied and the number of k-points were varied based on the respective unit cell sizes. For surface calculations, a vacuum layer of at least 14 Å was added perpendicular to the slab surface, only one k-point was applied in this direction together with a dipole correction to avoid artificial interaction of repeated slabs. The charge distributions in the CuAg compositions were determined *via* Bader charge decomposition. Both the bulk and surface compositions at varying Cu/Ag ratios were sampled by comparing all symmetrically inequivalent atom distributions and optimizing both the atomic positions and lattice cell parameters. Bulk structures consisting of up to 64 atoms were considered. The most stable structures at each simulated CuAg composition were chosen for the analyses in this article. Segregation energies were calculated as the potential energy difference of a 6-layer thick Cu-slab being doped by Ag on the surface or in the 4th layer.

All theoretical data and analysis routines can be retrieved from https://gitlab.com/gkastlun/cuag_for_c2.git.

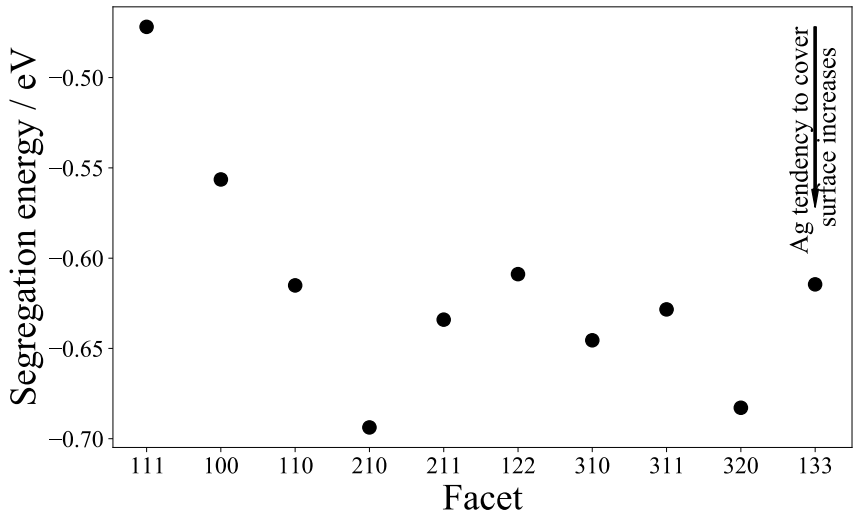

Figure A.21 ***Surface segregation energy of dilute Ag in Cu on a series of surface facets.***

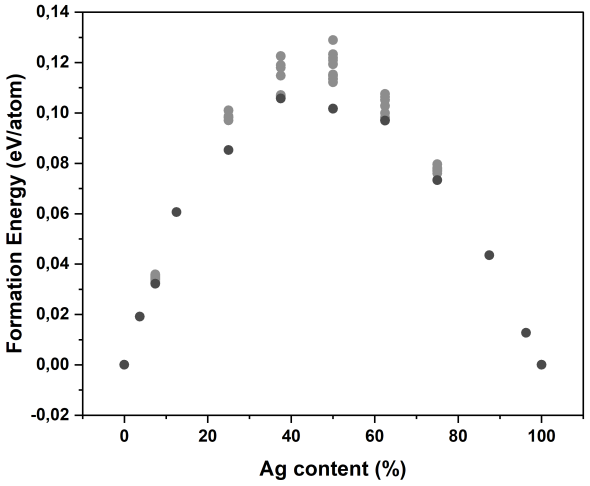

Figure A.22 ***DFT-Calculated formation energies of CuAg crystals with varying composition.*** *All possible CuAg arrangements in 2x2x2 and 3x3x3 unit cells were sampled. No stable phase of a CuAg alloy has been identified.*

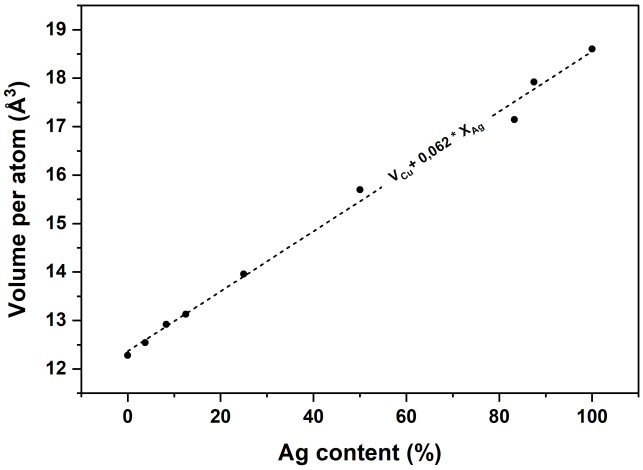

Figure A.23 ***DFT-Calculated volume per atom in a CuAg bulk crystal in dependence of the Ag content.*** *The volume per atom was chosen instead of the lattice constant as varying arrangements of Ag in Cu lead to slight deviations from the cubic symmetry into a tetragonal crystal.*

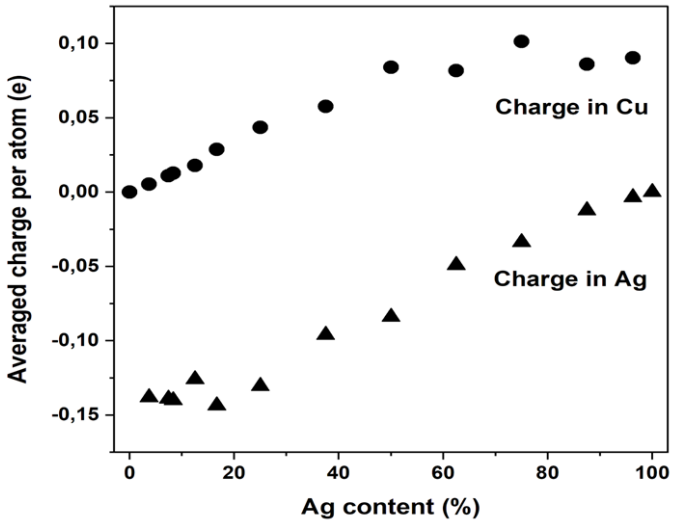

Figure A.24 ***Net mean charge per atom for Cu and Ag atoms in a bulk fcc crystal*** *of varying composition, resulting from Bader charge analysis.*

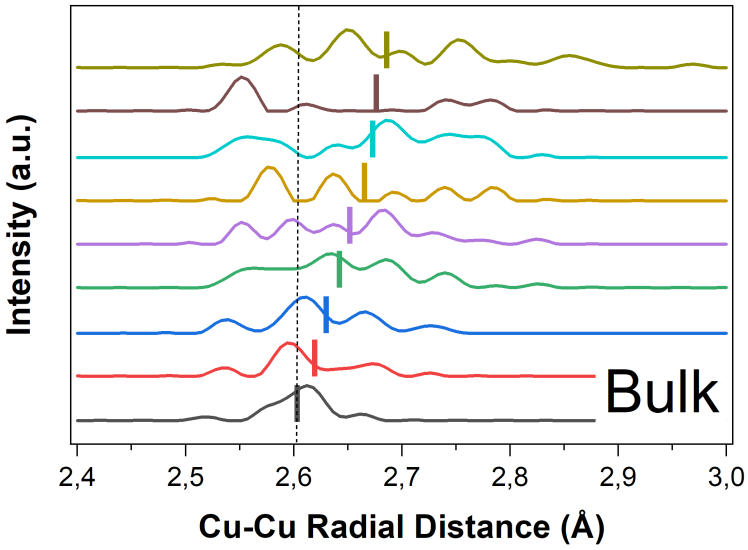

Figure A.25 ***DFT calculated Cu-Cu radial distance in CuxAg100-x at varying Ag content*** *right next to the introduced Ag atoms in bulk.*

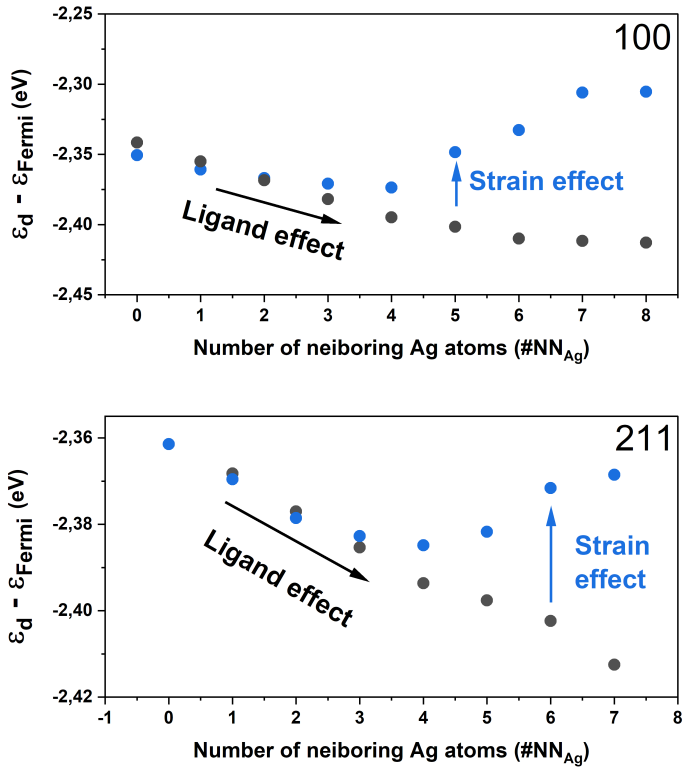

Figure A.26 ***DFT calculated Cu d-band centers*** *in dependency of the number of Ag nearest neighbors.*

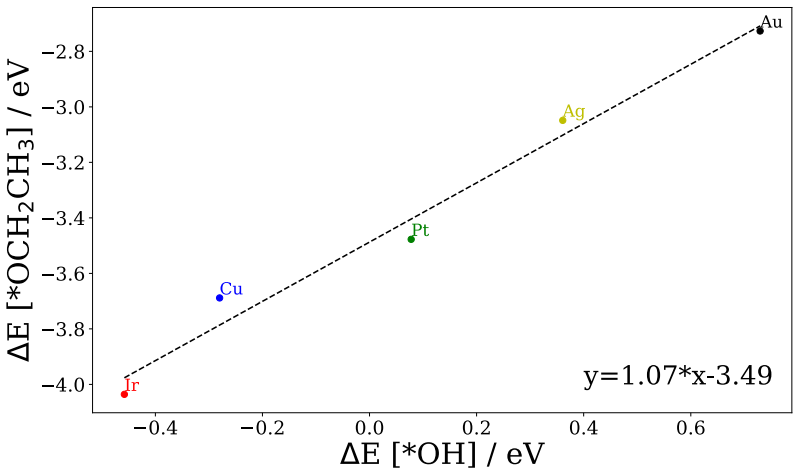

Figure A.27 ***DFT calculated scaling line of *OCH₂CH₃ with *OH****, justifying the use of the latter as a descriptor for the binding of oxygenate intermediates.*

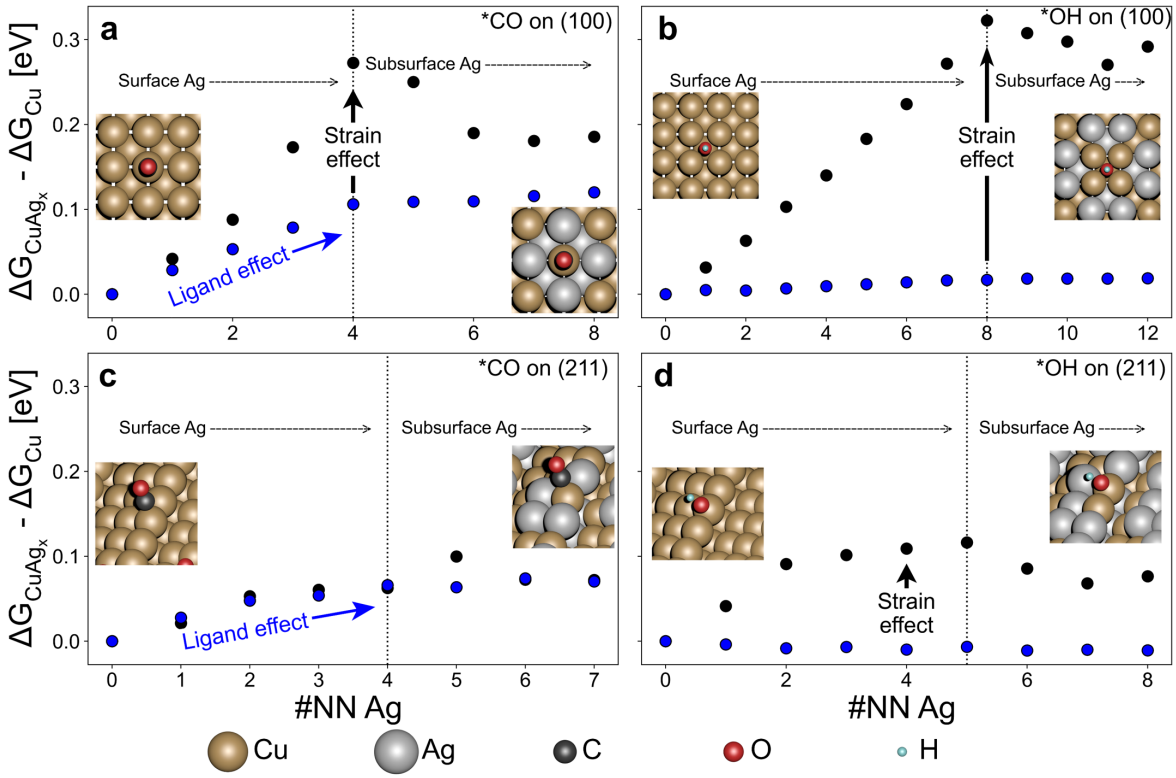

Figure A.28 ***DFT-calculated Gibbs free energy of *CO binding*** *on a) *CO on Cu (100), b) *OH Cu (100), c) *CO on Cu (211), and d) *OH on Cu (211) facets with the varying number of nearest neighboring Ag atoms (#NN Ag).*

C. Submitted Manuscript

Mechanistic Insights into Aldehyde Production from Electrochemical CO_2 Reduction on CuAg Alloy via *Operando* X-Ray Measurements

Yu Qiao, Georg Kastlunger*, Ryan C. Davis, Carlos Andres Giron Rodriguez, Andreas Lynge Vishart, Wanyu Deng, Shaofeng Li, Peter Benedek, Junjie Chen, Johanna Schröder, Joseph Perryman, Dong Un Lee, Thomas F. Jaramillo, Ib Chorkendorff, Brian Seger*

ABSTRACT: CO_2 electrolysis converts the greenhouse gas CO_2 into valuable fuels and chemicals, such as carbon monoxide, ethylene, ethanol, etc. Currently, Cu is the only known monometallic catalyst capable of producing multicarbon products from electrochemical CO_2 reduction reaction (eCO2RR), while the poor selectivity limits its further use. It has been found that introducing Ag atoms into the Cu lattice can modulate product preference. However, the synergistic effects between Cu and Ag, and thus the catalytic performance, are strongly influenced by catalyst morphology, electrolyzer configuration, reaction conditions, etc. *Operando* measurements can provide explicit information on the catalyst dynamic variation during the reaction, but their operation and analysis are challenging. Herein, we prepared CuAg multiphase alloy catalysts by magnetron sputtering, which allowed for investigating the intrinsic interaction between Cu and Ag. eCO2RR performance exhibited an improved selectivity towards carbonyls at the expense of hydrogen and hydrocarbons. The partially alloyed Cu and Ag phases were confirmed by *operando* X-ray diffraction. By means of combining *operando* X-ray measurements and density functional theory (DFT) calculations, the preferred carbonyl production is attributed to the reduced electron density and compressive strain of Cu due to Ag incorporation, which leads to a deeper d-band center and therefore weakened intermediate adsorption and oxophilicity. This work provides evidence of the intrinsic structural and electronic interaction between Cu and Ag during eCO2RR. The obtained information will facilitate the design of new bi-/multi-phase metallic or alloy electrocatalysts.

INTRODUCTION

Climate change driven by the continuously increasing CO_2 concentration in the atmosphere is one of the greatest threats facing humans. The Intergovernmental Panel on Climate Change (IPCC) released a special report (SR15) in 2018, proposing that in order to limit global warming to the safe limit, which is 1.5 ^{0}C above preindustrial levels, the global net CO_2 emission needs to reach "net zero" by 2050[1]. Electrochemical CO_2 reduction (eCO2RR) converts CO_2 into valuable fuels and chemicals, and thus helps with closing the anthropogenic carbon cycle. Among all the reported eCO2RR catalysts, Cu is the only monometallic catalyst that produces both hydrocarbons and oxygenates, while the poor selectivity limits its further use[2,3]. C_{2+} products (e.g., C_2H_4, C_2H_6, ethanol, and propanol) generally have higher energy densities and larger economic values compared to C1 products (CO, CH_4, and formate), and therefore provide a more attractive direction to aim for[4].

Ethylene and ethanol are of great interest because they are economically and energetically valuable and are produced in substantial quantities globally (> 30 MtC/yr)[2]. Literature has found that these two products share the same generation pathway after C-C coupling[5,6], which is believed to be the rate-determining step (RDS) of C_{2+} product formation[7–9]. Considering that C-C coupling usually requires a high surface CO coverage (i.e. high θ_{*CO}), and that Cu is sluggish in converting CO_2 to *CO, tandem catalysts combining Cu and a CO-selective metal (Ag, Au, and Zn) have shown to be advantageous in C_{2+} product generation[5,10–22].

Taking advantage of the high electrical conductivity, eCO2RR activity, and cost-effectiveness, Cu-Ag bimetallic/alloy catalysts have been widely investigated[18–20,23–29]. The reported Cu-Ag interaction is strongly dependent on the interplay between Ag deposition content, preparation procedures, and the resulting catalyst structure/morphology, as well as phase miscibility, which has led to different product distributions. For example, Higgins et al. synthesized a CuAg alloy with physical vapor deposition (PVD).[23] Compared to pure Cu, the CuAg selectivity of acetaldehyde increased at the expense of ethanol. This was attributed to the reduced oxophilicity when introducing Ag in the Cu lattice, which weakened the adsorption of acetaldehyde and thus its further reduction to ethanol. A similar phenomenon was also observed on CuAg bimetallic catalysts with separated Cu and Ag phases[20,30]. Although with distinctive catalyst structures (Ag nanoparticle-decorated Cu nanocubes[30] and galvanically exchanged Cu foil with Ag[20]), Clark et al. and Herzog et al. both attributed the weakened carbonyl-containing intermediate adsorption to the locally compressive strain by introducing Ag in the Cu surface. In contrast, Su et al. suggested an improved oxygen affinity for oxygen-adsorbed intermediates instead, resulting in improved ethanol production when the Cu/Cu_2O composite was dispersed with trace amounts of

Ag[31].

The above divergencies demonstrate a yet-to-be-fully-understood mechanism of the interaction between Cu and Ag in eCO2RR, which generally falls into three aspects: i) if Cu and Ag have miscible phases, ii) if there is electronic and/or structural interaction between Cu and Ag, and if so, iii) how is the intermediate adsorption influenced and the resultant variation in selectivity. Being able to track the catalysts' variations in crystallite and coordination environment in the eCO2RR environment can provide more insightful information regarding the above points. Therefore, *operando* measurements are indispensable in helping support traditional H-cell fundamental work.

Herein, CuAg multiphase alloys with various Ag concentration were prepared by magnetron sputtering, which not only ensures Cu/Ag interfaces, but also produces a consistent deposition that rules out potential inconsistencies in facet distributions or morphology. This approach allows for the focus to be on the intrinsic performance of the Cu-Ag interaction. The result presented herein showed eCO2RR performance with an improved selectivity towards carbonyls at the expense of H_2 and hydrocarbons upon Ag introduction. To provide further insight, the structural and electronic effects between Cu and Ag were investigated by *operando* grazing incident X-ray diffraction (GIXRD) and grazing-incident X-ray absorption spectroscopy (GIXAS). Combined with density functional theory (DFT) calculations, these analyses lead us to conclude the altered product propensity was attributed to the shared electron cloud density redistribution and strain effect due to Ag incorporation, which lowers the d-band center of Cu and therefore weakens the adsorption of CO and other oxygen-containing intermediates. Although several previous studies on similar systems have proposed a variety of possible Cu-Ag interaction mechanisms, this work evidenced these hypotheses by *operando* X-ray measurements combined with computational simulations to make the argument more solid.

RESULTS AND DISCUSSION

Catalyst preparation and *ex situ* characterizations. All catalysts were co-deposited on a Si wafer by magnetron sputtering, which not only enables a controllable composition, but has also been shown to yield metastable miscibility between this two thermodynamically immiscible metals[24]. In such a way, the Cu/Ag interfaces are also ensured, which minimized the influence of geometric and structural engineering and therefore enables focusing on the intrinsic performance of the CuAg system.

The near-surface Cu/Ag composition of each sputtered sample was examined by X-ray photoelectron spectroscopy (XPS). Figure 1 shows the *ex situ* XPS spectra of all as-prepared catalysts with various Ag concentrations. No impurity element was found in the survey scans (Figure S1) of as-prepared and post-mortem catalysts. Low Energy Ion Scattering (LEIS) spectra (Figure S2) of post-mortem samples also exhibit an absence of impurity elements. Two satellite peaks in Cu 2p orbital (Figure 1a) indicate the existence of Cu^{2+}, which is inevitable for ex *situ* XPS measurements considering that Cu is easily oxidized once exposed to air. The weaker peak intensity of Ag 3d scans (Figure 1b) after eCO2RR compared to their as-prepared counterparts appeared in all compositions suggests a less concentrated Ag surface composition after eCO2RR. Near-surface composition (5-10 nm) of all samples before and after eCO2RR are listed in Table S1. It is worth pointing out that since Cu and Ag are both susceptible to oxygen in the air, information on the oxidation state and near-surface element composition obtained from ex situ XPS can only provide a preliminary evaluation, while *operando* X-ray measurements (*vide infra*) will be able to give better insight into the catalyst in its active state. Note that although the real Cu-Ag composition is slightly different than expected, the nominal composition was used in this paper for convenience and simplification.

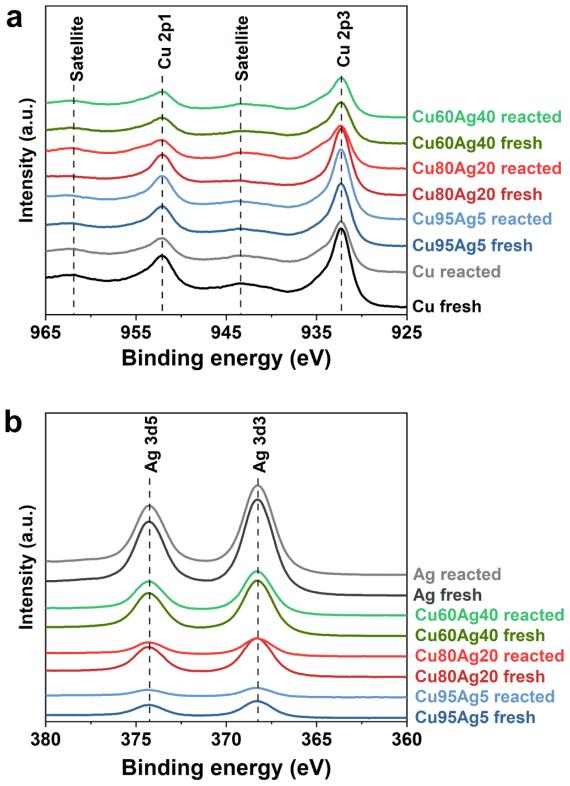

Figure 1. ***Ex situ*** **high-resolution XPS element scan spectra** of samples with various Ag compositions: a) Cu 2p orbital and b) Ag 3d orbital.

To understand the influence of Ag incorporation on the crystal structure of Cu, *ex situ* grazing incident (GI)XRD patterns (Figure 2) of as-prepared samples were collected. Both pure Cu and Ag samples agree well with the characteristic Cu and Ag peaks without noticeable position shifting. After Ag was introduced into the Cu, two broad peaks appeared at a 2θ of 35-45^0, where peak A (blue area) and peak B (green area) most likely stem from the shifted and broadened Ag (111) and Cu (111) peaks, respectively. Peak shifting indicates lattice strain of the Cu and Ag phases induced by each other[32,33]. Additionally, the reduced signal-to-charge ratio and broadened peaks may be attributed to the worse atomic arrangement and smaller crystallite size, respectively, as a result of inter-diffused Cu and Ag domains. Thus, these XRD results suggest the formation of multiphase alloys in the CuAg samples, where one is Cu-rich (with Ag being the minority), and the other is Ag-rich

(with Cu being the minority). This conclusion is supported by the DFT-based convex hull, shown in Figure S12. No uniform phases of CuAg with fixed composition could be identified by theoretically sampling varying CuAg compositions and arrangements, suggesting a phase separation proficiency of the two elements. Nevertheless, since it is the Cu sites that produces multicarbon products, the Cu-rich phase is expected to be dominating. Therefore, our following analyses will be mainly focusing on the Cu-rich phase (however both phases will still be considered for H_2 and CO production as explained below).

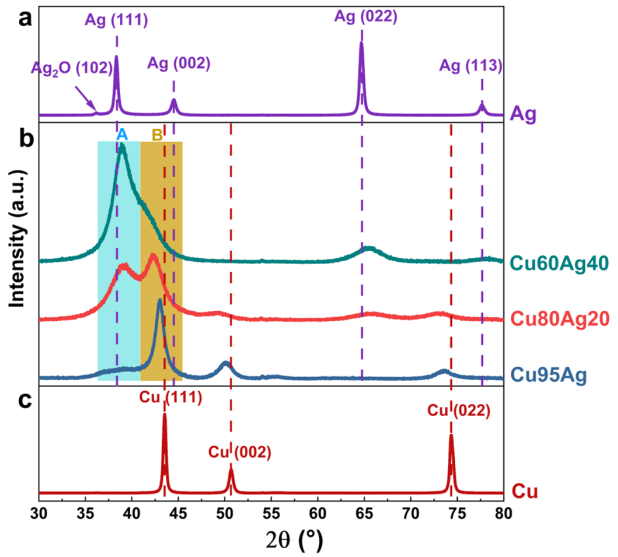

Figure 2. ***Ex situ* XRD pattern** of a) Ag, b) Cu_xAg_{100-x}, and c) Cu. Dash lines indicate the peak position of each facet in the pure metal samples. Highlighted A and B areas indicate the Ag- and Cu-rich phase, respectively.

The absence of peaks related to oxidized Cu in the pure Cu sample indicates that the incident beam penetrated much deeper than the topmost sample layers. Although *ex situ* XRD measurements were conducted in a grazing incident geometry, the incident angle could only be as shallow as 0.7^0 beyond which the signal-to-noise ratio was insufficiently high for an accurate analysis.

ELECTROCHEMICAL CO_2 REDUCTION PERFORMANCE

Figure 3a gives an overview of the distribution of all detected products for Cu, Ag and various Cu-Ag alloys as reflected by their Faradaic Efficiency (FE). (Selectivity regarding the produced number of moles of each detected product was plotted in Figure S4.) In contrast to Cu being able to produce a variety of products, Ag mainly produces CO, as well as a small amount of H_2 and formate under eCO2RR conditions. The slightly above 100% total FE may be due either to an experimental error in measuring or not using outlet flow rates from the reactor due to experimental difficulties. Either way, this slight offset is not expected to affect the trends and conclusions of this work.

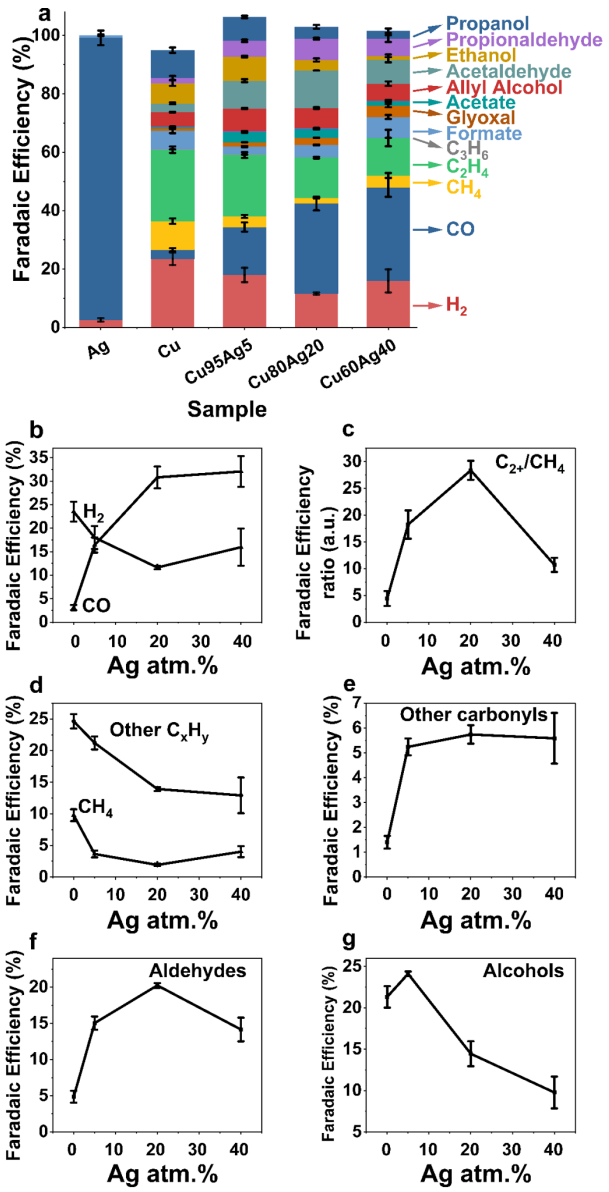

Figure 3. **eCO2RR performance test** conducted in an H-cell with CO_2-saturated 0.1 M $KHCO_3$ aqueous solution at -1 V vs. RHE for 2 hours. The electrolyte was continuously purged with CO_2 at 10 sccm during eCO2RR. a) Faradaic Efficiency of all detected products. b) Faradaic Efficiency of H_2 and CO as a function of Ag content, and c) Faradaic Efficiency ratio between C_{2+} products and CH_4 (all are *CO-originated) as a function of Ag content. d) Faradaic Efficiency of CH_4 and other hydrocarbons (CH_4, C_2H_4, C_2H_6, C_3H_6, and C_3H_8) as a function of Ag content. e)-g) Faradaic efficiencies of *CO-originated products containing C-O bond as a function of Ag content: e) other carbonyls (glyoxal, acetate, and hydroxy acetone; formate is not included), f) aldehydes (glycolaldehyde, acetaldehyde, and propionaldehyde), g) alcohols (ally alcohol, ethanol, and propanol).

Figure 3b shows a promoted CO while suppressed H_2 production, as the Ag concentration increased. This is as expected given that Cu is known to have a higher H_2 selectivity, whereas Ag has a strong selectivity towards CO. In CuAg alloys, CO produced on Ag can also create a high local CO partial pressure at the adjacent Cu sites[14,18,20], leading

to a CO-enriched local environment, which facilitates the following C-C coupling and thus suppresses direct *CO hydrogenation to produce CH_4, as shown in Figure 4b and c. Previous DFT calculations also revealed weakened *H binding on the Cu surface as *CO coverage increases[34] with experimental results validating this[35]. Considering that Cu is located at the weak binding side of the volcano plot of H_2 evolution, a weaker *H binding energy will further suppress H_2 production[36]. This may be one reason for the hampered production of H_2 (Figure 3b)[20,37].

Aldehydes and other carbonyls (excluding formate since it branches from CO and other *CO-originated products in an early stage[2]) both exhibit a selectivity peak with $Cu_{80}Ag_{20}$ (Figure 3e and f), accompanied by restrained alcohol (Figure 3g) and hydrocarbon (Figure 3d) production.

to form a chemical bond with oxygen atoms of intermediate molecules) of Cu, leading to weakened adsorption of carbonyl intermediates on the Cu surface[20,40,41]. Another theory that has been proposed to explain the reduced oxophilicity of Cu is that electron density shifts from Cu to Ag at the interface, driven by the difference in their electrochemical potential[15,42]. The above electronic interaction would decrease the electron density of Cu[15,32,41,43] at a negative potential[30,44,45]. As a result, aldehyde would desorb from the catalyst surface before being further reduced to alcohols[20,30,45].

To gain more insights into the effects of Ag on C-C coupling, Figure 3c looks at the branching point between C-C coupling to C_{2+} products versus protonation to the C1 product CH_4. The promoted C_{2+}/CH_4 ratio primarily occurs by the suppressed CH_4 formation upon alloying with Ag, as

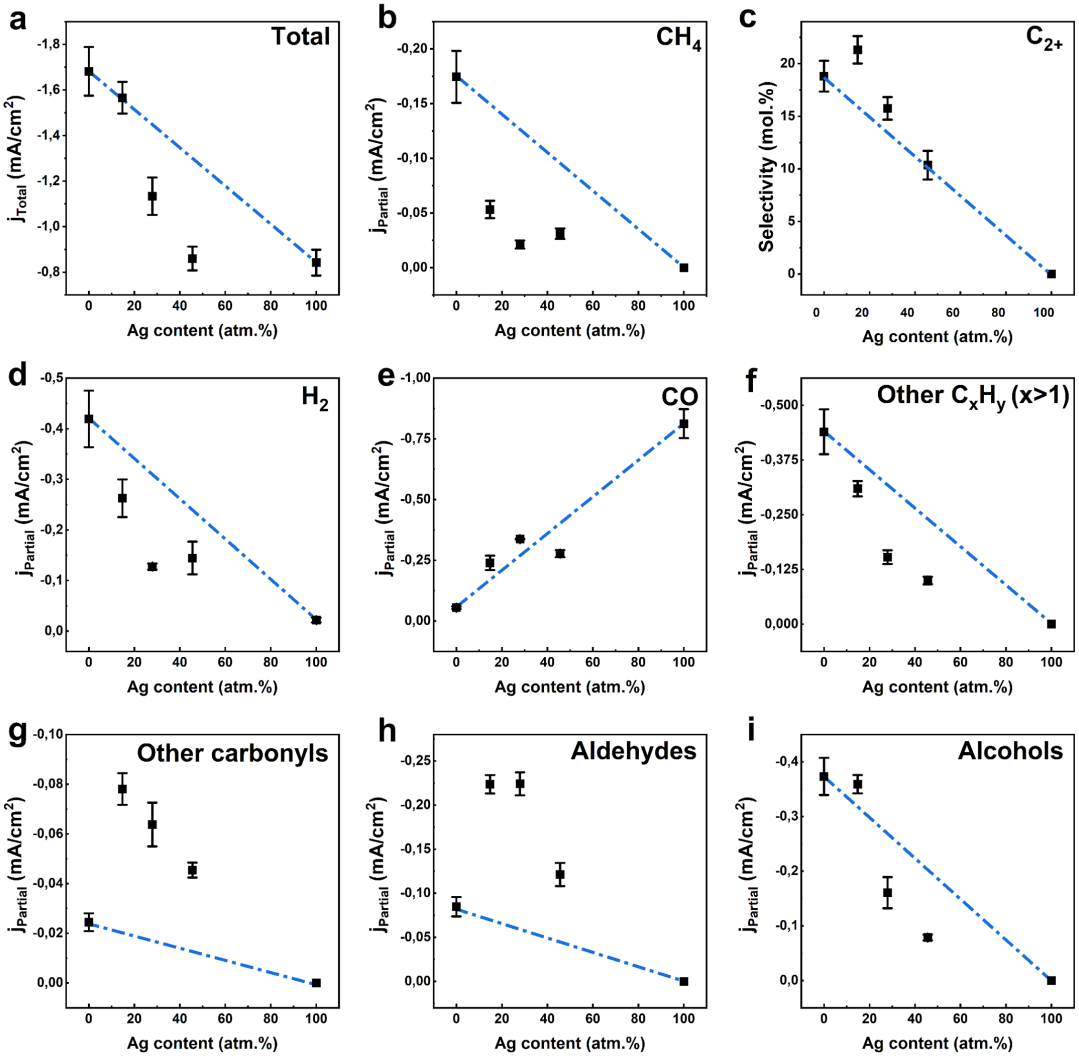

Figure 4. **Current density as a function of Ag content.** a) Total current density. Partial current density of b) CH_4, c) C_{2+} products, d) H_2, e) CO, f) other C_xH_y excluding CH_4, g) other carbonyls excluding aldehydes, h) aldehydes, and i) alcohols.

Introducing Ag would be expected to lead to a local compressive strain of the Cu lattice, due to the larger atomic size of Ag (r ~ 172 pm) compared to Cu (r ~ 128 pm). This strain effect should shift the Cu valence band structure to deeper levels, which reduces the binding energy of intermediates[38,39] as well as the oxophilicity (the tendency

shown in Figure 4b. This can be a convolution of multiple reasons: i) modified adsorption strength of *CO versus *H as mentioned above (because previous studies have found that the rate-limiting step for methane production is involved with *H [46]), ii) preferential Ag deposition on undercoordinated sites versus terraces, and iii) Ag tends to ag-

glomerate into small islands due to its lower surface energy[47]. A prominent decline of the C_{2+}/CH_4 ratio occurs with alloys with Ag content greater than 20 atm.%. This could be attributed to that as Ag composition continuously increases, the excessive Ag atoms will cover too many Cu sites, leaving less Cu-Cu neighbors where CO* adsorption and C-C coupling happen. Considering that C-C coupling requires two adsorbed CO* in adjacent while CH_4 formation only requires one, a lower C_{2+}/CH_4 ratio is expected. This phenomenon has been observed by scanning electron microscope (SEM) on CuAg thin films under eCO2RR conditions, where the importance of an optimal CO* availability was emphasized for an efficient C-C coupling[42].

Current density (at a constant potential) as a function of the near-surface Ag composition (as measured *via* XPS) enables investigating the reaction kinetics influenced by Ag incorporation. This is plotted in Figure 4. The dashed lines are linear predictions by assuming that the Cu and Ag sites function separately without interaction between them. The lower total current density relative to the linear expectation shown in Figure 4a indicates a reduced overall activity upon Ag introduction. DFT calculations on the segregation energy of Ag on various Cu facets indicate the propensity of introduced Ag to distribute on the Cu undercoordinated sites compared to terraces (Figure S11). Considering that literature has widely shown that undercoordinated sites are generally more active than terraces in polycrystalline Cu[2,48–50], the overall activity is expected to be reduced. Moreover, previous studies have found that by occupying Cu undercoordinated sites with Ag, not only was *H binding energy weakened and thus suppressed HER (as explained in Figure 3b)[23], but further reduction of acetaldehyde to ethanol would also be mitigated[26]. With Ag preferentially depositing on the undercoordinated sites, this effect can also influence the C_{2+} versus methane product ratio.

The good agreement of Figure 4 (partial current density) and Figure 3 (Faradaic Efficiency) of each product classification reveals a synergistic effect between Cu and the incorporated Ag on the facilitated aldehydes/other carbonyls production at an expense of H_2/C_xH_y formation.

From the above discussion, the altered product preference could be a convolution of several effects created by introducing Ag in Cu, including spatial effects, compressive strain, oxophilicity variations, electronic interaction between Cu and Ag, CO* and *H adsorption, Ag incorporation site, etc. To deconvolute these possibilities, *operando* X-ray measurements were employed to provide structural and electronic information on the Cu-Ag interaction in the course of eCO2RR. Considering that the most promising performance (i.e. the most promoted aldehydes/other carbonyls generation and facilitated C-C coupling) occurs on sample $Cu_{80}Ag_{20}$, this alloy was used in the following synchrotron measurements.

OPERANDO GRAZING INCIDENT X-RAY DIFFRACTION (GIXRD)

To monitor the crystal structure of the catalyst during eCO2RR, *operando* GIXRD was conducted. Given that catalysis occurs at the surface, the surface sensitivity of the measurement geometry was analyzed with pure Cu initially. Since Cu is known to be easily oxidized when exposed to air, the top surface is expected to resemble an oxidized Cu (CuO_x). Figure 5a exhibits a prominent peak related to CuO at open circuit voltage (OCV), which is in stark contrast to its absence at -1 V vs. RHE. Oxidized Cu being reduced to metallic Cu under eCO2RR conditions have been widely observed by SERS. [51,51,52] The poor signal-to-charge ratio is a consequence of the fast scan rate due to beamtime limitations. Nevertheless, the disappearance of the prominent CuO(211) peak at negative potential further validated the surface sensitivity of the incident angle of 0.15^0 (this is much shallower than what was used in *ex situ* XRD since the *operando* X-ray beam source energy is higher), corresponding to ~2.8 nm of penetration depth (~13.3 monolayers). The corresponding X-ray attenuation depth and penetrated monolayer numbers of each sample were listed in Table S2.

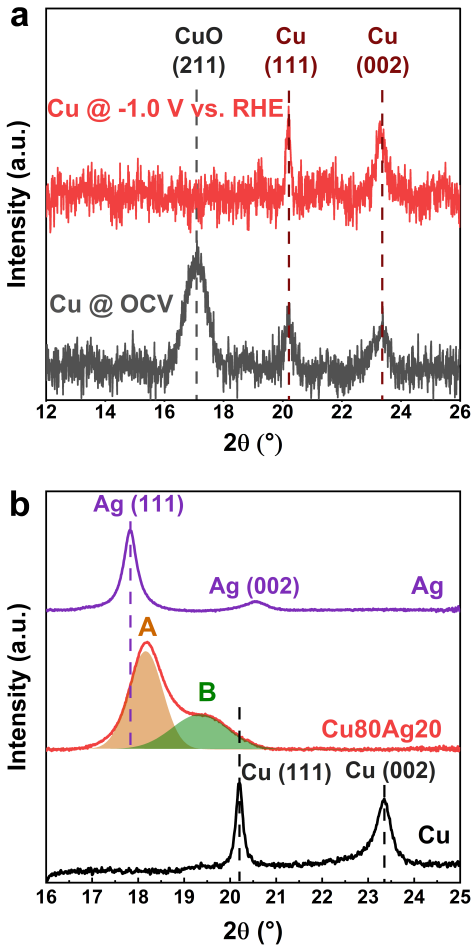

Figure 5. **a) *Operando* GIXRD surface sensitivity verification on Cu at the incident angle of 0.15^0.** The broad peak between 2θ 16-18^0 in the OCV scan (black) is assigned to the phase resulting from the mixture of CuO (0 0 2) and (1 1 -1), and its disappearance at -1.0 V vs. RHE (red) indicates the absence of oxidized Cu, which validates the surface sensitivity. **b) *Operando* GIXRD spectra of Ag (top), $Cu_{80}Ag_{20}$ (middle), and Cu (bottom), respectively.** Dashed lines indicate the peak position of corresponding facets in pure metal samples. Dashed lines indicate the corresponding peak position in the

pure Cu and Ag samples. Highlighted area A and B indicate the deconvoluted Ag- and Cu-rich phase in the $Cu_{80}Ag_{20}$ sample, respectively. Backgrounds are removed.

The different peak position from that in *ex situ* XRD is induced by the applied X-ray source energy. Table S3 demonstrates peak matching between *ex situ* (8.04 keV) and *operando* (17 keV) GIXRD measurements.

During operando measurements, a working electrode potential of -1 V vs. RHE was applied to the catalyst and kept for 1 hour, during which 6 consecutive scans (~10 min for each scan) were collected and averaged to reduce the signal/noise ratio. Figure 5b shows the same phenomenon regarding peak shift as seen via ex situ measurements (Figure 2).

OPERANDO GRAZING X-RAY ABSORPTION SPECTROSCOPY (XAS)

An XAS spectrum is comprised of two regions: the X-ray absorption near edge structure (XANES) region, which is located within ~100 eV around the absorption edge; and the extended X-ray absorption fine structure (EXAFS) region, which extends up to ~1000 eV after the absorption edge. The XANES spectra identify the oxidation state and local geometric structure of the absorber atom; while the EXAFS region contains information on the local chemical environment surrounding the central absorber atom, such as coordination number, atomic shell distance, etc.[53]

The surface sensitivity of GIXAS was verified by comparing XANES spectra taken at different incident angles. In order to produce a reasonable signal-to-charge ratio, an incident angle of 0.25^0 corresponding to a penetration depth of ~2.9 nm (13.9 monolayers) was used for the following GIXAS measurements. Further details can be found in Figure S5. At the bottom of Figure 6a, both pure Cu and Cu_2O reference XANES spectra are shown. While the absorption edge (8980-8982 eV) has a subtle difference, there is a notable difference in the energy range of 8990-9020 eV under open circuit voltage (OCV) and eCO2RR (-1 V vs. RHE) conditions: metallic Cu has one peak in the energy range of 8991-8997 eV (noted as A1) and one peak at ~9002 eV (noted as A2), with the same intensity; while Cu_2O only exhibits one peak in A1. Since XANES gives integral information of all detected Cu atoms regardless of oxidation state, a combination of metallic and oxidized Cu would have a higher intensity of A1 relative to A2, since both oxidation states contribute to the former while only metallic Cu contributes to the latter. Therefore, the more distorted intensity of A1 to A2 is, the more Cu_2O there is. This enables a qualitative indication of the transformation from Cu_2O to Cu at the surface.

The top four scans in Figure 6a show the pure Cu sample at OCV and subsequently being exposed to eCO2RR conditions (@ -1.0 V vs. RHE). The spectra at OCV appear to be primarily metallic Cu, which is expected given that the penetration depth of 2.9 nm is a bit thicker than the native oxide layer, entailing a strong background Cu signal. However, a detailed look at the data showed there is a noticeable difference. To make the spectra difference more explicit, Figure 6b enlarges the energy range of 8985-9010 eV and transforms it into a heat map plot. It can be clearly seen that A1 has a higher intensity than A2 at OCV while both areas reached the same intensity under eCO2RR conditions.

Figure 6c compared pure Cu to the $Cu_{80}Ag_{20}$ sample, where an evident difference can be seen. The worse signal-to-noise ratio of the $Cu_{80}Ag_{20}$ spectra can be attributed to the lower Cu composition as well as smaller crystallite sizes and/or worse crystallinity, as also indicated by the XRD results (Figure 5). In contrast to pure Cu, where two separated peaks in A1 and A2 are present, only one wide wave in the energy range of 8985-9010 eV exists in the

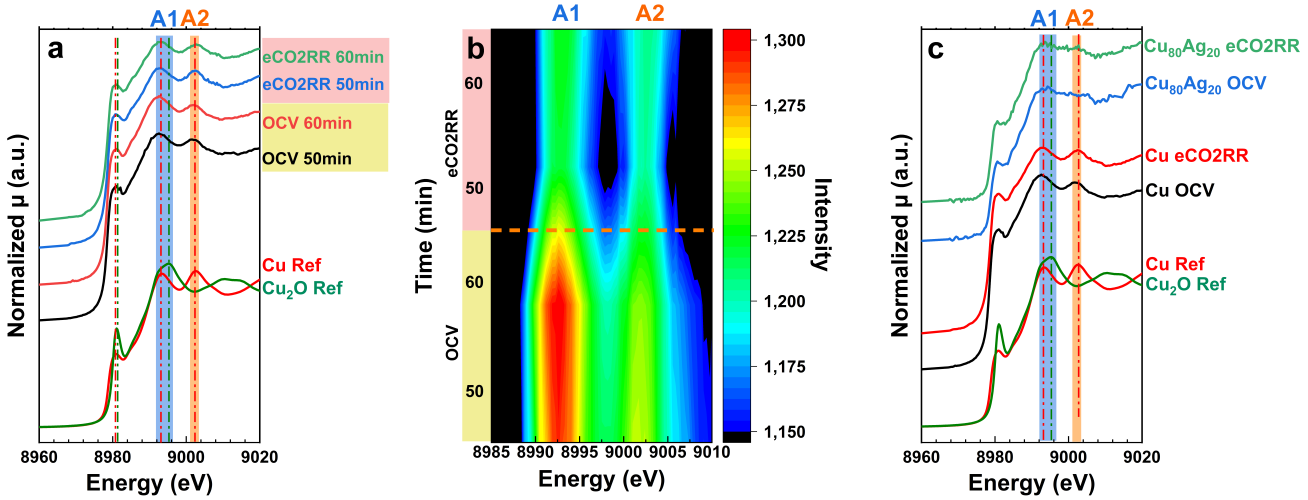

Figure 6. ***Operando* XAS scans at the Cu K-edge.** a) XANES region of Cu and Cu_2O references (bottom), and the pure Cu sample at open circuit voltage (OCV) and -1 V vs. RHE (eCO2RR), respectively. The labels 50 min and 60 min mean the amount of time the samples had been exposed to the corresponding conditions. b) Heat map of the highlighted energy ranges A1 and A2 in a) within 8985-9010 eV. c) Comparison of Cu and $Cu_{80}Ag_{20}$ samples at OCV and COR conditions, respectively. Each spectrum was the average of two scans at 50 and 60 min being exposed to the corresponding condition, respectively. Spectra of the Cu and Cu_2O references are plotted at the bottom. Each spectrum was subtracted by its pre-edge background and normalized by the edge height.

$Cu_{80}Ag_{20}$ spectra. Thus, these spectra appear to be more similar to the Cu_2O reference. This suggests a reduced electron density in the Cu phase upon introducing Ag, compared to the case of pure Cu. Furthermore, this reduced electron density would also suggest that less electron density variation would be seen when switching from open circuit voltage to eCO2RR conditions. As expected, a zoom-in of the $Cu_{80}Ag_{20}$ during the transition from OCV to eCO2RR similar to Figure 6b shows a much less noticeable variation in A1 relative to A2 in the corresponding energy range (Figure S6). XANES spectra at the Ag L3-edge were also analyzed but did not show significant changes as Ag composition varied (Figure S10). In order to build a concrete conclusion from these trends, DFT calculations were also employed later in this work.

COMPUTATIONAL SIMULATIONS

In order to verify the strength of the found charge transfer and strain effects and their influence on the binding of eCO2RR reaction intermediates, we performed DFT calculations on the CuAg system. Although our XRD results indicate the existence of two phases, one Cu-rich and the other Ag-rich (Figures 2 and 5), considering that both the nominal and near-surface composition (Table S1, Figure S1, and S2) indicates the dominating composition of Cu in general, and that it is the Cu sites that are active for C_{2+} product formation, our simulation focused on the Cu-rich phase. Both the bulk and surface structures of Cu with varying Ag content (x_{Ag}) were screened, where for each x_{Ag} all symmetrically unique atomic arrangements were sampled and the most stable motifs were identified (see Methods section for further details). Note that only metallic Cu was considered in the simulations based on the experimentally observed disappearance of CuO_x under eCO2RR conditions.

The performed DFT calculations support the spectroscopic suggestions of an electron density shifting in the Cu phase upon Ag introduction compared to pure Cu. In the case of dilute Ag concentrations in the bulk crystal (< 30 atm.%) where Ag atoms are generally surrounded by Cu, each Ag atom gains *ca.* 0.14 electrons on average, leading to a charge redistribution in the surrounding Cu atoms in order to keep a neutral charge in the crystal (Figure S14). The same qualitative behavior was found for Ag covering the Cu crystal surface, as shown in Figure 7a-c for the (111), (100) and (211) facets of Cu with varying Ag surface coverage. However, the magnitude of the charge on Ag is reduced with respect to the bulk crystal as the number of neighboring Cu-atoms is decreased on the surface. The determined charge per Ag atom linearly decreases beyond an Ag coverage of 30%, as Ag atoms start to adjoin each other.

Our calculations indicate that introducing Ag into a Cu bulk crystal leads to an overall increase in the Cu-Cu distances (Figure S15) as a consequence of the crystal lattice expanding linearly with the Ag content (Figure S13), reflecting the GIXRD measurements (Figure 5b). In contrast, introducing Ag atoms on the Cu surface leads to a net compressive strain among surface Cu atoms, as shown in Figure 7d-f. The compressive strain is significant on the terrace facet (100) and (111), where a reduction in the mean Cu-Cu distances up to 0.1Å with increasing Ag surface coverage is found. In contrast, surface steps, exemplarily simulated as the (211) facet, experience no significant strain. The varying strain on different facets suggests that surface terraces might react more strongly to an introduction of Ag on Cu. On the other hand, we emphasize that Ag tends to preferably segregate on Cu-steps rather than terraces, leading to a more pronounced deactivation of under-coordinated sites for the reaction towards products beyond CO (Figure S11).

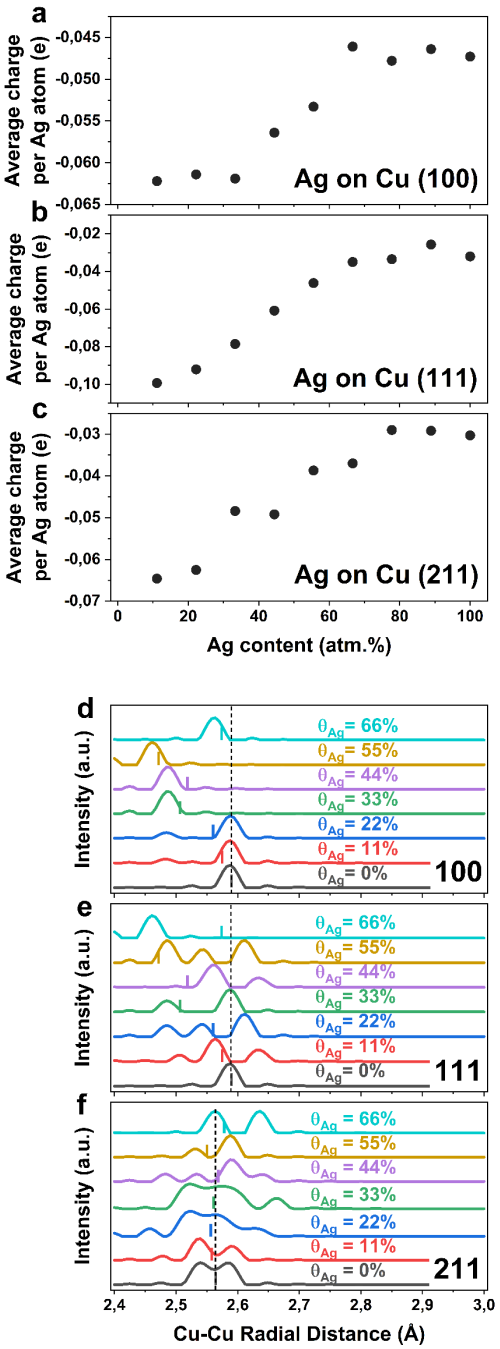

Figure 7 ***DFT calculated charge transfer and Cu-Cu distances on CuxAg100-x surfaces.*** *a-c) Average partial charges per Ag atom in Cu_xAg_{100-x} when Ag atoms are introduced on Cu (100) (a), (111) (b), and (211) (c) facets, respectively. d-f) Cu-Cu radial distance distribution in CuxAg100-x when Ag atoms are introduced to Cu (100) (d), Cu (111) (e), and Cu (211) (f), respectively. Averaged Cu-Cu bond length of each Ag content on*

each facet is indicated by a bar with the same color. Dashed lines represent the Cu-Cu bond length without Ag introduction.

In order to identify the magnitude of the respective effects arising from introducing Ag on the surface of Cu-rich domains, we further studied the effect of Ag on eCO2RR adsorbate binding. We note that although Ag generally tends to segregate to the surface (Figure S11), the binding of *CO on surface-Ag is strongly disfavored compared to Cu-sites. Thus, the latter is likely responsible for the activity and we focus on the ligand and strain effects surface Cu-atoms experience from neighboring Ag-atoms. The two effects are intertwined and a rigorous splitting of them is, in principle, impossible. In order to distinguish between them, in this work, we define ligand effects as the effect on adsorbate binding upon exchanging Cu atoms neighboring the active site with Ag at fixed atomic geometry, while strain effects are referred to the change in binding strength resulting from geometric rearrangement on the catalyst surface. The main focus is to evaluate which effect plays the dominant role in the altered production distributions.

specific neighbors. Atomic relaxation leads to a distancing of the Cu-atoms from Ag, while at the same time reducing the distance to the neighboring Cu-atoms. This created compressive strain adds to the ligand effect in the reduction of *CO binding strength, as indicated by the black arrow in Figure 8a and c. In the case where Cu is completely surrounded by Ag on the surface, the effect of strain maximizes. Upon further increasing the number of Ag neighbors, the Cu atom is lifted slightly above the original surface plane, increasing its distance to all neighbors and the second layer (distance to second layer increased up to ~0.3 Å). This weakened coordination strength of Cu to the neighboring atoms enhances *CO binding again.

Figure 8 depicts the binding energy of *CO (a,c) and *OH (b,d), on Cu (100) and (211) facets, respectively. *CO is a descriptor for eCO2RR activity, while *OH binding can be used as a descriptor for the binding of oxygen-bound species (*OR), as verified by the scaling of $*OCH_2CH_3$ with *OH in Figure S17. The Cu(100) surface terrace and (211) step were chosen, as the former is often identified as the most active facet for CO-dimerization[54,55], while surface steps

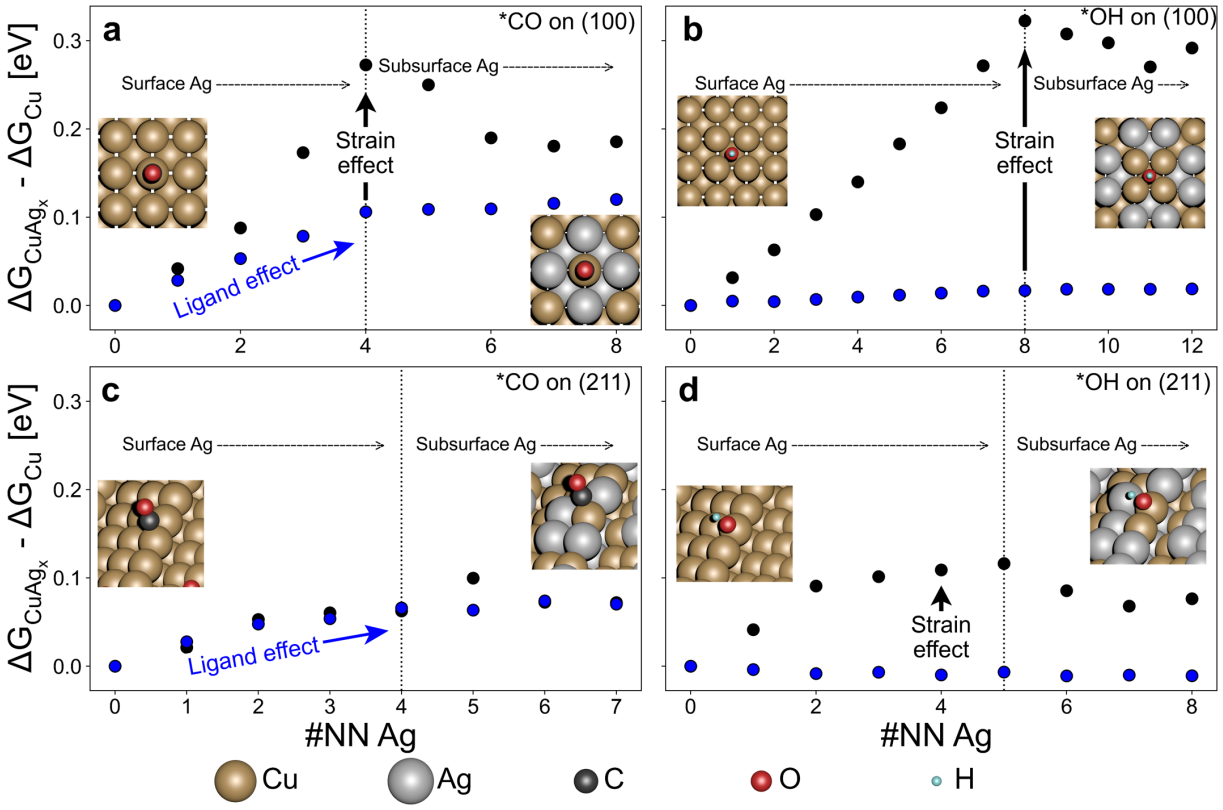

Figure 8 ***DFT-calculated Gibbs free energy of *CO binding*** *on a) *CO on Cu (100), b) *OH Cu(100), c) *CO on Cu(211), and d) *OH on Cu (211) facets with varying number of nearest neighboring Ag atoms (#NN Ag).*

The *CO binding energy reduces upon increasing the number of neighboring Ag atoms (#NNAg) due to a pure ligand effect, as shown in blue in Figures 8a and c. Interestingly, the reduction in binding strength only occurs when in-plane neighbors of the *CO-adsorbing Cu atom are substituted with Ag, whereas introducing Ag to the subsurface layer did not have a significant effect. We attribute this reduced effect in the subsurface to a higher saturation of Ag in the subsurface, reducing the charge transfer from

are generally considered as most relevant for the adsorption of weak binding reaction intermediates[56], such as acetaldehyde. The nearest neighbors (NN) to the Cu-atoms binding the corresponding intermediates were chosen as the Ag deposition sites. All possible Ag arrangements were sampled but only the most stable CuAg surface structures were considered in Figure 8. In all four considered scenarios, Ag energetically favored substituting all neighboring surface Cu-atoms before substituting the subsurface.

In order to first simulate the pure ligand effect, plotted as blue dots in Figure 8, as defined above, we first introduced Ag on Cu while keeping the atomic positions frozen, i.e., the introduced forces resulting from substituting Cu with Ag were not allowed to relax. Subsequently, the atoms were allowed to relax the introduced forces, giving rise to a strain effect, as presented in black dots in Figure 8.

Independent of the adsorbate and surface facet, adsorption strength is reduced upon introducing Ag, a consequence of a downshift in the d-band center (Figure S18). Furthermore, the effect of introducing Ag is strongly enhanced on the (100) terrace (Figure 8 a-b) compared to the (211) step sites (Figure 8 c-d).

In contrast to *CO, the *OH binding strength responds barely to a pure ligand effect. Note that while *CO tends to adsorb in a top site, we identified the binding site of *OH as the fourfold-hollow site on the (100) facet (Figure 8b) and in a bridge site on the (211) step (Figure 8d). These binding motifs make *OH much more sensitive to strain effects compared to *CO. Considering that carbonyl products, especially aldehydes, bind on Cu with *O before desorbing or being further reduced, the large reduction in binding strength due to strain explains their promoted production.

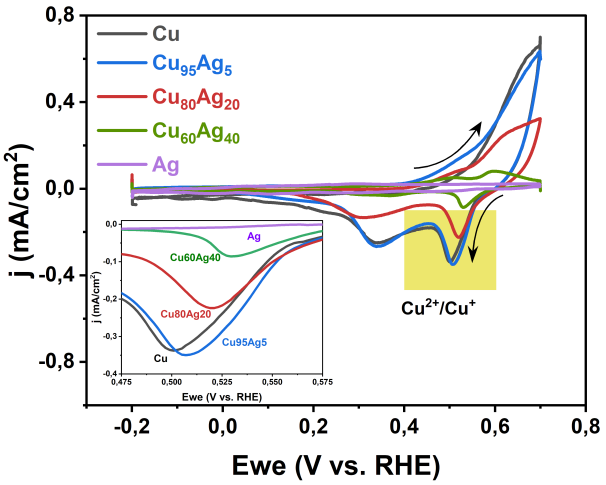

Figure 9. **Cyclic voltammetry scans for determining oxophilicity of Cu from Ag incorporation** in CO_2-saturated 0.1 M $KHCO_3$ at the scan rate of 50 mV/s. Inset is the enlarged highlighted area of the Cu^{2+}/Cu^{+} wave.

It has been found that both a compressive strain and the slightly reduced electron density in the Cu sites, as demonstrated by XANES results, could shift the pristine Cu d-band center to a deeper level and hence weaken the intermediate adsorption[38–41], which coincides with the attenuated Cu-C*/O* shell (peak B) in EXAFS spectra on the Cu K-edge shown in Figure S8. More details and analysis regarding EXAFS data can be found in Supporting Information Section 3.3.

The compressive strain was also found to reduce the oxophilicity of transient metals[31,57,58] and thus weaken the adsorption of species binding on the metal surface with O* (e.g., aldehydes and other carbonyls). It has been found that the oxophilicity of transition metal surfaces is highly correlated with their standard reduction/oxidation potential[20]. Therefore, cyclic voltammetry scans in the potential window between -0.2 to 0.7 V vs. RHE were performed to investigate the redox properties (Figure 9). As expected, an anodic shift of the Cu^{2+}/ Cu^{+} reduction wave is observed, confirming a reduced oxophilicity upon the introduction of Ag in Cu[20]. This is further evidence to help explain the promoted production of aldehydes and other carbonyls observed in Figure 3. *It is worth pointing out that for Cu catalysts, it is often the Cu^{2+}/Cu^{+} onset potential is compared to evaluate the catalysts' oxophilicity. However, onset potential of bimetallic catalysts involves with kinetic effects. Specifically, an earlier onset potential occurs not only due to a lower oxophilicity, but also with a higher surface Cu composition. In this regard, CV feature position is more straightforward.*

CONCLUSIONS

In this work, we prepared a series of CuAg multiphase alloys with varying Ag content for a better understanding of product selectivity resulting from electrochemical CO_2 reduction. Among the alloys, $Cu_{80}Ag_{20}$ (nominal composition) exhibited the highest selectivity towards C-C coupling and carbonyl production. *Operando* GIXRD confirmed the spatial strain effect between Cu and Ag phases. The Cu K-edge XANES suggests a slight electron density decrease in the Cu phase upon Ag introduction, compared to pure Cu. DFT calculations demonstrated both the electronic interaction and strain effect of Cu upon Ag incorporation, which shifted the Cu d-band center to a deeper level and thus weakened intermediate adsorption. The oxophilicity of Cu was also reduced as a consequence of compressive strain. Taking together, the facilitated generation of multicarbon aldehydes and carbonyls at the expense of H_2 and hydrocarbon production can be attributed to a combined effect of a deeper d-band center and reduced oxophilicity as Ag is introduced. This work provides insights into the interaction between alloyed metals during electrochemical CO_2 reduction on an atomic scale, which can be used to direct new bi-/multi- metallic/alloy designs in this field.

ASSOCIATED CONTENT

Supporting Information. Experimental and simulation methods, details of element distribution acquired from *ex situ* XPS, sample configuration of *operando* XAS measurements on the Ag L_3-edge, LEIS spectra and peak assignment, surface sensitivity verification and penetration depth of *operando* X-ray measurements, *operando* XRD and *ex situ* XRD 2θ match, DFT-calculated facet-dependent Ag surface segregation energies, DFT-calculated convex-hull, DFT-calculated lattice expansion with Ag content, Bader charges on Cu and Ag in the bulk crystal, calculated Cu-Cu radial distances in the bulk crystal, calculated effect of pure strain on the binding of *CO and *OH, scaling of the binding energy of $*OCH_2CH_3$ with the binding strength of *OH, d-band center shift with the $\#NN_{Ag}$.

AUTHOR INFORMATION

Corresponding Authors

* Brian Seger[a]: brse@fysik.dtu.dk

* Georg Kastlunger[b]: geokast@dtu.dk.

Present Addresses

[a] *Surface Physics and Catalysis (SurfCat) Section, De-partment of Physics, Technical University of Denmark, 2800 Kgs. Lyngby, Denmark*
[b] *CatTheory Center, Department of Physics, Technical University of Denmark 2800 Kongens, Lyngby, Denmark*

Authors

Yu Qiao – Surface Physics and Catalysis (SurfCat) Section, Department of Physics, Technical University of Denmark, 2800 Kgs. Lyngby, Denmark
Ryan C. Davis – Stanford Synchrotron Radiation Light source, SLAC National Accelerator Laboratory, Menlo Park, California 94025, United States
Carlos Andres Giron Rodriguez – Surface Physics and Catalysis (SurfCat) Section, Department of Physics, Technical University of Denmark, 2800 Kgs. Lyngby, Denmark
Andreas Lynge Vishart – Atomic Scale Materials Modelling Section, Department of Energy Conversion and Storage, Technical University of Denmark 2800 Kongens, Lyngby, Denmark
Wanyu Deng – Key Laboratory for Green Chemical Technology of Ministry of Education, School of Chemical Engineering and Technology, Tianjin University 300072, China; Collaborative Innovation Center of Chemical Science and Engineering (Tianjin), Tianjin 300072, China
Shaofeng Li – Surface Physics and Catalysis (SurfCat) Section, Department of Physics, Technical University of Denmark, 2800 Kgs. Lyngby, Denmark
Peter Benedek – Department of Chemical Engineering, Stanford University, 443 Via Ortega, Stanford, California 94305, United States of America; SUNCAT Center for Interface Science and Catalysis, SLAC National Accelerator Laboratory, 2575 Sand Hill Road, Menlo Park, California 94025, United States of America
Junjie Chen – Department of Chemical Engineering, Stanford University, 443 Via Ortega, Stanford, California 94305, United States of America; SUNCAT Center for Interface Science and Catalysis, SLAC National Accelerator Laboratory, 2575 Sand Hill Road, Menlo Park, California 94025, United States of America
Johanna Schröder – Department of Chemical Engineering, Stanford University, 443 Via Ortega, Stanford, California 94305, United States of America; SUNCAT Center for Interface Science and Catalysis, SLAC National Accelerator Laboratory, 2575 Sand Hill Road, Menlo Park, California 94025, United States of America
Joseph Perryman – Department of Chemical Engineering, Stanford University, 443 Via Ortega, Stanford, California 94305, United States of America; SUNCAT Center for Interface Science and Catalysis, SLAC National Accelerator Laboratory, 2575 Sand Hill Road, Menlo Park, California 94025, United States of America
Dong Un Lee – Department of Chemical Engineering, Stanford University, 443 Via Ortega, Stanford, California 94305, United States of America; SUNCAT Center for Interface Science and Catalysis, SLAC National Accelerator Laboratory, 2575 Sand Hill Road, Menlo Park, California 94025, United States of America
Thomas F. Jaramillo – *Department of Chemical Engineering, Stanford University, 443 Via Ortega, Stanford, California 94305, United States of America; SUNCAT Center for Interface Science and Catalysis, SLAC National Accelerator Laboratory, 2575 Sand Hill Road, Menlo Park, California 94025, United States of America*
Ib Chorkendorff – *Surface Physics and Catalysis (SurfCat) Section, Department of Physics, Technical University of Denmark, 2800 Kgs. Lyngby, Denmark*

Notes

The authors declare no competing financial interest.

ACKNOWLEDGMENT

B.S., G.K., and Y.Q. acknowledge European Union's Horizon 2020 research and innovation programme under grant agreement no. 85144, (SELECT-CO2) as well as the Villum Center for the Science of Sustainable Fuels and Chemical grant 9455. Use of the Stanford Synchrotron Radiation Lightsource, SLAC National Accelerator Laboratory, is supported by the U.S. Department of Energy, Office of Science, Office of Basic Energy Sciences under Contract No. DE-AC02-76SF00515. Part of this work was performed by the Liquid Sunlight Alliance, supported by the US Department of Energy, Office of Science, Office of Basic Energy Sciences, Fuels from Sunlight Hub under award DE-SC0021266. Part of this work was performed at the Stanford Nano Shared Facilities (SNSF), supported by the National Science Foundation under Award ECCS-1542152. Y.Q. acknowledges Otto Mønsted for the travel grant. The authors gratefully thank Christian Danvad Damsgaard and Chao Wei for insightful X-ray data discussion; Qiucheng Xu, Clara Bruun Jensen, Sahil Garg, and Melissa Kreider for help with preparing and testing samples; Kevin Stone, Charles Troxel Jr, Matthew Latimer, Erik Nelson, and Sarah Gooding for technical support at SSRL; Christopher Hahn for valuable input in the early stage of this work; José Zamora Zeledón, Sihe Zhang and Bjørt Óladóttir Joensen for help with synchrotron measurements; Thomas Bligaard for valuable discussion on the separation of strain and ligand effects in DFT simulations.

REFERENCES

1. Masson-Delmotte, V., P. Zhai, H.-O. Pörtner, D. Roberts, J. S., P.R. Shukla, A. Pirani, W. Moufouma-Okia, C. Péan, R. Pidcock, S. Connors, J.B.R. Matthews, Y. Chen, X. Zhou, M.I. Gomis, E. L. & T. Maycock, M. Tignor, and T. W. (eds. . *Global warming of 1.5°C. Journal of the International Commission on Radiation Units and Measurements* https://www.ipcc.ch/sr15/ (2019).
2. Nitopi, S. *et al.* Progress and Perspectives of Electrochemical CO2 Reduction on Copper in Aqueous Electrolyte. *Chem. Rev.* **119**, 7610–7672 (2019).
3. Clark, E. L. *et al.* Standards and Protocols for Data Acquisition and Reporting for Studies of the Electrochemical Reduction of Carbon Dioxide. *ACS Catal.* **8**, 6560–6570 (2018).
4. Jia, H. *et al.* Symmetry-Broken Au–Cu Heterostructures and their Tandem Catalysis Process in Electrochemical CO2 Reduction. *Adv. Funct. Mater.* **2101255**, 1–11 (2021).
5. Shen, S. *et al.* AuCu Alloy Nanoparticle Embedded Cu Submicrocone Arrays for Selective Conversion of CO2 to Ethanol. *Small* **15**, 1–7 (2019).
6. Li, Y. C. *et al.* Binding Site Diversity Promotes CO2 Electroreduction to Ethanol. *J. Am. Chem. Soc.* **141**, 8584–8591 (2019).
7. Kortlever, R., Shen, J., Schouten, K. J. P., Calle-Vallejo, F. & Koper, M. T. M. Catalysts and Reaction Pathways for the Electrochemical Reduction of Carbon Dioxide. *J. Phys. Chem. Lett.* **6**, 4073–4082 (2015).
8. Song, H., Song, J. T., Kim, B., Tan, Y. C. & Oh, J. Activation of C2H4 reaction pathways in electrochemical CO2 reduction under low CO2 partial pressure. *Appl. Catal. B Environ.* **272**, 119049 (2020).
9. Kim, Y. *et al.* Time-resolved observation of C-C coupling intermediates on Cu electrodes for selective electrochemical CO2reduction. *Energy Environ. Sci.* **13**, 4301–4311 (2020).
10. Zhang, Z. *et al.* Tailoring the Surface and Interface Structures of Copper-Based Catalysts for Electrochemical Reduction of CO2 to Ethylene and Ethanol. *Small* **18**, 1–24 (2022).
11. Su, X. *et al.* Hierarchically porous Cu/Zn bimetallic catalysts for highly selective CO2 electroreduction to liquid C2 products. *Appl. Catal. B Environ.* **269**, 118800 (2020).
12. Jia, F., Yu, X. & Zhang, L. Enhanced selectivity for the

electrochemical reduction of CO2 to alcohols in aqueous solution with nanostructured Cu-Au alloy as catalyst. *J. Power Sources* **252**, 85–89 (2014).
13. Gao, J., Ren, D., Guo, X., Zakeeruddin, S. M. & Grätzel, M. Sequential catalysis enables enhanced C-C coupling towards multi-carbon alkenes and alcohols in carbon dioxide reduction: A study on bifunctional Cu/Au electrocatalysts. *Faraday Discuss.* **215**, 282–296 (2019).
14. Lum, Y. & Ager, J. W. Sequential catalysis controls selectivity in electrochemical CO2 reduction on Cu. *Energy Environ. Sci.* **11**, 2935–2944 (2018).
15. Huang, J., Mensi, M., Oveisi, E., Mantella, V. & Buonsanti, R. Structural Sensitivities in Bimetallic Catalysts for Electrochemical CO2 Reduction Revealed by Ag-Cu Nanodimers. *J. Am. Chem. Soc.* **141**, 2490–2499 (2019).
16. Zhong, Y. *et al.* Adjusting Local CO Confinement in Porous-Shell Ag@Cu Catalysts for Enhancing C-C Coupling toward CO2 Eletroreduction. *Nano Lett.* **22**, 2554–2560 (2022).
17. Lee, S., Park, G. & Lee, J. Importance of Ag-Cu Biphasic Boundaries for Selective Electrochemical Reduction of CO2 to Ethanol. *ACS Catal.* **7**, 8594–8604 (2017).
18. Chen, C. *et al.* Cu-Ag Tandem Catalysts for High-Rate CO2 Electrolysis toward Multicarbons. *Joule* **4**, 1688–1699 (2020).
19. Wang, X. *et al.* Efficient upgrading of CO to C3 fuel using asymmetric C-C coupling active sites. *Nat. Commun.* **10**, 5186 (2019).
20. Clark, E. L., Hahn, C., Jaramillo, T. F. & Bell, A. T. Electrochemical CO2 Reduction over Compressively Strained CuAg Surface Alloys with Enhanced Multi-Carbon Oxygenate Selectivity. *J. Am. Chem. Soc.* **139**, 15848–15857 (2017).
21. Feng, Y. *et al.* Laser-Prepared CuZn Alloy Catalyst for Selective Electrochemical Reduction of CO2 to Ethylene. *Langmuir* **34**, 13544–13549 (2018).
22. Dongare, S., Singh, N. & Bhunia, H. Oxide-derived Cu-Zn nanoparticles supported on N-doped graphene for electrochemical reduction of CO2 to ethanol. *Appl. Surf. Sci.* **556**, 149790 (2021).
23. Higgins, D. *et al.* Guiding Electrochemical Carbon Dioxide Reduction toward Carbonyls Using Copper Silver Thin Films with Interphase Miscibility. *ACS Energy Lett.* **3**, 2947–2955 (2018).
24. Higgins, D. *et al.* Copper Silver Thin Films with Metastable Miscibility for Oxygen Reduction Electrocatalysis in Alkaline Electrolytes. *ACS Appl. Energy Mater.* **1**, 1990–1999 (2018).
25. Gibbons, B. M. *et al.* In Situ X-Ray Absorption Spectroscopy Disentangles the Roles of Copper and Silver in a Bimetallic Catalyst for the Oxygen Reduction Reaction. *Chem. Mater.* **32**, 1819–1827 (2020).
26. Wang, L. *et al.* Selective reduction of CO to acetaldehyde with CuAg electrocatalysts. *Proc. Natl. Acad. Sci. U. S. A.* **117**, 12572–12575 (2020).
27. Nishimura, Y. F. *et al.* Guiding the Catalytic Properties of Copper for Electrochemical CO2 Reduction by Metal Atom Decoration. *ACS Appl. Mater. Interfaces* **13**, 52044–52054 (2021).
28. Farmand, M. *et al.* Electrochemical flow cell enabling: Operando probing of electrocatalyst surfaces by X-ray spectroscopy and diffraction. *Phys. Chem. Chem. Phys.* **21**, 5402–5408 (2019).
29. Zhang, H. *et al.* Computational and experimental demonstrations of one-pot tandem catalysis for electrochemical carbon dioxide reduction to methane. *Nat. Commun.* **10**, 1–9 (2019).
30. Herzog, A. *et al.* Operando Investigation of Ag-Decorated Cu2O Nanocube Catalysts with Enhanced CO2 Electroreduction toward Liquid Products. *Angew. Chemie - Int. Ed.* **60**, 7426–7435 (2021).
31. Su, W. *et al.* Highly dispersive trace silver decorated Cu/Cu2O composites boosting electrochemical CO2 reduction to ethanol. *J. CO2 Util.* **52**, 101698 (2021).
32. Lv, X. *et al.* Electron-Deficient Cu Sites on Cu3Ag1 Catalyst Promoting CO2 Electroreduction to Alcohols. *Adv. Energy Mater.* **10**, 1–8 (2020).
33. Kuhn, A. N. *et al.* Engineering Silver-Enriched Copper Core-Shell Electrocatalysts to Enhance the Production of Ethylene and C2+ Chemicals from Carbon Dioxide at Low Cell Potentials. *Adv. Funct. Mater.* **31**, 2–11 (2021).
34. Zhang, Y.-J., Sethuraman, V., Michalsky, R. & Peterson, A. Supporting information for Competition between CO2 reduction and H 2 evolution on transition-metal electrocatalysts. *ACS Catal.* **4**, 3742–3748 (2014).
35. Cave, E. R. *et al.* Trends in the Catalytic Activity of Hydrogen Evolution during CO2 Electroreduction on Transition Metals. *ACS Catal.* **8**, 3035–3040 (2018).
36. Nørskov, J. K. *et al.* Trends in the Exchange Current for Hydrogen Evolution. *J. Electrochem. Soc.* **152**, J23 (2005).
37. Hahn, C. *et al.* Engineering Cu surfaces for the electrocatalytic conversion of CO2: Controlling selectivity toward oxygenates and hydrocarbons. *Proc. Natl. Acad. Sci. U. S. A.* **114**, 5918–5923 (2017).
38. Hammer, B. & Nørskov, J. K. Electronic factors determining the reactivity of metal surfaces. *Surf. Sci.* **343**, 211–220 (1995).
39. Ruban, A., Hammer, B., Stoltze, P., Skriver, H. . & Nørskov, J. . Surface electronic structure and reactivity of transition and noble metals1Communication presented at the First Francqui Colloquium, Brussels, 19–20 February 1996.1. *J. Mol. Catal. A Chem.* **115**, 421–429 (1997).
40. Chang, Z., Huo, S., Zhang, W., Fang, J. & Wang, H. The Tunable and Highly Selective Reduction Products on Ag@Cu Bimetallic Catalysts Toward CO2 Electrochemical Reduction Reaction. *J. Phys. Chem. C* **121**, 11368–11379 (2017).
41. Martić, N. *et al.* Ag2Cu2O3-a catalyst template material for selective electroreduction of CO to C2+products. *Energy Environ. Sci.* **13**, 2993–3006 (2020).
42. Hoang, T. T. H. *et al.* Nanoporous Copper-Silver Alloys by Additive-Controlled Electrodeposition for the Selective Electroreduction of CO2 to Ethylene and Ethanol. *J. Am. Chem. Soc.* **140**, 5791–5797 (2018).
43. Xu, Y. *et al.* Tuning the Selectivity of Liquid Products of CO2RR by Cu-Ag Alloying. *ACS Applied Materials and Interfaces* vol. 14 11567–11574 (2022).
44. Chen, X. *et al.* Controlling Speciation during CO2 Reduction on Cu-Alloy Electrodes. *ACS Catal.* **10**, 672–682 (2020).
45. Chang, C. J. *et al.* Dynamic Reoxidation/Reduction-Driven Atomic Interdiffusion for Highly Selective CO2Reduction toward Methane. *J. Am. Chem. Soc.* **142**, 12119–12132 (2020).
46. Peng, H. J., Tang, M. T., Halldin Stenlid, J., Liu, X. & Abild-Pedersen, F. Trends in oxygenate/hydrocarbon selectivity for electrochemical CO(2) reduction to C2 products. *Nat. Commun.* **13**, 1–11 (2022).
47. Vitos, L., Ruban, A. V., Skriver, H. L. & Kollár, J. The surface energy of metals. *Surf. Sci.* **411**, 186–202 (1998).
48. Tang, W. *et al.* The importance of surface morphology in controlling the selectivity of polycrystalline copper for CO2 electroreduction. *Phys. Chem. Chem. Phys.* **14**, 76–81 (2012).
49. Möller, T. *et al.* Electrocatalytic CO2 Reduction on CuOx Nanocubes: Tracking the Evolution of Chemical State, Geometric Structure, and Catalytic Selectivity using Operando Spectroscopy. *Angew. Chemie - Int. Ed.* **59**, 17974–17983 (2020).
50. Karapinar, D., Creissen, C. E., Rivera De La Cruz, J. G., Schreiber, M. W. & Fontecave, M. Electrochemical CO2Reduction to Ethanol with Copper-Based Catalysts. *ACS Energy Lett.* **6**, 694–706 (2021).
51. Chang, X. *et al.* Understanding the complementarities of surface-enhanced infrared and Raman spectroscopies in CO adsorption and electrochemical reduction. *Nat. Commun.* **13**, 1–12 (2022).
52. An, H. *et al.* Sub-Second Time-Resolved Surface-Enhanced Raman Spectroscopy Reveals Dynamic CO Intermediates during Electrochemical CO2 Reduction on Copper. *Angew. Chemie - Int. Ed.* **60**, 16576–16584 (2021).
53. Baker, M. L. *et al.* K- and L-edge X-ray absorption spectroscopy (XAS) and resonant inelastic X-ray scattering (RIXS) determination of differential orbital covalency (DOC)

of transition metal sites. *Coord. Chem. Rev.* **345**, 182–208 (2017).
54. Kastlunger, G. *et al.* Using pH Dependence to Understand Mechanisms in Electrochemical CO Reduction. *ACS Catal.* **12**, 4344–4357 (2022).
55. Montoya, J. H., Shi, C., Chan, K. & Nørskov, J. K. Theoretical insights into a CO dimerization mechanism in CO2 electroreduction. *J. Phys. Chem. Lett.* **6**, 2032–2037 (2015).
56. Ledezma-Yanez, I., Gallent, E. P., Koper, M. T. M. & Calle-Vallejo, F. Structure-sensitive electroreduction of acetaldehyde to ethanol on copper and its mechanistic implications for CO and CO2 reduction. *Catal. Today* **262**, 90–94 (2016).
57. Lim, J. *et al.* Ga-Doped Pt-Ni Octahedral Nanoparticles as a Highly Active and Durable Electrocatalyst for Oxygen Reduction Reaction. *Nano Lett.* **18**, 2450–2458 (2018).
58. Xia, Z. & Guo, S. Strain engineering of metal-based nanomaterials for energy electrocatalysis. *Chem. Soc. Rev.* **48**, 3265–3278 (2019).

SYNOPSIS TOC (Word Style "SN_Synopsis_TOC"). If you are submitting your paper to a journal that requires a synopsis graphic and/or synopsis paragraph, see the Instructions for Authors on the journal's homepage for a description of what needs to be provided and for the size requirements of the artwork.

To format double-column figures, schemes, charts, and tables, use the following instructions:

Place the insertion point where you want to change the number of columns
From the **Insert** menu, choose **Break**
Under **Sections**, choose **Continuous**
Make sure the insertion point is in the new section. From the **Format** menu, choose **Columns**
In the **Number of Columns** box, type **1**
Choose the **OK** button

Now your page is set up so that figures, schemes, charts, and tables can span two columns. These must appear at the top of the page. Be sure to add another section break after the table and change it back to two columns with a spacing of 0.33 in.

Authors are required to submit a graphic entry for the Table of Contents (TOC) that, in conjunction with the manuscript title, should give the reader a representative idea of one of the following: A key structure, reaction, equation, concept, or theorem, etc., that is discussed in the manuscript. Consult the journal's Instructions for Authors for TOC graphic specifications.

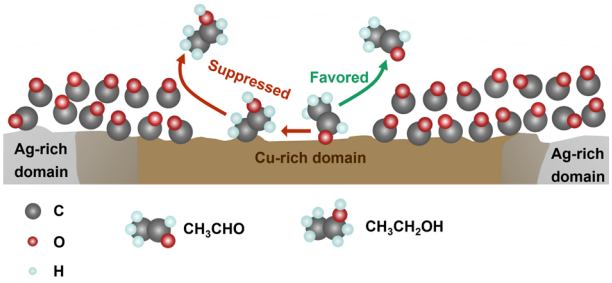

Insert Table of Contents artwork here

Supporting Information for

Mechanistic Insights into Aldehyde Production from Electro-chemical CO_2 Reduction on CuAg Alloy via Operando X-Ray Measurements

Yu Qiao[a], Georg Kastlunger[b,*], Ryan C. Davis[c], Carlos Andres Giron Rodriguez[a], Andreas Lynge Vishart[d], Wanyu Deng[e,f], Shaofeng Li[a], Peter Benedek[g,h], Junjie Chen[g,h], Johanna Schröder[g,h], Joseph Perryman[g,h], Dong Un Lee[g,h], Thomas F. Jaramillo[g,h], Ib Chorkendorff[a], Brian Seger[a,*]

[a] Surface Physics and Catalysis (SurfCat) Section, Department of Physics, Technical University of Denmark, 2800 Kgs. Lyngby, Denmark

[b] CatTheory Center, Department of Physics, Technical University of Denmark 2800 Kongens, Lyngby, Denmark

[c] Stanford Synchrotron Radiation Light source, SLAC National Accelerator Laboratory, Menlo Park, California 94025, United States

[d] Atomic Scale Materials Modelling Section, Department of Energy conversion and storage, Technical University of Denmark 2800 Kongens, Lyngby, Denmark

[e] Key Laboratory for Green Chemical Technology of Ministry of Education, School of Chemical Engineering and Technology, Tianjin University 300072, China

[f] Collaborative Innovation Center of Chemical Science and Engineering (Tianjin), Tianjin 300072, China

[g] Department of Chemical Engineering, Stanford University, 443 Via Ortega, Stanford, California 94305, United States of America

[h] SUNCAT Center for Interface Science and Catalysis, SLAC National Accelerator Laboratory, 2575 Sand Hill Road, Menlo Park, California 94025, United States of America

* **Corresponding Author**

Brian Seger: brse@fysik.dtu.dk

Georg Kastlunger: geokast@dtu.dk

1. THIN FILM CATALYST FABRICATION AND CHARACTERIZATION

Cu_XAg_{100-X} (X = 100, 95, 80 and 60, nominal content) were fabricated with a high vacuum (base pressure < 1 x 10-7 mbar) magnetron sputtering chamber (AJA International, Inc.) using direct current (DC) mode. The Cu and Ag targets (Kurt–Lesker, 99.9999%) were (co)-deposited on 75 nm thick Si wafers (Wafer World Inc., boron-doped, resistivity < 0.025 Ohm-cm) or Kapton foil (DuPont, only for XAS at Ag L3-edge) as the substrate. In both cases, the substrate was sputter-cleaned by Ar at 40 W for ~5min to remove any surface contaminations and oxide layers. A ~5 nm thick Ti adhesive layer was then sputtered at a rate of ~0.7 Å/s, followed by a ~50 nm thick Cu_XAg_{100-X} catalyst layer deposited at a rate of ~1.0 Å/s. The deposition rate and nominal composition as well as the thickness of the deposited catalyst layer were calibrated by a quartz crystal microbalance (QCM). All samples were deposited under a 5 mTorr, 10 sccm Ar (N5, Air Liquide) atmosphere at room temperature.

X-ray photoelectron spectroscopy (XPS) was performed by a ThermoScientific Thetaprobe instrument equipped with an Al Kα X-ray source. The operating base pressure was kept below 1.0×10^{-10} mbar. Survey and high-resolution elemental scans were recorded with a step size of 1.0 eV and 0.1 eV, respectively; while in all cases pass energy of 200 eV and dwell time of 50 ms were used. The data were acquired and analyzed with Thermo Avantage (Thermo Fisher Scientific). Low energy ion scattering (LEIS) was processed on the same instrument, utilizing a focused He ion gun (1 keV) at a base pressure of 2.0×10^{-7} mbar. The LEIS spectra were acquired with a step size of 1.0 eV.

X-ray diffraction (XRD) was conducted on a Malvern Panalytical Empyrean X-ray diffractometer in the grazing incident geometry with the incident beam angle at 0.7°. An Empyrean Cu LFF HR gun ($K\alpha_1$ = 1.540598 Å, 8.04 keV) was used as the X-ray source and operated at 45 kV and 40 mA.

Table S1 ***Element composition acquired from ex situ XPS.*** *Three spots were taken on each sample and the average is listed in the table.*

Sample (nominal composition)	Element Distribution										
	As-prepared					After CO2ER					
	Cu	Ag	Cu in CuAg	O	C	Cu	Ag	Cu in CuAg	O	C	K
Cu	37.0	0	100.0	42.2	20.8	26.1	0	100.0	42.8	31.1	0
$Cu_{95}Ag_5$	33.4	5.8	85.2	38.1	22.7	36.5	2.9	92.6	42.29	17.4	1.5
$Cu_{80}Ag_{20}$	36.4	14.1	72.1	28.7	20.8	28.4	7.4	79.4	41	23.17	0
$Cu_{60}Ag_{40}$	24.9	20.8	54.4	28.3	26.0	25.2	14.9	62.8	34.6	25.0	0
Ag	0	49.2	0.0	13.5	37.3	0.0	44.8	0.00	13.6	41.6	0

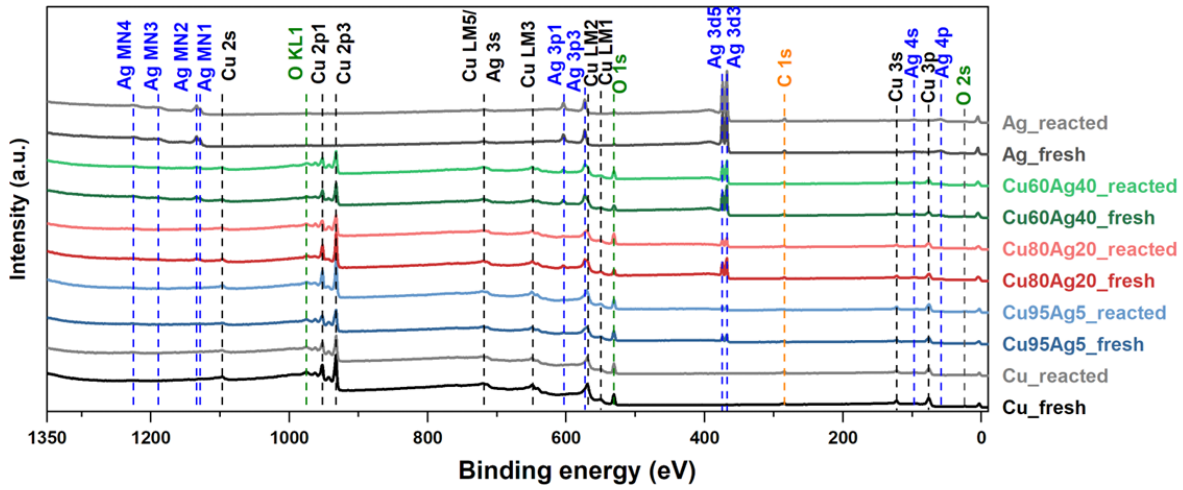

Figure S1 XPS survey of samples with varying Ag contents.

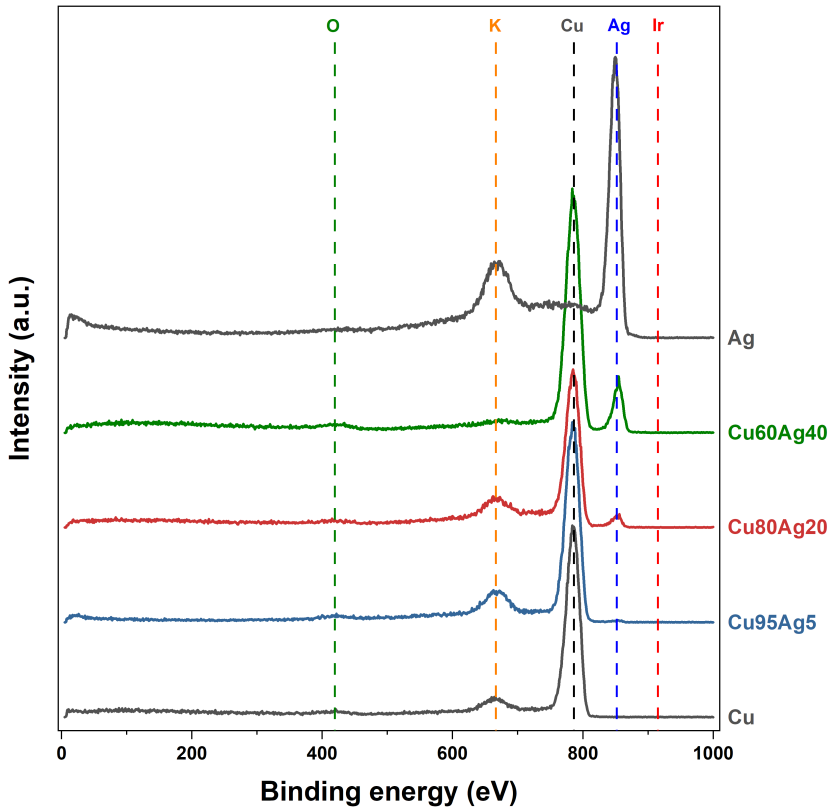

Figure S2 ***LEIS survey of postmortem samples with various Ag concentrations after eCO2RR for 2 hours.*** *The sample surface was carefully rinsed with MilliQ water and dried with pressed air before the test. Dash lines indicate the peak position of the corresponding element. K was from the not fully removed electrolyte after eCO2RR. No signal related to Ir was found in any sample.*

2. ELECTROCHEMICAL CO_2 REDUCTION MEASUREMENTS

K_2CO_3 solutions were prepared by dissolving K_2CO_3 (99.995% trace metals basis, Aldrich) into MilliQ water (18.2 MΩ.cm @25°C, 2ppb TOC, Q-POD®). 0.1M $KHCO_3$ solution was prepared by purging CO_2 (N45, Air Liquide) into 0.05 M K_2CO_3 solution for at least 30min, until pH~6.8.

Electrochemical CO_2 reduction was carried out in a 2-chamber H-cell in the 3-electrode configuration. The two chambers were separated by a hydrocarbon-based ion-exchange membrane (Selemion AMV, AGC Engineering CO., LTD.), activated in 0.1 M KOH (99.995% trace metals basis, Sigma-Aldrich) overnight, and stored in MilliQ water. The liquid volume of both chambers is 6.5 mL, whereas the actual electrolyte volume was 6.0 mL in both chambers. The cathode chamber was purged with CO_2 at 10 sccm for the duration of the experiment. An IrO_2-coated carbon paper (1.0 cm x 1.0 cm, Dioxide Materials) and a miniature leak-free Ag/AgCl/Saturated KCl electrode (Innovative Instruments Inc.) were used as the counter and reference electrode, respectively.

A stagnant H-cell was chosen because the current is more stable without electrolyte flow. Moreover, it allows for concentrating on the intrinsic performance of the catalysts by minimizing potential influence from unstable liquid flow and/or dead volumes, as well as varied mass transfer conditions in different runs.

Electrochemical experiments were controlled using a BioLogic SP-200 potentiostat. Unless otherwise stated, the working electrode potential (E_{WE}) was recorded and referenced against the Ag/AgCl reference electrode (RE), which was then converted and reported in terms of the reversible hydrogen electrode (RHE) scale following the equation below. The RE was calibrated following the procedure described in [1] before use.

$$\mathrm{E_{RHE}} = \mathrm{E_{WE}} + \mathrm{E_{RE}} + 0.059 \times \mathrm{pH} \quad (1)$$

Prior to each measurement, a 10 min chronoamperometry (CA) at -0.2 V vs. RHE was applied to reduce the CuO_x layer, which was naturally formed when metallic Cu (or the Cu phase in CuAg bimetallic catalysts) was exposed to air. This potential was chosen because it is more negative than the CuO_x reduction potential (0.35 V vs. RHE) while not sufficiently reductive to produce detectable products. Cyclic voltammetry (CV) was then scanned in the potential window of -0.2 to +0.7 V three times. The redox features were used to primarily check the consistency of the same sample in different runs. A constant potential of -1.0 V vs. RHE was then applied and kept for 2 hours. Gas products were analyzed *in situ* with gas chromatography (GC, Thermo-Scientific, TRACE 1300), while liquid products were collected at the end of the experiment and analyzed with high-performance liquid chromatography (HPLC, Agilent 1200 series). eCO2RR measurements were conducted three times for each sample.

Figure S3 is a screenshot of the HPLC data processing software (since the diode array detector (DAD) was used for detecting acetaldehyde, only DAD signals are shown here). Insert is enlarged area highlighting acetaldehyde. Different products are ladled in highlighted area. Four spectra are shown here: 0.1 M KHCO3 electrolyte (red), post-mortem electrolyte after CO2R reaction on Cu (purple), Cu80Ag20 (yellow), and Cu60Ag40 (green). It gives an example to show the sensitivity of our HPLC equipment in detecting acetaldehyde. It can be seen that the signal-to-noise ratio is sufficient even at

the lowest acetaldehyde concentration (*i.e.*, on pure Cu, read line) for accurately investigating product selectivity.

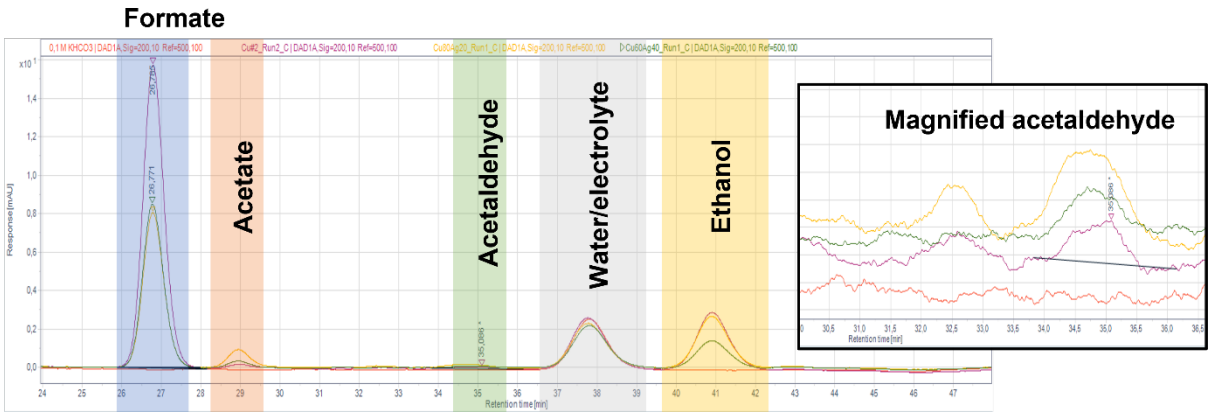

Figure S3 Screenshot of the HPLC data processing software. Insert is enlarged area highlighting acetaldehyde. Different products are ladled in highlighted area. Four spectra are shown here: 0.1 M $KHCO_3$ electrolyte (red), post-mortem electrolyte after CO2R reaction on Cu (purple), $Cu_{80}Ag_{20}$ (yellow), and $Cu_{60}Ag_{40}$ (green). The selectivity of each product was determined by its Faradaic efficiency, following Faraday's law:

$$\mathrm{FE_i} = \frac{\mathrm{z} \times \mathrm{F} \times n_\mathrm{i}}{\mathrm{I_T} \times \mathrm{t}} \times 100\% \tag{2}$$

where, *z* is the number of transferred electrons for producing species *i*, *F* is the Faraday's constant (96485 C/mol), n_i is the number of moles of produced species *i*; I_T is the total current of the reaction, and *t* is the reaction time.

Specifically, gas products are calculated following the equation:

$$\mathrm{FE_i} = \frac{\mathrm{z} \times \mathrm{F} \times \mathrm{P} \times \mathrm{v_{Total}}}{\mathrm{I} \times \mathrm{R} \times \mathrm{T}} \times A_{\mathrm{i,GC}} \times \mathrm{f_{i,GC}} \times 100\% \tag{3}$$

where, *P* is the atmosphere pressure (101.325 kPa), v_{Total} is the inlet CO_2 gas flow rate (10 sccm), *T* is room temperature (300 K), $A_{i,GC}$ is the integrated peak area of species *i* in GC, and $f_{i,GC}$ is the calibration factor of species *i* in GC. (As the total conversion is small, inlet CO_2 gas flowrate is a reasonable approximation for outlet flow rate in this situation.)

Liquid products are measured by the following equation:

$$\mathrm{FE_i} = \frac{\mathrm{z} \times \mathrm{F} \times \mathrm{V_{Total}} \times \frac{\mathrm{A_{i,HPLC}}}{\mathrm{f_{i,HPLC}}}}{\mathrm{Q}} \times 100\% \tag{4}$$

where, V_{Total} is the total volume of the cathode chamber (6 mL), *T* is room temperature (300 K), $A_{i,HPLC}$ is the integrated peak area of species *i* in HPLC, and $f_{i,GC}$ is the calibration factor of species *i* in HPLC.

Current densities were based on the geometric area of the working electrode (2.25 cm^2). Partial current density of each product was evaluated by the following equation:

$$j_i = j_{Total} \times FE_i \quad (5)$$

where, j_{Total} is the total geometric current density.

Productivity S_i of each product with respect to the produced number of moles are calculated in the following way:

$$S_i = \frac{n_i}{\sum_{i=1}^{i=n} n_i} \times 100\% \quad (6)$$

For gas products:

$$n_i = \frac{P \times v_{Total}}{R \times T} \times A_{i,GC} \times f_{i,GC} \quad (7)$$

For liquid products:

$$n_i = \frac{V_{Total} \times \frac{A_{i,HPLC}}{f_{i,HPLC}}}{Q} \quad (8)$$

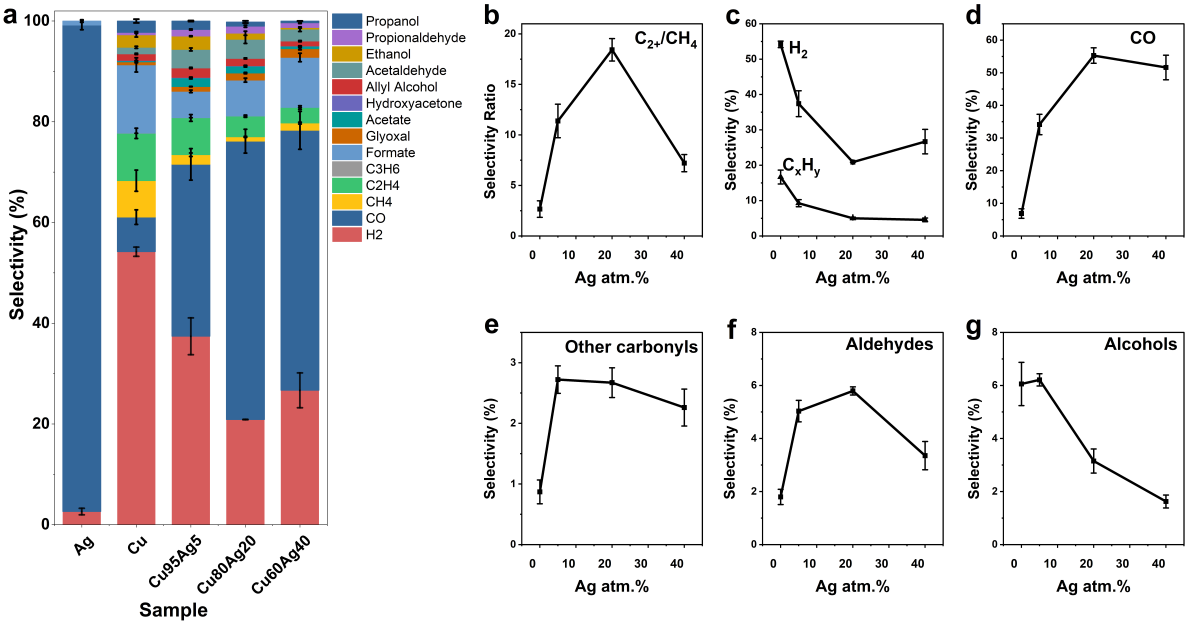

*Figure S4 eCO2RR performance test conducted in an H-cell in CO_2-saturated 0.1 M $KHCO_3$ aqueous solution at -1 V vs. RHE for 2 hours, plotted in selectivity regarding produced number of moles. CO_2 was continuously purged to the solution at 10 sccm during eCO2RR. a) Faradaic efficiency of all detected products. b) Faradaic efficiency ratio between *CO-originated products depending on the involvement of C-C coupling during formation process as a function of Ag contents. c) Faradaic efficiency of H_2 and C_xH_y (CH_4, C_2H_4, C_2H_6, C_3H_6, and C_3H_8) as a function of Ag content. d) Faradaic efficiencies of CO_2 as a function of Ag content. e)-g) Faradaic efficiencies of *CO-originated products classified on C-O bond as a function of Ag content: e) other carbonyls (glyoxal, acetate, and hydroxy acetone; formate is not included), f) aldehydes (glycolaldehyde, acetaldehyde, and propionaldehyde), g) alcohols (ally alcohol, ethanol, and propanol).*

3. OPERANDO X-RAY MEASUREMENTS

3.1 Experimental Details

All *operando* X-ray measurements were conducted at the Stanford Synchrotron Radiation Lightsource (SSRL) at ambient pressure and room temperature. Electrochemistry was controlled using a BioLogic SP-200 potentiostat.

Operando GIXRD was conducted at beamline 2-1, using a Si (111) monochromator and beam energy of ~17 KeV (0.729 Å). *Operando* GIXAS on the Cu K-edge in both X-ray absorption near edge structure (XANES) and the extended X-ray absorption fine structure (EXAFS) regions were collected at beamline 11-2, using a Si (220) LN2-cooled monochromator and a 100-pixel monolithic solid-state Ge detector array, in the transmission mode.

A previously designed 3D-printed flow cell was employed in XRD and XAS at the Cu K-edge (~ 9 keV) to enable the grazing incident configuration of the sample while maintaining a higher horizontal alignment of the sample and also maintaining a high transmissivity for X-ray incidence as described in [2]. During *operando* XAS, the electrolyte being purged with CO_2 gas was pumped through the cell by a 2-channel peristaltic pump (SHENCHEN LabN6) at 50 mL/min. Cu_XAg_{100-X} catalyst samples were prepared on a Si (111) substrate, as described in Session 2.1. Two 50 µm diameter Pt wires (Alfa Aesar, 99.99%) and a miniature Ag/AgCl electrode (Innovative Instruments Inc.) served as the counter and reference electrode, respectively.

XAS data analysis was processed using SixPack156 [3], Athena and Artemis software [4].

3.2 X-ray Diffraction (XRD)

Table S2 ***Operando XRD surface sensitivity verification:*** *attenuation and penetration depth calculation at α = 0.15°, E = 17 keV.*

Sample	Density (g/cm3)[#]	Penetration depth (nm)[¤]	Lattice spacing (Å) [£]	Penetrated monolayer numbers
Cu	8.96	2.76	2.08	13.89
Ag	10.49	2.42	2.35	10.77
Ag-rich phase in $Cu_{80}Ag_{20}$	N/A	N/A	2.31	N/A
Cu-rich phase in $Cu_{80}Ag_{20}$	N/A	N/A	2.17	

[#] The density of each phase in $Cu_{80}Ag_{20}$ cannot be estimated by assuming a linear combination of the density of Cu and Ag., because we do not know how much of Cu is in the Ag-rich phase and vice versa.

[¤] Penetration depth was calculated based on Beer-Lambert law.

[£] Lattice spacing was calculated from XRD, based on (111) facet for both Cu and Ag, as it is the most prominent phase shown in XRD.

Table S3 ***XRD peak match between operando and ex situ measurements***

Facet	2θ (°)	
	Operando (17keV)	**Ex situ (8.04 keV)**
Ag (1 1 1)	17.88	38.33
Ag (0 0 2)	20.67	44.54
Ag (0 0 2)	29.29	64.56
Cu (1 1 1)	20.23	43.54
Cu (0 0 2)	23.36	50.63
Cu (0 2 2)	33.24	74.34
CuO (2 1 1)	17.01	36.43
CuO (1 1 1)	18.07	38.75
CuO (2 0 0)	18.15	38.93
CuO (1 1 -3)	28.04	61.55

3.3 X-ray Absorption Spectroscopy (XAS) on the Cu K-edge

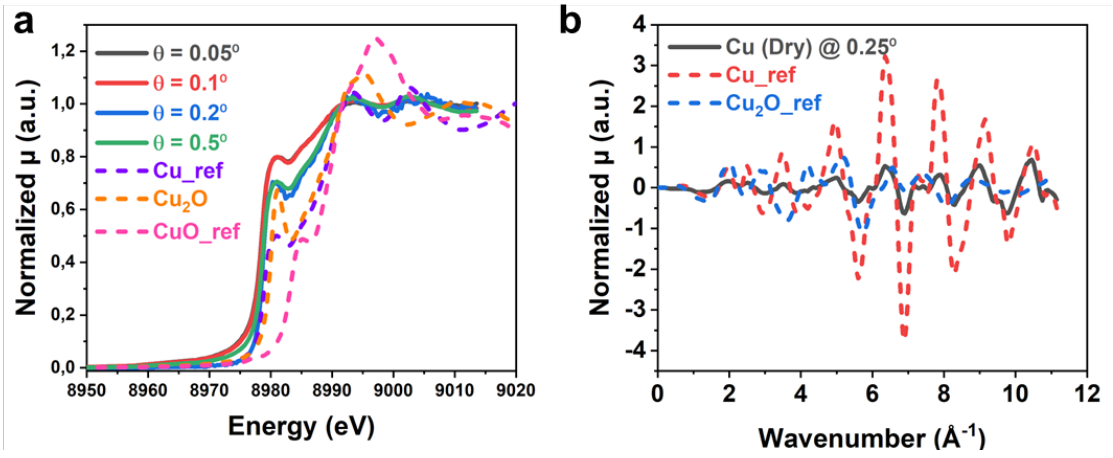

Figure S5 ***Operando GIXAS surface sensitivity verification on Cu****: a) XANES region at different grazing incident angles. Solid lines: XANES scans at various incident angle ϑ; dash lines: reference scans of different Cu oxidation state that were previously taken at the same beamline with the identical setup* [2]*. The stronger absorption intensity at ϑ < 0.2° at the edge energy (~ 9 keV) compared to ϑ ≥ 0.2° indicates the more oxidative Cu state. However, a slightly large incident angle is necessary to compensate the weak absorption intensity. Therefore, 0.25° was chosen as the incident angle for the following GIXAS measurements. B) EXAFS plotted in the k space at ϑ 0.25°. Solid line: scan plotted in the k space at the incident angle ϑ 0.25°. Dashed lines: reference scans of Cu and Cu₂O.*

Table S4 ***Operando GIXAS surface sensitivity verification:*** *attenuation and penetration depth calculation at α = 0.25°, E = 9 keV*

Sample	Density (g/cm3)	Penetration depth (nm)[¤]	Lattice spacing (Å)[£]	Penetrated monolayer numbers
Cu	8.96	2.89	2.08	13.89
Ag	10.49	2.53	2.35	10.77

[¤] Penetration depth was calculated based on Beer-Lambert law.

[£] Lattice spacing was calculated from XRD, based on (111) facet for both Cu and Ag, as it is the most prominent phase shown in XRD.

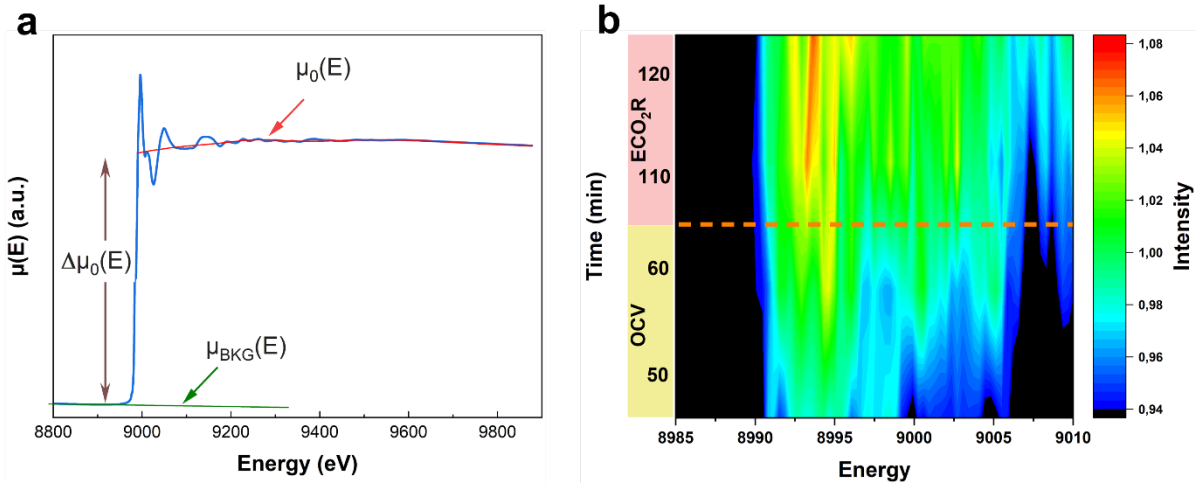

Figure S6 ***a) Illustration of XANES data normalization****: the raw data ($\mu(E)$) is extracted by the sooth background ($\mu_{BKG}(E)$), and divided by peak height ($\Delta\mu_0(E)$). This is to eliminate the influence of energy absorbed by other compartments other than the sample itself. In the case of CuAg alloy, the energy can also be absorbed by Ay atoms in the pre-edge region. $\mu_0(E)$ is the smooth "bare-atom" background in the EXAFS fine-structure function and is not for XANES.* ***b) Heat map of operando XAS scans ay the Cu K-edge in the zoomed in XANES region*** *of 8985-9010 eV of the $Cu_{80}Ag_{20}$ sample.*

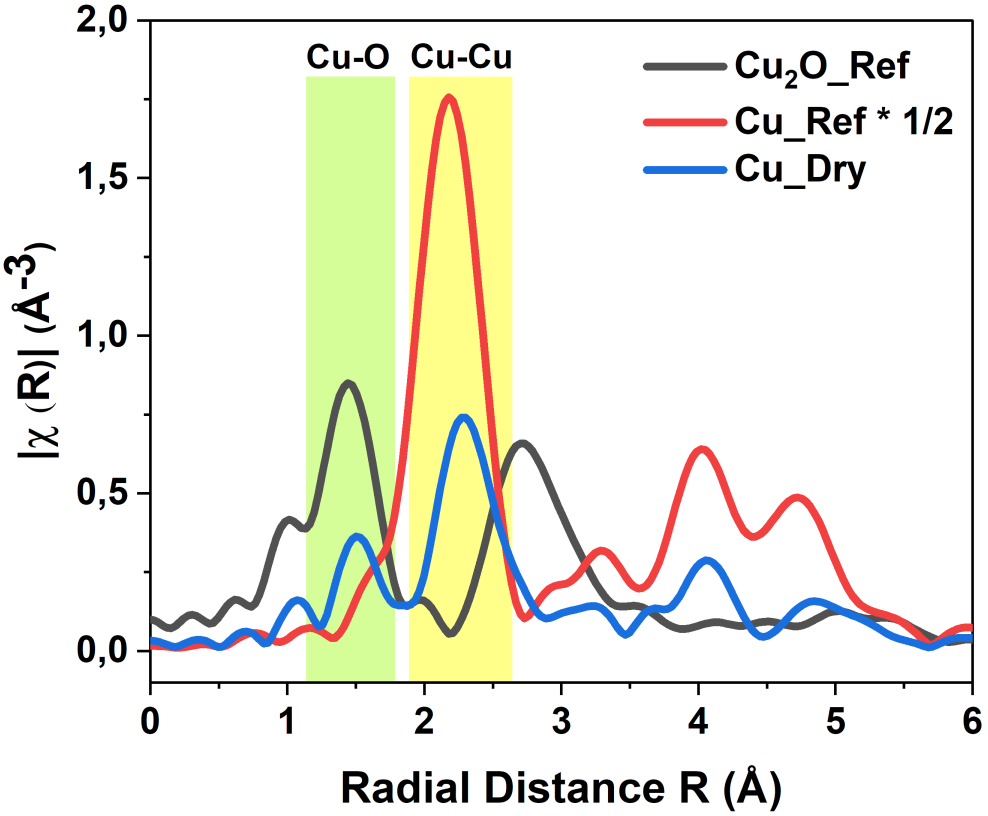

Figure S7 ***XAS R space (k-2 weight) peak identification on the Cu K-edge.***

In order to investigate how the electronic interaction contributes to the facilitated acetaldehyde and other carbonyl production, EXAFS measurements on the Cu-edge were Fourier-transformed to radial distance R (i.e., R space) to inspect its local chemical environment. Figure S6 gives a primary assignment of peak positions in the pure Cu sample compared with the metallic and Cu_2O references, where the interatomic distance information surrounding the central atom (i.e., Cu) is given as the R-value. Since atoms in the first shell predominantly contribute to the coordination environment of the central atom [5], [6], only R values below 3 Å are considered in this work. This is because 3 Å is normally the maximal bond length of the first shell and greater R numbers usually suggest atoms beyond the first shell or multiple scattering [7]. The peak at R ~2.25 Å is assigned to the first Cu-Cu shell (all R values in this work are phase uncorrected without further notice), while the peak located at ~1.6 Å is attributed to the first Cu-O shell, which agrees with the previous studies [8], [9].

Figures S7b and S7c depicted R space starting after 30 minutes of testing (Cu-30 min) on Cu and $Cu_{80}Ag_{20}$, respectively. The observed peaks can be attributed to two main areas contributed by different atomic shells, as compared to Cu and Cu_2O references (Figure 8a). The peak centered at ~R 1.5 Å is usually assigned to the Cu-O or Cu-C shell, which is normally attributed as the indication of CuO_x [5], [10]. However, our GIXRD (Figure 5) and XANES (Figure 6a) results have pointed out that Cu was in its metallic state after the first 20 min. Additionally, considering that all intermediates produced during eCO2RR bind on the Cu surface with either C or O atom(s), and that EXAFS only indicates the existence of an atom at a given distance while fails in atom identification, one potential explanation

for peak B is the adsorption of intermediate species. Therefore, the greatly attenuated peak B upon Ag adsorption might suggest a suppressed intermediate adsorption upon Ag incorporation.

The peak centered at ~R 2.25 Å is normally attributed to the first Cu-Cu or Cu-Ag shell [8], [10], [11]. Again, since EXFAS does not identify the neighboring atoms, and considering the close atomic number of Cu and Ag, both shells can contribute to this wide peak. Additionally, considering that XRD results (Figure 5) indicate the co-existence of two phases in the sample, one to be Cu-rich (where Cu is the majority while Ag is the minority) and the other Ag-rich (where Cu is the minority while Ag is the majority), and that EXAFS gives an averaged information for all the detected Cu atoms, the current peak at ~R 2.25 Å exhibits the interatomic bond distance convoluted with six circumstances upon Ag introduction: i) Cu-Cu right next to Ag in the Cu-rich phase, ii) Cu-Cu outreached the close neighbor of Ag in the Cu-rich phase, iii) Cu-Ag in the Cu-rich phase, iv) Cu-Cu right next to Ag in the Ag-rich phase, v) Cu-Cu outreach the closest neighbor of Ag in the Ag-rich phase, and vi) Cu-Ag in the Ag-rich phase. With such a complicated and convoluted information, it is difficult to draw any concrete conclusion on the strain effect of Ag introduction on the Cu-Cu bond.

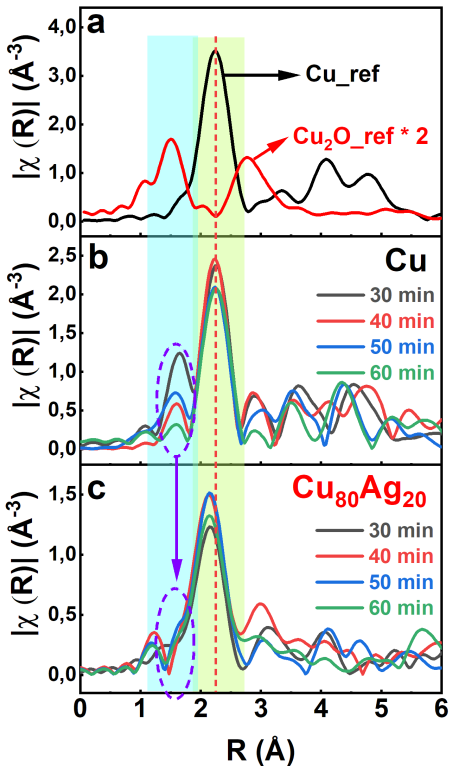

Figure S8 ***Fourier-transformed EXAFS R space spectra (k-2 weight) on the Cu K-edge*** *on a) Cu and Cu_2O references, b) pure Cu sample, and c) $Cu_{80}Ag_{20}$ sample as a function of time during eCO2RR.*

Ag L_3-edge (~ 3.4 keV) tender XANES was performed at beamline 4-3 using a LN2 cooled Si (111) monochromator at φ =0°, in the fluorescence mode with a Lytle detector. A custom-designed back illumination bottle cell allowed the X-ray incident to transmit [12]. Owing to the soft excitation energy required for Ag L_3-edge, the catalysts were deposited on an ultra-thin 7.5 µm thick Kapton foil to mitigate X-ray attenuation. The layer configuration from the bottom (right next to the substrate) to the top is as the following (Figure S1): i) Ti interlayer (~10 nm) providing a better adhesion); ii) Cu

sublayer (~ 100 nm) to help maintain the mechanical stability without introducing foreign elements in addition to Cu and Ag during deposition; and iii) the catalyst layer CuAg (~ 5 nm), which is so thin that the incident X-ray beam can easily reach the catalyst/electrolyte interface. The total transmission at the Ag L-edge energy (~3.35 keV) was calculated to be above 85% [13]. During the *operando* XANES scans, CO_2 was continuously purged in the electrolyte at 10 sccm. A graphite rod (Ted Pella) and the same miniature Ag/AgCl electrode as abovementioned functioned as the counter and reference electrode, respectively. While XANES experiments were also employed to record the Ag L_3-edge, these variations were quite small and were relatively inconclusive.

3.4 X-ray Absorption Spectroscopy (XAS) on the Ag L-edg

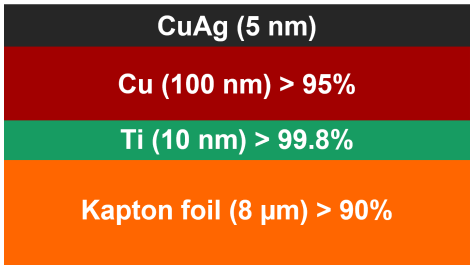

Figure S9 ***Sample configuration and X-ray transmission of each layer*** *of back-scattered bottle cell used for XAS measurements on the Ag L_3-edge at beamline 4-3*

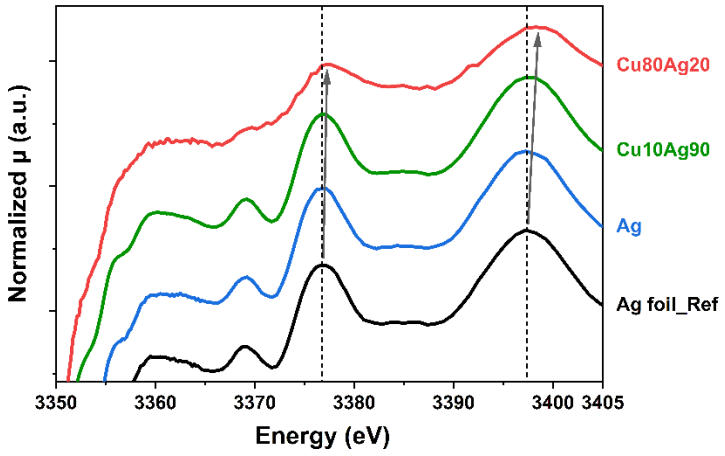

Figure S10 ***Operando XAS scans at Ag L3-edge in the near-edge region (XANES)*** *durinng eCO2RR of samples with different Ag content, compared with the Ag foil reference, indicated by dashed lines. Arrows emphasize peak position shift.*

4. COMPUTATIONAL METHODS

The first principles analyses have been performed by density functional theory (DFT) calculations applying the Vienna ab initio package (VASP) [14]. A plane wave cut-off energy of 500 eV was used throughout, combined with the BEEF-vdW exchange correlation functional [15]. Periodic boundary conditions where applied and the number of k-points were varied based on the respective unit cell sizes. For surface calculations, a vacuum layer of at least 14 Å was added perpendicular to the slab surface, only one k-point was applied in this direction together with a dipole correction to avoid artificial interaction of repeated slabs. The charge distributions in the CuAg compositions were determined via Bader charge decomposition. Both the bulk and surface compositions at varying Cu/Ag ratios were sampled by comparing all symmetrically inequivalent atom distributions and optimizing both the atomic positions and lattice cell parameters. Bulk structures consisting of up to 64 atoms were considered. The most stable structures at each simulated CuAg composition were chosen for the analyses in this article. Segregation energies were calculated as the potential energy difference of a 6-layer thick Cu-slab being doped by Ag on the surface or in the 4th layer.

All theoretical data and analysis routines can be retrieved from https://gitlab.com/gkastlun/cuag_for_c2.git.

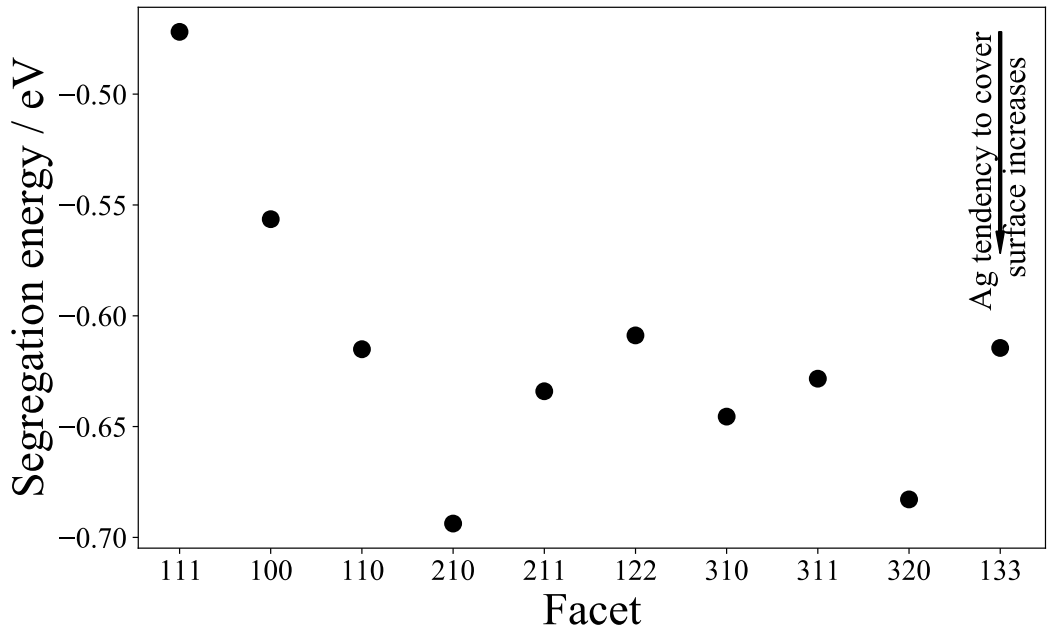

Figure S11 Surface segregation energy of dilute Ag in Cu on a series of surface facets

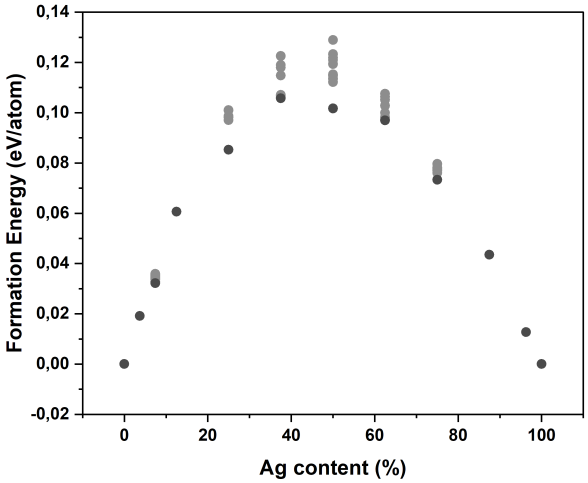

Figure S12 DFT-Calculated formation energies of CuAg crystals with varying composition. All possible CuAg arrangements in 2x2x2 and 3x3x3 unit cells were sampled. No stable phase of a CuAg alloy has been identified

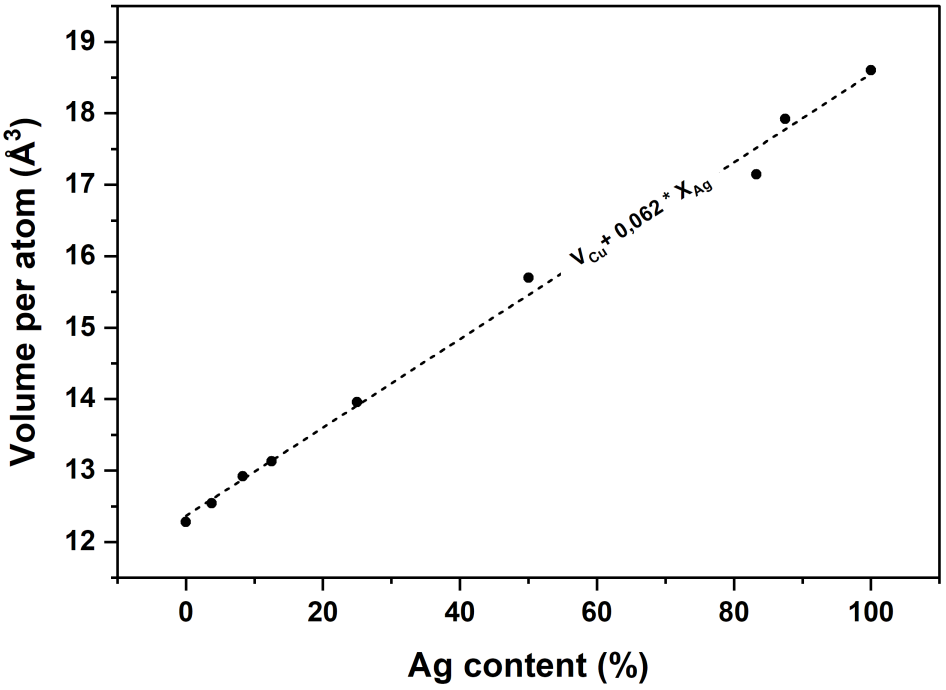

Figure S13 DFT-Calculated volume per atom in a CuAg bulk crystal in dependence of the Ag content. The volume per atom was chosen instead of the lattice constant as varying arrangements of Ag in Cu lead to slight deviations from the cubic symmetry into a tetragonal crystal.

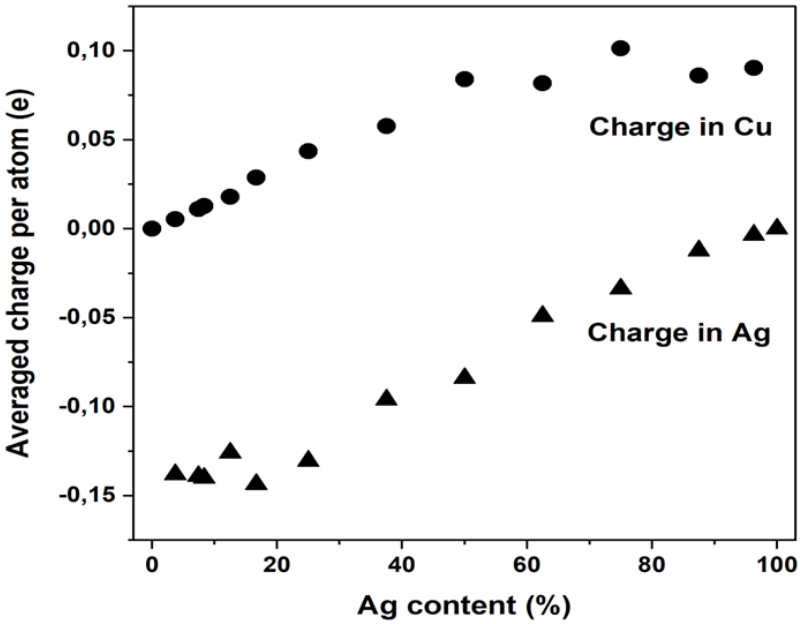

Figure S14 Net mean charge per atom for Cu and Ag atoms in a bulk fcc crystal of varying composition, resulting from Bader charge analysis.

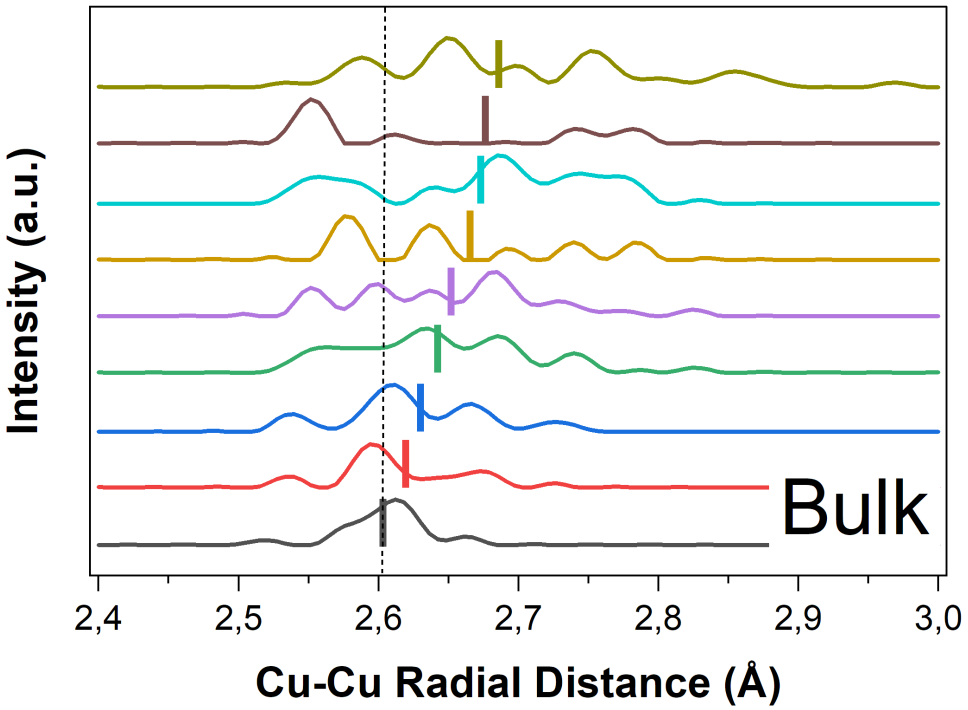

Figure S15 DFT calculated Cu-Cu radial distance in CuxAg100-x at varying Ag content right next to the introduced Ag atoms in bulk.

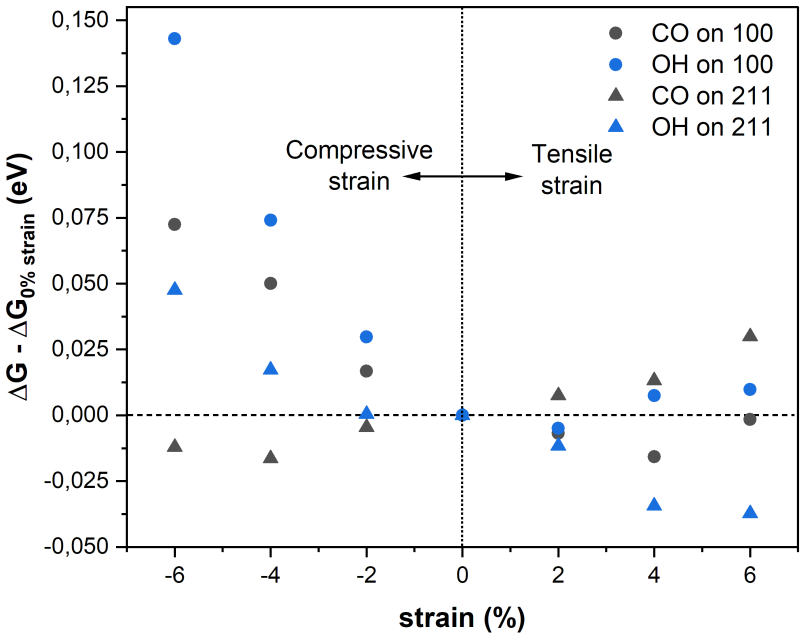

*Figure S16 DFT calculated binding energies of *CO and *OH on the (100) and (211) facets of Cu at varying amounts of strain on the crystal.*

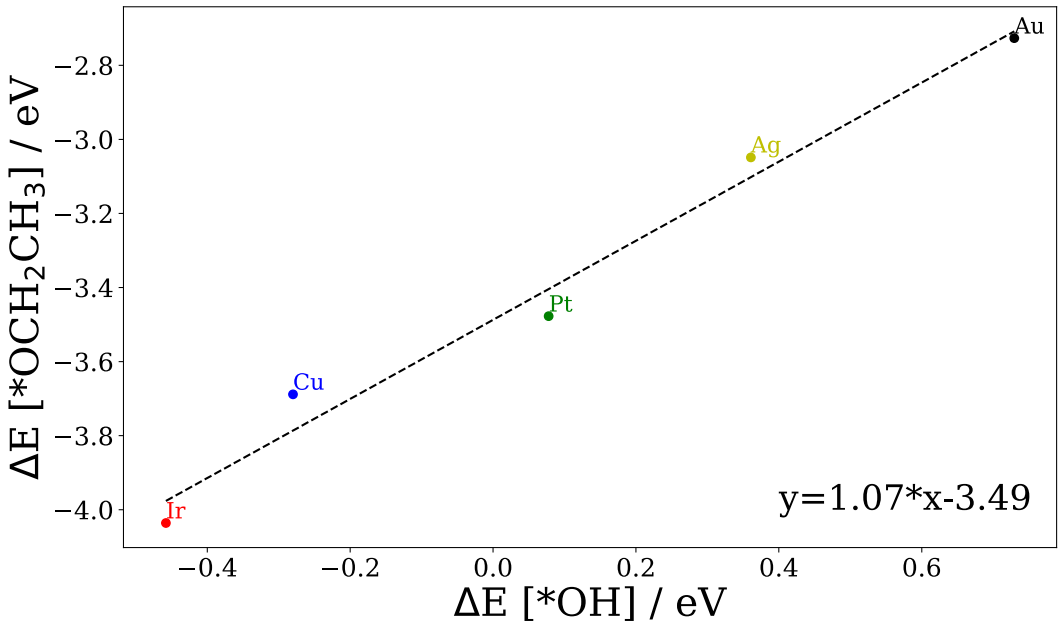

*Figure S17 DFT calculated scaling line of *OCH_2CH_3 with *OH, justifying the use of the latter as a descriptor for the binding of oxygenate intermediates.*

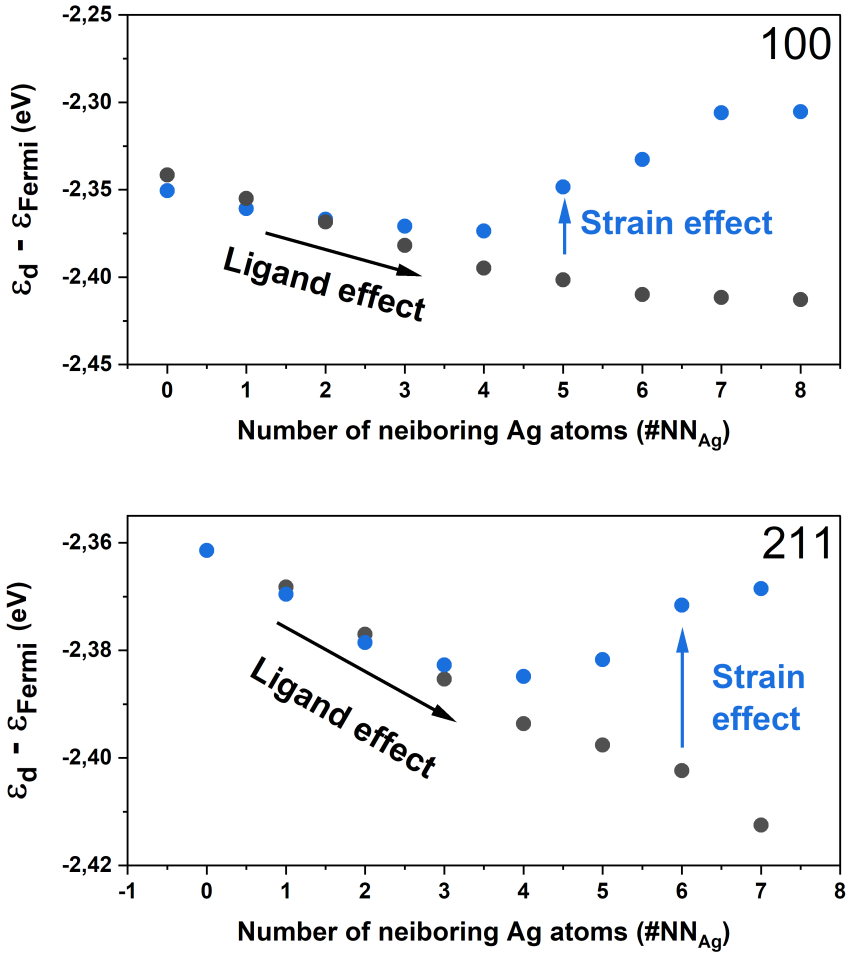

Figure S18 DFT calculated Cu d-band centers in dependency of the number of Ag nearest neighbors.

5. REFERENCES

[1] J. A. Zamora Zeledón, A. Jackson, M. B. Stevens, G. A. Kamat, and T. F. Jaramillo, "Methods—A Practical Approach to the Reversible Hydrogen Electrode Scale," *J. Electrochem. Soc.*, vol. 169, no. 6, p. 066505, 2022, doi: 10.1149/1945-7111/ac71d1.

[2] M. Farmand *et al.*, "Electrochemical flow cell enabling: Operando probing of electrocatalyst surfaces by X-ray spectroscopy and diffraction," *Phys. Chem. Chem. Phys.*, vol. 21, no. 10, pp. 5402–5408, 2019, doi: 10.1039/c8cp07423b.

[3] S. M. Webb, "SIXpack: A graphical user interface for XAS analysis using IFEFFIT," *Phys. Scr. T*, vol. T115, pp. 1011–1014, 2005, doi: 10.1238/Physica.Topical.115a01011.

[4] B. Ravel and M. Newville, "ATHENA, ARTEMIS, HEPHAESTUS: Data analysis for X-ray absorption spectroscopy using IFEFFIT," *J. Synchrotron Radiat.*, vol. 12, no. 4, pp. 537–541, 2005, doi: 10.1107/S0909049505012719.

[5] A. Herzog *et al.*, "Operando Investigation of Ag-Decorated Cu2O Nanocube Catalysts with Enhanced CO2 Electroreduction toward Liquid Products," *Angew. Chemie - Int. Ed.*, vol. 60, no. 13, pp. 7426–7435, 2021, doi: 10.1002/anie.202017070.

[6] X. Wang *et al.*, "Efficient upgrading of CO to C3 fuel using asymmetric C-C coupling active sites," *Nat. Commun.*, vol. 10, no. 1, p. 5186, Dec. 2019, doi: 10.1038/s41467-019-13190-6.

[7] M. Newville, "Fundamentals of XAFS," *Rev. Mineral. Geochemistry*, vol. 78, no. 1, pp. 33–74, Jan. 2014, doi: 10.2138/rmg.2014.78.2.

[8] C. J. Chang *et al.*, "Dynamic Reoxidation/Reduction-Driven Atomic Interdiffusion for Highly Selective CO2Reduction toward Methane," *J. Am. Chem. Soc.*, vol. 142, no. 28, pp. 12119–12132, 2020, doi: 10.1021/jacs.0c01859.

[9] Y. Xu *et al.*, "Tuning the Selectivity of Liquid Products of CO2RR by Cu-Ag Alloying," *ACS Applied Materials and Interfaces*, vol. 14, no. 9. pp. 11567–11574, 2022, doi: 10.1021/acsami.2c00593.

[10] T. T. H. Hoang *et al.*, "Nanoporous Copper-Silver Alloys by Additive-Controlled Electrodeposition for the Selective Electroreduction of CO2 to Ethylene and Ethanol," *J. Am. Chem. Soc.*, vol. 140, no. 17, pp. 5791–5797, 2018, doi: 10.1021/jacs.8b01868.

[11] T. Kottakkat *et al.*, "Electrodeposited AgCu Foam Catalysts for Enhanced Reduction of CO2 to CO," *ACS Appl. Mater. Interfaces*, vol. 11, no. 16, pp. 14734–14744, 2019, doi: 10.1021/acsami.8b22071.

[12] B. M. Gibbons *et al.*, "In Situ X-Ray Absorption Spectroscopy Disentangles the Roles of Copper and Silver in a Bimetallic Catalyst for the Oxygen Reduction Reaction," *Chem. Mater.*, vol. 32, no. 5, pp. 1819–1827, 2020, doi: 10.1021/acs.chemmater.9b03963.

[13] B. L. Henke, E. M. Gullikson, and J. C. Davis, "X-ray interactions: Photoabsorption, scattering, transmission, and reflection at E = 50-30, 000 eV, Z = 1-92," *Atomic Data and Nuclear Data Tables*, vol. 54, no. 2. pp. 181–342, 1993, doi: 10.1006/adnd.1993.1013.

[14] G. Kresse and J. Furthmüller, "Efficiency of ab-initio total energy calculations for metals and semiconductors using a plane-wave basis set," *Comput. Mater. Sci.*, vol. 6, no. 1, pp. 15–50, 1996, doi: 10.1016/0927-0256(96)00008-0.

[15] J. Wellendorff *et al.*, "Density functionals for surface science: Exchange-correlation model development with Bayesian error estimation," *Phys. Rev. B*, vol. 85, no. 23, p. 235149, Jun.

2012, doi: 10.1103/PhysRevB.85.235149.